An implantable optical fibre sensing system for multiplexed brain monitoring

Zhang, Yuqian (张雨倩)

Department of Chemical Engineering

Imperial College London

Submitted for the Degree of Doctor of Philosophy and the Diploma of Imperial College London

May 2024

Declaration of Originality

I hereby declare that the work presented in this thesis is the result of my own original work and any reference to the work of others has been appropriately cited.

Yuqian Zhang,

May 2024

Copyright Declaration

The copyright of this thesis rests with the author. Unless otherwise indicated, its contents are licensed under a Creative Commons Attribution-Non Commercial 4.0 International Licence (CC BY-NC).

Under this licence, you may copy and redistribute the material in any medium or format. You may also create and distribute modified versions of the work. This is on the condition that: you credit the author and do not use it, or any derivative works, for a commercial purpose.

When reusing or sharing this work, ensure you make the licence terms clear to others by naming the licence and linking to the licence text. Where a work has been adapted, you should indicate that the work has been changed and describe those changes.

Please seek permission from the copyright holder for uses of this work that are not included in this licence or permitted under UK Copyright Law.

Abstract

Brain monitoring is pivotal in medical diagnostics and treatment, offering real-time insights into brain function that empower healthcare professionals in the effective management of various brain disorders. However, traditional monitoring methods like microdialysis-based or electrochemical sensor-based systems suffer from limitations such as low temporal resolutions, insufficient selectivity, and poor stability. Recent advancements in optical sensing, microfabrication, signal processing, and machine learning present innovative solutions to surmount these constraints and enhance monitoring capabilities. Therefore, this thesis aims to develop an optical fibre sensing system for implantable and multiplexed brain monitoring. In its initial phase, a reflection optical fibre-based sensing system was engineered to enable the continuous monitoring of four brain biomarkers—pH, oxygenation, glucose, and temperature—simultaneously. Leveraging optical sensing techniques and novel film fabrication methods, highly sensitive and selective biosensors were developed and seamlessly integrated onto the tip of a reflection fibre for four distinct brain biomarkers monitoring. To further improve the sensing performance, in the subsequent stage, an optical fibre bundle-based sensing system was proposed, aiming to incorporate two additional biomarkers, Na^+ and Ca^{2+}, while reducing the sensor size for minimally invasive measurements. Polymer-encapsulated fluorescent receptors were adopted for the sensor fabrication to enhance the sensing sensitivity and reversibility. Characterisation test results affirmed the sensors' high sensitivity, specificity, reversibility, and environmental robustness in measuring all six biomarkers. Mathematical modelling algorithms, including machine learning and deep learning models, were employed for spectrum processing, environmental compensation, and precise biomarker concentration readings. The proposed sensing system successfully identified three commonly encountered brain complications accurately using ex vivo brain models. In the end, a fully automated sensing system was prototyped by integrating the optical components and algorithms, enabling continuous online brain biomarker monitoring. The proposed multiplexed brain monitoring system underwent successful validation using real human cerebrospinal fluid samples, showcasing its potential for clinical application.

Acknowledgements

This thesis is only possible because of the immeasurable love, unwavering support, inspiration, and discipline generously bestowed upon me from a huge number of individuals, each deserving my heartfelt acknowledgment and deepest gratitude.

First and foremost, I would like to extend my deepest gratitude to my PhD supervisor Dr. Ali K. Yetisen for offering me this invaluable and unforgettable opportunity to work with him at his esteemed research group. I am grateful for his invaluable mentorship and unwavering support that extended beyond academic realms, shaping every facet of my life. His guidance provided diverse training opportunities that not only enhanced my research prowess but also honed my soft skills, which I am sure will be extremely beneficial in my following adventures.

I would like to express sincere gratitude to our research associate Dr. Yubing Hu and Prof. Nan jiang for their generous guidance, steadfast support, and unwavering belief in my capabilities during my studies. I am also thankful for all the memorable moments we have shared together that are beyond our research duties. Additionally, I am thankful to Imperial College London, Department of Chemical Engineering, for the esteemed departmental scholarship that has alleviated financial concerns, allowing me to wholeheartedly focus on my research during a time of global economic uncertainty.

Furthermore, my heartfelt appreciation extends to my colleagues, Dr. Samuel Davis, Yuqi Shi, Yue Wu, and Yihan Zhang for all the help and assistance throughout my research. Special shot out to my colleague Dr. Naihan Zhang, Dr. Aydan Agan, Eleni Chatzilakou, Fu Liu, and Siying Liu who have also become my lifelong friends. Thank you all for always having my back and encouraging me. Your presence not only enriched my research endeavours but also provided unwavering support during both challenging and triumphant times. Thank you for making my PhD life so amazing and unforgettable.

I am profoundly grateful to my parents for their unwavering love, encouragement, and sacrifices throughout my academic journey. Their boundless support, both emotionally and practically, has always made me feel secure no matter where my journey led, and it has been a constant source of strength. Their sacrifices and unwavering belief in myself have been instrumental in reaching this milestone.

In the end, I want to thank myself for the hard work and unyielding dedication throughout my student life. The research journey can often be lonely and daunting. I commend myself for fearlessly embracing the unknown and tackling challenges beyond my comfort zone. In the past years, I once hesitated, stumbled, but I am grateful that I hold through, chose growth, and ventured into uncharted territories. Having a PhD marks the beginning of the next chapter in my journey. I will always be loyal to myself running towards the ideal and freedom in my future adventures.

Table of Contents

Declaration of Originality 2
Copyright Declaration 2
Abstract 3
Acknowledgements 4
List of Figures 8
List of Tables 12
List of Abbreviations 13
List of Publications 17
The following paper has been submitted for publication. 17
Chapter 1 Introduction 18
1.1 Research background 18
1.2 Thesis objective and outline 20
Chapter 2 Literature Review 23
2.1 History of brain neurochemical monitoring 23
2.2 Commonly monitored brain biomarkers 25
2.2.1 Brain metabolites 25
2.2.2 Brain neurotransmitters 30
2.3 Sampling methods for brain neurochemical monitoring 32
2.4 Electrochemistry methods for in vivo brain neurochemical monitoring 37
2.4.1 Principle of amperometric sensor 37
2.4.2 Principle of voltametric sensor 38
2.4.3 Applications of EC sensors in brain monitoring 39
2.5 Optical spectroscopy methods for in vivo brain neurochemical monitoring 44
2.5.1 Fluorescence spectroscopy 45
2.5.2 Raman spectroscopy 48
2.5.3 Near infrared spectroscopy (NIRS) 51
2.5.4 Surface plasmon resonance (SPR) spectroscopy 52
2.5.5 Optical fibre sensors 55
2.6 Computational methods for sensing signal processing and readout 59
2.6.1 Machine learning regression models 60
2.6.2 Regression model evaluation metrics 62
2.6.3 Application example 63
2.7 Conclusion 67
Chapter 3 Reflection-Based Multiplexed Optical Fibre Sensors for Dynamic Brain Monitoring 70
3.1 Introduction 70
3.2 System design and development 71

3.3 Materials and methods 76
3.3.1 Chemical reagents and materials 76
3.3.2 Instrument and Experimental Setup 77
3.3.3 pH Sensor fabrication and characterisation 78
3.3.4 Temperature Sensor fabrication and characterisation 83
3.3.5 DO sensor fabrication and characterisation 84
3.3.6 Glucose sensor fabrication and characterisation 87
3.3.7 ACSF and ex vivo measurement 88
3.3.8 Algorithm Design for signal post processing 89
3.3.9 *Ex vivo* measurement using lamb brain models 95
3.3.10 Cellular studies on the biocompatibility of the multiplexed fibre sensor 98
3.3.11 Miniaturization of the multiplexed fibre sensor 98
3.4 Obtained optical spectra using the system 99
3.5 Performances of the optical fibre pH sensor. 101
3.5.1 Encapsulation matrix optimization 102
3.5.2 pH sensing results 104
3.6 Performances of the optical fibre temperature sensor 108
3.7 Performances of the optical fibre DO sensor 112
3.8 Performances of the optical fibre glucose sensor 117
3.9 Multiplexed measurement 123
3.9.1 Multiplexed calibration of the optical fibre sensing system 123
3.9.2 Regression model-based concentration calculation 126
3.9.3 Ex vivo validation for continuous monitoring of brain biomarkers 129
3.10 System biocompatibility and miniaturization 133
3.11 Conclusion 137
Chapter 4 Optical Fibre Bundle Sensing System for Multiple Brain Biomarkers Measurement 139
4.1 Introduction 139
4.2 Design and construction of optical fibre bundle sensing system 140
4.3 Design of the 6 biomarker sensing films 147
4.4 Materials and Methods 150
4.4.1 Materials and equipment 150
4.4.2 Sensor Fabrication 152
4.4.3 Sensing film coating methods 155
4.4.4 Sensor characterisation 156
4.4.5 Multiplexed sensing characterisation 164
4.4.6 Signal deconvolutional algorithms 165
4.4.7 System validation using ex vivo brain models 170
4.5 Characterisation of individual fluorescent sensors 172

4.5.1 Temperature sensor characterisation 172
4.5.2 Dissolved oxygen (DO) sensor characterisation 175
4.5.3 pH sensor characterisation 178
4.5.4 Na^+ sensor characterisation 180
4.5.5 Ca^{2+} sensor characterisation 183
4.5.6 Glucose sensor characterisation 187
4.6 Multiplexed sensing and concentration calculation 190
4.6.1 Multiplexed sensing calibration 190
4.6.2 Multivariate regression-based concentration calculation 191
4.7 Multiplexed sensing validation 196
4.8 Conclusion 198
Chapter 5 A Fully Automated and AI-assisted Optical Fibre Sensing System for Multiplexed Biomarker Monitoring 201
5.1 Fully-automated and multiplexed sensing system 201
5.2 Materials and Methods 203
5.2.1 Machine learning model for multiplexed biomarker concentration prediction 204
5.2.2 Deep Learning model for multiplexed biomarker prediction 212
5.2.3 Fully automated brain monitoring system calibration 218
5.2.4 Real time monitoring using clinical human CSF sample 219
5.3 Multiplexed sensing system characterisation using aCSF sample 222
5.4 Machine learning for multi-biomarker concentration calculation 225
5.5 CNN-based multitask learning for biomarker calculation 230
5.6 System prototyping and validation using clinical CSF samples 234
5.6.1 System prototyping and assembling 234
5.6.2 Continuous measurement using clinical human CSF samples 235
5.7 Conclusion 237
Chapter 6 Conclusions and Future Work 238
6.1 Discussions 238
6.2 Conclusions 242
6.3 Future work 244
References 247
Appendices 268
1. Readout box design and UI design 268
2. Results—UI design 269
2.1 Control panel 270
2.2 Calibration panel 272
2.3 Measurement panel 273
Permissions summary 276

List of Figures

Figure 2-1 Major events associated with brain neurochemical monitoring. 24
Figure 2-2 Recent technologies for brain neurochemical monitoring. 25
Figure 2-3 Energy metabolism of brain. 27
Figure 2-4 Principle of microdialysis 33
Figure 2-5. Comparison between two sampling methods.. 34
Figure 2-6. 3D printed microfluidic systems for brain neurochemicals monitoring. 35
Figure 2-7. A microdialysis/droplet-based microfluidic chip system for in vivo measurement of the HS^- concentration in rat's brain. 36
Figure 2-8. An integrated push-pull sampling system with a droplet-based microfluidics system for the detection of neurochemicals. 37
Figure 2-9. Schematic of amperometric sensing of glucose. 38
Figure 2-10. Amperometric sensor for multi-analyte monitoring. 40
Figure 2-11. A silicon-based EC device for choline and glutamate sensing. 41
Figure 2-12. A multichannel flexible optoelectronic fibre device for wireless AA sensing and opto stimulation. 42
Figure 2-14. Primate-use platform for chronic dopamine sensing in vivo 44
Figure 2-15. Schematic representation of sensing principles of four technology. 44
Figure 2-16. Principle of fluorescence spectroscopy. 45
Figure 2-17. Miniaturized, ultrathin, lightweight wireless photometry systems for deep-brain Ca2+ measurements 48
Figure 2-18. Principle of Raman spectroscopy. 49
Figure 2-19. SERS sensor for glucose and lactate detection 50
Figure 2-20. Schematic of a non-invasive neurometabolic optical monitor for the monitoring of brain oxygen saturation and blood flow. 52
Figure 2-21. An SPR based optical-electrochemical nanosensor for dopamine and serotonin sensing. 53
Figure 2-22. An SPR sensor for the detection of brain DA 55
Figure 2-23. Optical fibre oxygen sensor for muscular oxygenation measurement 57
Figure 2-25. Recent advances in optical fibre sensors. 59
Figure 2-26. Comparisons of PCR and PLSR in prediction analyte concentrations. 65
Figure 2-27. Methods in circuit design and post signal processing algorithm. 66
Figure 3-1. A multiplexed optical fibre-based sensing platform for dynamic monitoring of biomarkers in brain CSF.. 73
Figure 3-2. Design and photograph of the sensing probe and system. 74

Figure 3-3.Photograph of the integrated AI-based multiplexed sensing platform 75
Figure 3-4. DO measurement set u 85
Figure 3-5. Algorithm flow chart of the AI model for biomarker level prediction. 90
Figure 3-6. Spectrum feature extraction. 91
Figure 3-7. Grid search for hyperparameter tuning. 94
Figure 3-8. Grid search python code for execution..... 95
Figure 3-9. Sensing results with and without isolation film. 100
Figure 3-10. Example of the raw data and computational methods for the calculation of normalized reflectance spectrum 101
Figure 3-11. Optical fibre pH sensor sensing principle, fabrication method, and structure..... 101
Figure 3-12. Morphology tests of the optical sensing film.. 102
Figure 3-13. Optimization of the sensing films 104
Figure 3-14. Calibration curves of the pH sensing films fabricated with different TEOS and GLYMO molar ratios. 104
Figure 3-15. Calibration of the optical fibre pH sensor in PBS solutions..... 105
Figure 3-16. 1931 CIE chromaticity diagram.. 105
Figure 3-17. Reversibility test of the pH sensor 106
Figure 3-18. Characterisation of the pH sensor for continuous monitoring..... 107
Figure 3-19. Environmental robustness of the pH sensor. 107
Figure 3-20. Selectivity test of the pH sensor. 108
Figure 3-21. Schematic demonstration of the optical fibre temperature sensor..... 109
Figure 3-22. Calibration of the optical fibre temperature sensor in PBS solution. 110
Figure 3-23. 1931 CIE chromaticity diagram...... 111
Figure 3-24. Repeatability of the temperature sensor for temperature measurement 111
Figure 3-25. Stability and pressure dependence of the pH sensor..... *112*
Figure 3-26. Schematic demonstration of the optical fibre DO sensor, including the sensing principle and structure. 113
Figure 3-27. Characterisations of the optical fibre DO sensor 114
Figure 3-28. Response time of the DO sensor 115
Figure 3-29. Characterisation of the DO sensor for continuous monitoring..... 116
Figure 3-30. Environmental robustness tests of the DO sensor. 117
Figure 3-31. Schematic demonstration of the optical fibre glucose sensor 118
Figure 3-32. Characterisations of the optical fibre glucose sensor..... 119
Figure 3-33. CIE image of the sensing film color..... 120
Figure 3-34. Characterisation of the glucose sensor. 121
Figure 3-35. Environmental dependence tests of the glucose sensor..... 122
Figure 3-36. Characterisations of the multiplexed optical fibre sensor i]..... 124

Figure 3-37 Reversibility test of the multiplexed optical fibre sensor in aCSF 125
Figure 3-38. Stability measurement in aCSF buffer solutions. 126
Figure 3-39. Machine learning model results for biomarker concentration prediction..... 129
Figure 3-40. Photographs of the ex vivo experimental setup and details 129
Figure 3-41. Ex vivo measurements using the multiplexed fibre sensor. 131
Figure 3-42. Multiplexed and dynamic monitoring for simulated TBI disease using an ex vivo lamb brain. 133
Figure 3-43. Biocompatibility and cytotoxicity study of the sensing film..... 134
Figure 3-44. Miniaturization of the optical fibre sensor. 136
Figure 4-1. Schematic of the optical fibre bundle sensing system for multiplexed biomarker monitoring in brain CSF..... 142
Figure 4-2. Schematic and photograph of the sensing system setup..... 143
Figure 4-3. Optical fibre bundle manufacturing and testing 145
Figure 4-4. Optimization of dip coating speed and layers 146
Figure 4-5. Schematic demonstration of the temperature sensing principle 172
Figure 4-6. Temperature probe Ru(dpy)3 concentration optimization..... 173
Figure 4-7. Characterisation of the optical fibre sensor for temperature monitoring. 174
Figure 4-8. Environmental dependence and selectivity of the temperature fibre sensor 175
Figure 4-9. Schematic demonstration of the design and principle of the DO sensor. 176
Figure 4-10. DO probe PdOEP concentration optimization. 176
Figure 4-11. Design and characterisation of the PdOEP-containing PDMS DO sensor..... 177
Figure 4-12. Environmental dependence and selectivity of the optical DO sensor. 178
Figure 4-13. pH probe HCC concentration optimization. 179
Figure 4-14. Design and characterisation of the HCC-containing sol-gel pH sensor 180
Figure 4-15. Design and characterisation of the optical fibre Na+ ion sensor..... 182
Figure 4-16. Sodium sensing probe CoroNa Green concentration optimization. 183
Figure 4-17. Schematic drawing of the Ca2+ ion sensor and sensing principle 184
Figure 4-18. Calcium ion sensor optimization. 185
Figure 4-19. Design and characterisation of the optical fibre Ca2+ sensor 186
Figure 4-20. Environmental dependence and selectivity of the Ca2+ sensor. 187
Figure 4-21. Schematic demonstration of the design and principle of the glucose sensor..... 188
Figure 4-22. Design and characterisation of the optical fibre glucose sensor..... 189
Figure 4-23. Environmental dependence and selectivity of the glucose sensor. 190
Figure 4-24. Multiplexed sensing using the designed optical fibre bundle. 191
Figure 4-25. Flowchart of the post-processing method. 192
Figure 4-26. Spectrum post processing. 192

Figure 4-27. Spectra postprocessing method and concentration prediction for sodium and temperature.. 193
Figure 4-28. Biomarker concentration prediction results using the proposed algorithms 194
Figure 4-29. Photobleaching compensation algorithm results for the 6 sensors. 195
Figure 4-30. Temperature and pH compensation algorithm results for the 6 sensors. 196
Figure 4-31. Multiplexed sensing using the optical fibre bundle sensors in lamb brain models with three mimicked brain complications in TBI. 198
Figure 5-1. A brain monitor based on optical sensors and computational software. 203
Figure 5-2. Pipeline for machine learning model development. 204
Figure 5-3. Merged signal of three optical spectra obtained with 405nm, 488nm, and 520nm lasers in one scan. 206
Figure 5-4. Feature extraction. 208
Figure 5-5. Tuned hyperparameter list for regression models 210
Figure 5-6. Dataset split methods for training, validation, and testing. 211
Figure 5-7. The architecture of CNN model. 213
Figure 5-8. Max pooling in CNN for feature dimension reduction. 215
Figure 5-9. Obtained spectrum after resizing before feeding into CNN models. 216
Figure 5-10. Proposed architecture of the CNN model. 218
Figure 5-11. Sensor characterisation using the multiplexed optical fibre bundle sensing system. 225
Figure 5-12. Feature evaluation and selection using Pearson correlation coefficient. 227
Figure 5-13. Performance of the Bayesian regression model on the calculation of 6 biomarker concentrations. 230
Figure 5-14. Optimization and fine tuning of hyperparameters of the CNN model 232
Figure 5-15. Final structure of the optimized CNN model. 233
Figure 5-16. Performance of the CNN model for 6 biomarker concentrations monitoring. 234
Figure 5-17. Design and photo of the readout using black acetal sheets. 235
Figure 5-18. Continuous monitoring of clinical human CSF sample using the prototyped system in spiking test. 237
Figure S1. Software design of the whole sensing system. 270
Figure S2. Main frame and control panel of the system, where user can select the measurement mode and sensing parameters. 271
Figure S3. UART protocol for laser control. 272
Figure S4. Calibration panel of the software. 273
Figure S5. Dynamic monitoring mode of the system and user readout frame. 274
Figure S6. Multiplexed monitoring mode of the system and the software readout frame. 275

List of Tables

Table 2-1 Summary of major brain neurochemicals 32
Table 2-2. Comparison between three sensing methods. 68
Table 3-1. Composition of sol-gel coating solutions 79
Table 3-2. Composition of interference solutions 81
Table 3-3. aCSF buffer preparation 88
Table 3-4. Feature extraction 92
Table 3-5. Hyperparamters for regression models 93
Table 3-6. Hyperparameters selected for each model 127
Table 3-7. Biomarker concentration prediction results using different regression models 128
Table 4-1. Commercially available fluorescent probes for Ca2+ and Na+ detection 254, 255. 149
Table 4-2. Selected fluorescent probes for the 6 target biomarkers. 150
Table 4-3. Characterisation of the 6 optical fibre sensors. 163
Table 4-4. Buffer solution preparation for multiplexed sensor characterisation 164
Table 4-5. aCSF buffer solution preparation for different brain scenarios. 171
Table 5-1. Buffer solution 1preparation for multiplexed sensor characterisation 219
Table 5-2. The tuned hyperparameters of extracted input obtaining from Grid search CV. 228
Table 5-3. Machine learning model results for 6 biomarker concentration calculation. 229
Table 5-4. Model performance with different hyperparameters 232
Table S1. Calibration buffer solutions 268

List of Abbreviations

artificial CSF (aCSF)

artificial Intelligence (AI)

adenosine diphosphate (ADP)

adenosine triphosphate (ATP)

atomic force microscope (AFM)

ascorbic acid (AA)

acetylcholine (Ach)

bromocresol green (BCG)

brain neurochemical monitoring (BNM)

3,3',5,5'-Tetrabromo-m-cresolsulfonphthalein (BCG)

calcium ions (Ca^{2+})

cyclic voltammetry (CV)

cerebrospinal fluid (CSF)

convolutional neural networks (CNN)

cholesteryl nonanoate (CN)

cholesteryl oleyl carbonate (COC)

cholesteryl benzoate (CB)

calcium chloride ($CaCl_2$)

dissolved oxygen (DO)

differential pulse voltammetry (DPV)

direct current (DC)

decision tree (DT)

dopamine (DA)

deionized (DI)

Dimethyl sulfoxide (DMSO)

electrochemistry (EC)

Electroactive (EA)

epinephrine (EP),

electroencephalography (EEG)

fast-scan cyclic voltammetry (FSCV)

Field Programmable Gate Array (FPGA)

glucose (Gluc)

glutamate(Glut)

glycidoxypropyltrimethoxysilane (GLYMO)

γ-aminobutyricacid (GABA)

high-performance liquid chromatography (HPLC)

hydrochloric acid (HCl)

7-Hydroxycoumarin-3-carboxylic acid (HCC)

dissociation constant (Kd)

jugular venous oxygen saturation (SjVO2)

intracranial pressure (ICP)

intensive care unit (ICU)

light-emitting diode (LED)

lactate (Lac)

linear regression (LR)

limit of detection (LOD)

least square regression (LSR)

microdialysis (MD)

mass spectroscopy (MS)

mean absolute error (MAE)

mean squared error (MSE)

multivariate curve regression (MCR)

N,N'-Methylenebisacrylamide (MBA)

magnetic resonance (MR)

machine learning (ML)

magnesium chloride ($MgCl_2$)

near-infrared spectroscopy (NIRS)

norepinephrine (NEP)

nitric acid (HNO_3)

Non-electroactive (NE)

Neurotransmitters (NTs)

3,3',5,5'-tetramethylbenzidine (TMB), glucose oxidase (GOD), and peroxidase (POD)

Pyruvate (Pyru)

peroxidase (POD)

phosphate buffered saline (PBS)

Polyethylene glycol (PEG)

poly(propyl methacrylate)(PPMA)

principle component regression (PCR), Partial Least Squares Regression, PLSR(PLSR)

2,3,7,8,12,13,17,18-Octaethyl-21H,23H-porphine palladium(II) (PdOEP,)

Poly(ethylene glycol) diacrylate (PEGDA)

random forest (RF)

reference electrode (RE)

root mean square error (RMSE)

sodium chloride (NaCl)

sodium ions (Na^+)

serotonin (5-HT),

potassium chloride (KCl)

sodium pyruvate (Pyru)

sodium phosphate dibasic (Na_2HPO_4)

sodium phosphate monobasic (NaH_2PO_4)

sodium hydroxide (NaOH)

tris(4,7-diphenyl-1,10-phenanthroline)ruthenium(II) dichloride complex (Ru(dpp))

Tris(2,2’-bipyridyl)dichlororuthenium(II) hexahydrate ($Ru(bpy)_3$

surface plasmon resonance spectroscopy (SPRS)

Support Vector Regression (SVR)

Support Vector Machine (SVM)

sodium nitrite ($NaNO_2$)

scanning electron microscope (SEM)

traumatic brain injury (TBI)

tetraethoxysilane (TEOS)

Tetrahydrofuran (THF)

tricarboxylic acid (TCA)

3,3’,5,5’-tetramethylbenzidine (TMB)

uric acid (UA)

universal asynchronous receiver transmitter (UART)

working electrode (WE)

zinc chloride ($ZnCl_2$)

List of Publications

The following papers have been published during my PhD studies.

1. Yuqian Zhang, Yubing Hu, et al., Ali K. Yetisen, “Multiplexed optical fiber sensors for dynamic brain monitoring”, Matter,189(10):113351, 2022.
2. Yuqian Zhang, Nan Jiang, Ali K. Yetisen, “Brain Neurochemical Monitoring.”, Biosensors and Bioelectronics,189(10):113351, 2022.

The following paper has been submitted for publication.

1. Yuqian Zhang, Yubing Hu, et al., Ali K. Yetisen, “An AI-assisted and Fully Automated Optical Fiber Sensing System for Multiplexed Brain Monitoring”, Advanced Materials, 2023.

Chapter 1 Introduction

1.1 Research background

Clinical monitoring and bedside monitoring play vital roles in medical diagnosis and treatment by providing real-time insights into physical function, enabling healthcare professionals to diagnose and manage various physical disorders effectively. In the intensive care unit (ICU) and other healthcare settings, brain monitoring serves as a critical component of patient care, aiding in the early detection of neurological abnormalities, monitoring the progression of brain injuries [1, 2], guiding treatment decisions [2, 3], and assessing the efficacy of therapeutic interventions[1]. In clinics, traditional monitoring techniques, such as electroencephalography (EEG) [4, 5], intracranial pressure (ICP) monitoring [6], and cerebral blood flow assessment [7], have greatly assisted clinicians in making clinical decisions and interventions.

Among various neurological disorders, traumatic brain injury (TBI) presents a major socioeconomic problem and is a leading cause of mortality and disability around the globe [8]. It is the leading cause of brain damage among children and young adults, and it plays a leading role in disability due to trauma [9]. TBI is characterized as a silent epidemic neurological disorder that may not reveal the severity of the issue in the initial medical check [10]. However, following the initial injury, TBI patients are at risk of experiencing secondary brain injury, which can lead to further and more severe neurological damage and complications [11]. Secondary brain injury occurs due to a cascade of complex physiological processes, including increased intracranial pressure, cerebral edema, reduced cerebral blood flow, and metabolic disturbances [11]. Therefore, effective medical monitoring plays a crucial role in preventing or mitigating secondary brain injury by allowing healthcare providers to closely monitor the patient's intracranial dynamics and neurophysiological parameters. It has been studied and reported that clinical monitoring of TBI patients could lead to early detection and ultimately prevention of secondary injury and potential complications [11]. However, current challenges in brain monitoring, including insufficient temporal resolution and limited biomarkers that can be monitored, may hinder continuous and prolonged monitoring, limiting the clinician's ability to obtain comprehensive and accurate information regarding the patient's brain health.

Currently, only limited metabolic or physical biomarkers are being routinely measured and monitored to follow the course of neurological related disorders or diseases such as TBI in the clinic[12]. The commonly used devices include brain oxygenation monitor together with brain pressure and temperature monitor and microdialysis system for brain neurochemical monitoring. However, these usually require several separated probes to be inserted in the brain tissue together, which can lead to an increased risk of infection[12]. Besides, the microdialysis system for brain neurochemical monitoring requires frequent bedside cerebrospinal fluid (CSF) sampling for a continuation of several days and it is an ex vivo method, which requires frequent human intervention and suffers from low temporal and spatial resolutions and unable to detect abrupt brain physiological changes.

In recent years, with the advances in material science, microfabrication, and analytical chemistry, numerous studies have been conducted to develop in situ and in vivo monitoring devices for the continuous monitoring of various brain metabolic biomarkers. The most widely developed technique is electrochemistry (EC)-based biomarker monitoring sensors, which have been designed for the measurement of brain glucose, glutamate, dopamine, acetylcholine, and various ions[12, 13]. The technique can also be applied for multiplexed biomarker monitoring by incorporating several bioelectrode on a single substrate. Despite advances in multimodality monitoring, concerns remain with current diagnostic approaches including high cost, limited sample frequency, artefact, drift and failure of measurements, and scattering caused by metal components on magnetic resonance (MR) imaging. These electronic probes are at best MR conditional, as none are free of metals, or includes cables for electrical currents, impeding their utility in clinical settings.

Optical based method is another commonly adopted method for brain monitoring, such as fluorescence spectroscopy, Raman spectroscopy, and surface plasmon resonance[12]. Optical fibre sensors, even though have not been widely applied in brain neurochemical, offer several advantages over EC sensors. Optical fibre sensors can be constructed to be sensitive, offer long-term real time monitoring, are minimally invasive, immune to electromagnetic interference, and can perform remote measurement, having a good application prospect in real-time and long-time detection in vivo. However, only few studies have been conducted to develop optical based sensors for real-time and

continuous multi-analyte sensing using one optical fibre due to the interference between multiple optical sensors and background noise.

Artificial intelligence (AI) has revolutionized the field of signal analysis, enabling researchers and healthcare professionals to extract valuable insights from complex biological data with unprecedented accuracy and efficiency [14, 15]. In this domain, AI techniques such as machine learning and deep learning have become indispensable tools for analyzing various biosignals, including electrocardiograms, electroencephalograms, and electromyograms[16]. By leveraging the powerful pattern recognition capabilities of AI, researchers can detect and interpret subtle changes in biosignals or optical signals and reveal the actual signal patterns detected noisy signals. In recent years, more and more studies have integrated AI algorithms with biosensors for accurate and robust biomarker detection and monitoring.

1.2 Thesis objective and outline

The aim of this thesis is to develop a fully automated, multiplexed, and implantable optical fibre sensing system for multiplexed and continuous brain monitoring to assist brain disorder diagnosis and treatment. This multiplexed sensing system is able to perform continuous monitoring of multiple clinical-relevant physiological biomarkers to assess abrupt metabolic and neuronic changes, reflecting brain pathophysiological status and brain metabolism response following brain trauma or treatments in real-time. Moreover, the system is designed to be MR-compatible, enabling high spatial and temporal brain measurement together with MR.

Therefore, the thesis objective can be divided into the following sub-objectives, which correspond to the main chapters of the thesis:

Chapter 2: In the second chapter, a comprehensive literature review is presented. The history of brain monitoring, clinical-relevant biomarkers, three brain monitoring techniques, and computational methods for accurate monitoring readout are introduced. It first reviews the development of brain monitoring technologies in chronological order and discusses the gaps and limitations in the recent techniques. A brief summary of several commonly monitored brain biomarkers and their correlation

with neurological disorders/diseases is also presented for reference. Then the chapter reviews three commonly used techniques: sampling-based, electrochemical-based, and optical-based techniques for continuous brain monitoring. The sensing mechanisms, application methods, and recent relevant studies are included with a discussion on the pros and cons of these technologies. In the end, the chapters reviewed the current advances in computational methods for the enhancement of sensing performance and discussed their potential in future brain monitoring.

Chapter 3: This chapter discusses the fabrication and application of 4 reflection spectroscopy-based sensors as a preliminary exploration of dynamic brain pH, dissolved oxygen, temperature, and glucose monitoring. The sensors' performance including sensitivity, selectivity, and stability are discussed for each individual sensor, following which the four sensors are multiplexed together on a silica film, and measured using a y-shape reflection probe for the measurement of 4 biomarkers together. Computational methods for biomarker concentration readout and ex vivo validation results are presented and discussed. The limitation of the designed system is discussed.

Chapter 4: This chapter introduces the development of a miniaturized optical fibre bundle sensing system based on fluorescent spectroscopy with two more biomarkers to be monitored and better sensing performance compared to the system presented in Chapter 3. The system is capable of measuring 6 biomarkers: pH, temperature, dissolved oxygen (DO), calcium ions (Ca2+), sodium ions (Na+), and glucose. In this chapter, the individual characterisation results of the six sensors are presented and discussed. Later on, the individual fibre sensors are multiplexed together as a fibre bundle for the monitoring of 6 biomarkers simultaneously. Therefore, the design and manufacturing results of the optical fibre bundle are presented. Then fibre bundle tips are functionalized with the developed fluorescent sensing films and calibrated for multiplexed measurement. To achieve an accurate readout of each biomarker, robust mathematical algorithms are proposed to remove signal noise, subtract baseline, and separate overlapped optical spectra. The system is then validated using ex vivo brain models to demonstrate the overall system functionality.

Chapter 5: In this chapter, a fully automated and robust brain monitoring device is presented to receive, record, analyse, and display 6 biomarker concentration values. Optimized biomarker

concentration calculation algorithms based on machine learning and deep learning models are demonstrated for enhanced biomarker concentration readout accuracy. The prototyping methods including device communication, AI-based concentration prediction, user interface (UI) development, and readout box manufacturing are presented here. In the end, the system is validated using clinical human CSF samples.

Chapter 6: This chapter presents the discussions and conclusions of the thesis, including the connections between chapters and the major contributions and achievements of the thesis. In addition, limitations and future directions are elaborated, highlighting the contributions of the project to the various field and potential impact on society.

Chapter 2 Literature Review

2.1 History of brain neurochemical monitoring

Due to the importance of brain neurochemicals in the neural system, brain neurochemicals monitoring has been widely studied for better understandings of brain neurotransmissions and physiological functions. Interests in brain neurochemical monitoring can be dated back to the 1950s when neurochemicals began to be detected and monitored in the brain using fluorescence or colorimetric methods[17, 18]. As the first enzyme-based EC measurement was proposed and applied for brain chemical sensing in 1965[19, 20], researchers were inspired and started to get involved in the field of brain analytical chemistry using EC techniques. In the meantime, microdialysis (MD), which is a sampling method, was first proposed in 1960 for in vivo body fluid sampling[21]. In the beginning, MD was only used on animals and in research labs, and until 1987, the first human application was published for measuring adipose glucose levels[22]. In the 1990s, MD studies on in vivo human bran application started to emerge, and the MD became approved for widespread clinical use in Europe and the USA[23, 24]. Optical methods, being another powerful technology with great potential in biomarker sensing, have achieved fast improvement since the 1970s and started to be applied for in vivo brain monitoring. For example, in 1977, brain oxygenation was first monitored using near-infrared spectroscopy[25]. Furthermore, due to the advances in modern affordable optical fibres, optical fibre-based biosensors started to be used for in vivo optical sensing of brain neurochemicals from the early 1980s[26]. Since 1990, increasing achievements have been achieved in Raman spectroscopy-based in vivo neurochemical detection and brain tumour classification[27, 28], while surface plasmon resonance in biosensing has also started to be explored[29]. Since then, progresses being made in brain neurochemical monitoring have switched to the designing of novel non-enzymatic recognition elements for more sensitive and selective recognition of target analytes[30-32], nanoscale materials for surface modification[33], and many other novel technologies such as microfluidic sensing systems and multiplexed sensing (**Figure 2-1**).

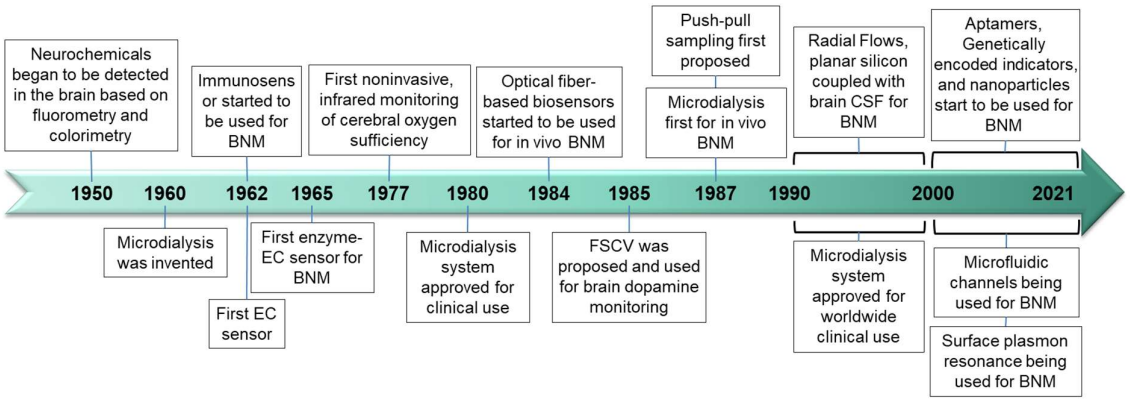


Figure 2-1 Major events associated with brain neurochemical monitoring. BNM: brain neurochemical monitoring. EC: Electrochemical; BNM: Brain neurochemical monitoring; FSCV: Fast-scan cyclic voltammetry

Until now, the most predominant techniques for brain neurochemical monitoring are still based on three technologies, sampling combined with separate analysers, electrochemistry, and optical spectroscopy (**Figure 2-2**). Each of these technologies has its distinct advantages and disadvantages. In general, microdialysis is simple to use, which makes it widely used in the clinic for long-term neurochemical monitoring. However, due to its sampling nature, it has long time delays and limited temporospatial resolution. Electrochemistry and optical spectroscopy, whereas, can be used for in vivo and in situ measurements, offering high temporal resolutions, but as a result, they suffer from poor stability due to their high sensitivity, unsatisfied selectivity due to cross-interference from in situ measurement, and poor biocompatibility caused by long-term implantation.

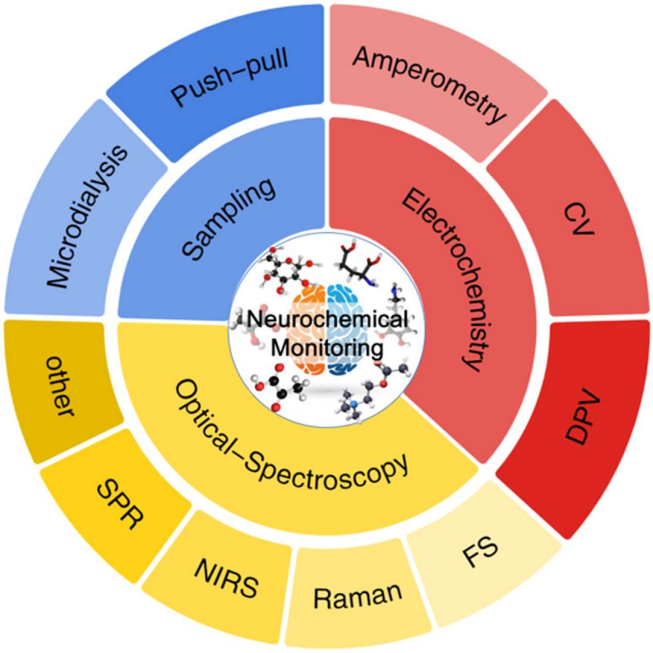


Figure 2-2 Recent technologies for brain neurochemical monitoring. Technologies developed for brain neurochemical monitoring can be divided into three groups, electrochemistry, optical spectroscopy.

2.2 Commonly monitored brain biomarkers

In this section, the most commonly monitored and studied biomarkers are introduced including their functions in maintaining brain physiological functions. The correlation with neurological disorders or diseases is also introduced (**Table 2-1)**.

2.2.1 Brain metabolites

One of the most monitored biomarkers is pH, owing to its importance in brain physiology and the less complexity to be measured. Tight control of pH is crucial for maintaining brain function, which is usually realized through specific mechanisms for CSF pH adjusting. These include modifying bicarbonate concentration and respiration to eliminate carbon dioxide, a key factor influencing CSF acidity [34-36]. Continuous monitoring of brain CSF pH provides doctors insights into potential disruptions in brain chemistry. Researchers generally agree on healthy brain tissue and CSF hover around a slightly alkaline range between 7.35 and 7.45. A rise in pH can disrupt the activity of enzymes crucial for brain function which can lead to confusion, seizures, and even coma in extreme

cases [35, 37]. Decreased pH can, however, impair cellular communication, hinder energy production, and ultimately lead to cell death, which is commonly linked to various neurological conditions like stroke, head trauma, and even migraines [34].

Another commonly measured biomarker is brain temperature. Just like with pH, monitoring brain temperature provides valuable information about the brain's health. In clinics, brain temperature is usually monitored by measuring temperatures in nearby regions for non-invasive estimation or by placing an electronic probe into the brain tissue for patients with severe brain damage[38, 39]. Studies suggested that the average healthy brain temperature is around 38.5°C and can be increased up to 40°C in the deeper brain. Increased brain temperature (hyperthermia), which can be caused by fever, infections, or heatstroke, may lead to headaches, confusion, seizures, and even brain damage, whereas, a significant drop in brain temperature can disrupt nerve function and lead to coma[39-41].

Brain function relies heavily on a constant supply of oxygen. Brain oxygen plays an important role in brain energy production as it acts as fuel for brain cell activities[42-44]. It is also essential for maintaining proper neurotransmitter functions for cell communication. Monitoring brain oxygenation, therefore, becomes a valuable tool for assessing brain health[45]. In clinical settings, brain oxygenation is usually monitored through near-infrared spectroscopy (NIRS) non-invasively[43, 46], or by measuring jugular venous oxygen saturation (SjVO2) that requires inserting a catheter into a major neck vein[47]. Brain oxygenation level is usually maintained at a saturation between 50% and 70%. Low brain oxygenation (Hypoxia), occurring due to reasons including stroke, cardiac arrest, or severe head injury, may lead to confusion, dizziness, or even cell death and brain damage[48]. High brain oxygenation (Hyperoxia) can trigger inflammation and oxidative stress, potentially damaging brain tissue.

Apart from the above basic biomarkers, several other biomarkers are also of high interests in reflecting brain functions. Glucose is the main energy substrate of brain and is consumed mainly by astrocytes. Apart from glucose, neurons and astrocytes also utilize lactate, pyruvate, glutamate, and glutamine as energetic substrates [49, 50] as shown in **Figure 2-3**. In Astrocytes, with the uptake of

glutamate, the activity of Na^+/K^+-ATPase is stimulated, which in turn allows glucose to cross the blood brain barrier and enter the astrocytes from the vasculature. A large amount of the entered glucose is then sent to the glycolytic pathway to be metabolized into lactate. The generated lactate is first released into the extracellular space and then absorbed by neurons to be transformed into pyruvate, which is used as an energetic substrate in the tricarboxylic acid (TCA) cycle[42, 51]. Another important cycle in astrocytes is the glutamate-glutamine cycle. In astrocyte, glutamate is first converted into glutamine, and glutamine will be transported to neurons and converted back into glutamate[42, 51]. Glutamates and glutamine are also involved in the TCA cycles in astrocytes and neurons[49]. These related chemicals all play very important roles in the maintaining of brain functions and have been monitored in the clinic as indicators of various brain disorders, including anaerobic metabolism, energy failure and secondary injury after TBI[52-56].

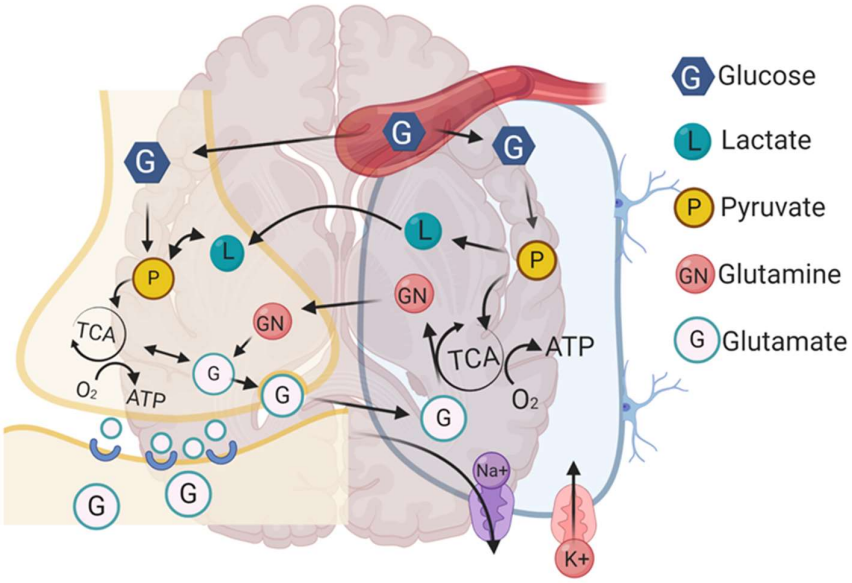


Figure 2-3 Energy metabolism of brain. Under the stimulation of Na+/K+-ATPase, glucose is released from the blood to astrocytes through the blood brain barrier. The entered glucose is then metabolized into pyruvate and lactate. Lactate is first released into the extracellular space and later absorbed by neurons to generate pyruvate, which is used as energetic substrate in the tricarboxylic acid (TCA) cycle. In astrocyte, glutamate is converted into glutamine, which is then transported to neurons and converted back into glutamate. (Reprinted with permission from ref. 50. Copyright 2013 Elsevier B.V.)

Glucose (Gluc)

As mentioned above, glucose is a metabolite that serves as the primary energy supply to the brain. Glucose maintains the basic brain physiological functions by producing ATP, supporting neuronal and non-neuronal cells, and generating important neurotransmitters such as glutamate (**Figure 2-3**) [57]. Dysregulation of glucose metabolism will, therefore, cause various brain pathophysiological disorders, such as secondary brain injury [58], and neurodegenerative diseases [59-61].

In recent years, several studies have focused on the development of glucose sensors for glucose monitoring in the brain. Glucose is a non-electroactive molecule, and the traditional methods for glucose detection are based on enzyme electrodes, in which glucose oxidase enzyme is immobilized onto the electrode surface to induce a measurable signal that is proportional to the glucose concentration. The chemical reactions related to the glucose sensing are:

$$\mathrm{D-glucose} + O_2 \xrightarrow{GOx} D-gluconolactone + H_2O_2 \text{ (Eq. 2-1)}$$

$$H_2O_2 \xrightarrow{+600} 2H^+ + O_2 + 2e^- \text{ (Eq. 2-2)}$$

Lactate (Lac)

Lactate is generated in the glycolysis process of glucose in astrocyte, and is transported to neurons for energy supply and neuronal function maintenance[62]. In the early 20th century, lactate has been considered as the end product in the metabolism, and has a 'bad reputation' of being "useless" if not toxic[62, 63]. However, more recent studies have acknowledged lactate as an important adequate energy substrate in the brain and a signalling molecule, which modulates the neuronal excitability, plasticity and neuroprotection[64-67]. An abnormality in lactate may indicate several brain disorders, such as memory disorders[62, 68, 69], brain injury[70, 71], bipolar disorder and schizophrenia[72]. Lactate is non-electroactive, and amperometry electrode coated with lactate oxidase is widely used for lactate detection. The chemical reactions related to the glucose sensing are:

$$\mathrm{Lactate} + O_2 \xrightarrow{LOx} pyruvate + H_2O_2 \text{ (Eq. 2-3)}$$

$$H_2O_2 \xrightarrow{+600m} 2H^+ + O_2 + 2e^- \text{ (Eq. 2-4)}$$

Pyruvate (Pyru)

Pyruvate is also an important metabolite that is involved in several biochemical pathways. In the brain, when the brain tissue is experiencing an oxygen or glucose deficiency, the brain will utilize other less efficient energy source such as pyruvate to protect brain functions[73]. Pyruvate is also involved in the synthesis of fatty acids and amino acids and_it has direct impacts on epigenetic modifications and neuronal activity[74-77].

In clinical studies, pyruvate has been found to be useful in rescuing brain cells from death after the cascade of excitotoxic activity[77]. It was also found that a combined pyruvate and glucose administration could reduce the neuronal death by 70–90% in hypoglycaemia-induced brain injury[76]. In another study, the authors found that ethyl pyruvate could significant reduce the complications of brain edema, including motor impairment and neurological deficits in brain injured patients[77, 78]. Therefore, a close monitoring of pyruvate concentrations in the brain would facilitate precision treatments of brain disorders in the clinic.

Similar to glucose and lactate, pyruvate is also a non-electroactive molecule that requires pyruvate enzyme for the oxidation reaction, and the chemical reaction is as follows:

$$\text{Pyruvate} + \text{P}O_4^{3-} + H_2\text{O} + O_2 \xrightarrow{PyOx} acetyl\ phosphate + H_2O_2 + CO_2 \quad \textbf{(Eq. 2-5)}$$

$$H_2O_2 \xrightarrow{+600mV} 2H^+ + O_2 + 2e^- \quad \textbf{(Eq. 2-6)}$$

Adenosine triphosphate (ATP)

ATP, the universal energy currency of the living cells, plays a crucial role in the cellular metabolism, cellular activities, and cellular functions[79]. A large amount of ATP is formed in the mitochondria through the oxidative phosphorylation process of adenosine diphosphate (ADP) catalyzed by the enzyme of ATP synthase (ATPase) [80]. In the brain, ATP is mainly used to maintain the transmembrane ion gradient and support the releasing and receiving of neurotransmitters by pumping Na^+ and K^+ across the cellular membrane, indicating that ATP also plays a major role in supporting the

neurotransmitter cycles and maintaining neuron activities and signal propagations in the brain.[79] In the clinic, abnormal ATP concentrations have been observed in various brain disorders such as Parkinson's disease and autism[81,82]. Therefore, monitoring of ATP concentrations in the brain is essential in both biomedical studies and clinical research.

2.2.2 Brain neurotransmitters

There are about 80 billion neurons in the brain that serve as essential elements for information processing and communication. Neurotransmitters (NTs), being the elementary chemicals, are released from neurons to propagate signals between neuron cells as a messenger that carries out the information communication inside brain. NTs play an important role in many brain functions, including memory, motor function, stress, psychomotor, gastrointestinal, and inter-neuronal communication, thus any abnormalities in NTs may indicate some kind of brain damage or disorders (e.g., Parkinson's, Alzheimer's, schizophrenia, glaucoma, Huntington's, epilepsy, arrhythmias, thyroid hormone deficiency, congestive heart failure, sudden infant death syndrome, depression and anxiety).[83-85] More than 100 of NTs have been discovered and can be categorized into two classes based on their structure, monoamine NTs and amino acid NTs, where monoamine NTs contains NTs such as dopamine (DA), serotonin (5-HT), acetylcholine, norepinephrine (NEP) and epinephrine (EP), and amino acid NTs contains NTs such as glutamic acid, γ-aminobutyricacid (GABA), and tryptophan.

Glutamate (Glut)

Glutamate is the most prominent excitatory neurotransmitter in the central nervous system (CNS) of mammals[86]. It has been reported that glutamate acts as an indicator for developing cerebral ischemia after Aneurysmal Subarachnoid Hemorrhage[87], and dysregulation of glutamate is commonly observed in severe neuropathological conditions, such as epilepsy and glioma due to the reduced uptaken in glial cells[88, 89]. Because glutamate is an excitatory neurotransmitter in the brain, excessive extracellular glutamate release will overstimulate glutamate receptors, causing excitotoxicity,

neuronal injury and even death[90, 91]. Glutamate has been measured for the diagnosis of sleeping and addictive disorders and have been used to study the brain reward circuitry[92-94].

Glutamate is non-electroactive within the conventional applied potential window of bioelectrochemical sensors, due to which extraction and purification of glutamate oxidase are needed in the development of glutamate electrochemical sensors.

$$\text{Glutamate} + O_2 \xrightarrow{GluOx} \alpha - ketoglutarate + NH_3 + H_2O_2 \quad \textbf{(Eq. 2-7)}$$

$$H_2O_2 \xrightarrow{+600} 2H^+ + O_2 + 2e^- \quad \textbf{(Eq. 2-8)}$$

Dopamine (DA)

Dopamine is a monoamine neurotransmitter that regulates movement, rewarding, motivation and reinforcement learning[95]. Mapping of dopamine release has been widely carried out in various clinical research as a disruption in dopamine may indicate many neurological and neuropsychiatric disorders, such as Parkinson's disease, Alzheimer's, schizophrenia, and depression[95-97]. However, measuring dopamine release in the brain is challenging owing to its fast changes and low concentration in the brain. Different from the above mentioned neurochemicals, dopamine is an electroactive molecule, and thus can be directly measured without enzyme coatings. The release of dopamine have been measured by several sensing methods, including amperometry[98, 99], voltammetry[100-102], and optical technologies[103-105], among which FSCV has shown promising results as it offers high temporal resolution, good sensitivity and selectivity.

Acetylcholine

Acetylcholine (Ach) is the first identified neurotransmitter that binds two types of receptors: nicotinic and muscarinic. Ach plays an important role in the cholinergic system as it is used to induce impulses on the cholinergic synapse, thus abnormal alterations of cholinergic transmission may lead to several brain disorders including Parkinson's disease, Alzheimer's disease, epilepsy, addiction, schizophrenia, and depression [106, 107]. In recent years, great effort has been devoted to develop sensors

for Ach concentration measurement.[108, 109] ACh is non-electroactive within the potential window used for in vivo brain detection, therefore, enzyme-based amperometric sensors are used for Ach measurement. Because Ach breaks down to choline when the signal terminated in the synapses[110], either choline oxidase or a combination of acetylcholinesterase and choline oxidase can be used as enzyme coatings for the Ach measurement.

For acetylcholine detection, $\text{Acetylcholine} + H_2O \xrightarrow{AChE} Choline + CH_3COO^- + H^+$(**Eq. 2-9**)

For choline detection, $\text{Choline} + O_2 \xrightarrow{ChOx} betaine\ aldehyde + H_2O_2$(**Eq. 2-10**)

Table 2-1. Summary of major brain neurochemicals

Neurochemical	**CSF Concentration**	**Electroactivity**	**Roles in brain function**	**Reference**
Glucose	2.8–4.4 mmol L^{-1}	NE	Primary energy supply	[111]
Lactate	1.3 – 2.4 mmol L^{-1}	NE	Energy substrate, modulates neuronal excitability, plasticity, and neuroprotection	[111]
Pyruvate	0.03-0.15 mmol L^{-1}	NE	Less efficient energy source; rescuing brain cells from excitotoxic activity	[112]
ATP	2.3 mmol L^{-1}	NE	Maintain the transmembrane ion gradient; Support the releasing and receiving of neurotransmitters	[113]
Glutamate	1.4 µmol L^{-1}	NE	The most prominent excitatory neurotransmitter	[114]
DA	0.09 nmol L^{-1}	EA	regulates movement, rewarding, motivation, and reinforcement learning	[115]
Acetylcholine	6.14 – 393.6 nmol L^{-1}	NE	induce impulses on the cholinergic synapse	[116, 117]
Serotonin	9.6 nmol L^{-1}	EA	regulating sleep, mood regulation, and feeding behaviors	[118]

NE: Non-electroactive; EA: Electroactive

2.3 Sampling methods for brain neurochemical monitoring

Sampling, being one of the most adopted methods for brain neurochemical monitoring especially in clinic, contains a capillary probe to extract the CSF and a separate analyser for molecule detection.

Because the CSF sample is analysed separately in an analyser such as high-performance liquid chromatography (HPLC) and mass spectroscopy (MS) sampling methods for brain neurochemical monitoring is usually considered as an ex vivo measurement. To date, two types of sampling methods, namely microdialysis and push-pull sampling, have been developed and applied in neurochemical monitoring [119].

MD consists of a probe/catheter with a semipermeable membrane at the tip for brain CSF sampling. It is performed by pumping artificial CSF (aCSF) into the probe (**Figure 2-4**) that allows the diffusion of molecules across the probe membrane driven by the concentration gradient. MD offers high sensing sensitivity and selectivity because the sampled CSF is usually analysed separately with well-established analysers such as HPLC. However, MD suffers from several limitations. First, owing to its sampling nature, it usually takes 10−20 min for CSF sampling, and thus it suffers from low temporal resolution and longtime delays. Besides, the semipermeable membrane has a large exchange area (usually diameter of 400 μm, length of 1−4 mm), which limits the spatial resolution of MD[120]. The catheter can only permit limited mass transfer across the membrane, as a result only small molecules can be analysed with the MD-based system. Furthermore, it requires human interventions to move the sample between the sampling devices and the analyser, which can be tedious, time-consuming, and error-prone.

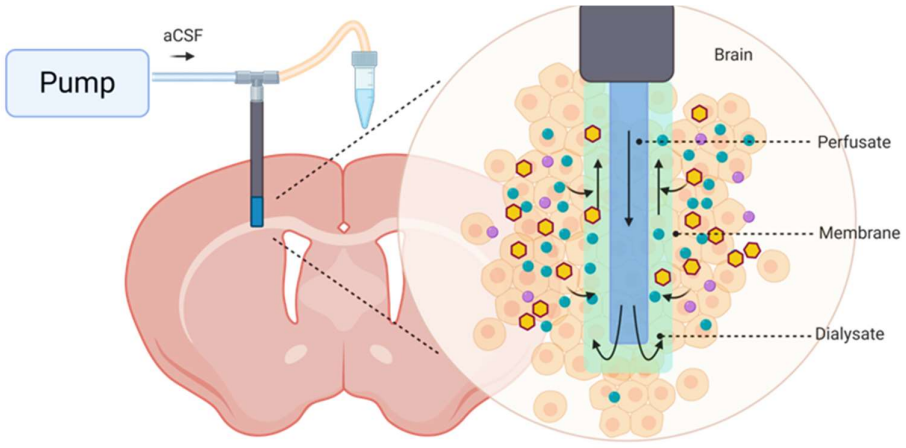


Figure 2-4 Principle of microdialysis. A microdialysis probe is surgically inserted into a specific brain region of interest. Artificial CSF is pumped into the microdialysis probe for brain molecular sampling. Brain molecules are then freely enter the semipermeable membrane of the probe driven by sample concentration gradient to a point

when the dialysate has the same (ideally) molecule concentration as the CSF. The gathered dialysate is then sent to an analyser for brain molecule identification and measurement.

Push-pull sampling systems are developed in the recent decade to improve the temporospatial resolution and recovery rate of sampling-based brain neurochemical monitoring systems[121]. Instead of sampling brain neurochemicals under the concentration diffusion between aCSF and real CSF (**Figure 2-5(a)**), the push-pull sampling system performs "direct sampling", which samples CSF from the probe tip, resulting a better sampling efficiency with sampling time reduced from 30 min to a few seconds and thus, a better temporospatial resolution compared to MD probes[122]. (**Figure 2-5(b)**).

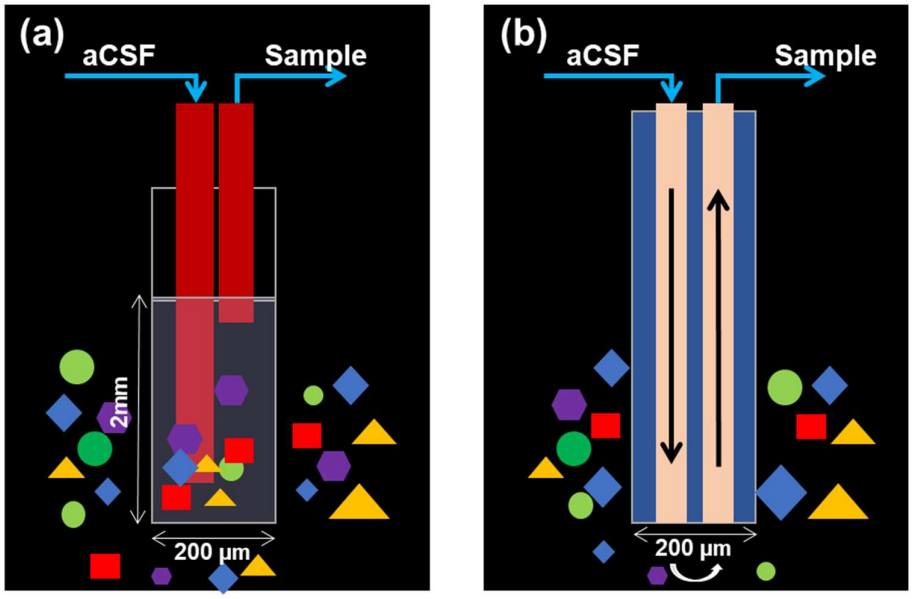


Figure 2-5. Comparison between two sampling methods. (a) In MD, samples are collected via concentration gradient and are collected in the membrane area. (b) In push-pull system, sample is withdrawn directly from the brain tissue, and aCSF is infused to the brain to replace the sample at the same speed. Samples are collected only from the probe tip.

Microfluidic system and segmented flows

Miniaturized and microfluidic-based MD systems have shown great promise in brain monitoring as it largely reduces the sampling time and improves temporal resolution compared with the conventional MD system[122-124]. Recently, a fully integrated portable microfluidic analysis system was developed for real-time monitoring of the dynamic changes of glucose and lactate in the brain (**Figure 2-6**)[123-125]. The system contained a commercially available microdialysis tube for the sampling of CSF and a 3D

printed microfluidic chip that housed glucose and lactate detection biosensors. Electrochemical based sensors were adopted in their study for the sensing of glucose and lactate because they provide fast analysis and require minimum procedures (**Figure 2-6 (a-c)**). Due to the small size of the designed microfluidic chip (**Figure 2-6 (d)**), the system could be placed beside the patient's head, which largely reduced the CSF transporting time, achieving a short time latency of 15 s. Moreover, this system also contained an auto-calibration system, which could be used to constantly correct the system drift, and thus offers long-term monitoring. In vivo monitoring tests were conducted on pigs, and the results suggested that the system could successfully assist clinicians in monitoring brain metabolite changes (**Figure 2-6(e)**)[124].

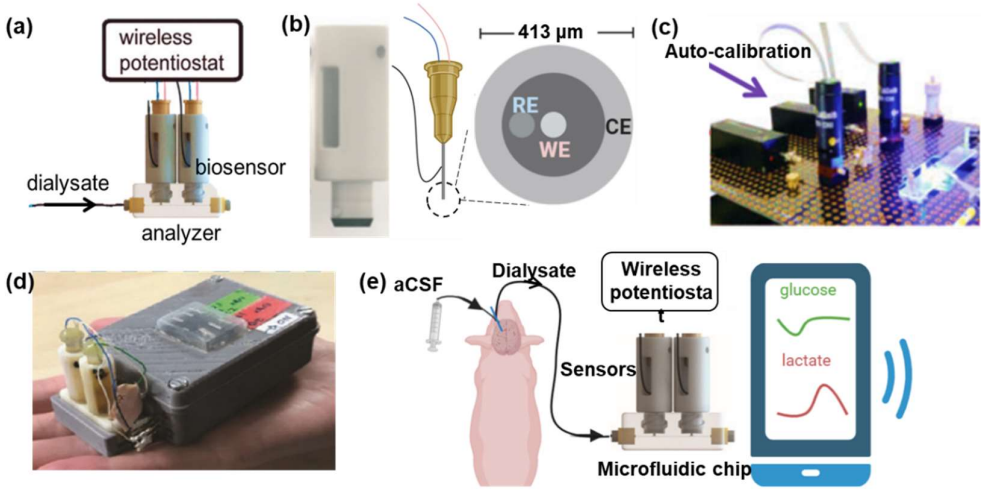


Figure 2-6. 3D printed microfluidic systems for brain neurochemicals monitoring. 3D printed microfluidic systems for brain neurochemicals monitoring. (a) Sampled dialysate is sent to biosensors via a probe for neurochemical measurement. (b) Sensing probe structure and 3D printed hard cover for probe stabilizing. (c) A 3D printed microfluidic chip for dialysate measurement. An autocalibration system is used to remove the drift. (d) Photo of the 3D printed microfluidic system. (e) In vivo application for the study of cardiac condition monitoring using porcine model. Reprinted with permission from ref. [124]. Copyright Royal Society of Chemistry 2020.

Droplet microfluidic-based microdialysis system coupled with embedded analysers for intracellular fluid monitoring has attracted great attention for the improvement of temporal resolution as it removes Taylor dispersion and allows for rapid axial mixing[122, 126]. A microdialysis/droplet-based microfluidic chip system was designed by Gu et al. for continuous measurement of hydrogen sulfide (H_2S) in the brain using fluorescence measurement (**Figure 2-7**) [126]. After being mixed with fluorophores, the extracted sample was sent to the fluorescence detector for the measurement of H_2S. The temporal resolution of the system was largely improved by employing a droplet microfluidic-

based sampling system. A linear range of 5.0 μmol^{-1} to 40 μmol^{-1} and a limit of detection (LOD) of 2.5 μmol^{-1} was achieved by the fluorescence measurement, and the system achieved an improved temporal resolution of 4.6 ± 0.3 s and a reduced lag time of 10 min between the microdialysis probe and the fluorescence detector. An online calibration system was also incorporated by injecting standard Na_2S, which enabled the system to perform continuous monitoring of rat brain for hours[126].

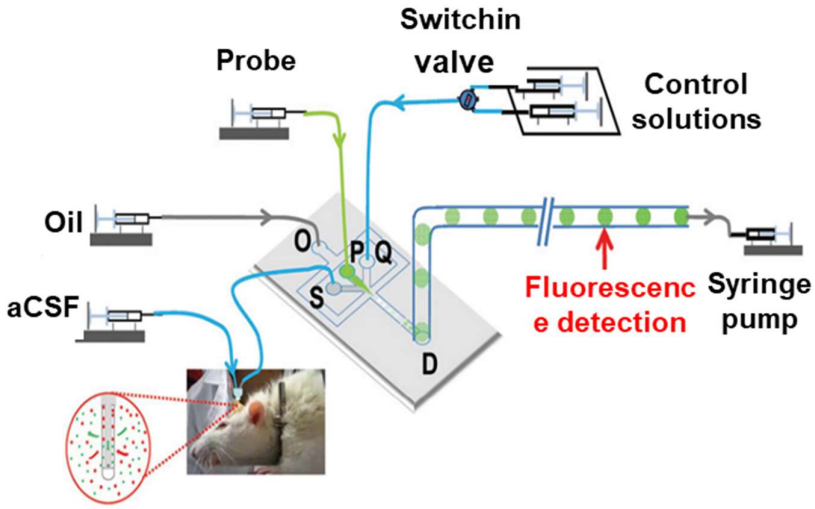


Figure 2-7. A microdialysis/droplet-based microfluidic chip system for in vivo measurement of the HS− concentration in rat's brain. Reprinted with permission from ref. [126]. Copyright Royal Society of Chemistry 2015.

In another work, a microfabricated push-pull sampling probe and droplet-based microfluidics were designed and used with MS analyser for the measurement of Glut, glutamine, acetylcholine, and GABA in brain CSF simultaneously (**Figure 2-8**) [122]. Due to the implementation of the push-pull system, the probe size was largely reduced, and a 1000-fold better spatial resolution (sampling area: 20 µm × 60 µm) was achieved compared to the commonly adopted capillary-based MD sampling probes. The nanoliter droplet-based microfluidics also yielded a 6 s temporal resolution, demonstrating great potential in studying chemical dynamics. The sampled CSF was then sent to MS for analysis, which yield low LODs of 90 $nmol^{-1}$, 60 $nmol^{-1}$, 20 $nmol^{-1}$, and 2 $nmol^{-1}$ for glutamine, Glut, GABA, and Ach, respectively. Although the temporal resolution has been largely improved in these studies, it is still not adequate for sensing the changes in neurotransmitters as it requires subsecond resolution.

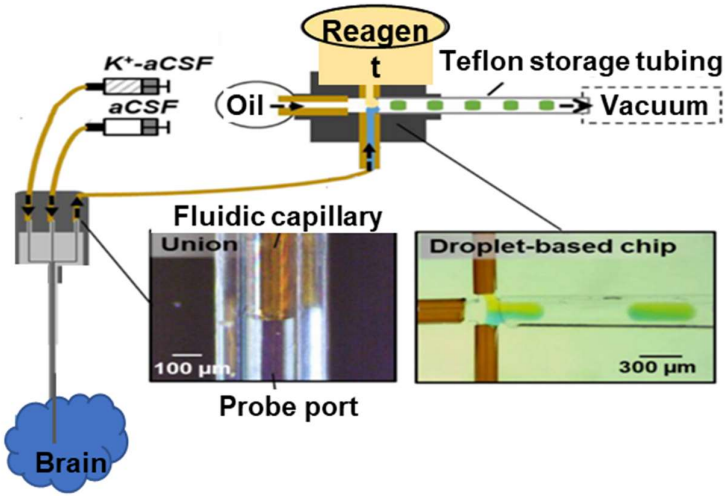


Figure 2-8. An integrated push-pull sampling system with a droplet-based microfluidics system for the detection of neurochemicals. Artificial aCSF and K+-aCSF were injected from the first two channels. Collected CSF samples were pulled from the last channel and sent to a Teflon tubing for offline analysis. Fluorescence dyes were added to sample for measurement. Reprinted with permission from ref. [122]. Copyright © 2018 American Chemical Society.

The above cases indicate that current advances in sampling-based methods have greatly improved the temporal resolution to several seconds for biomarker measurement by integrating the sampling and analyser together utilizing microfluidic techniques without the need for human intervention. The application of online calibration by measuring standard buffers regularly has greatly improved the system's accuracy, enabling long term and precise measurement. However, with all the advances, the system can not provide spatial information of the sample due to its sampling nature.

2.4 Electrochemistry methods for in vivo brain neurochemical monitoring

Electrochemical (EC) sensors convert in the chemical reaction-induced system current changes into a quantitative signal. To date, dynamic EC techniques such as amperometry and voltammetry have been widely utilized for real-time and *in vivo* sensing of brain neurochemicals[127-132].

2.4.1 Principle of amperometric sensor

In amperometry, a constant direct current (DC) potential is applied between a working electrode (WE) and a reference electrode (RE), under which the target analyte undergoes a redox reaction and generates a current (**Figure 2-9**). The current, which is proportional to the analyte concentration, passes across the electrodes of the sensor and is measured at the WE. Amperometry provides fast and

high sensitivity sensing of neurochemicals. However, in in vivo applications, many neurochemicals may undergo redox reactions under the given potential simultaneously, leading to poor selectivity of the sensor [133].

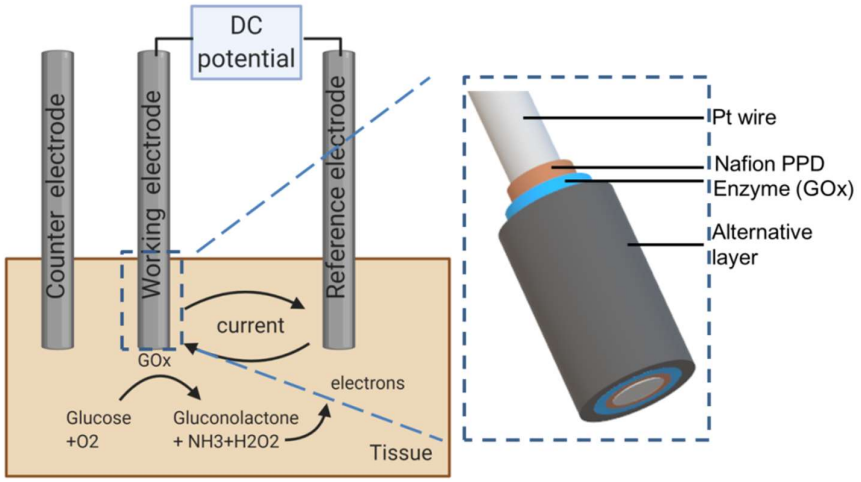


Figure 2-9. Schematic of amperometric sensing of glucose. Amperometric sensor has three electrodes, working electrode (WE), reference electrode (RE), and counter electrode (CE). A constant DC potential is applied between WE and RE. For glucose detection, the working electrode is usually fabricated with a pt wire and coated with a Nafion PPD layer to remove the interferences, a glucose enzyme layer, and the third layer is an alternative layer that can be used to reject interference or improve sensing performance. Under the DC potential, glucose is oxidized to gluconolactone and generates a current between WE and RE that is measured to calculate glucose concentration.

2.4.2 Principle of voltametric sensor

A variety of voltametric techniques have been utilized to measure neurochemicals, including differential pulse voltammetry (DPV)[134-137], cyclic voltammetry (CV)[137], and fast-scan cyclic voltammetry (FSCV)[130, 131, 138-140]. DPV, CV, and FSCV adopt different waveforms and frequencies to induce compound oxidation and reduction. Among the three methods, DPV has relatively higher sensitivity; however, the temporal resolution it offers is not high enough to capture the subsecond changes in neurotransmitters. FSCV, on the contrary, offers subsecond-level of temporal resolution, making it of particular interest among the recent studies[137, 141].

There are some drawbacks of voltammetry measurements. The selectivity of the sensor is also a major concern especially when the surrounding interferences oxidize and reduce at similar potentials,

such as monoamines DA, 5-HT, and norepinephrine. Therefore, in previous studies, different post-processing algorithms and pharmacological manipulation have been investigated to selectively identify the target analyte, such as using Principal component regression to selectively identify the target analyte voltammogram and designing novel voltammetry waveform and frequencies [130, 142, 143].

2.4.3 Applications of EC sensors in brain monitoring

In developing brain neurochemical monitoring sensors, many groups seem to favor the use of several biomarkers to show reliable and comprehensive patterns of energy metabolism and neurotransmitter deteriorations [144-146]. Multi-analyte sensing based on electrochemistry has been achieved by bundling multiple sensors together (**Figure 2-10 (a) and (b)**) and fabricating several electrodes on a single substrate (**Figure 2-11**). For example, a device for the detection of several brain metabolites has been developed by bundling three separate sensors, glucose, lactate, and pyruvate sensors together (**Figure 2-10 (b)**) [146]. In in vitro calibration, these three sensors showed adequate selective and sensitive (100 nA/mmol L^{-1}) responses for in vivo brain neurochemical monitoring. The system was then applied to rats for in vivo monitoring and was able to reflect the biomarker concentrations in the brain for more than an hour. However, simply bundling several Pt-based sensors together would lead to a large sensor size, which might be a limitation of this sensor as it would cause brain damage in long-term monitoring.

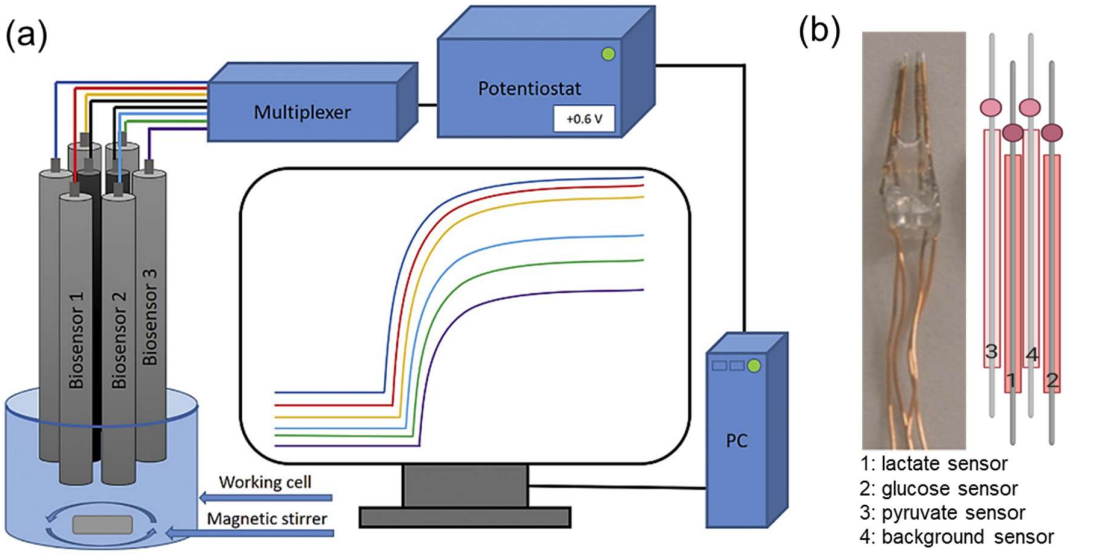


Figure 2-10. Amperometric sensor for multi-analyte monitoring.(a) Schematic representation of multi-analyte sensing by bundling six sensors together. (b) Image of the multiplex microbiosensor device (left) and the schematic representation of the multiplex microbiosensor device (right). (Reprinted from [144, 146] with permission from © 2019, 2014 Elsevier B.V.).

Recently, an implantable multifunctional neural microprobe was developed based on the amperometric technique for multi-analyte sensing with a small size (**Figure 2-11**) [145]. Different from using separate electrodes for multiple metabolites sensing, in this study, glutamate and choline sensors were fabricated on a silicon substrate for simultaneous sensing (**Figure 2-11 (a-c)**). The designed sensor was 9 mm long, 15 µm thick, and had a 10 × 20 µm channel dimension, which iss much smaller than clinical-widely used brain probes or catheters that are usually larger than 1 mm. Using the microprobe, glutamate could be detected with a sensitivity of 74.8 ± 4 µA/mmol L^{-1} cm^{-2} and choline can be detected with a sensitivity of 84.7 ± 15 µA/mmol L-1 cm−2 (**Figure 2-11 (d-e)**). A response time of 2 s was achieved which is much faster than currently used microdialysis method and hold the potential to measure abrupt chemical changes in brain. The study realized the successful measurement of multiple biomarkers simultaneously on a minimized substrate with high potential for in vivo and real-life applications.

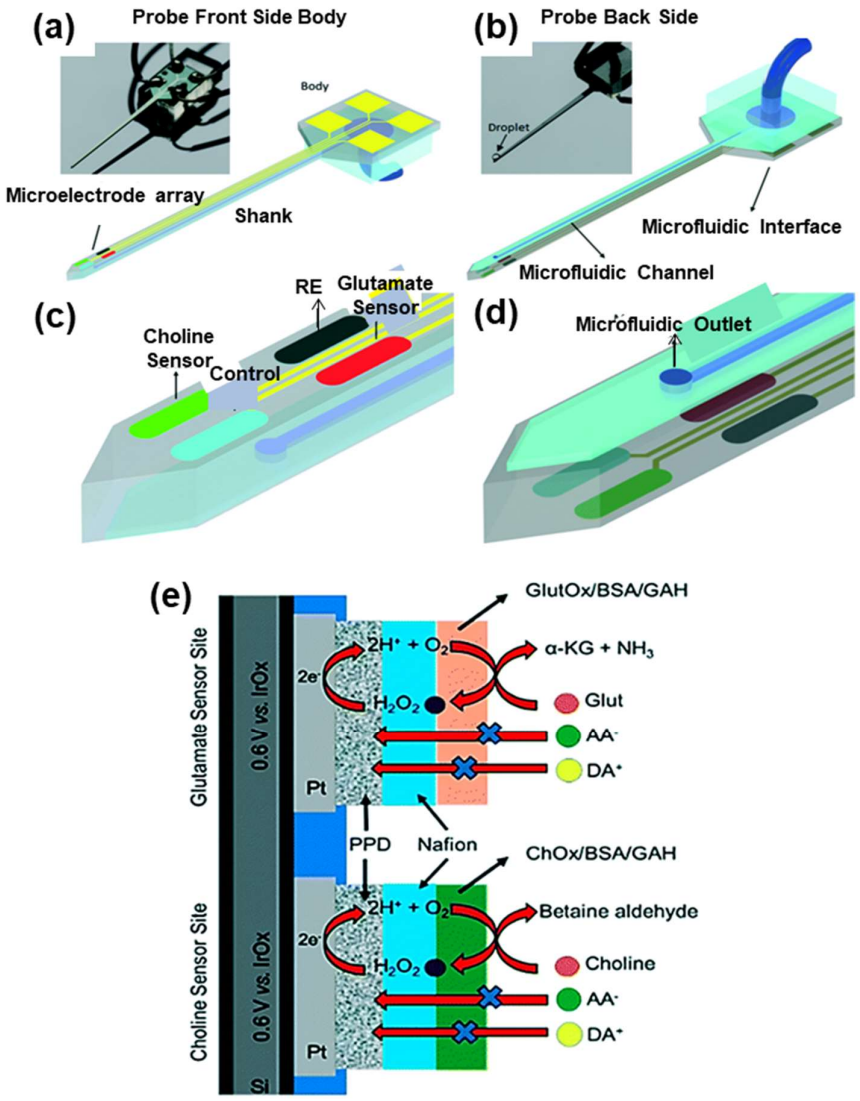


Figure 2-11. A silicon-based EC device for choline and glutamate sensing. (a)-(d) Front and back side design of the device. (e) Calibration curve of glutamate. e) Schematic representation of sensing principle. (Reprinted from [145] with permission from Royal Society of Chemistry.).

EC sensors have also been designed into implantable and wireless sensors that allow for chronic monitoring of brain neurochemicals in freely moving animals, which is critical in revealing the connections between neuronal processes and animal behaviors. Besides the general challenges in developing neurochemical monitoring sensors, additional challenges for implantable sensor starts from the moment when it is implanted inside the brain tissue. When the sensor is first implanted, the initial foreign-body response starts immediately, and a series of body rejection responses would happen within the next few days caused by the immune system. The warm and saline environment of brain tissue would accelerate the degradation of the sensor function, greatly impeding the lifetime of

the sensor down to several days[147]. For enzyme-based sensors, a fibrotic capsule would be formed around the sensor; and for metal electrode or silica optical fibres, metal corrosion and mechanical deformation at the implanted sites may lead to tissue inflammation and further discomfort to patients. To minimize these adverse consequences, studies have been carried out to fabricate biocompatible sensors for implantable applications.

In recent years, Huang's group has designed a few innovative wireless platforms for implantable neurotransmitter monitoring. For better biocompatibility, soft polymers were used as the substrate to adapt the curved surface of brain tissues (**Figure 2-12**) [148]. Multichannel flexible fibres (polymethyl methacrylate) were utilized for optoelectrical stimulation, on which 32 flexible electrode arrays were fabricated for spontaneous/evoked spike signals and ascorbic acid (AA) detection. A central wireless circuit was connected to the fibres and arrays to provide programmable light waves and collect the current signals. The collected signals were then amplified and transmitted to a monitoring device wirelessly. After implantation for 4 weeks, the device showed significantly reduced immunoreaction compared to the implanted gold-coated tungsten electrodes, indicating the potential for implantable and long term monitoring.

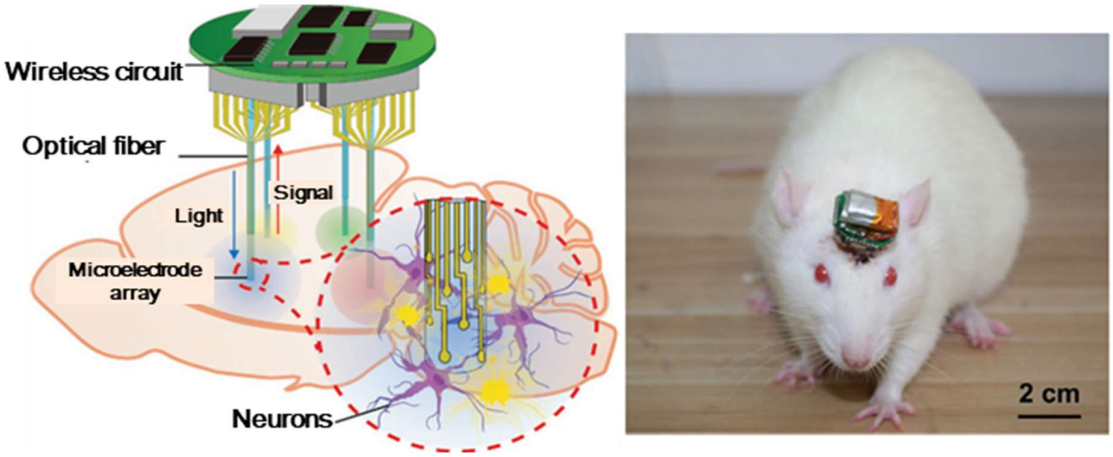


Figure 2-12. A multichannel flexible optoelectronic fibre device for wireless AA sensing and opto stimulation. (Reprinted with permission from [149]. Copyright 2020 Wiley-VCH GmbH)

Another device they designed was also a wireless platform that can be used to monitor calcium, sodium, and potassium concentrations in distributed brain regions (**Figure 2-13**) [150]. The

system was also fabricated with polymers, which showed great biocompatibility after implanted for 6 weeks, indicating great prospects in revealing the correlation between neuron chemical signals and external stimulations in long-term behaviour studies. Miniaturized carbon fibre combined with FSCV also offers promising methods for chronic neurotransmitter sensing.

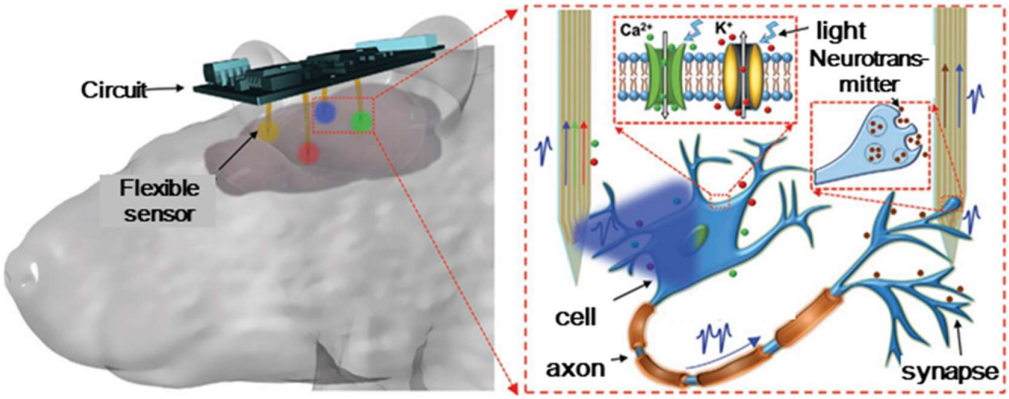


Figure 2-13. An implantable, flexible, and wireless device for opto-electrical stimulation and Ca2+, K+, Na+ sensing. (Reprinted with permission from [150]. Copyright 2020 WILEY-VCH Verlag GmbH & Co. KgaA, Weinheim.)

Using FSCV, a platform for in vivo dopamine sensing in living primates was developed **(Figure 2-14 (a)** [130]. The system allowed simultaneous dopamine monitoring in different brain sites by integrating several 7 μm diameter electrodes inserted into different sites in the striatum (**Figure 2-14 (b, c)**). A modular implant platform was developed for system control and signal processing. Using this system, dopamine release was monitored with a stable sensitivity between 30-40 nA/umol L^{-1} in primates for 170 days. In addition, the sensor did not cause big scaring or damage to the brain due to the small diameter and low cytotoxicity of the carbon fibre. The studies suggest that electrochemical sensors integrated with flexible carbon fibre, regional brain biomarkers can be potentially monitored for several months. It also indicated the potential for multiplexed long-term monitoring when different sensors are fabricated on the fibre tips.

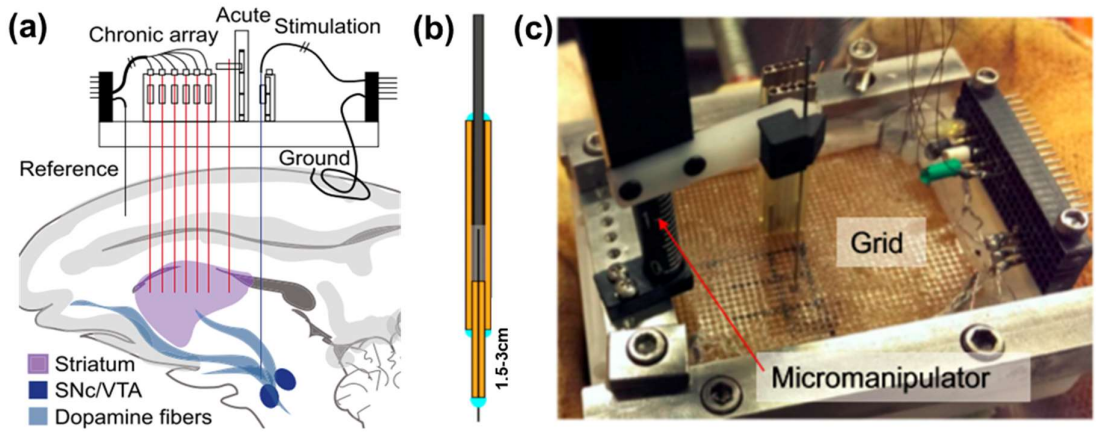


Figure 2-14. Primate-use platform for chronic dopamine sensing in vivo. (a) Schematic representation of the sensing system. (b) Design and structure of the probe. (c) Photo of the sensing system. (Figure reprinted with permission from ref. [130]).

2.5 Optical spectroscopy methods for in vivo brain neurochemical monitoring

Apart from the above-mentioned electrochemical methods, optical spectroscopy has also shown great potential in terms of in vivo brain neurochemical monitoring, as it is particularly beneficial for remote and high precision monitoring[151-154]. In optical sensing, the target analyte interacts with the molecular Recognition elements, leading to changes in certain optical properties that can be transduced to a measurable signal by the transducers. To date, a variety of optical techniques have been used for brain neurochemical monitoring, including fluorescence spectroscopy[155], NIRS[156], Raman spectroscopy[157-159], and surface plasmon resonance spectroscopy (SPRS) [154, 160-163] **(Figure 2-15)**.

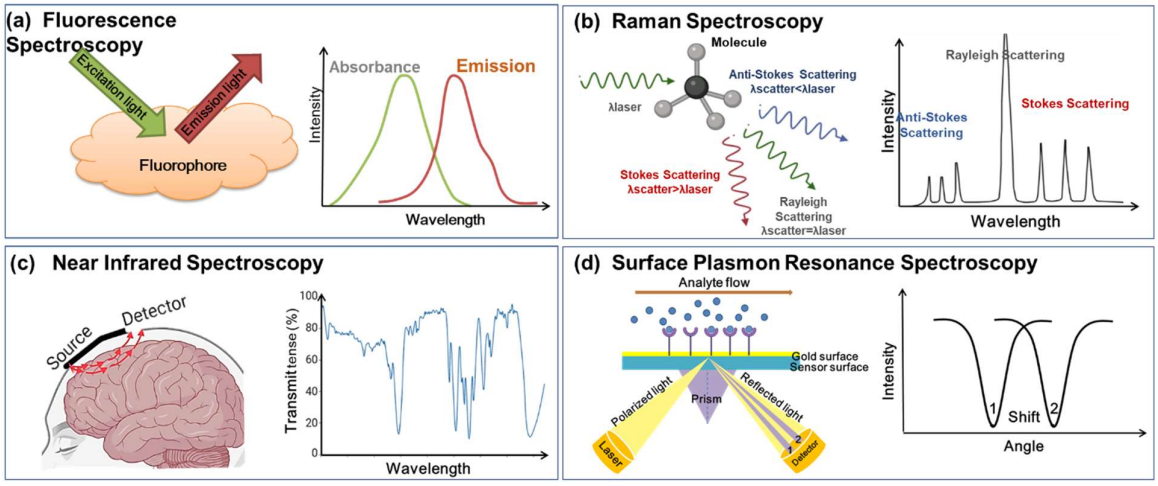


Figure 2-15. Schematic representation of sensing principles of four technology. Fluorescence spectroscopy (a), Raman spectroscopy (b), Near infrared spectroscopy (c), and surface plasmon resonance spectroscopy (d).

2.5.1 Fluorescence spectroscopy

Fluorescence is based on the phenomenon that for a specific type of material when illuminated with excitation light, it emits light with a different wavelength. This type of material is called fluorophores, and it has also been named as labeling reagent, fluorescence dyes, or stains (**Figure 2-16 (a)**). Fluorophores usually absorb lights at a low wavelength and emit lights at a longer wavelength. This phenomenon happens when the electron of the fluorophore becomes excited to an excited state after absorbing a photon and then relaxes back to the original ground state by emitting a photon (**Figure 2-16 (b)**). The emitted photon has relatively lower energy than the excitation photon and thus has a longer wavelength (**Figure 2-16 (c)**). Fluorescence spectroscopy is therefore a type of electromagnetic spectroscopy that examines a sample by measuring its fluorescence properties. In general, the fluorescence-based measuring system consists of four key elements: a light source, a filter or monochromator for wavelength selection, a fluorescence probe assay that interacts with target analytes, and a photodetector (**Figure 2-16 (d)**).

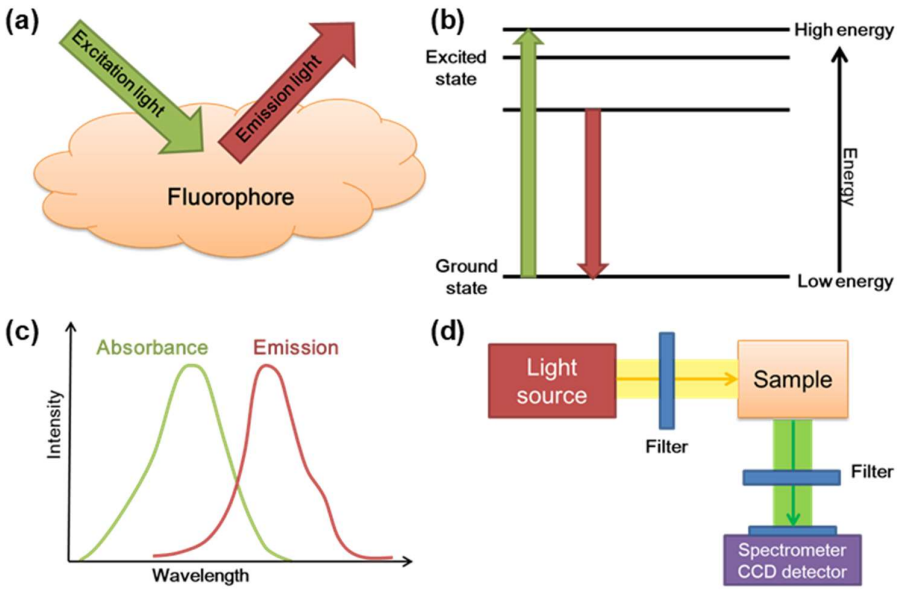


Figure 2-16. Principle of fluorescence spectroscopy. (a) Fluorophores are the type of material that emits light at a different wavelength from its excitation light, which is commonly used in fluorescence spectroscopy to label the target analyte. (b) Jablonski diagram. After the electron of the fluorophore absorbs a high-energy photon, the electron becomes excited. It then relaxes vibrationally and eventually back to the original ground state by emitting a photon at longer wavelength (lower energy). (c) Excitation and emission spectrum. The absorption peak shows the wavelength of the excitation light, and the emission peak shows the wavelength of the light emitted from fluorophore. (d) The sensing system of fluorescence spectroscopy consists of a light source, a filter or

monochromator for wavelength selection, a fluorescence probe assay that interact with target analyte, and a photodetector.

Based on the fluorescence quenching effect of DA, several monitoring sensors have been designed for the quantification of DA in the brain or in other biological samples. Govindaraju et al. [164] used self-synthesized nanoclusters bovine serum albumin gold nanoparticles (BSA-Au NCs) for selective DA detection in CSF. BSA-Au-NCs are auto-fluorescent particles, and their fluorescent intensity decreased due to the quenching effect of DA. Thus, based on the quenched fluorescence intensity of the BSA-Au NCs, DA can be quantitively detected. Tested with brain CSF, the sensor showed a LOD of 0.830 nmol L^{-1} for DA detection. In another study [165], a DA nanosensor was fabricated with single-strand (GT) 6 oligonucleotides functionalized single-wall carbon nanotubes. The system showed a 24-fold emission intensity when increased DA from 10nM to 100 μM and showed good selectivity toward DA from interferences including GABA, glutamate, and acetylcholine. When tested in brain slices, it showed comparable response time as FSCV equalled to 0.4s, and achieved a subsecond temporal resolution and a spatial resolution of up to 1 μm. These sensors also showed good potential for in vivo brain monitoring. The results indicate the high sensitivity and selectivity of fluorescent sensors in the measurement of dopamine with great response speed, suggesting a high temporal resolution.

In recent years, nanoparticle-based, quantum dots-based, and especially genetically-encoded protein-based fluorescence platforms have demonstrated a promising sensing perspective for in vivo brain neurochemical monitoring as it offers great temporospatial resolution and picomolar detection limit[166]. For example, in 2018, Patriarchi et al. developed a series of genetically encoded G-protein-coupled indicators called GRAB for in vivo DA monitoring[167]. These indicators convert conformational changes in the DA receptor into optical responses by inserting conformation-sensitive fluorescent protein in the natural DA receptor's third intracellular loop. Two years later, they further improved the sensor and developed the second-generation red fluorescent GRAB sensor, which achieved 2-3-fold higher dynamic range and in vivo performance. The sensor achieved subcellular resolution, subsecond responses, and nanomolar-to-submicromolar binding affinity[168], indicating that

fluorescent sensors can be used to measure biomarkers with a wide concentration range and high fluctuation speed.

In addition, due to different fluorophores have different emission wavelengths, multi-analyte sensing with multiple fluorophores becomes possible in fluorescence-based measurement. For example, after proposing the genetically encoded DA receptors, Patriarchi et al. engineered another red-shifted DA sensor RdLight1 to use with other green protein-based fluorescence sensors for multiplexed brain monitoring. Using genetically encoded iGluSnFR together with RdLight1, they successfully monitored glutamate and dopamine simultaneously with subsecond temporal resolution and cellular spatial resolution in freely behaving rats[169]. Fluorescence spectroscopy has great potential in studying cell-type-specific neuronal activity by offering precise neurochemical monitoring. However, the research on fluorescence spectroscopy for in vivo brain monitoring is much less than that of EC, which might be due to the lack of mature, low-cost, and non-cytotoxic fluorophores for neurochemical detection.

In another study, a miniaturized and implantable fluorescence sensor was developed for chronic monitoring of calcium fluorescence in the deep brain of mice (**Figure 2-17)** [153]. Low bending stiffness material polyimide and polydimethylsiloxane (PDMS) were used as the sensor substrate. In order to reduce tissue lesions and avoid the fibre impedance on animal movement, a wireless transponder for signal transmission was used instead of using optical fibres. The wireless system showed great ability in reducing the brain lesions in chronic implant and less impedance towards the mice movement while maintaining a comparable calcium monitoring performance as the traditional way of using optical fibres. The designed system was then used to study the secretion of calcium in accordance with award stimulation and other neuroscience studies.

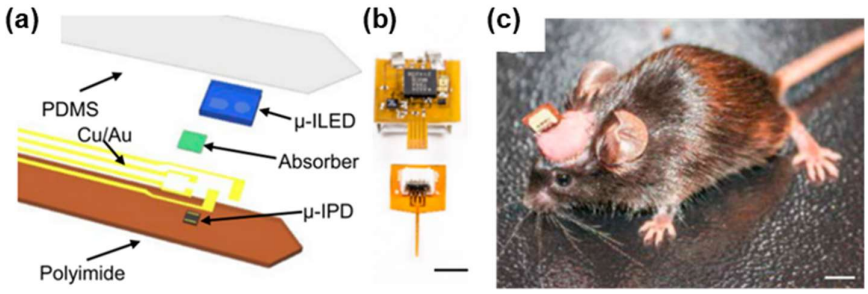


Figure 2-17. Miniaturized, ultrathin, lightweight wireless photometry systems for deep-brain Ca2+ measurements. (a) Schematic representation of the injectable, ultrathin photometry probe. (b) Schematic representation of the transponder. Scale bar = 4 mm. (c) Image of a freely moving mouse with a photometry system. Scale bar = 7 mm (Figure reprinted with permission from Reference 153.

In these studies, the indicators used for analyte recognition are either injected into the tissue prior to the detection or coated on the tip of fibre for brain monitoring. In the case when it is injected into the body, it will normally be excreted from the body with metabolism, therefore, the signal stability will decrease as the fluorophore concentration decreasing. Coating fluorophores on the tip of optic fibres, on the contrary, can improve the analysis length and reduce the complex sample preparation required in fluorescence sensing, but the spatial resolution will be compromised.

2.5.2 Raman spectroscopy

Raman spectroscopy (RS) relies upon the inelastic scattering of photons collected from tissue surfaces after interacting with excitation light. The wavelength shift in Raman scattering provides information about the vibration, rotation, or other low-frequency transitions in the target molecules, and thus serves as the fingerprint of the molecule (**Figure 2-15(b), Figure 2-18**)[170]. However, in real practice, approximately one in ten million photons undergo Raman scattering while the rest of photons undergo Rayleigh scattering, suggesting that the Raman signal is very weak and needs a long integration time to obtain a Raman spectrum. To solve this, techniques such as resonance Raman[171], spatially-offset Raman spectroscopy (SORS)[157, 172], and surface-enhanced Raman scattering (SERS)[157, 158, 173] have been developed to enhance Raman signals. SERS has gained popularity in brain neurochemical sensing, owing to its ultrahigh sensitivity and selectivity, and rapid response.

In Raman based molecular monitoring, a laser beam is used to illuminate the sample and the electromagnetic radiation of the sample is collected with an objective lens and sent through filters (notch filter, edge pass filter or band pass filter) to remove the Rayleigh scattered radiation. The rest of the light, which only includes Raman scattered light, is detected with a photodetector and spectrometer to obtain the Raman spectrum. (**Figure 2-18 (b)**).

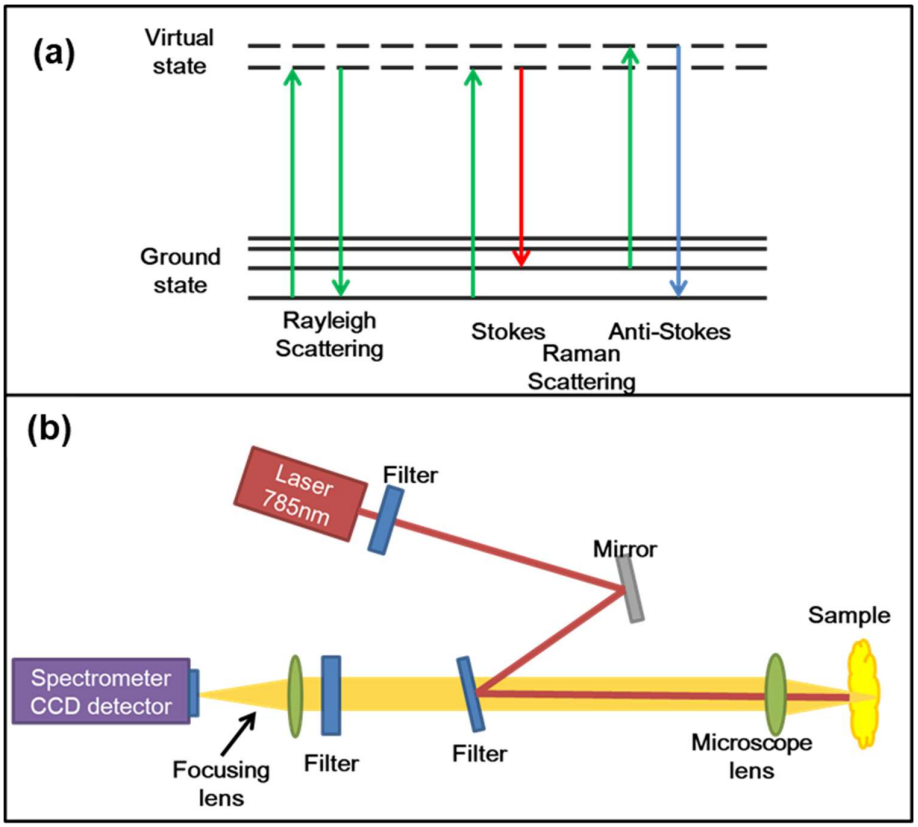


Figure 2-18. Principle of Raman spectroscopy. (a) Energy level schematic of Rayleigh and Raman scattering processes. Rayleigh scattering is an elastic scattering process, in which the excited photon relaxes back to its original vibrational state. In Raman scattering, two kinds of processes may happen. In the Stokes Raman process, the excited photon relaxes back to a higher vibrational state than it had originally. In the Anti-Stokes Raman process the excited photon relaxes back to a lower vibrational state than it had originally. (b) Schematic of the sensing system used for the Raman Spectroscopy measurements.

In a study, a gold nanoparticle enhanced bioassay was developed for the detection of glucose and lactate in brain CSF sampled by microdialysis (**Figure 2-19**)[173]. AuNPs were fabricated into an organic framework MIL-101, which is a porous and thermally stable metal. The fabricated AuNPs@MIL-101 could oxidize a Raman inactive reporter leucomalachite green to the active

malachite green (MG) under the presence of H_2O_2. Therefore, when assembled with glucose and lactate oxidase, the fabricated nanoparticles could be used to monitor glucose and lactate concentrations using SERS technology. In the calibration, the designed assay showed a linear range of 10 – 200 µmol L^{-1} and a LOD of 4.2 µmol L^{-1} for glucose, and a linear range of 10 – 200 µmol L^{-1} and a LOD of 5.0 µmol L^{-1} for lactate. A considerable challenge associated with SERS is its response is highly influenced by the fabricated substrate. However, in the substrate fabrication, random metallic nanoparticles are usually adopted, leading to a high variability and poor repeatability. Therefore, electrohydrodynamic microlithography was proposed to microengineer reproducible optofluidic for signal enhancement instead of using nanoparticles in a recent study [158]. With this method, the designed SERS sensor showed high reproducibility and stability. Besides, the sensor was able to detect N-acetylasparate (NAA), S100B and glial–fibrillary acidic protein (GFAP) simultaneously with a linear range of 1 fmol L^{-1} to 100 nmol L^{-1} for all the three chemicals and promising LODs of 0.12 pmol L^{-1}, 0.19 pmol L^{-1}, and 0.02pmol L^{-1} respectively, indicating that the proposed sensor can be used to measure multiple biomarkers simultaneously with great signal to noise ratio and high reliability.

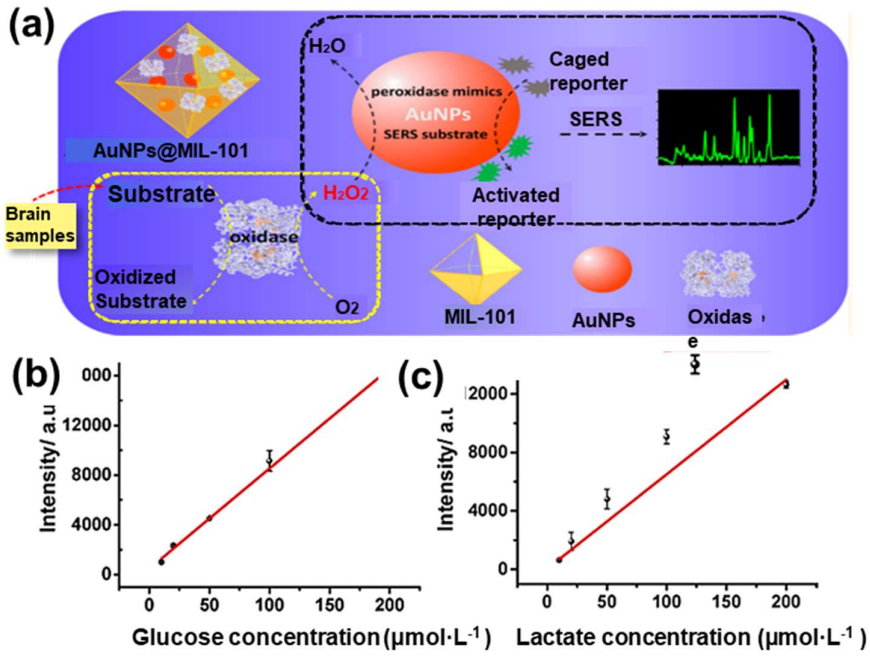


Figure 2-19. SERS sensor for glucose and lactate detection. (a) Schematic illustration of the function of AuNPs@MIL-101 for generation Raman signals. (b) Plots of Raman intensity versus glucose concentrations. (c) Plots of Raman intensity versus lactate concentrations. (Reprinted with permission from ref.[173] Copyright 2017, American Chemical Society)

Raman technology is capable of multi-analyte sensing with minimum sample pre-preparation and relatively simple device setup. The use of metal NPs can largely improve the signal-to-noise ratio and offer high sensitivity and selectivity of molecular measurement. Only one fibre is needed to both give the incident light and detect the scattered light, which reduces the device complexity and tissue damage. However, in real applications, Raman signal is usually very weak, and the spectrum is very noise due to background noise from autofluorescence and turbidity, which would require a highly controlled environment during the measurement and advanced post-signal processing techniques to remove the background noise.

2.5.3 Near infrared spectroscopy (NIRS)

NIRS a non-invasive technique that measures the concentration of an analyte based on the transmission or adsorption spectrum in the near-infrared light range (700–1000 nm) as it passes through tissue (**Figure 2-15 (c)**). Measuring cerebral regional tissue oxygen saturation using NIRS has shown its distinct advantages for non-invasive sensing and, as a result, has been commonly used in ICU[156]. Near-infrared light is widely used for oxygenation measurement because of its promising penetration property, allowing non-invasive brain oxygenation measurement through brain scalp and skull (**Figure 2-20**). The measurement of brain oxygenation is based on the Lambert-Beer law, where the absorptive capacity of a dissolved substance is directly proportional to its concentration in a solution. In the brain, hemoglobin is the main substance that attenuates the near-infrared light; thus, the absorption or transmission spectrum changes simultaneously as the concentration of oxygen changes in the tissue. However, similar to the EC-based commercially available Clark electrode for brain oxygen saturation measurement, NIRS based method could only reflect the oxygen saturation at a focal point. To monitor both regional and global brain oxygenation information, recent studies have proposed to use multiple oxygen sensing pairs located at different locations in the brain[174].

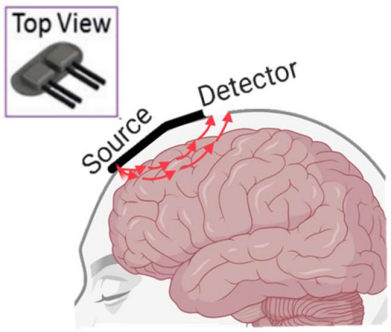


Figure 2-20. Schematic of a non-invasive neurometabolic optical monitor for the monitoring of brain oxygen saturation and blood flow.

The major advantage of NIRS-based measurement is that it is a non-invasive technique. However, there are some limitations in NIRS technology: only regional brain oxygen saturation can be reflected and combining several NIRS-based electrodes for a global measurement needs a large voltage supply and the weight of the system would be increased. Moreover, many factors, such as age, blood pressure, ICP, bone thickness, intracranial hemorrhage, and intracranial gas accumulation can affect the results of NIRS-based oxygenation measurement[175, 176].

2.5.4 Surface plasmon resonance (SPR) spectroscopy

SPR spectroscopy can be used to monitor brain neurochemicals based on the changes in the refractive index of surrounding media when the target molecule binds to the sensor receptor. In SPR-based sensors, a thin layer of a chemically inert and highly conductive metal such as gold is usually fabricated on the sensor surface for the generation of SPR, above which molecular recognition elements are immobilized for the recognition of target molecules [177]. For the detection of the bonded receptor-analyte complexes, polarized light from the laser source excites the surface plasmon polaritons, which are coherent charge-density waves in the metal, and the reflective light is detected with a photodetector at an angle depending on the refractive index of the surface (**Figure 2-15(d)**)[177]. After the bonding is formed, changes in the refractive index will lead to a change in the angle of the reflected light, which is detected as a shift in the reflected light spectrum. Therefore, variations of

neurochemical concentrations (c)n the sensing medium can be determined by measuring the refractive index changes in the interface.

A multimodality sensing array was designed by combining CV and SPR methods for the sensing of DA and serotonin in the brain tissue [163]. The sensing array was a hybrid structure of gold NPs and nanohole array, which presented high conductivity and high localized SPR sensitivity (**Figure 2-21**). CV was applied to induce the oxidation and reduction of DA and serotonin around the sensor, during which both electrical and spectral responses on the sensor surface were measured through transmission spectrum and voltammogram. Both sensing modalities demonstrated good integrity. The CV detection system achieved LODs of 14.86 $\mu molL^{-1}$ and 22.52 $\mu molL^{-1}$ for DA and serotonin respectively. Whereas, in the SPR system, relatively lower LODs of 12.45 $\mu molL^{-1}$ and 10.61 $\mu molL^{-1}$ were achieved for DA and serotonin detection. In addition, the SPR system presented a higher signal to noise ratio compared to the CV system, which might be because the SPR detection system has good robustness against interference like buffer solution, pH, and AA.

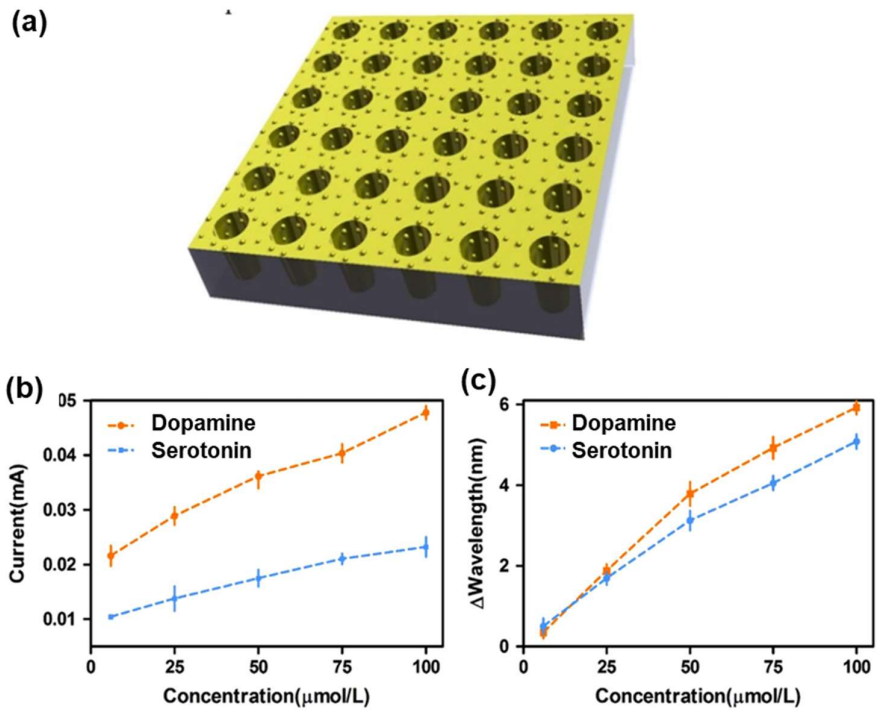


Figure 2-21. An SPR based optical-electrochemical nanosensor for dopamine and serotonin sensing. (a) Sensor design and schematic representation. (b) Calibration curve of EC sensor. (c) Calibration curve of SPR sensor. (Reprinted with permission from ref.[163] Copyright 2016 Elsevier B.V.)

Current studies on SPR for brain neurochemical monitoring are mostly conducted using sampled CSF or brain slice. Whereas SPR coupled with optical fibre offers cost-effective and simple-to-implant alternatives for in-situ and *in vivo* neurochemical measurements. Due to the miniaturized size and remote sensing ability of optical fibre, SPR optical fibre can be potentially used to sense hard-to-reach spaces. For example, a nanoscale SPR optical fibre was designed for dopamine concentration measurement (**Figure 2-22**)[178]. In the study, a metal-coated tilted fibre Bragg grating (TFBG) was used for DA sensing. A selective DNA aptamer layer and a graphene layer were fabricated above the fibre cladding for highly sensitive detection of dopamine. When the DNA aptamer captures DA molecules, a well-defined conformational change would occur and amplify the refractive index of the fibre surface, leading to alternations in bragg shifts, based on which DA concentration can be determined. The use of grating in the study could effectively excite and accurately measure plasmon resonances, which in turn improved the sensor sensitivity and reduced the LOD to picomolar level. In in vitro calibration, the designed SPR optical fibre presented a sensitivity of 0.29 dB/logmol L^{-1}, a linear range of 0.1 pmol L^{-1}-10 nmol L^{-1}, high selectivity, and a LOD of 0.1 pmol L^{-1}, which was adequate to monitor the DA fluctuations in the human brain. In addition, due to the property of TFBG, the designed sensor can perform self-calibration of the temperature and light power, which determined the high stability of the SPR optical fibre.

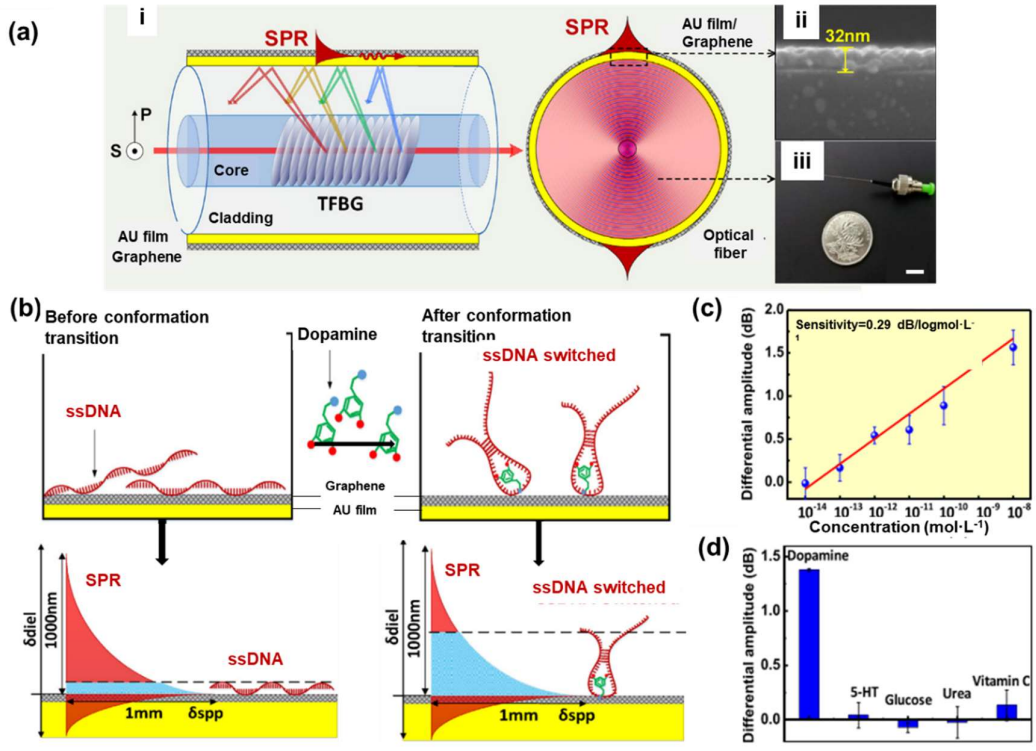


Figure 2-22. An SPR sensor for the detection of brain DA. (a) (i) Schematic representation of the plasmonic fibre-optic sensing system. (ii) SEM image of the sensor coatings. (iii) Photography of the designed sensor. (b) Schematic representation of dopamine sensing mechanism using the designed sensor: ssDNA aptamer is used for the recognition of dopamine molecules. Upon binding with dopamine, the overlap area between the plasmon energy field of the sensor surface and ssDNA aptamer would be changed due to the conformation of the ssDNA, leading to a larger plasmon phase velocity change and a shift in the SPR spectrum. (c) Calibration curve of dopamine detection with the designed optical fibre. (d) Comparison of the sensor response to targeted dopamine (10−9 mol L-1) and some other potential interferents (10−6 mol L-1 5-HT, 10−3 mol L-1 glucose, 10−3 mol L-1 urea, and 10−3 mol L-1 vitamin C) under the same experimental conditions. (Reprinted with permission from ref.[178] Copyright 2018 Elsevier B.V.)

SPR offers simple, high sensitivity, robustness, high reproducibility, and rapid detection of brain neurochemicals, which also allows multi-analyte detection. It is a label-free technique and can be used for small sample volume detection. However, related studies on in vivo brain neurochemical monitoring are still in their infancy, and further studies are needed to test its ability for in vivo sensing. Another major limitation associated with SPR is the heterogeneity of the surface sites, which leads to relatively low repeatability, and therefore, novel fabrication methods need to be developed for better deposition of the particles.

2.5.5 Optical fibre sensors

Optical fibre sensors have emerged as transformative tools in healthcare applications, revolutionizing the landscape of medical diagnostics and patient care. These sensors leverage the properties of light

transmission through optical fibres to detect and quantify various biological parameters with exceptional precision and sensitivity. Their small size, adaptability, remote sensing abilities, and minimally-intrusive nature render them especially beneficial for healthcare purposes. Optical fibre sensors offer a diverse range of capabilities, including monitoring vital signs, assessing biomarkers, and tracking physiological changes in real time. Their resilience in demanding environments like tissues or bodily fluids makes them invaluable in diagnostics, personalized medicine, assisting MRI for intraoperative guidance, and ensuring continuous patient monitoring. By providing reliable and accurate data while minimizing patients' discomfort, optical fibre sensors hold promise in enhancing the quality of healthcare delivery and driving advancements in early disease detection and treatment monitoring.

Optical fibre oxygen sensor has been developed for intramuscular oxygen monitoring with an aim for early diagnosis of acute compartment syndrome (**Figure 2-23**) [179]. In this study, a novel fluorescent oxygen probe was proposed that presents high sensitivity toward intramuscular dissolved oxygen levels based on the oxygen quenching effects. Various encapsulation matrix has been tested to achieve best sensing performance. Among various matrices, includingsol-gel, Pt(II)−pivaloyl in Cavilo, and poly(propyl methacrylate)(PPMA) matrix, PPMA exhibited the best encapsulation properties, leading to robust and reliable intramuscular oxygen measurement. Therefore, the synthesized oxygen probe is encapsulated in PPMA and coated on a 200μm core optical silica fibre. The authors further assembled the oxygen fibre sensor with a micro-LED, and a micro-spectrometer for portable continuous monitoring. The portable device has been successfully tested in vivo in a live porcine model, owing to the high adaptability of the fluorescent optical fibre sensor under various environmental conditions and its high selectivity and stability.

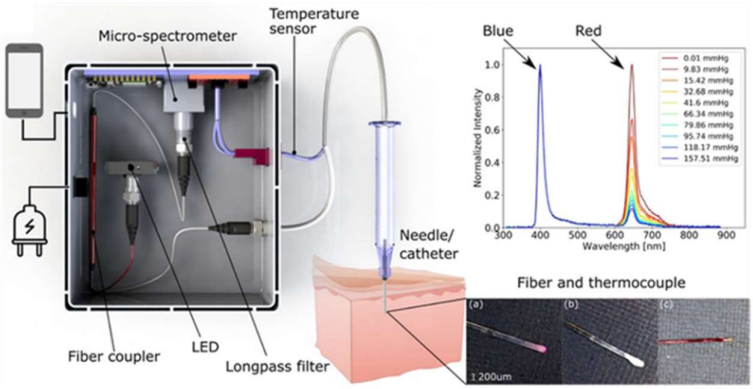


Figure 2-23. Optical fibre oxygen sensor for muscular oxygenation measurement. Reprinted with permission from ref. [179]. Copyright © 2021, American Chemical Society

In optical fibre-based sensors, the signal intensity is largely determined by the fibre core diameter, as a larger diameter leads to a larger sensing area, which in turn increases the signal intensity. However, a larger diameter would lead to greater tissue damage. Therefore, tapered fibre has been utilized to both increase the sensing area and remain a relatively small fibre diameter. In a recent study, a near-field optical probe system was designed for the continuous monitoring of cortisol in biological samples (**Figure 2-24**)[180]. Evanescent field effects of the tapered optical fibre were utilized to eliminate the impact of background noise. Polyethylene glycol (PEG) polymer chains were utilized to functionalize the fibre to minimize biofouling, insulate the sensor from nonspecific binding, as well as enhancing the attachment of the probes. Using an embedded system Arduino for system control and signal processing, the designed system successfully monitored cortisol fluctuation and concentrations in artificial CSF, indicating a great potential for in vivo clinical applications. Tapered fibres provide a larger sensing area and when integrated with biocompatible hydrogels, long term and implantable measurement can be successfully realized for various biomarker monitoring by changing the recognition probes.

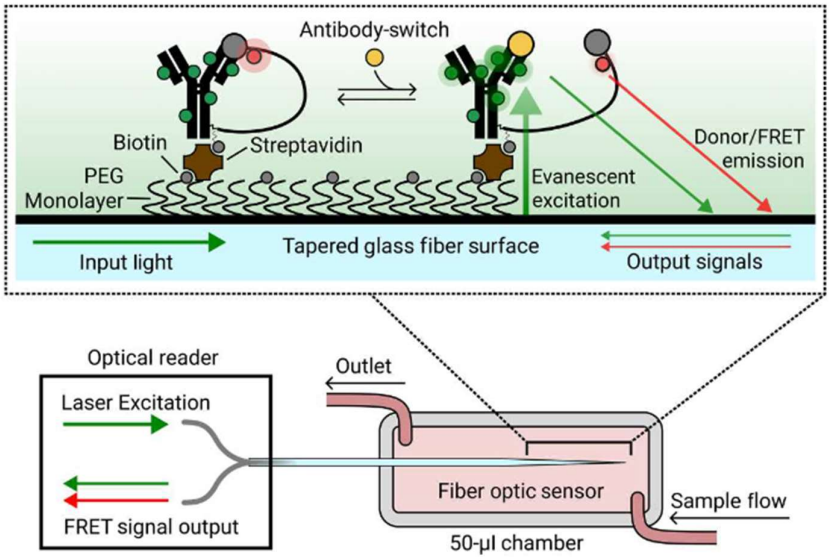


Figure 2-24. A near-field tapered fibre for the continuous monitoring of cortisol in biological samples. Reprinted with permission from ref. [180].

Optical fibre has also been integrated with Raman spectroscopy for in situ intraoperative, label-free cancer detection (**Figure 2-25 (a)**)[181]. Optical fibre was utilized to both excite the tissue and the Raman signal is detected through the same fibre for Raman spectroscopy. Using the system, various molecules can be detected, based on which cancer tissue can be distinguished from normal tissue, assisting in intraoperative cancer biopsy and resection with high accuracy (Area under curve = 0.9). Moreover, in order to improve biocompatibility, more and more studies have focused on designing soft hydrogel fibres to replace traditional silica fibres to reduce biofouling in long term in vivo measurement. In a study (**Figure 2-25 (b)**)[182], hydrogel fibres have been developed and optimized that have a poly(acrylamide-co-poly(ethylene glycol) diacrylate) p(AM-co-PEGDA) core and a Ca^{2+} alginate cladding for high efficient light transmission. Glucose receptor 3-(acrylamido)-phenylboronic acid is integrated into the hydrogel fibre structure for glucose measurement. Binding with glucose molecules changes the refractive index of the hydrogel fibre, leading to changes in the transmission of the incident light, based on which glucose concentration can be quantitatively measurement. The optical fibre sensor has demonstrated great ability in measuring glucose

concentrations and the system is believed to have improved biocompatibility and suitable for long-term in vivo or implantable measurement.

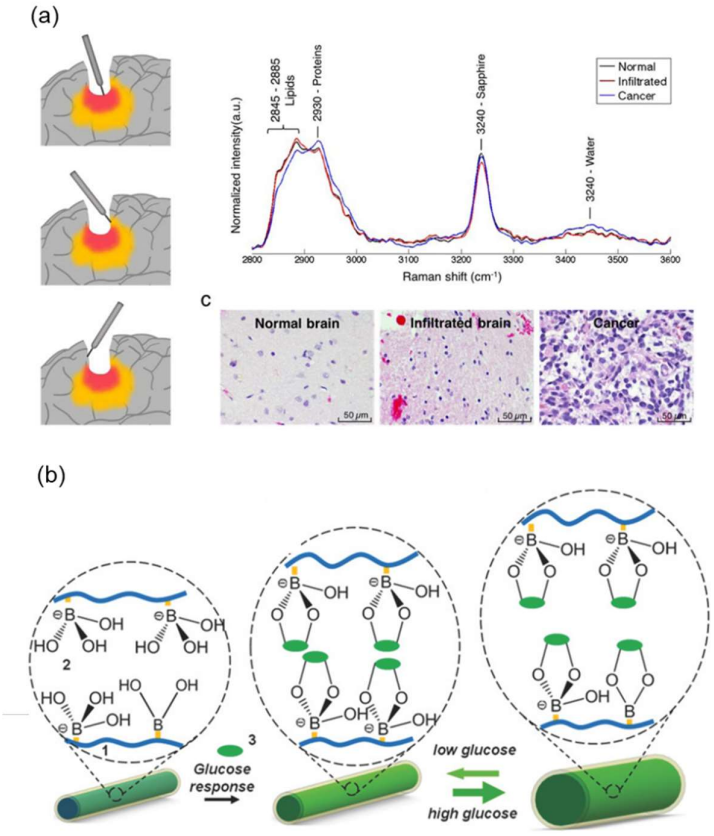


Figure 2-25. Recent advances in optical fibre sensors. (a) Optical fibre sensor for in vivo cancer detection. Reprinted with permission from ref. [181]. (b) Hydrogel fibre for glucose measurement. Reprinted with permission from ref. [182].

2.6 Computational methods for sensing signal processing and readout

Apart from novel sensor fabrication and development methods, biosensor signal post processing using advanced machine learning and computational algorithms also stand at the forefront of revolutionizing biosensor development and healthcare monitoring by overcoming the limitations in the hardware design. These advanced algorithms play a pivotal role in refining sensor capabilities, optimizing designs for heightened sensitivity, and improving the accuracy of data interpretation. They empower biosensors to not only detect minute biomarkers or physiological signals but also to process vast streams of data in real-time. This enables the extraction of intricate patterns and trends crucial for

disease diagnosis, treatment monitoring, and predicting patient outcomes. Here potential machine learning models especially regression models are introduced, and the integration methods are provided.

2.6.1 Machine learning regression models

Linear Regression (LR):

LR based biomarker concentration calculation fits a straight line to the data, assuming a linear relationship between the obtained biosensing signal (independent variable, x) and the biomarker (dependent variable, y). It models the x and y using equation (**Eq. 2-11**) and uses the least square to find the optimal weights (w) for each x. It is simple to understand and interpret. However, it is not suitable for non-linear relationships between signal and biomarker, and it does not perform well if there are outliers in the dataset. It might also lead to overfitting when a small dataset is used.

$$y = w_1x_1 + w_2x_2 + \ldots + w_nx_n + b \quad \textbf{(Eq. 2-11)}$$

Ridge Regression:

Similar to linear regression, Ridge regression has a penalty term which is called L2 regularisation for multicollinearity conditions that solves issues with outliers and smaller datasets, mitigating the possibility of overfitting. However, same as LR, it can only model linear relationships. Different from LR, in ridge, due to the L2 regulation, the weight for each input feature can be calculated using equation **2-12**, where X is the input feature vector/matrix, y is the biomarker concentration, I is the unit vector, and λ is the regulation index.

$$W = (X^TX + \lambda I)^{-1}X^Ty \quad \textbf{(Eq. 2-12)}$$

Lasso Regression:

Similar to ridge regression, lasso applies L1 regulation to solve the multicollinearity condition when a smaller dataset is used and for higher robustness towards outliers with high performance to higher

dimensional datasets. The weights are calculated using the equation **Eq. 2-13**. Here, β is calculated as $ai = \frac{1}{\sqrt{ei}+\varepsilon}$, where ei is the L1 regulation as penalty.

$$W = (X^T X + \lambda \beta^T \beta)^{-1} X^T y \text{ (Eq. 2-13)}$$

Decision Tree (DT):

DT makes a series of yes/no decisions based on the features (biosensing signals) to classify or predict a continuous value (biomarker). It is classified as a non-parametric supervised learning model and can be used for the classification and regression of non-linear relationships. Decision tree is a simple method for regression tasks, however, may easily cause overfitting and minor differences in the dataset can have significant impacts on the results.

Random Forest (RF):

RF is an ensemble learning that combines multiple decision trees to improve prediction accuracy and reduce overfitting. In the training process, the original dataset is divided randomly into two groups. The first group is used to build multiple trees according to the number of estimators. This technique merges the results from the generated trees to improve the accuracy and robustness. The remaining data of the original is used as a validation set to evaluate the model's performance and reduce the overfitting problem.

Support Vector Machine (SVM):

The Support Vector Regression (SVR) is a variant of the Support Vector Machine (SVM), which is a supervised learning technique commonly employed for both classification and regression problems. SVMs find a hyperplane that best separates data points belonging to different classes or output values. Many types of kernels are available for selection based on the dataset types, which transform the data into a space with a higher number of dimensions, enabling linear separation. SVR is effective for high-dimensional data, however, tuning hyperparameters can be complex, and may not be ideal for highly non-linear relationships.

Polynomial Regression:

Polynomial regression fits a higher-order polynomial curve to the data, capturing non-linear relationships between signal and biomarker. However, same as linear regression model it is prone to overfitting if the polynomial order is too high, and if the dataset is small.

Bayesian Regression:

Bayesian regression treats the regression coefficients as random variables with associated probability distributions. It explicitly models uncertainty in the parameter estimates, allowing for more robust predictions and the quantification of uncertainty. In Bayesian regression, parameter estimation involves computing the posterior distribution of the regression coefficients given the data and prior knowledge. This is done using Bayes' theorem, which combines the likelihood of the data with prior beliefs about the parameters to obtain the posterior distribution. Bayesian regression allows for the incorporation of prior knowledge or beliefs about the parameters into the analysis. This prior information can help regularize the estimates and improve the robustness of the model, especially when dealing with limited data.

2.6.2 Regression model evaluation metrics

Firstly, R^2 is one of the commonly used indicators to evaluate the accuracy of regression models [183]. The coefficient of determination is a statistical measure of the closeness of the data to the fitted regression line. The value is within [0,1] with 1 indicateing a perfect fitting and 0 meaning that the data do not obey the fitting model at all. The mathematical equation of R^2 is as **Eq. 2-14**, where N is sample numbers.

$$R^2 = 1 - \frac{\sum_i (y_{predicted} - y_{mean})^2}{\sum_i (y_{actual} - y_{mean})^2} \quad \textbf{(Eq. 2-14)}$$

Secondly, the root mean square error (RMSE) is another popular indicator used to evaluate the regression model. RMSE quantifies the mean discrepancy between the predicted values and the actual values. A superior performance is indicated when a mall RMSE number is obtained. Moreover, RMSE

possesses the advantage of expressing the degree of error in the identical unit as the target, facilitating its interpretation [183].

$$RMSE = \sqrt{\sum_{i=1}^{N} \frac{(y_{predicted} - y_{actual})^2}{N}} \textbf{(Eq. 2-15)}$$

The mean absolute error (MAE) between predicted values and actual values is another indicator commonly employed to evaluate the efficacy of a regression model. MAE directly measures the differences between the predicted value and the actual value with the same unit disregarding their direction, and it is widely used as the loss function in deep learning-based regression model [183]. It is calculated using the equation:

$$MAE = \frac{1}{N}\sum_{i=1}^{N}\left|y_{actual} - y_{predicted}\right| \qquad \textbf{(Eq. 2-16)}$$

Apart from mean absolute value, mean squared error (MSE) is another similar and commonly used indicator for the evaluation of regression model performance. Instead of taking the absolute difference between the predicted value and the actual value, MSE uses the square value of the two differences to enlarge the difference. Compared with MAE, MSE gives a much larger value when outliers exist in the dataset. MSE is calculated as:

$$MSE = \frac{1}{N}\sum_{i=1}^{N}(y_{actual} - y_{predicted})^2 \qquad \textbf{(Eq. 2-17)}$$

2.6.3 Application example

In a recent study [184], convolutional neural networks (CNN) were utilized to identify bacteria and pathogens from Raman spectra. Due to the integration of CNN networks, 30 bacterial pathogens were identified with high accuracy from Raman spectra, offering a potential solution for antibody testing and pathogen identification, which would make an impact on medical diagnosis. Apart from this, the combination of Raman and CNN has also been applied in other areas including intraoperative cancer resection[185], liver cancer diagnosis[186], and breast cancer identification[185], in which CNN has greatly contribute the signal processing and pattern recognition that significantly boosted the accuracy of diagnosis.

In recent years, regression models such as principle component regression (PCR), Partial Least Squares Regression, PLSR(PLSR), have received great attention in chemical, pharmaceutical, food and plastic industries.[187-191] It is a common technology that has been applied in spectral measurements related studies as these studies usually contain highly related variables.[190, 192] PLSR is particularly useful when the predicted variables are collinearly or the number of predicted variables is greater than the number of observations. Similar to PCR, PLSR also simplifies the number of predictive variables into a series of uncorrelated components (also known as components) and carries out least squares regression on these components. In PLSR, the selection of components considers not only the variance explained by the various orthogonal components but also the correlation between these components and the response output. Taking FSCV as an example, PCR focuses on the maximizing of covariance in the obtained voltammograms for the separation of various cofactors and PLSR focuses on both voltammograms and the correlation between voltammograms and concentrations.[193, 194]

A study was conducted recently to compare these two regression methods in predicting analyte concentrations using FSCV measurement.[133] A total of 650 and 1500 voltammograms obtained from the solution made with five neurochemicals at various concentrations and pHs values were used as test dataset for the prediction of a single substance and mixture of substances respectively. Absolute error and mean absolute percentage error of the estimated concentration and the real concentration were used for the evaluation of different models. The results showed that compared with PCR, PLSR has significant smaller errors both in the prediction of single substance concentrations and in the prediction of mixtures concentrations. In addition, PLSR also showed significantly higher selectivity when the solution is a mixture of various substances (**Figure 2-26**).

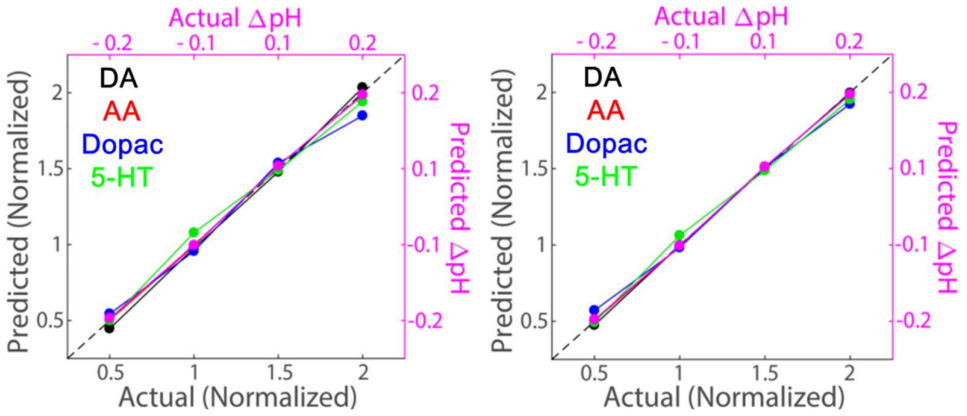


Figure 2-26. Comparisons of PCR (left) and PLSR (right) in prediction analyte concentrations.(Reprinted with permission from ref. [133])

Apart from using algorithms for signal enhancement, optimization has also been made in changing the waveform of FSCV. [142, 143] Furthermore, in amperometric sensors, only the analyte concentration lies within linear range can be calculated, which may have constrained the sensor application. Thus Hilbert- transformation was proposed for the concentration calculation in non-linear range to enlarge the detection range and improved the sensor accuracy.[195]

Post signal enhancing strategies can also be achieved by using headstage circuit. For example, as shown in **Figure 2-17(a)**,[196] to reduce the thermal noise generated by the feedback resistor in the transimpedence amplifier, a switched-capacitor paradigm was used to avoid large ohmic resistors in the system, which also retained as much of the physiological information in the signal because no digital or analog filter was used. To further minimize the corruption caused by the various noises from the environment the captured signal was digitalized immediately. The converted digital signal was then sent to the digital signal processing circuit board to display the molecule concentration at a user interface. In addition, Field Programmable Gate Array (FPGA) was used for the real-time visualization and post-processing of the collected data due to its high speed, multithread computing and high stability. In another study, physical separation of the sensing system or channel shielding was adopted in order to minimize the cross talk between different signals in the multimodality monitoring device (**Figure 2-27(b)**).[197]

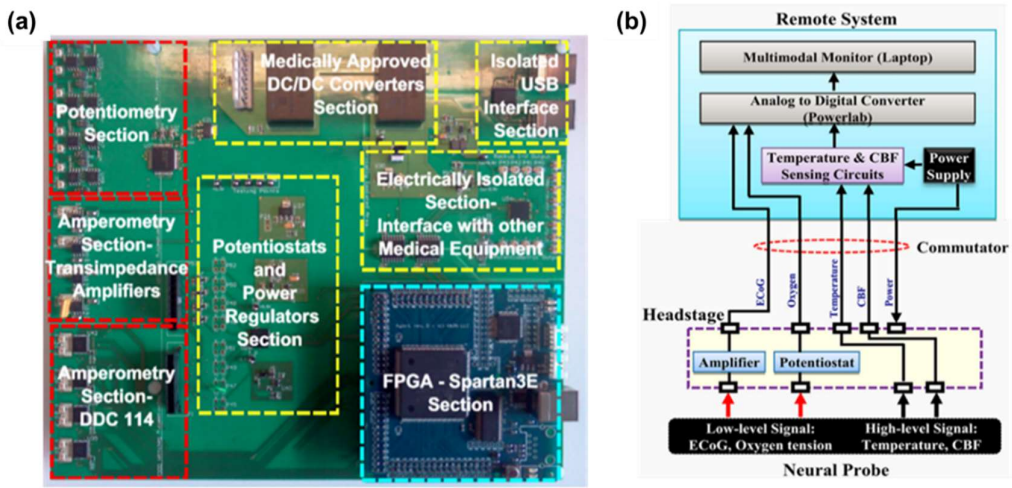


Figure 2-27. Methods in circuit design and post signal processing algorithms. (a) custom PCB on optimizing the trolley setup for TBI monitoring (Reprinted with permission from [196]Copyright 2016 Papadimitriou, Wang, Rogers, Gowers, Leong, Boutelle and Drakakis.). (b). The proposed system is capable of simultaneously recording ECoG, brain oxygen tension, cortical temperature, and cerebral blood flow in awake tethered rats (Reprinted with permission from [197]. Copyright 2016 Limnuson, Narayan, Chiluwal, Golanov, Bouton and Li.).

Apart from assisting in accurate readout, computer algorithms have also helped in horizon prediction and concentration forecasting before signal stabilizes to reduce response time and also for in time prevention. In a study[14], gaussian processes (GP), logistic regression, and autoregressive Ordinal-Regression have been used together with brain oxygenation and ICP sensor for the prediction of brain physiology conditions 30 minutes in advance to prevent adverse effects. The algorithms study the temporal changes in the sensor response signal and model the reactions for signal forecasting, which has a great potential for the treatment of TBI. In order to reduce sensing response time and fully achieve real-time monitoring, researchers have modelled sensor responses from the perspective of binding affinity and equilibrium to study the mechanisms in the sensing responses and inverse the physical kinetic for the prediction of biomarker concentrations before the signal stabilized. Frequency studies have also been utilized to further correct the prediction and compensate for the background noise impact and molecule's reaction speed for highly accurate prediction.

Moreover, the integration of machine learning allows for the personalization of monitoring systems, considering individual variations and enabling tailored healthcare interventions. These algorithms facilitate the creation of wearable sensors and remote monitoring systems, enabling

continuous, non-invasive tracking of health parameters, thereby shaping the future of proactive, personalized, and precise patient care.

2.7 Conclusion

In conclusion, in this section, advances in three different technologies are analysed for brain neurochemical monitoring, and the advantages and disadvantages of these three sensing technologies are summarized in **Table 2-2**. Droplets-based sampling system combined with online analyser using microfluidic system showed a promising future for brain monitoring in the clinic. These newly designed systems have significantly shorter time delays and higher temporospatial resolution compared to the conventional microdialysis-based sensing systems. In terms of EC-based biosensors, recent advances in microfabrication and surface modification have aided the design of highly sensitive EC sensors. However, when used in long term and in vivo studies, unsatisfied selectivity and biocompatibility are two big concerns. As an alternative to the EC sensors, optical spectroscopy enables brain neurochemical sensing with cellular scale spatial resolution, subsecond temporal resolution, high selectivity, and long lifetime. More importantly, Raman and NIRS also provide the possibility for non-invasive monitoring. However, far less research has made attempts for optical-based in vivo brain neurochemical monitoring compared with EC sensors, which might be owing to the lack of low-cost, non-toxic, and biocompatible indicators and optical fibres.

Fibre based optical sensors offer several advantages over electrochemical sensors in neurochemical sensing. Optical fibre sensors offer high performance in deep tissue measurement with minimized size and high stability. The sensor can be constructed to be label-free, is able to perform long-term real time monitoring, are small in size, immune to electromagnetic interference, and can perform in vivo calibration, offering a good application prospect in real-time and long-time detection in vivo. Although optical fibre sensors may face the challenge of limited number of materials available for fibre fabrication and noisy signals, by integrating with robust signal processing techniques, biomarker signals can be identified and monitored with high accuracy, providing new solutions for multiplexed and implantable brain monitoring.

Table 2-2. Comparison between three sensing methods.

	Microdialysis	**Electrochemical**	**Optical**
Advantages	(Sensing performance defined by analyser); Low detection limit (<1 nM); High sensitivity; High selectivity; Able to perform multianalye monitoring Measuring basal levels.	High temporal resolution (μs to ms); High spatial resolution (<100 μm); Low detection limit (<1 μM); Fast response; Miniaturizible; Implantable.	Low detection limit (<1 nM); High temporal resolution (<ms); High spatial resolution (<1 μm); High selectivity; Immune to electromagnetic field; Non-invasive sensing (Raman, NIRS); High robustness; Long stability.
Disadvantages	Long time delays (minutes); Low temporal resolution (seconds to minutes); Low spatial resolution (>100 μm); Ex vivo.	Limited selectivity; Limited number of analytes; Limited lifetime.	Limited in vivo studies and available reports; Interfered by tissue absorption or autofluorescence. Relatively longer response time

Recent advances in hardware and data analysis offer the potential for large and fast neurophysiological recordings analysis, transient pathophysiology identification with high resolutions both temporally and spatially.[198-200] Various statistical modelling methods including regression models, and some other machine learning algorithms can be used as post signal processing techniques. These algorithms provide promising solutions to process electrochemical and optical signals as they have demonstrated great potential in noise elimination, non-linear signal modelling, and detection weak signals. The advancement in microcomputer and FPGA also facilitate the development of neurochemical monitoring devices with high processing speed and stability.[196]

Therefore, micorbiosensors combined with optimized algorithm and circuit design is expected to break through the existing barriers and realize clinical neurochemical monitoring.

The interplay between technical advancements in microsensors and progress in brain neurochemical monitoring has enabled breakthroughs in biomedical and neurological applications. Novel solutions for brain monitoring have demonstrated the great potential of interdisciplinary integration in technology innovations. As various novel technologies in material science, chemistry, biology, and computing continue to evolve, this interplay will fuel the development of continuous high accurate and multimodality neurochemical monitoring devices and eventually pave the way for the next medical revolution.

Chapter 3 Reflection-Based Multiplexed Optical Fibre Sensors for Dynamic Brain Monitoring

Dynamic brain monitoring can mitigate TBI deterioration and enable precise treatment. Despite many studies on brain monitoring systems for neuroscience applications, current technologies are limited in providing a continuous and real-time readout of multiple brain biomarkers simultaneously due to limited sensor performance and signal interference. Regression modelling, being a subfield of machine learning (ML) algorithm, offers great advantages in signal enhancement and pattern recognition. However, studies on ML-integrated optical fibre sensors for precise brain monitoring have been rarely reported. Here, a multiplexed optical fibre sensor regulated by regression algorithms is developed for the dynamic monitoring of brain pH, temperature, DO, and glucose levels due to their importance in brain physiological function (Section 2.2) and the abundant sensing probe options for the selective detection of these biomarkers. The proposed sensing system has demonstrated good sensing abilities and can perform dynamic monitoring of multiple biomarker fluctuations in lamb brain models. The results indicate the possibility of the multiplexed optical fibre sensor for continuous brain physiology reflection, suggesting a promising prospect for clinical applications.

3.1 Introduction

In this chapter, I first proposed a multiplexed optical fibre sensor integrated with a programmed AI prediction platform for dynamic monitoring of pH, temperature, DO, and glucose levels in artificial CSF (aCSF) simultaneously. The chosen of these four biomarkers is due to their importance in brain physiology (Section 2.2) and, to date, the dynamic monitoring of these biomarkers simultaneously in TBI patients has yet to be realized due to the lack of long-term and real-time multiplexed monitoring systems in clinical settings. Highly sensitive and selective indicators were physically encapsulated in silicate and transparent sol-gel films to reduce leaching and improve stability. The sensing films for the detection of four biomarkers were then fixed on the tip of a flexible optical fibre through a self-made sheath for *in-situ* sensing. Reflection spectra of the optical fibre sensors were obtained and analysed based on machine learning regression models, which could eliminate the cross interferences and provide a quantitative and accurate readout of the biomarker concentrations dynamically. To

validate the developed sensing platform in measurement biomarker concentrations under various environment, I performed *in-situ* and *ex vivo* tests using lamb brains to mimic four simplified TBI stages and test the sensor's performance in measurement brain biomarkers while implanted in brain tissues instead of clear buffer solutions. The designed multiplexed optical fibre sensor demonstrated high sensitivity, selectivity, and stability in monitoring the four brain biomarkers simultaneously with low time latency. The developed sensor indicated the potential to reflect dynamic changes of the biomarker and identify the transition of various stages, indicating its ability in real-time and continuous monitoring of multiple physiological biomarkers for the applications in clinical settings.

3.2 System design and development

The first sensing system proposed for the aim of the thesis is a reflection fibre-based sensing system for the measurement of brain pH, temperature, glucose, and dissolved oxygen levels. A flexible optical fibre sensor was designed for multiplexed dynamic monitoring of brain biomarkers (**Figure 3-1**). The optical fibre sensor is composed of a flexible reflection optical fibre that is designed to be inserted into brain tissue. In this design, I chose to use only one reflection fibre for multiplexed biomarker monitoring to reduce system complexity, and reflection fibre has the advantage of a large and adjustable sensing field of a reflection fibre. The mixed reflection light from the film was detected with the reflection fibre and decoded with the spectrometer. Several studies have reported leveraging colorimetric and fluorescent methods for the measurement of pH, temperature and glucose in human samples. One commonly seen application is the urine strips that measure multiple biomarkers including pH, glucose, and proteins by dipping into the urine samples based on the color changes. Therefore, in this study, I tried to integrate multiple colorimetric/fluorescent sensing films with optical reflection fibre for brain sample monitoring and direct quantitative readout.

During measurement, the sensors are placed in front of the reflection fibre, and the sensing field can be adjusted by tailoring the distance of the air gap between the sensors and the fibre tip. The mixture of the reflection light of the sensors within the sensing region is detected by the reflection fibre that contains the information of all sensors in the region, which can be analysed using post analysis algorithms. In this design, the tip of the fibre attaches four sensing films through a black

sheath for four biomarkers sensing simultaneously (**Figure 3-1 (a)**). The black sheath was designed to reduce the background noise and fix the sensors at a constant distance in front of the fibre tip. The reflection Y-type optical fibre was also used to transmit the broadband light to excite the sensing films and send the reflected light continuously to a spectrometer for spectra acquisition and dynamic brain biomarker analysing (**Figure 3-1(b)**). A microcontroller was used to analyse the reflection spectra and calculate the measured biomarker concentrations. To eliminate the interferences between the four optical sensors and provide a high-accurate and quantitative readout of the biomarker concentrations, machine learning-based regression models were developed and optimized based on the features of the reflection spectra.

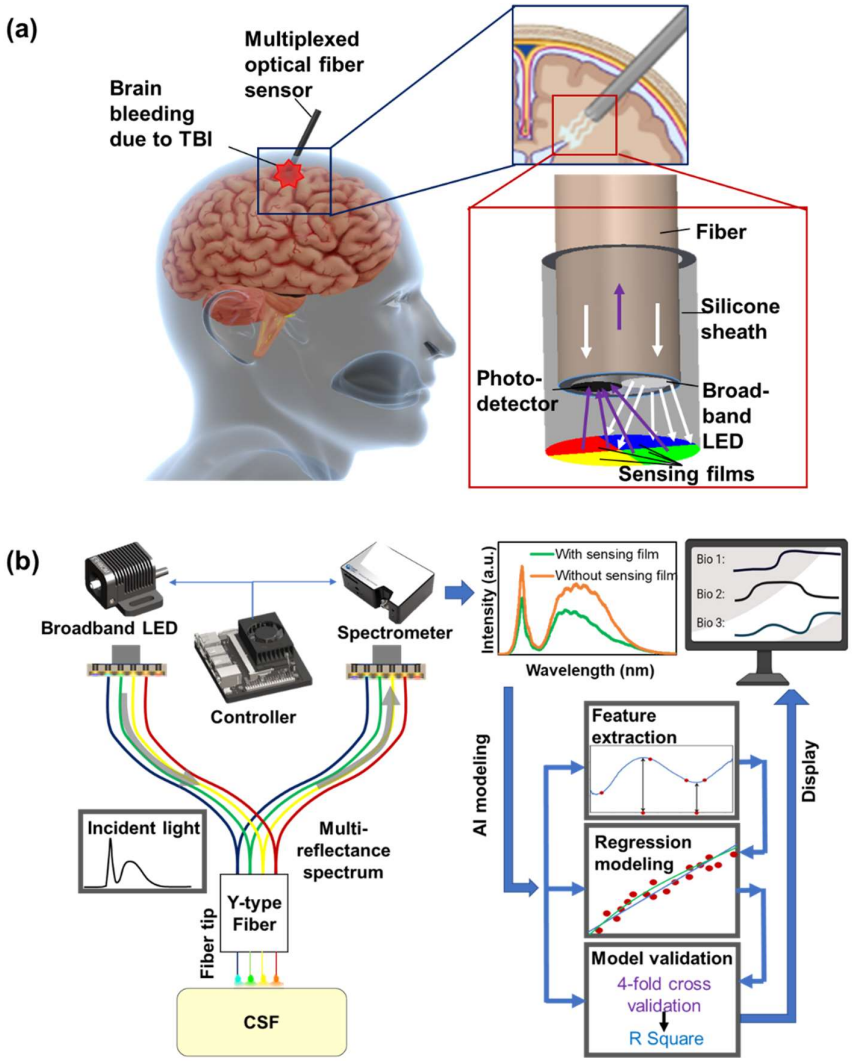


Figure 3-1. A multiplexed optical fibre-based sensing platform for dynamic monitoring of biomarkers in brain CSF. (a) Schematic of the designed optical fibre sensor for brain CSF dynamic monitoring in clinical settings. Four sensing films are attached to the optical fibre tip and inserted into brain tissue for in situ measurement. (b) Schematic illustration of the analytical equipment and data analysis for a multiplexed sensing Y-type optical fibre. The Y-type optical fibre was used to deliver broadband light to the sensor and transmit the reflected light to a spectrometer (left). AI regression models for biomarker concentrations prediction. The prediction accuracy is evaluated with the index R Square (right).

One of the most important designs after deciding on the optical sensing setup is therefore the fabrication of the sensing films. The working mechanisms of the four optical sensors were based on the changes in their photophysical properties upon the interactions between the sensing films and the target biomarkers (**Figure 3-2 (a)**). Similar to the colorimetric sensing strips, in this study, the sensing films were also fabricated by encapsulating sensing probes/indicators in a matrix. However, different from paper-based strips, in order to achieve great sensing stability and improve reusability, the probes need to be encapsulated in a solid and stable non-water-soluble matrix. For stable, robust, and

biocompatible sensing, the indicators were encapsulated in transparent silicate films (**Figure 3-2 (b, c)**). The sensing film was fabricated using an organic-modified sol-gel process, which has been widely used in sensor fabrication and probe encapsulation. Sol gel is a three-dimensional network porosity silicate structure that has great water permeability and small and adjustable pore sizes [201]. Sol gel has been widely used in various biomedical sensor fabrication due to its great biocompatibility [202]. Sol-gel films could effectively ensure the biomarkers move freely into the film and interact with the sensing probes and in the meantime avoid the indicators leaching from the films. To achieve simultaneous monitoring of 4 biomarkers, the corresponding four sensing films were cut into equivalent ¼ round shapes and multiplexed at the tip of reflection fibre to form a round shape via a silicone sheath. The sensing film was placed 4 mm above the fibre tip by adjusting the sheath to allow for signal detection of all sensing films *via* the optical fibre. A shorter distance would lead to a higher intensity and thus a higher signal-to-noise ratio and a smaller sensing region. A reflection isolation film made with glass microfibres was coated on the surface of the four sensing films to enhance reflection optical signals and block the background noise. A photograph of the designed optical fibre sensor is shown in **Figure 3-2 (c),** where a black silicone sheath with four sensing films on the top is fixed on the distal tip of an optical fibre. The overall size of the sensing area is 2 mm in diameter.

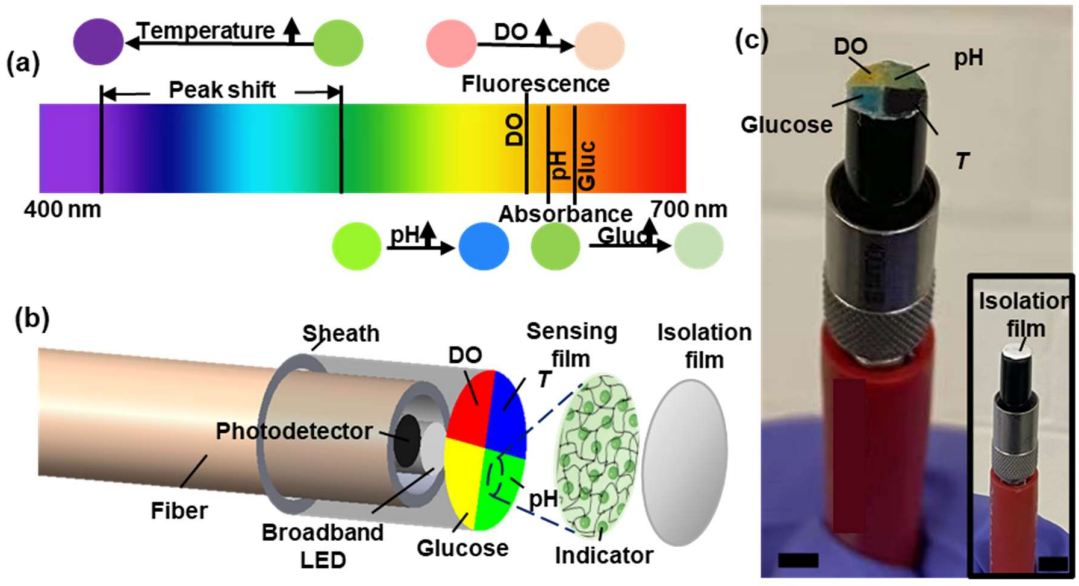


Figure 3-2. Design and photograph of the sensing probe and system.(a) Sensing mechanisms of pH, temperature (T), DO, and glucose (gluc) sensors. (b) Schematic and fabrication methods of the multiplexed optical fibre

sensor. (c) photograph of pH, temperature, DO, and sensing films being fixed at the distal tip of the fibre through a silicone sheath. Scale bar = 1.0 mm. Inset: photograph of the isolation film. Scale bar = 2 mm.

The optical setup for *in vitro* measurement is shown in **Figure 3-3**, where one end of the Y-type optical fibre with the sensing films on the tip was inserted into aCSF in a cuvette. One end of the Y-type optical fibre was connected to a light-emitting diode (LED) light driven by an LED controller, and the other end was connected to the spectrometer for reflection spectra analysis. The spectrometer was connected to a microcomputer for optical signal post-processing and visualization. Several optical features were extracted upon obtaining the captured reflection spectra. By learning the extracted features, regression models were built and implemented on the microcomputer to predict the biomarker concentrations and provide a dynamic quantitative readout of the target biomarkers. The prediction accuracy of the model was also used to evaluate the feasibility of the developed sensing platform.

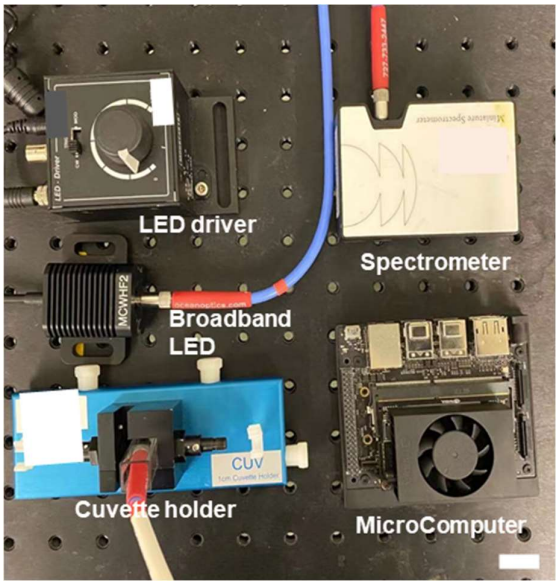


Figure 3-3.Photograph of the integrated AI-based multiplexed sensing platform. Scale bar = 1.5 cm.

The selection of biomarker indicators directly determines the sensing performance of the sensing films. In this study, I decided to use commercially available and widely validated methods for these four biomarkers as the aim of the project is the development of an optical sensing system for sensor

multiplexing. The selection of the indicators should also ensure that the maximum reflection peaks of the sensors in the reflection spectrum when exposed under broadband LED are not completely overlapped. Overlapping is unavoidable in the reflection spectrum as the reflection peaks usually have broad peak widths, however, partial overlapping can be tolerated and separated using post signal processing algorithms. The chosen biomarker indicators are listed below:

For pH measurement, Bromocresol green (BCG) was selected as it has a pka at around 7 when encapsulated in sol gel silicate. The temperature sensing probe was designed to use cholesteric liquid crystals, which have different physical properties under various temperatures. The DO sensing film was made with tris(4,7-diphenyl-1,10-phenanthroline)ruthenium(II) dichloride complex (Ru(dpp)) encapsulated in sol gel. It is a fluorescent indicator and can be quenched by oxygen. The glucose sensing film detects glucose based on the production of H_2O_2 in glucose redox reaction. Therefore, in glucose sensor film development, 3,3',5,5'-tetramethylbenzidine (TMB), glucose oxidase (GOD), and peroxidase (POD) were encapsulated in sol gel matrix for H_2O_2 detection, and reaction catalysation.

3.3 Materials and methods

Four sensing films are fabricated, optimized, characterized, and evenly placed on the fibre tip for multiplexed measurement. Here detailed methods are presented for the development of the reflection fibre based multiplexed biomarker monitoring system, including the optical sensing system setup, and sensing film fabrication methods for pH, temperature, DO, and glucose. System validation methods using artificial CSF and ex vivo brain models and the biocompatibility test of the system using cell culture methods. In the end a miniaturization method is presented to reduce the sensing probe dimensions. The results for the following experiments are included in section 3.4-3.10.

3.3.1 Chemical reagents and materials

Glycidoxypropyltrimethoxysilane (GLYMO) (98%), tetraethoxysilane (TEOS) (98%), tris(4,7-diphenyl-1,10-phenanthroline)ruthenium(II) dichloride complex (Ru(dpp)), D-(+)-glucose (99.5%), 3,3',5,5'-tetramethylbenzidine (TMB), peroxidase (POD), cholesteryl nonanoate (CN), cholesteryl oleyl carbonate (COC), cholesteryl benzoate (CB), 3,3',5,5'-Tetrabromo-m-cresolsulfonphthalein

(BCG) (95%), Triton x-100, phosphate buffered saline (PBS), sodium chloride (NaCl) (99.5%), calcium chloride ($CaCl_2$) (93%), potassium chloride (KCl) (99%), magnesium chloride ($MgCl_2$) (98%), zinc chloride ($ZnCl_2$) (98%), sodium phosphate dibasic (Na_2HPO_4) (99%), sodium phosphate monobasic (NaH_2PO_4) (99%), copper (II) chloride (93%), D-(+)-glucose (Glu) (99.5%), L-ascorbic acid (AA) (99%), uric acid (UA) (99%), sodium nitrite ($NaNO_2$) (97%), albumin from porcine serum (alb) (98%), hydrochloric acid (HCl) (37%), nitric acid (HNO_3) (70%), sodium hydroxide (NaOH) (97%), 5-hydroxyindole-3-acetic acid (5HT) (98%), and ethanol (99%) were purchased from Sigma Aldrich. Sodium L-lactate (La) (98%), sodium pyruvate (Pyru) (99%), and dopamine hydrochloride (DA) (99%) were purchased from Alfa Aesar. Dulbecco's Modified Eagle Medium (DMEM) and penicillin-streptomycin (P/S) were purchased from Gibco. Fetal Bovine Serum (FBS) was purchased from PAN-Biotech (Germany). Trypsin was purchased from Biosharp. Cell counting kit-8 (CCK-8) was purchased from APExBIO. LIVE/DEAD™ Viability/Cytotoxicity Kit was purchased from Beyotime. Microglass fibres were purchased from Whatman. All the chemicals were reagent grade and used as received without further purification.

3.3.2 Instrument and Experimental Setup

A fibre-Coupled LED (Thorlabs, MCWHF2) and a 450 nm Collimated Laser Diode (Thorlabs, CPS450) were used as a broadband light source and a 450 nm excitation light source, respectively. A T-cube LED driver (Thorlabs, LEDD1B) was used to control the light intensity. The reflection light was guided by a 400 μm premium bifurcated fibre (QBIF400-VIS-NIR, Ocean Insight) and measured using a FLAME-S-VIS-NIR-ES spectrometer assembly (350 nm-1000 nm) (Ocean Insight) due to the signals to be detected are in visible ranges. The absorbance was measured using a microplate reader (Molecular Devices, USA). The micrographs were obtained by an upright microscope for polarisation (DM2700 P, Leica). A fluorescence microscope (MSHOT, Guangzhou Micro-shot Technology Co., Ltd) was used to capture fluorescence micrographs. A hot plate stirrer (Fisherbrand Isotemp) was used to homogenize the sol-gel precursor solutions and control the temperature of the buffer solutions during experiment. A pH meter (FiveEasy F20, Mettler Toledo) was used to measure the pH value. An oxygen benchtop meter (HI-2004 Edge®, Hanna Instruments) was used as a golden standard to

prepare DO buffer solutions. The spectrometer was connected with Jetson Xavier NX Developer Kit (Nvidia) to visualize and capture the spectra. The reflection spectra obtained during the experiment were analysed offline using a Python code. Ocean View 2.0 and Thermo Scientific Skanlt were used as the software to analyze data from a spectrometer and a microplate reader, respectively. The camera of a smartphone iPhone 11 was used to capture the photographs of the sensing system and the sensor films and all photos were taken with the same white balance and exposure settings. An Apreo S scanning electron microscope (SEM) was used to examine the film morphologies. The accelerating voltage was maintained at 15 kV. Atomic force microscope (AFM) (MultiMode 8 SPM, Bruker) images were taken to examine the roughness of the sensing film.

3.3.3 pH Sensor fabrication and characterisation

Fabrication of sol-gel sensing film

Sol gel films were used to encapsulate the indicators to prevent leaching and improve stability[203, 204]. TEOS and GLYMO were mixed and used together to encapsulate the pH indicator and fabricate uniform pH sensing films[205]. Triton 100 was used to reduce the film tensions. The ratios of the chemicals used for the fabrication of the sensing films were optimized as described below to achieve the optimal morphology and sensing performance.

The fabrication methods followed a similar procedure introduced in [201]and [36]. I optimized the procedure by tailoring the formulation and ratio of GLYMO and TEOS. Sol-gel precursor solutions (1 mL) containing TEOS and GLYMO (single precursor or mixture), 1.2 mL of ethanol, 0.4 mL of HCl, 16 mg of BCG, and surfactant (Triton X-100) were mixed according to **Table 3-1** to obtain sol-gel coating solutions. The mixture was homogenized for 3 h using a hot plate stirrer that allowed for subsequent aging at a room temperature for at least 72 h[205].

Silica sol was obtained by using 500 µL of TEOS and 600 µL of ethanol. This solution was added into a mixture of HCl (25 µL, 1 mol L-1) and DI water (125 µL) with constant stirring under 60°C to accelerate the hydrolysis and condensation reactions. 1.6 mg of the pH indicator was added to the solution under stirring for 60 min. The sol was then spin coated on a transparent plastic film to form a uniform layer (500 rmp, 1 min). The film was then air dried for a thorough gelation and indicator

stabilization, followed by rinsing with DI water to remove weakly entrapped dyes. SEM, AFM, and microscope images were taken to examine the morphology of the sensing film. Sensitivity and film morphology were studied to optimize the sensing film fabrication formula. The optimal fabrication formula was also applied to DO and glucose sensing film fabrication. An isolation film made from glass microfibre (Whatman, Grade GF/C), which has high reflection properties and high-water permeability, was placed above the sensing films and the edges of both layers were glued together using epoxy glue.

Table 3-1. Composition of sol-gel coating solutions

Sol-gel coating solutions	The molar ratio of TEOS: GLYMO	BCG (mg)	Triton X-100 (2×10^{-3} mol L^{-1}, mL)	DI (mL)	HCl (0.1 mol L^{-1}, mL)	Ethanol (mL)
T (1:0)	1:0	16	0	0.2	0.4	1.2
TS (1:0)	1:0	16	0.2	0	0.4	1.2
TG (1:0.1)	1:0.1	16	0	0.2	0.4	1.2
TGS (1:0.1)	1:0.1	16	0.2	0	0.4	1.2
TG (1:0.2)	1:0.2	16	0	0.2	0.4	1.2
TG (1:0.3)	1:0.3	16	0	0.2	0.4	1.2
TG (1:0.4)	1:0.4	16	0	0.2	0.4	1.2
TG (1:0.5)	1:0.5	16	0	0.2	0.4	1.2
TGS (1:0.5)	1:0.5	16	0.2	0	0.4	1.2
TG (1:0.6)	1:0.6	16	0	0.2	0.4	1.2
TG (1:0.7)	1:0.7	16	0	0.2	0.4	1.2
TG (1:1)	1:1	16	0	0.2	0.4	1.2
TGS (1:1)	1:1	16	0.2	0	0.4	1.2

Fabrication comparisons

Based on the morphology and the calibration curve of each sensing film fabricated following the formulation in **Table 3-1**, the optimal fabrication method was determined and used for the following film characterisation experiment and the same fabrication formula were applied to the fabrication of other sensing films. The results are introduced in Section 3.5.

Characterisation of pH sensing film

Buffer preparation

PBS solutions were prepared by dissolving PBS tablets in DI water (one tablet in 200 mL of DI water), which yielded 0.01 mol L^{-1} of PBS, 0.0027 mol L^{-1} of potassium chloride, and 0.137 mol L^{-1}

of sodium chloride. The original buffer pH was 7.45 at 24 °C, and PBS solutions with pH values at 6.0, 6.4, 6.8, 7.2, 7.6, and 8.0 were adjusted by adding HCl or NaOH. The ionic strength of the buffer was adjusted to 150 mmol L^{-1}.

pH sensitivity

The fabricated optical fibre sensor was characterized using the prepared standard PBS solutions. The optical fibre sensor was immersed in the PBS solutions and the reflection intensity was recorded in each buffer solution after the signal stabilized. The correlation between various pH buffers and the reflection intensities at 623 nm was evaluated. The sensitivity of the sensor is calculated by the slope of the calibration curve.

The sensing of biomarkers is based on the principle that the absorption abilities the pH indicator possesses vary under different pH levels [36]. To indicate the absorption abilities, normalized reflectance spectrum was calculated for the calibration of the sensing films, which is reversely correlated with the absorbance spectrum. The normalized reflectance spectra were calculated using the equation below:

$$I/I_0 = \frac{Spectrum\ (with\ sensing\ film) - Spectrum\ (background\ noise)}{Spectrum\ (without\ sensing\ film) - Spectrum\ (background\ noise)} \quad \textbf{(Eq. 3-1)}$$

where I denotes the intensity of the reflectance spectrum with sensing film, and I_0 denotes the intensity of the reflectance spectrum without sensing film. The higher the absorption ability the lower the I/I_0 in the normalized reflection spectrum.

Response time and reversibility

Response time was measured using the two extreme values pH 6.0 and pH 8.0 of PBS solutions. The response time is different when the pH changes between different values. The optical fibre sensor was immersed in pH 6.0 buffer first. When the signal stabilized, the optical fibre sensor was immersed in the pH 8.0 buffer. After the signal stabilized, the optical fibre sensor was moved back to pH 6 PBS solution. This procedure was repeated 10 times to evaluate the reversibility of the sensor. The reflection intensity at 625 nm was measured in a time dependent mode during the experiment. The collected data were then used to calculate the response time from pH 6.0 to pH 8.0 and pH 8.0 to pH 6.0 offline. The response time is calculated as the time required for the sensor output to stabilize from

the moment it is inserted to a new buffer solution. The repeatability is measured by calculating the standard deviation of the measured intensity at pH 6.0 and pH 8.0 during the 10 repeats.

Temperature dependence

The fabricated pH sensing films were placed in microplate wells and immersed in 5 mL of pH standard solutions (pH = 6.0, 6.4, 6.8, 7.2, 7.6, and 8.0). The microplate reader with an incubator was used to control the temperature and measure the absorbance at 623 nm of the soaked sensors under temperature of 25°C, 30°C, 35°C, and 40°C to study the temperature influence on sensing signals. These temperature values were selected as it covers human physiological range and room temperature.

Stability

To measure the stability for continuous monitoring, the reflection spectrum of pH 7.4 PBS solution measured with the proposed setup was taken every 2 h for a continuous 24 h monitoring as the first 24 hours is the most important for patients admitted to the hospital or in ICU[206].

Selectivity

Table 3-2. Composition of interference solutions

Interference solutions	Compounds added	Concentration in cerebrospinal fluid	Concentration in interference solutions
Na^+	NaCl	110-170 mmol L^{-1}	170 mmol L^{-1}
K^+	KCl	1.0-8.0 mmol L^{-1}	8 mmol L^{-1}
Ca^{2+}	$CaCl_2$	1.2 ± 0.0125 mmol L^{-1}	1.2 mmol L^{-1}
Mg^{2+}	$MgCl_2$	0.89 ± 0.11 mmol L^{-1}	0.9 mmol L^{-1}
Zn^{2+}	$ZnCl_2$	0.1 — 0.5 µmol L^{-1}	0.5 µmol L^{-1}
Cu^{2+}	$CuCl_2$	0.3125 µmol L^{-1}	0.3125 µmol L^{-1}
NO_2^-	$NaNO_2$	5.1 ± 0.8 µmol L^{-1}	0.01 mmol L^{-1}
Pyru	CH_3CH_2COONa	0.03 — 0.15 mmol L^{-1}	0.15 mmol L^{-1}
UA	Uric acid	5 — 25 µmol L^{-1}	25 µmol L^{-1}
AA	Ascorbic acid	100 — 200 µmol L^{-1}	200 µmol L^{-1}
Lac	Lactate	1.01 -2.09 mmol L^{-1}	2 mmol L^{-1}
Gluc	Glucose	2.5 — 4.4 mmol L^{-1}	4.4 mmol L^{-1}
DA	Dopamine Hydrochloride	30 pg mL^{-1}	30 pg mL^{-1}
Alb	Albumin	0 — 500 mg L^{-1}	500 mg L^{-1}
5HT	5-Hydroxyindole-3-acetic acid	2-3 µmol L^{-1}	3 mmol L^{-1}

Two types of selectivity tests were conducted. In the first selectivity test, the interference solutions were prepared by adding interference compounds into PBS solutions (**Table 3-2**). The pH values of

the solutions were adjusted by 1 mol L^{-1} HCl and 1 mol L^{-1} NaOH to pH 7.4. The optical fibre pH sensor was then immersed into the interference solutions (pH=7.4). The reflection intensity at 623 nm at different interference solutions was measured using the same sensing setup. In the second selectivity test, the inference analytes were added to PBS solutions (pH 7.4), and the reflectance spectra of the sensor were obtained without adjusting the solution's pH to 7.4.

Pressure dependence

The sensor performance at different brain intracranial pressure (ICP) was also studied. Brain ICP is in the range of 7.2-15.5 mmHg; therefore, the optical fibre sensor was dipped into the buffer solution at different depths (0-30 cm) to simulate human physiological pressure ranges according to the equation pressure= $\rho \cdot g \cdot h$, where ρ is the density of the buffer solution (approximate 1 g/cm^3) and g is the gravity constant. The sensing spectra at different depth were obtained and analysed. The same experiment was also conducted to the other three sensors.

Leaching test

The leaching test was conducted by immersing the fabricated sensing film in 10 mL of PBS for 3 days. Blank sol-gel films were fabricated using the same process without adding the indicator. Three types of leaching conditions were investigated: (i) pH 6.0; (ii) pH 7.0; and (iii) pH 8.0. The degree of indicator leaching was assessed by measuring the absorbance of the PBS solution after the sensing film being immersed for 3 days. The PBS solution with blank silicate gels was measured as a reference. Absorbance spectra were acquired by measuring a 180 μL buffer sample using the microplate reader. All tests were performed in triplicate. Leaching absorbance percentage, which is defined by the ratio of the solution absorbance to the immersed sensing film absorbance at the measured wavelength, is used to indicate the leaching severity over 3 days.

Leaching tests were also conducted to the other three sensing films (temperature sensing film, DO sensing film, and glucose sensing film) using the same protocol after fabrication.

3.3.4 Temperature Sensor fabrication and characterisation

Temperature sensing film fabrication:

The temperature sensor was fabricated based on the thermostats of cholesteric liquid crystals. The fabrication methods were taken from reference [207]. The cholesteric liquid crystals mixtures were achieved by mixing COC, CN and CB (weight ratio 0.35: 0.55: 0.10). 60 µL of the mixture drop was dipped between two transparent round shape contact papers (1 mm in diameter) and sealed to prevent leakage. The sensing film was then attached to the fibre tip sheath with medical grade tapes.

Temperature sensor characterisation:

Sensor calibration curve

Temperature sensors were characterized with a pH= 7.4 PBS. A hot plate was used to adjust the buffer temperature, which was monitored by a thermometer to precisely control temperature variations. The sensors were immersed in PBS solutions with temperature ranging from 34.0°C–42.0 °C. Reflection spectra were acquired in a reflection mode and the spectra peak shifts over temperature were recorded.

Temperature sensor response time and reversibility measurement

Response time was measured using two pH 7.4 PBS solutions with one at 36.0 °C and another one at 40.0 °C. The optical fibre sensor was immersed in a 36 °C buffer first. After the signal stabilized, the fibre sensor was moved to 40.0 °C buffer and the fibre sensor was moved back to 36.0 °C buffer after stabilizing. This procedure was repeated 10 times for the evaluation of reversibility. Reflection spectra were measured and the reflection peak at each measurement was calculated. The response time is defined as the time interval from the moment that sensor is immersed in a 36.0 °C or a 40.0 °C buffer solution until it reaches a stable value. The repeatability is measured by calculating the standard deviation of the measured intensity at 36.0°C and 40.0°C during the 10 repeats.

Temperature sensor stability for long term monitoring

The photostability for continuous temperature monitoring was also measured. The reflection spectra of the proposed optical fibre sensing setup in 37.0°C pH 7.4 PBS solution were taken every 2 h for a continuous 24 h monitoring.

3.3.5 DO sensor fabrication and characterisation

DO sensing film fabrication:

The fabrication procedures were same as the fabrication of pH sensor except here 22 mg of oxygen fluorophore Ru(dpp) was used instead of the pH indicator[208].

DO sensing film characterisation:

Buffer preparation

In the calibration of DO sensors, standard DO buffer solution preparation is very challenging as DO level is highly sensitive to many factors including temperature and pressure. A tiny change in the environment temperature, pressure, or vibration would change the DO level of the buffer. Here, I proposed a method to prepare standard DO buffer solutions with high repeatability by mixing 100% DO and 0% buffer solutions at various ratios. This method was stable, repeatable, and direct. In this method, two buffer solutions were prepared first. 100% DO buffer, which was prepared by bubbling 100% condensed air to a 10 mmol L^{-1} pH 7.4 PBS solution for 10 min, and 0% DO buffer, prepared by bubbling pure N_2 gas to a 10 mmol L^{-1} pH 7.4 PBS solution for 10 min.

Gradient DO level solutions were then prepared by mixing the 100% DO and 0% DO solutions at various ratios for sensor characterisation. A low oxygen (0% DO) solution was syringed to reduce DO level while 100% DO saturated DI water was used to increase DO level. The DO value of the mixed solution was measured using a benchtop oxygen meter in real time as golden standard (**Figure 3-4**). The method showed a corrected trend in DO buffer preparation and showed high repeatability. All the characterisation tests were conducted under a stable room temperature (25 ℃) and standard atmosphere.

Excitation and emission wavelength determination

The fabricated sensing films were first measured using a 96-well microplate reader for the determination of excitation and emission wavelengths. The Ru(dpp) indicator has an excitation wavelength at around 450 nm and an emission wavelength at around 600 nm. Therefore, for excitation spectrum measurement, 600 nm was used as emission wavelength. For emission spectrum measurement, 450 nm was used as an excitation wavelength.

Sensor calibration:

The optical system for the measurement of DO is as shown in **Figure 3-4 (d)**. The fabricated DO fibre sensor was inserted into the buffer solution using a three-neck flask. The sensing film was fixed to the sheath tip and dipped into the buffer solutions. Reflectance spectrum was utilized for the measurement of the fluorescence. A 450 nm LED source was used as the excitation of the sensing film. Reflectance spectra were measured using a spectrometer (from 450 to 780 nm). The emission intensity was used to calculate the relationship with the DO levels.

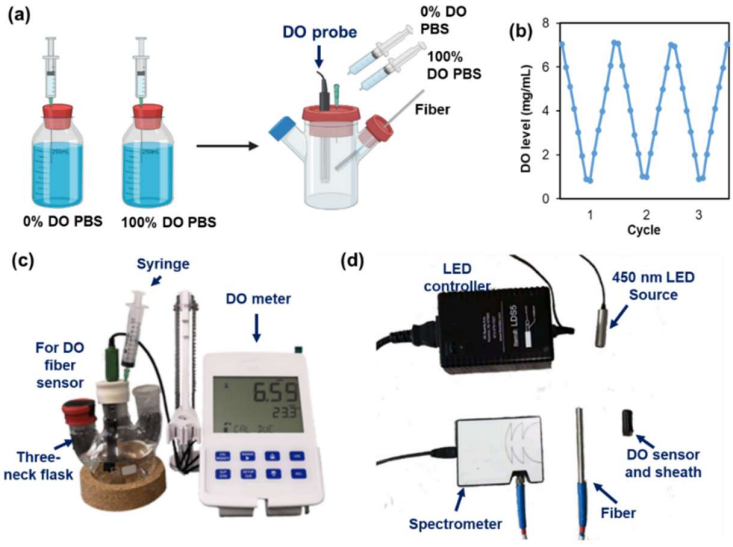


Figure 3-4. DO measurement set up. (a) Syringing buffer preparation method. (b) Reliability test of the syringe method for DO preparation. (c) Measurement setup. The oxygen probe and optical fibre sensors were inserted into a buffer solution together using a three-neck flask with one neck used for oxygen probe insertion, one neck for buffer injection, and one neck for fibre sensor insertion. (d) Optical setups for DO measurement using the fabricated DO sensor. 450 nm LED light source was used for the excitation of the DO sensing film. A flake spectrometer was used for the spectrum measurement.

Response time and reversibility

Response-time was measured using 0% (Nitrogen saturated PBS) and 100% (air saturated PBS) DO PBS solutions. The optical fibre sensor was immersed in a 0% DO buffer first. When the signal

became stable, the fibre sensor was moved to 100% DO buffer. After the signal stabilized, the fibre sensor was moved back to 0% DO buffer. This procedure was repeated 10 times to study the reversibility of the sensor. The collected data were then used to calculate the response time from 0% DO to 100% DO and 100% O_2 to 0% O_2 offline. The repeatability is measured by calculating the standard deviation of the measured intensity at 0% DO and 100% DO during the 10 repeats. Red/blue value was calculated as the integration of the fluorescence intensity in red spectral range (560 nm - 650 nm) and normalizing it to the excitation light intensity in blue spectral range (420 nm-500 nm).

Photostability

The sensor was exposed in water and the room temperature under an excitation light for 24 h. The emission spectra were measured every 2 h.

pH and temperature dependence

(pH) PBS solutions with pH value of 6.0 were prepared to make 100% DO by pumping compressed air into the solution for several minutes until the oxygen meter stabilized at around 8 $mg \cdot L^{-1}$ of DO value. The DO concentration was kept constant. The pH value of the buffer solution was adjusted by pipetting the NaOH solution under the monitoring of the pH meter. When the pH value was adjusted to 6.0, 6.5, 7.0, 7.5, and 8.0, the reflection spectra of the DO sensing film were measured. The experiment was repeated to study the pH dependence when the DO values are equal to 4 mg L^{-1} and 8.25 mg L^{-1}.

A temperature dependence test as operated using a hot plate. The sensors were excited at different temperatures and the emission intensities were recorded. The temperature of the solution was slightly increased from the room temperature (25 ℃) to 40 ℃ (human fever) with a step of 2 ℃ to cover human physiological range and room temperature.

Selectivity

Same interference solutions were prepared as used in the pH selectivity test (**Table 3-2**). Compressed air was then bubbled into the solutions to prepare air saturated PBS solutions for the DO measurement.

3.3.6 Glucose sensor fabrication and characterisation

Glucose sensing film fabrication:

The glucose biosensor was prepared by encapsulating 310.5 μg of TMB, 18 μg of GOD, and 105 μg of POD in the sol gel film optimized using pH sensing probe.

Glucose sensing film characterisation:

Glucose buffer preparation

Standard glucose buffer solutions were prepared by dissolving glucose into PBS solutions. In total, 1 mmol L^{-1}, 2 mmol·L^{-1}, 3 mmol L^{-1}, 4 mmol L^{-1}, 5 mmol L^{-1}, and 6 mmol L^{-1} of glucose buffers were prepared for the test. The ionic strength of the buffer was adjusted to 150 mmol L^{-1}.

Glucose sensing sensitivity

The optical fibre sensor was immersed in the buffer solutions and the reflection intensity was recorded in each buffer when the signal stabilized. The correlation between various glucose concentrations and the reflection intensities was evaluated. The sensitivity of the sensor was calculated by the slope of the calibration curve.

Response time

Response time was measured using 2 mmol L^{-1} and 5 mmol L^{-1} glucose PBS solutions. The optical fibre sensor was immersed in a 2 mmol L^{-1} buffer first. When the signal became stable, the fibre sensor was moved to 5 mmol L^{-1} buffer. The reflection intensity at 660 nm was measured in a time dependent mode during the experiment for response time calculation.

Selectivity

The same interference buffer solutions were prepared as described in pH selectivity test (**Table 3-2**). Two types of selectivity tests were conducted. In the first test, interference solutions without glucose were used and the reflectance spectra were measured for potential false detections as glucose. In the second selectivity test, 2 mmol L^{-1} of glucose solution was added to each interference solution and the reflection spectra were obtained, allowing an assessment of whether the interference analyte might impact glucose measurements.

Temperature and pH dependence

The sensor responses in pH 6.0-pH 8.0 buffer solutions under temperatures from 25 to 40 °C were measured using a microplate reader with reflectance measurement settings to evaluate the temperature influence on sensor readout.

Stability

Sensing stability in continuous measurement was conducted. To measure the film stability for dynamic measurement, the reflection spectra of the sensor in glucose buffer at 2 mmol L^{-1} were taken every 2 h for a 24 h continuous monitoring using the proposed optical fibre sensing setup.

3.3.7 ACSF and ex vivo measurement

Standard aCSF buffer solutions with different chemical concentrations were used for further evaluation.

ACSF buffer preparation:

aCSF buffer was prepared by mixing 0.0075 mol L^{-1} Na_2HPO_4, 0.0025 mol L^{-1} NaH_2PO_4, 0.0027 mol L^{-1} KCl, 0.137 mol L^{-1} NaCl, 0.0024 mol L^{-1} $CaCl_2$, and 0.0013 mol L^{-1} $MgCl_2$ in DI water . The following buffer solutions were prepared for pH, temperature, DO, and glucose sensing film characterisation using the multiplexed optical fibre sensor (**Table 3-3**).

Table 3-3. aCSF buffer preparation

	pH level	Temperature (°C)	DO level (mg L^{-1})	Glucose concentration (mmol L^{-1})
pH sensor calibration	6.0-8.0	37	8	4
Temperature sensor calibration	7.4	36-41	8	4
DO sensor calibration	7.4	25	1-8	4
Glucose sensor calibration	7.4	37	8	0-6

Multiple sensing film fabrication:

The fabricated sensing films for pH, temperature, DO, and glucose were fabricated and evenly placed on the tip of the sheath using a medical grade glue. The sheath was then fixed on the tip of the fibre for real-time measurement.

Multiplexed optical fibre sensor characterisation

Using the above-mentioned buffer solutions, the fabricated multiplexed optical fibre sensor was characterized. Calibration curve, sensitivity, reversibility and stability were measured using the same method as described for individual sensor characterisation.

3.3.8 Algorithm Design for signal post processing

2D (x, y) CIE 1931 chromaticity diagram

2D CIE 1913 diagram is a visualization tool used in color science to represent the entire range of colors visible to the human eye. It is also used here to present the color changes under various pH values. After obtaining the pictures of the sensing film using phone camera, the average RGB pixels values of the photos were calculated, following which the non-linear values were linearized by the following equations [209]:

$$R_l = \left(\frac{0.055 \times R_0}{1.055}\right)^{2.4} \quad G_l = \left(\frac{0.055 \times G_0}{1.055}\right)^{2.4} \quad B_l = \left(\frac{0.055 \times B_0}{1.055}\right)^{2.4} \quad \textbf{(Eq. 3-2)}$$

where R_0, G_0, B_0 represent the non-linear RGB values, and R_l, G_l, B_l corresponds to the values of linearized R_0, G_0, B_0, and a gamma correction of 2.4 was used here. Afterwards, the tristimulus values X, Y, Z were calculated using a base transformation [209]:

$$\begin{bmatrix} X \\ Y \\ Z \end{bmatrix} = \begin{bmatrix} 0.4124564 & 0.3575761 & 0.1804375 \\ 0.2126729 & 0.7151522 & 0.0721750 \\ 0.019339 & 0.1191920 & 0.9503401 \end{bmatrix} \begin{bmatrix} R \\ G \\ B \end{bmatrix} \quad \textbf{(Eq. 3-3)}$$

The tristimulus values X, Y, Z are transformed to the 2D (x, y) CIE 1931 chromaticity space as follows:

$$x_i = \frac{X}{X+Y+Z} \qquad y_i = \frac{Y}{X+Y+Z} \qquad \textbf{(Eq. 3-4)}$$

where i is defined as the number of calibration points.

Regression modelling for quantitative readout

Regression models were used for the calculation of 4 biomarkers based on the detected mixed optical reflection spectra. Four machine learning regression models were trained for the calculation of pH, temperature, DO, and glucose levels respectively. For model training, it involves the following steps (**Figure 3-5**). The training dataset was obtained by placing the sensing films in standard buffer solutions. The obtained spectrum from each buffer solution was labelled with the solution's pH, temperature, DO, and glucose levels. In total, 290 spectra were collected for the model development, which contains the spectra of the multiplexed sensing film in standard aCSF with different known biomarker concentrations and combinations of the four sensors.

After obtaining the dataset, features were extracted from each spectrum to represent the underlying patterns of the spectrum and fed into machine learning regression models for training. Based on the results the models were optimized and validated for highly accurate biomarker concentration prediction. The environmental effects were also considered in extracting the features to correct the environmental effects on the readout. After obtaining the models, they were used for continuous concentration readout.

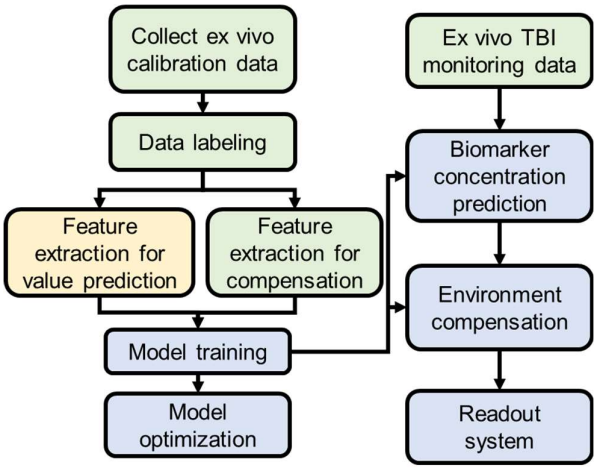


Figure 3-5. Algorithm flow chart of the AI model for biomarker level prediction.

Feature extraction

To eliminate the crosstalks between each optical sensing films, several features were extracted and used for machine learning model training to predict biomarker concentrations. The following features were extracted (**Table 3-4, Figure 3-6**):

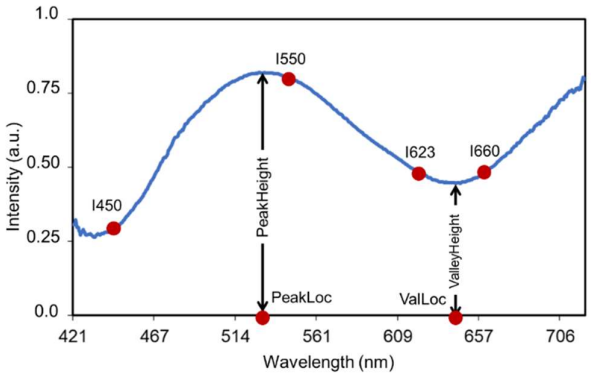


Figure 3-6. Spectrum feature extraction.

The features were selected based on the induced spectrum intensity changes from each sensor. The first feature extracted is I450, which is the reflection intensity value at 450 nm. It is not linked with any of the sensors, but it is used as a reference intensity that may fluctuate as light source intensity and background noise intensity. The second feature is peak location which reflects the peak shift degrees caused by the temperature level of the solution. The peak height is extracted as the third feature, which is a joint result of the pH and glucose sensor as a higher pH and a lower glucose led to a higher intensity value. The 4thfeature is I 550 which is another reference intensity value at 550 nm same as I450. I623 denotes the intensity value at 623 nm, which is directly related to the pH value as a low reflection value is found in a high pH solution. Valley location and valley depth are another two features extracted which are determined by both the pH and glucose sensors and thus carry the information of both sensors. I660 is the intensity at 660 nm and is determined by the glucose sensor as a high glucose level result in a low I660. I623/I450 and I660/I450 are calculated to reduce the background or baseline influences on the pH and glucose sensor readings. The above features were extracted from the spectra when white light LED was used for the training of pH, temperature, and glucose calculation machine learning models.

Two features were extracted when a 450 nm laser was used for the calculation of the DO level. The first feature was the temperature level calculated by the temperature machine learning model as the fluorescent-based DO sensor is also sensitive to temperature and the temperature results from the temperature model could compensate for the obtained spectra for DO calculation. The second feature was Red/Blue, which was calculated as the integration of the intensity from 420 nm to 500 nm divided by the integration of the intensity from 550 nm to 680 nm. This value is the corrected fluorescent emission intensity of the DO sensor that is directly related to the DO value.

Table 3-4. Feature extraction

Feature set 1 (pH, temperature, and glucose)	**Definition**
Peak Location (PeakLoc)	The wavelength where the peak is located
Peak height	The reflectance intensity at the peak wavelength
Valley location (ValLoc)	The wavelength where the valley is located
Valley depth	The reflectance intensity at the valley wavelength
Peak valley difference	Peak height-Valley depth
623 nm intensity (I623)	Reflection intensity at 623 nm
660 nm intensity(I660)	Reflection intensity at 660 nm
Reference intensity at 550nm (I550)	Reflection intensity at 550 nm
Reference intensity at 450 nm (I450)	Reflection intensity at 450 nm
623 nm intensity/Reference intensity at 450 nm	I623/I450
660 nm intensity/Reference intensity at 450 nm	I660/I450
Feature set 2 (DO)	**Definition**
Temperature	Temperature of the sample (calculated from the temperature model)
Red/Blue	Integration of the intensity from 420 nm to 500 nm divided by the integration of the intensity from 550 nm to 680 nm

Another two features were extracted when 450 nm laser was used for the calculation of DO level. The first feature was the temperature level calculated by the temperature machine learning model as the fluorescent-based DO sensor is also sensitive to temperature and the temperature results from the temperature model could compensate the obtained spectra for DO calculation. The second feature was Red/Blue, which was calculated as the integration of the intensity from 420 nm to 500 nm divided by the integration of the intensity from 550 nm to 680 nm. This value is corrected fluorescent emission intensity of the DO sensor that is directly related to the DO value.

Model Training

Machine learning models were trained using 75% of the dataset for the prediction of pH, temperature, DO and glucose respectively, and the rest 25% of the dataset was used as testing dataset.

After the features were extracted from each spectrum, they were labelled with the four biomarker levels and the features were properly normalized to have zero mean and unit variance to prevent bias following the equation below, where x denotes one feature vector of the whole dataset.

$$Normalized = \frac{x - \min(x)}{\max(x) - \min(x)} \textbf{(Eq. 3-5)}$$

To determine the best model training algorithm, machine learning models with different structures were trained and compared (Linear regression, polynomial regression, SVR, DT, RF, and Bayesian regression). For each model training, grid search was applied for hyperparameter tuning and the range and hyperparameters needed to be tuned are listed in **Table 3-5**.

Table 3-5. Hyperparameters for regression models

Model	Parameters	Values
SVR	Kernel type	['linear', 'rbf', 'poly']
	C (penalty parameter):	[0.1, 1, 10]
	Epsilon (tolerance):	[0.01, 0.1, 0.5]
Random Forest	Number of trees:	[50, 100, 200]
	Maximum depth:	[None, 10, 20]
	Minimum samples split:	[2, 5, 10]
Decision Tree	max_depth	[None, 10, 20]
	min_samples_split	[2, 5, 10]
Bayesian Regression	alpha_1	[1e-6, 1e-5, 1e-4]
	alpha_2	[1e-6, 1e-5, 1e-4]
Linear Regression	--	--

Instantiate a GridSearchCV object for each regression model. The models were first defined and the hyperparameters that need to be tuned and value range were defined.

The python code is as below:

```
# Define models and hyperparameter grids
models = {
    'Linear Regression': LinearRegression(),
    'Bayesian Regression': BayesianRidge(),
    'SVR': SVR(),
    'Decision Tree': DecisionTreeRegressor(),
    'Random Forest': RandomForestRegressor()
}
param_grids = {
    'Linear Regression': {},
    'Bayesian Regression': 15,
    'SVR': {'kernel': ['linear', 'rbf'], 'C': [0.1, 1, 10], 'epsilon': [0.01, 0.1, 0.5]},
    'Decision Tree': {'max_depth': [None, 10, 20], 'min_samples_split': [2, 5, 10]},
    'Random Forest': {'n_estimators': [50, 100, 200], 'max_depth': [None, 10, 20], 'min_samples_split': [2, 5, 10]}
}
# Define scoring function (mean squared error)
scorer = make_scorer(mean_squared_error, greater_is_better=False)
```

Figure 3-7. Grid search for hyperparameter tuning.

3. Perform Grid Search:

Fit the GridSearchCV object to the training dataset.

The code is as below:

Repeated 4-fold cross-validation was used to evaluate the regression model performance. To perform the validation, the extracted feature set was split into 4 subsets, where 3 subsets were used for model training and the remaining subset was used as an independent validation set. This process was repeated 4 times where each time a different and independent validation set was used. R square was used to measure the accuracy of the proposed models. It was calculated as below:

$$R^2 = 1 - \frac{\sum_i (y_i - \hat{y}_i)^2}{\sum_i (y_i - \bar{y}_i)^2} \quad \textbf{(Eq. 3-6)}$$

$$MSE = \frac{1}{N}\sum_{i=1}^{N}(y_{real} - y_{predicted})^2 \quad \textbf{(Eq. 3-7)}$$

$$MAE = \frac{1}{N}\sum_{i=1}^{N}\left|y_{real} - y_{predicted}\right| \quad \textbf{(Eq. 3-8)}$$

Python code:

```
for model_name, model in models.items():
    print(f"Grid search for {model_name}...")
    # Create a pipeline if necessary (e.g., when using StandardScaler)
    if 'SVR' in model_name:
        pipeline = make_pipeline(StandardScaler(), model)
    else:
        pipeline = model
    # Perform grid search
    grid_search = GridSearchCV(pipeline, param_grids[model_name], scoring=scorer, cv=5)
    grid_search.fit(X_train, y_train)

    # Print best parameters and best score
    print("Best Parameters:", grid_search.best_params_)
    print("Best Score:", grid_search.best_score_)
    # Evaluate on test set
    y_pred = grid_search.predict(X_test)
mse = mean_squared_error(y_test, y_pred)
mae = mean_absolute_error(y_test, y_pred)
```

Figure 3-8. Grid search python code for execution.

The above process was repeated four times for the training of pH, DO, temperature, and glucose models.

Model validation

The best combination of hyperparameters was obtained from grid search and used to retrain each model. The performance of each model was evaluated using the testing dataset. The performance of each model was compared using evaluation metrics such as MAE, MSE, and R^2, and the best method was determined and used for the *ex vivo* test.

3.3.9 *Ex vivo* measurement using lamb brain models

To further evaluate the developed sensing platform for the monitoring of brain physiological status in clinical scenarios, three stages of TBI progression were simulated and the proposed sensing system was used to provide continuous and dynamic monitoring of the disease of TBI. It is reported that TBI patients have a decreased pH of 6.59-7.17 in CSF due to the increase of CO_2[210]. Furthermore, the DO level in TBI patients could reach as low as 20% of the normal oxygenation value, which equals to 1.6 ppm[211]. An increased temperature above 38 °C and increased glucose of 4.8-5.8 mmol L^{-1} have also

been observed in patients with TBI [41, 212]. Therefore, PBS with pH of 7.0, pO_2 of 2 ppm, temperature of 38.5 °C, and glucose of 5.0 mmol·L^{-1} were prepared.

2 kg lamb brains purchased from grocery stores and were washed with DI water to remove the blood and original fluid for 10 min until the rinsed water became clear and placed in insulated glassware. The purpose of using clean lamb brains and having them immersed in standard buffer solutions for the measurement is for the following reasons. Firstly, the designed sensing system is based on colourimetric and fluorescent sensing techniques, which are very sensitive to background colours or light. In the previous validation test, all experiments were conducted using transparent PBS buffer solutions without the consideration of the reflection light from the background brain tissues. Using lamb brains and having the sensor inserted into the brain could allow me to test the sensor's properties when being used in real-life situations. The impact on brain tissue could be evaluated. Secondly, the proposed sensing films were unprotected and required direct contact with the sample. Using lamb brain allowed me to evaluate whether the physical contact between the sensing film and solid brain tissue impacts the sensor stability as the films are soft and distort the shape of the film. Considering the above two reasons, the amount of lamb brain for the test is not important but it's important to ensure the film is inserted into the brain tissue during the experiment.

The following stages were mimicked to study the performance of the designed sensing system in continuous *in situ* monitoring. I referred to TBI progression CSF changes to prepare the solutions.

Stage 1: Healthy stage

In this stage, an aCSF buffer with pH value of 7.4, temperature of 37 °C, 100% saturated DO (around 7.8 mg L^{-1}), and glucose concentration of 2 mmol L^{-1} was injected to the insulated glassware. Clean lamb brain was immersed in the buffer during the whole measurement.

Stage 2: Mild stage TBI

A mild TBI status was simulated using an aCSF buffer solution with a decreased pH value of 7.0, temperature of 38 °C, DO of 50% (around 4 mg·L^{-1}), and glucose of 4 mmol L^{-1}. The previous buffer was replaced with the prepared mild TBI buffer using syringes.

Stage 3: Severe stage TBI

A severe stage was simulated transitioning from an initial mild stage. This involved using an aCSF buffer set at a pH of 6.6, a temperature of 39°C, 20% saturation of DO (approximately 2 mg L^{-1}), and a glucose concentration of 5 mmol L^{-1}. The glassware was introduced with this buffer solution, replacing the previous one.

Stage 4: Back to mild stage

The last scenario was the mimic of after proper treatment, the severity of brain injury was improved to the mild status. In this stage, the mild TBI status was simulated using aCSF solution with an improved pH value of 7.2, temperature of 38 °C, 60% saturated DO (around 5 mg L^{-1}), and glucose concentration of 3 mmol L^{-1}. The new solution was syringed into the glassware to replace the previous one.

During the experiment, a benchtop DO meter was inserted into the brain tissue to ensure a corrected DO level throughout the whole measurement. Compressed air and nitrogen gas were bubbled into the system if the DO value was lower or higher than planned.

The multiplexed fibre sensor facilitated dynamic monitoring throughout the simulation of the four stages using an ex vivo brain model. During this process, the specifically designed optical fibre sensor was inserted into the brain dura and securely positioned. Real-time reflection spectra of the sensing films were continuously collected, enabling subsequent biomarker level calculations using optimal machine learning algorithms post-experimentation. The averaged value derived from three consecutive scans served as the output.

3.3.10 Cellular studies on the biocompatibility of the multiplexed fibre sensor

The system aims to perform continuous and implantable measurement of brain biomarkers, therefore, the cytotoxicity and biocompatibility of the sensing films need to be tested. Usually for TBI patients, they are monitored in ICU for less than 7 days. Therefore, for the safety test, the cells' viability after 7 days living with the sensing film were tested. The experiment followed the protocol introduced in ref. [213]

Cells culture: The mouse fibroblast L929 cells were grown in a Dulbecco's modified eagle medium supplemented with 10% bovine serum and 1% penicillin-streptomycin in a 12-well plate under 5% CO_2 atmosphere at 37 °C. After confluency, the cells were trypsinized with trypsin, and then concentrated by centrifugation and resuspended with the extracted cell culture medium to adjust the cell concentration to 1×10^4 cell/mL, then seeded cells with 2 mL media per well in 12-well plate and cultured for 1, 3, 5, 7 days. The cell culture medium was changed with the extracted solution every two days, and at each time point, the cytotoxicity and cell viability were examined.

Biocompatibility test: The fabricated pH sensing film was immersed in a fresh culture medium for 72 h. Subsequently, the film was taken out from the culture medium for cell culture of 7 days.

Cytotoxicity analysis: Cell proliferation is measured by CCK-8 (Cell counting kit-8) assay and quantified by a plate reader. 200 μL CCK-8 is added to each well, and after incubated at 37 °C for 4 h, 100 μL culture medium is transferred to a 96-well plate, the absorbance of which is then measured at 450 nm using a microplate reader.

Live/dead cell staining assay: LIVE/DEAD™ Viability/Cytotoxicity Kit was diluted 1000-fold, and 500 μL diluent was aspirated to the microplate wells after being washed using PBS. Subsequently, the cells were incubated at 37 °C with 5% CO_2 for 30 min. The cells were observed with a fluorescence microscope to determine the cell viability.

3.3.11 Miniaturization of the multiplexed fibre sensor

The sensing system has been validated from various aspects, including its sensing performance and biocompatibility. However, although the sensing area of the sensor is 2 mm, it has a large fibre body of up to 8 mm, which would lead to large tissue damage when being used in real-life. Therefore, here

I further explored whether the sensor body could be reduced by manually manufacturing a reflection fibre with two single pigtailed fibres.

I managed to fabricate a reflection fibre using two pigtailed multimode fibres (RS Pro, 62.5/125μm, Multimode). The fibre tips were stripped and flat cut using a fibre cleaver. A silicone tube (0.5 mm inner diameter and 1.5 mm outer diameter) was used as the silicone sheath for film attachment. The fibre tips were glued together and fixed inside the sheath. The sensing film was also attached to the sheath tip using glue. The gap between the fibre distal ends and the sensing film was 1 mm to allow light transmission and detection. A black sheath and an isolation film were used to block the background noise. The miniaturized fibre was further used for the measurement of the four sensing films to evaluate its performance using PBS solutions.

3.4 Obtained optical spectra using the system

This section presents the results of the experiments introduced in section 3.3, which indicates the characteristics of the designed sensing system. The characteristics of the individual sensing films are first demonstrated and then the sensing results after sensor multiplexing are listed. The results from the machine learning modelling for 4 biomarker concentration calculations are also presented. In the end, the system was used for continuous monitoring of brain biomarkers in ex vivo lamb brain models to mimic real-life scenarios and the sensing performance is discussed.

Since the measurement was conducted using broadband LED and reflection signal is obtained. To enhance the signal, a white microfibre film was placed outside of the sensing films as shown in **Figure 3-9**. The spectrum of the light source is in **Figure 3-9 (b)**. The reflection signal from the microfibre isolation film without the sensing film is around 50% of the original broadband LED, meaning that 50% of the light was lost during the process. Compared with sensing without the isolation film, the signal with the isolation film greatly reduced the light being lost and transmitted to the other side of the film and enhanced the signal being detected by the spectrometer (**Figure 3-9 (d)**).

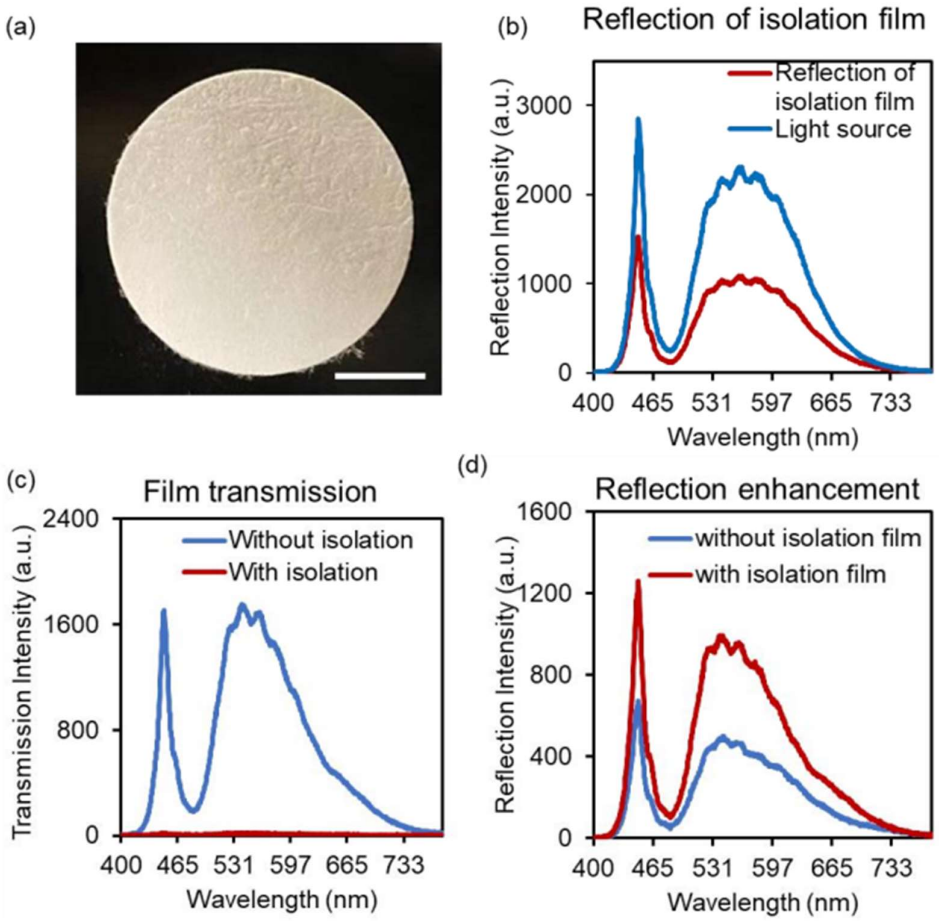


Figure 3-9. Sensing results with and without isolation film. (a) Picture of the isolation film. Scale bar = 1mm. (b) Reflectance spectrum of the isolation film. (c) Transmission spectra of the sensing film with and without isolation film. (d) Reflectance spectra of the sensing film with and without isolation film for signal enhancement.

The measurement of the reflection spectra of the films was calculated using equation **Eq. 3-1.** Reflection spectra is the opposite of the absorption spectra as the more the light is absorbed the less the light will be reflected. To remove the interference from the broadband light, the reflection spectra were calculated by the reflection spectrum from the sensing film divided by the spectrum of the broadband LED without any sensing films (**Figure 3-10**). As is shown in **Figure 3-10**, there is a reflection minimum at 630 nm, indicating the sensing film had a high absorption at 630 nm, which might change with pH changes and reflects the film's optical properties. The corrected reflection spectra were used throughout the study.

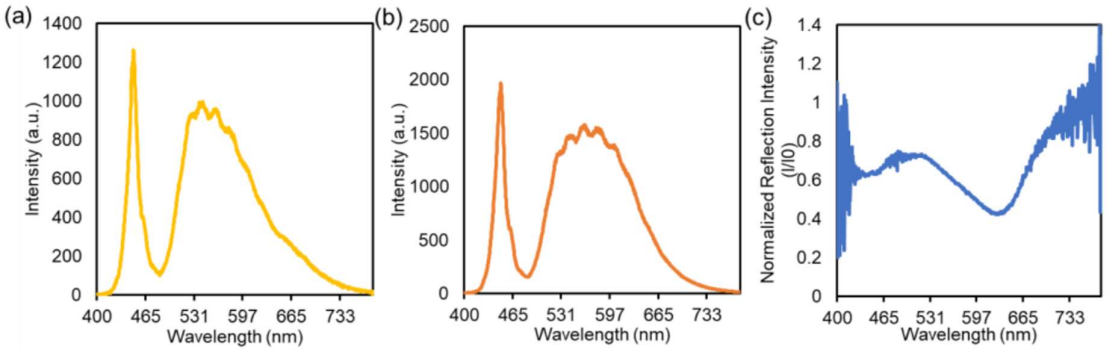


Figure 3-10. Example of the raw data and computational methods for the calculation of normalized reflectance spectrum. (a) An example of the reflectance spectrum with pH sensing film. (b) Reflection spectrum without pH sensing film. (c) The calculated normalized reflectance spectrum.

3.5 Performances of the optical fibre pH sensor.

pH regulates various cellular processes and influences the activity of ion channels and enzymes in the brain system[214,215]. pH also serves as an indicator of TBI, where a reduction of pH could be observed, due to disrupted anaerobic metabolism and increased acetic acid.[216] To date, several approaches have been developed to follow the progress of brain diseases for brain pH monitoring, including fluorescence spectroscopy[217, 218], electrochemical sensing[219], and colorimetric sensing[220]. In this study, the determination of pH in aCSF is based on the colorimetric property of a pH sensing film at the fibre tip. 3,3',5,5'-Tetrabromo-m-cresolsulfonphthalein was selected as the pH indicator since it has a pKa value in a physiological range when encapsulated in a sol-gel film that is suitable for brain pH measurement for both TBI patients and healthy people (**Figure 3-11**) [210, 221].

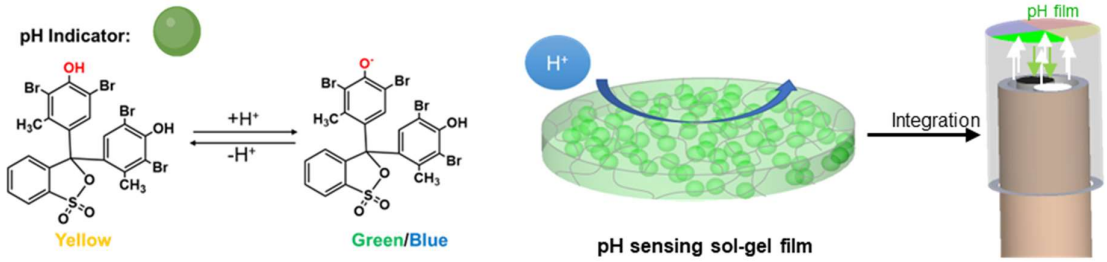


Figure 3-11. Optical fibre pH sensor sensing principle, fabrication method, and structure.

3.5.1 Encapsulation matrix optimization

Tetraethyl orthosilicate (TEOS) is one of the most widely used precursors for the sol-gel process. However, pure TEOS fabricated sol-gel films suffer from severe film cracks, which may lead to low film uniformity and high leaching. Glycidoxypropyltrimethoxysilane (GLYMO) is an organic precursor and has long carbon chains in the chemical structure. Using TEOS and GLYMO together as precursors can prevent cracking and improve the morphology and uniformity of the sensing film[205]. Therefore, an organic-inorganic hybrid sensing film was fabricated by encapsulating the pH indicator within the silicate matrix formed by TEOS and GLYMO through the sol-gel process. Surfactant Triton 100 was applied to reduce the surface tension of the sensing film to prevent from cracking and indicator leaching, and also improve the uniformity of the sensing film. The SEM and AFM images indicated a very smooth surface of the sensing film (**Figure 3-12**).

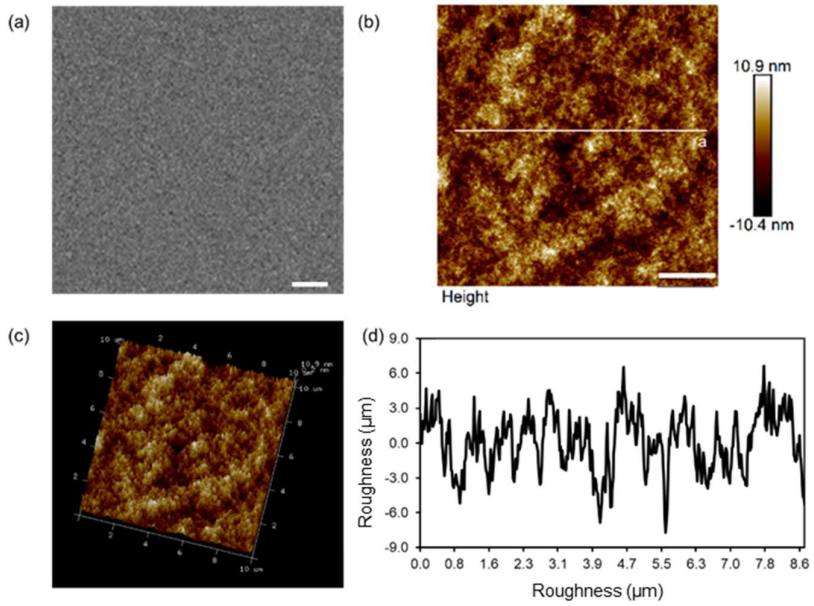


Figure 3-12. Morphology tests of the optical sensing film. (a) High-resolution SEM image of the sol-gel sensing film. Scale bar = 5 µm. (b) 2D AFM image of the optical sensing films. Scale bar = 2µm. (c) 3D image AFM of the optical sensing films. (d) Roughness measurement of the film at a line in figure (b).

In addition, the porosity of the sensing film allows for biomarkers to interact with the encapsulated indicators. The pH sensing film showed green color at a neutral pH and changed to red or blue color in an acidic or basic environment due to protonation or deprotonation, respectively. I optimized the

sensing film using different fabrication formula to achieve high uniformity, stability, and sensitivity (Section 3.3.3, **Table 3-1, Figure 3-13, 3-14**). I found that the increased concentration of GLYMO could improve the uniformity of the sensing film but increase the responding time due to the lower porosity in the organic-inorganic sensing film. Moreover, the increase in GLYMO resulted in reduced sensitivity since GLYMO could decrease the pKa of the sensing film[222]. Therefore, a concentration molar ratio of TEOS:GLYMO at 1:0.1 was used to ensure the sensing film has high surface uniformity, high sensitivity, and short response time.

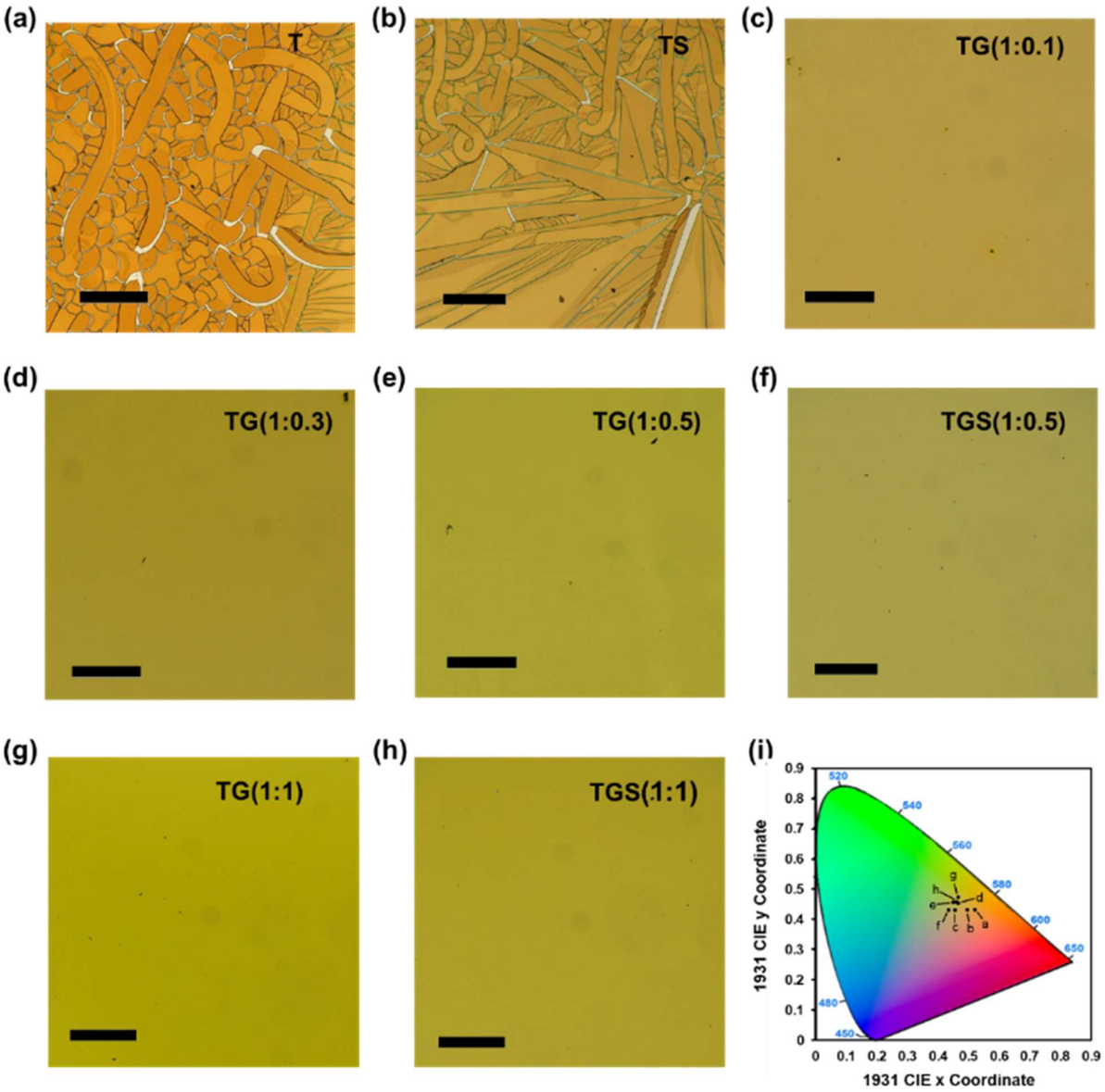


Figure 3-13. Optimization of the sensing films. Micrographs of (A) pH sensing film T. (B) pH sensing film TS. (C) pH sensing film TG (1:0.1). (D) pH sensing film TG (1:0.3). (E) pH sensing film TG (1:0.5). (F) pH sensing film TGS (1:0.5). (G) pH sensing film TG (1:1) and (H) pH sensing film TGS (1:1). (I) CIE 1931 chromaticity diagram according to micrograph from (A) to (H).

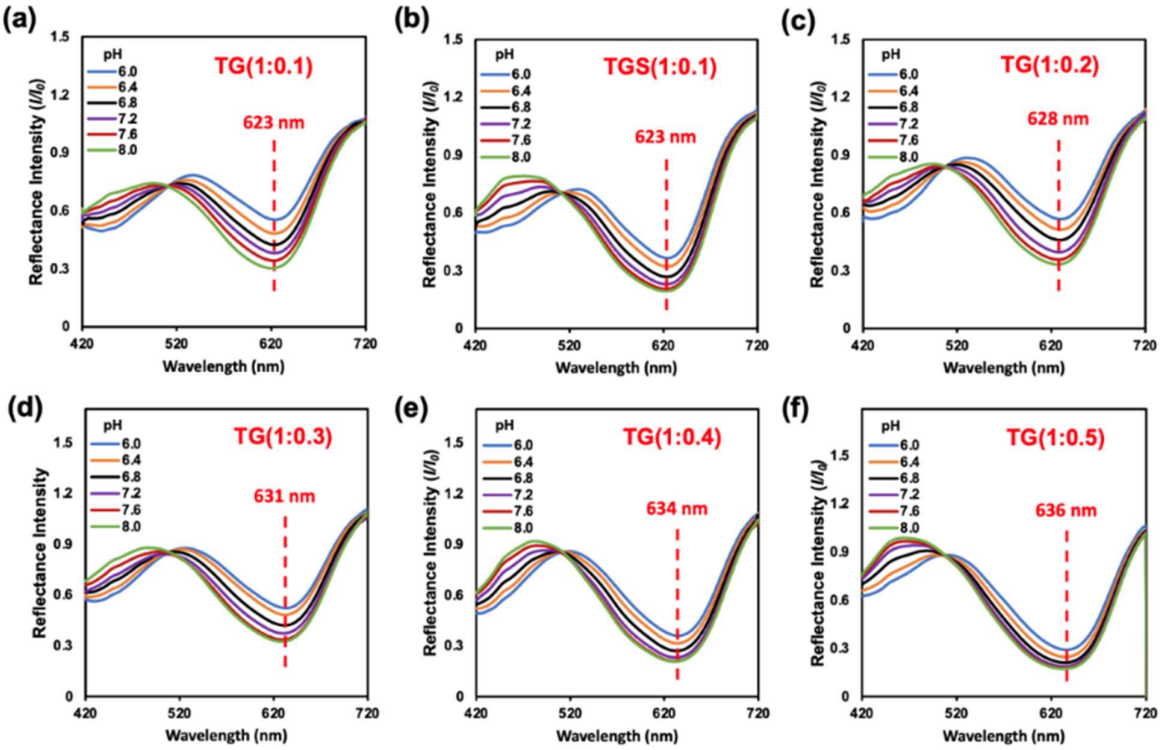


Figure 3-14. Calibration curves of the pH sensing films fabricated with different TEOS and GLYMO molar ratios. (a) Reflection spectra of film TG (1:0.1) at different pH values ranging from 6.0 to 8.0. (b) Reflection spectra of the sensing film TGS (1:0.1) at different pH values ranging from 6.0 to 8.0. (c) Reflection spectra of film TG (1: 0.2) at different pH values ranging from 6.0 to 8.0. (d) Reflection spectra of film TG (1: 0.3) at different pH values ranging from 6.0 to 8.0. (e) Reflection spectra of film TG (1:0.4) at different pH values ranging from 6.0 to 8.0. (f) Reflection spectra of film TG (1:0.5) at different pH values ranging from 6.0 to 8.0.

3.5.2 pH sensing results

As shown in **Figure 3-15 (a, b)**, the pH sensing film was tested in phosphate-buffered saline (PBS) solutions under pH ranging from 6.0 to 8.0 at room temperature (25 °C) due to human brain pH normally changes within this range [35]. The reflected spectra of the pH sensing film in PBS with different pH values were obtained by the spectrometer and normalized to the light source. The maximum absorbance of the pH indicator appears at 623 nm in the reflection spectra.

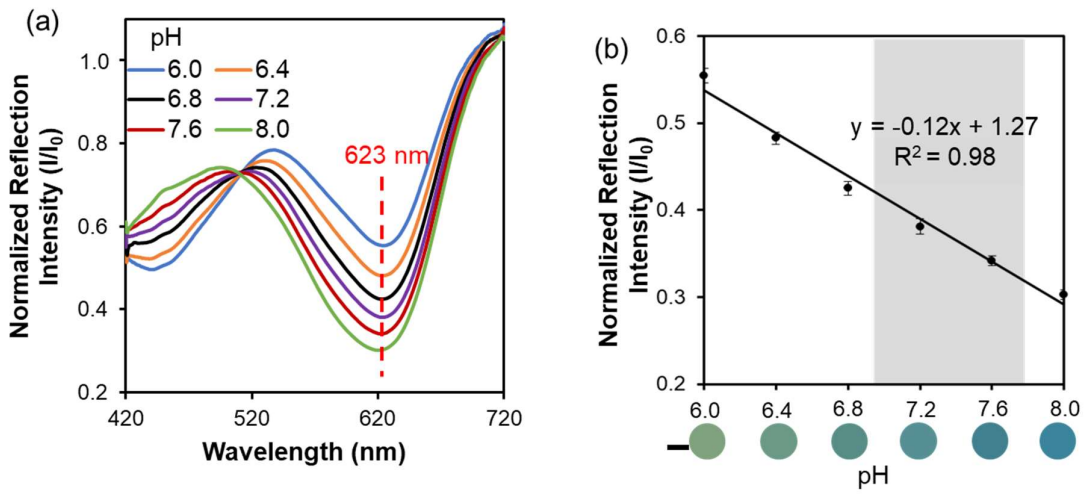


Figure 3-15. Calibration of the optical fibre pH sensor in PBS solutions (10 mmol L-1, 25 °C). (a) Reflection spectra of the optical fibre pH sensor when sensing in 6.0, 6.4, 6.8 ,7.2, 7.6, and 8.0 pH buffer. (b) Reflectance intensity of the pH sensing film at 623 nm under 6.0-8.0 pH buffer solutions. Shadows represent the physiological range of pH in human CSF. Insets show the color changes of the sensing film.

After being encapsulated in the silicate gel, the reflection intensity of the pH sensing film increased linearly as the pH value increased from 6.0 to 8.0 (**Figure 3-15 (b)**). According to the calibration curve, a sensitivity of 0.12/pH unit was achieved for the sensing of pH 6.0-8.0, which covers the physiological range of brain CSF. Photographs of the optical pH sensors show distinct color changes from yellow to blue, as the pH value increases from 6.0 to 8.0 (**Figure 3-15 (a)** inset). 1931 CIE chromaticity diagrams were analysed using the RGB value of the optical pH sensor (**Figure 3-16**).

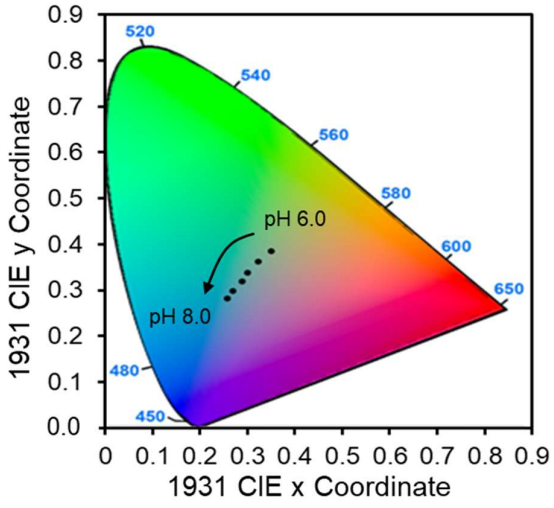


Figure 3-16. 1931 CIE chromaticity diagram. Color changes from 6.0-8.0 were denoted.

Reversibility, repeatability, and response time were further determined by dipping the optical fibre sensor in pH 6.0 and 8.0 buffer solutions to evaluate the sensor's ability for continuous monitoring (**Figure 3-17**). 6.0 and 8.0 were used as they are two extreme values in pH sensor characterization and smaller changes would have shorter response time. High reversibility and repeatability of the sensor with a standard error of 2.4% were observed after 10 cycles and more cycles can be further tested. The response time of the pH sensor was measured as less than 100 s, as the pH increased from 6.0 to 8.0, while the response time of 350 s was observed for the change from pH 8.0-6.0. The "asymmetry" of the response time is in line with the previously reported sol-gel sensor[204, 223].

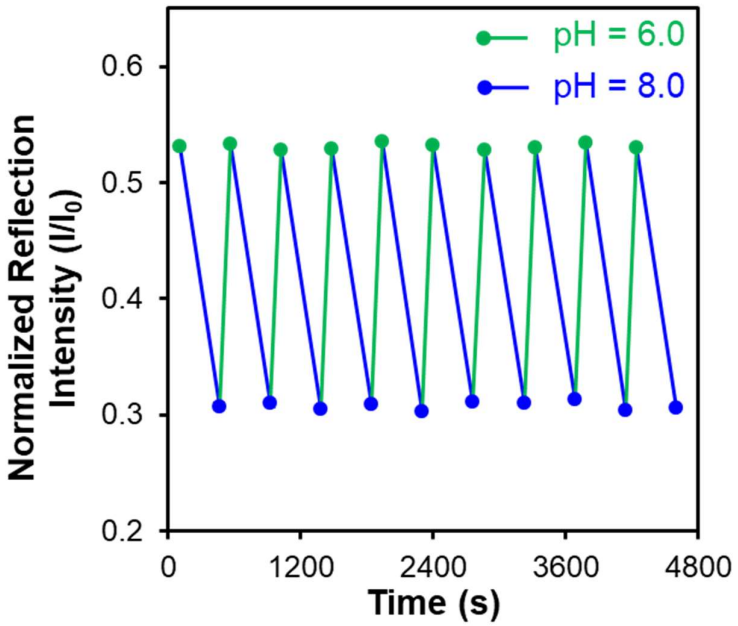


Figure 3-17. Reversibility test of the pH sensor in repeated sensing of pH 6.0 and pH 8.0 PBS solutions.

No obvious variation (standard deviation = 0.003) in the reflection intensity of the optical pH sensor (pH 7.4) was measured after exposure to a broadband light (20 mW) for 24 hours, indicating high stability of the pH sensor for long-term use (**Figure 3-18 (a)**). Leaching of the indicators from the sensing film is another index that maters for long-term clinical application of the sensor since the excessive leached indicators from the film increase cytotoxicity to biological tissues. The leaching results display a relatively high leaching rate of 3.09% at pH 8.0, and a lower rate leaching of 1.13% at pH 6.0 after three days (**Figure 3-18 (b)**). Only first 3 days were tested because the leaching signal

stabilized after the first 3 days. The differences in leaching behavior might be attributed to the larger sol-gel pore size in basic solutions.

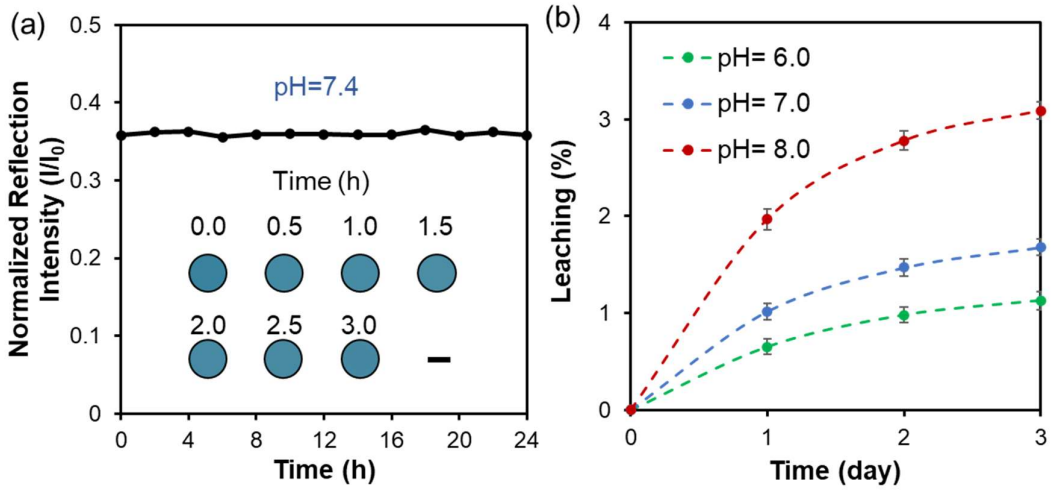


Figure 3-18. Characterisation of the pH sensor for continuous monitoring. (a) Sensing stability of the pH sensor for 24 hours. Insets show the photographs of color changes of the sensing film in the first 3 hours. (b) Leaching test of the fabricated pH sensor for 3 days.

Then sensor robustness towards environmental variations is tested. The temperature dependence of the fabricated optical pH sensor was tested from 25 to 40 °C that covers the majority of brain temperature, and no significant temperature interference was observed (**Figure 3-19 (a)**). The sensor has also demonstrated high robustness to be used under different physiological pressures (**Figure 3-19 (b)**).

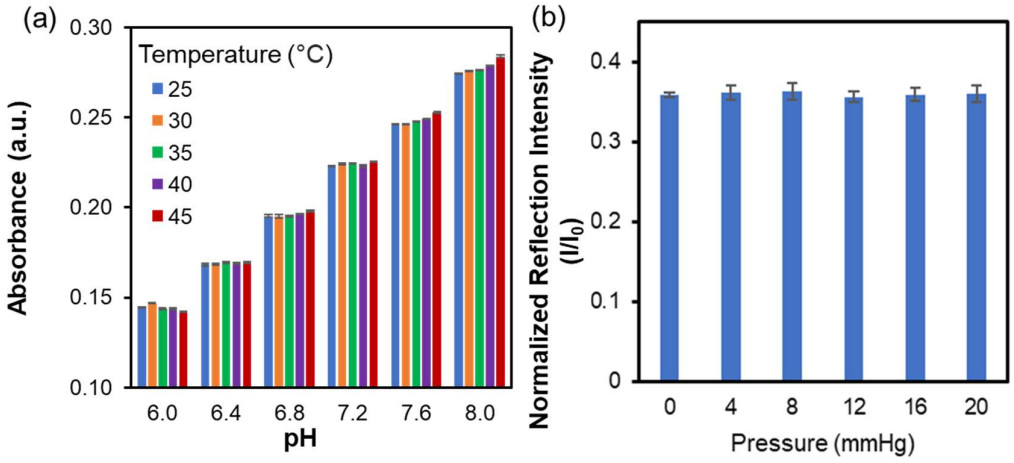


Figure 3-19. Environmental robustness of the pH sensor. (a) Temperature dependence of the pH sensor in measuring buffer pH levels. (b) Pressure dependence test of the sensor.

Two groups of selectivity tests were conducted to investigate the sensing performance of the optical fibre pH sensor in the presence of potential interferents in brain CSF such as electrolytes, metabolites, and neurotransmitters (**Table 3-2**). In the first group, the pH of the selectivity-testing PBS solution was readjusted to 7.4 after adding the interferents before sensing. In the second group, the pH was not readjusted to 7.4 before sensing (**Figure 3-20 (a, b)**). The results of the selectivity tests show that no major interferences in the two groups were observed, demonstrating a high selectivity and an promising capability of tracking pH changes using the designed multiplexed fibre sensor.

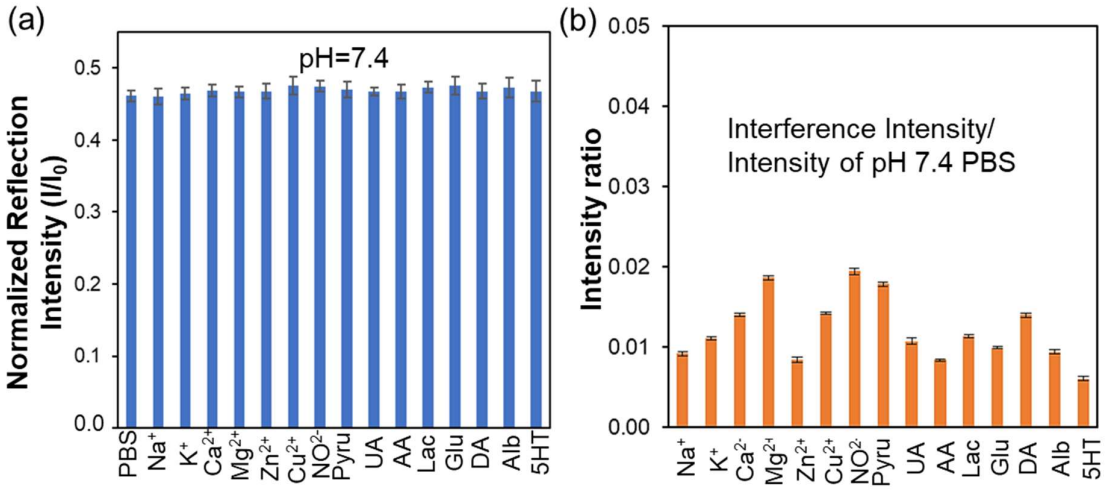


Figure 3-20. Selectivity test of the pH sensor. (a) Ability of the optical pH sensor against major interferents for pH 7.4 PBS solution sensing. (b) Signal variations after interferences were added to pH 7.4 PBS solution. The error bars (n=3) in the figures represent the standard deviation of the mean of three samples. The scale bars of all subfigures equal to 1 mm. Abbreviations: Pyru: Pyruvate; UA: Uric acid; AA: ascorbic acid; Lac: lactate; Glu: glucose; DA: dopamine; Alb: albumin; 5HT: Serotonin.

3.6 Performances of the optical fibre temperature sensor

Cerebral processes are extensively affected by temperature fluctuations[39, 224]. Due to the high temperature-dependent nature of the brain's energy expenditure, brain's thermal regulatory capability can be an indicator of its anatomical and physiological architecture, and reflect its processing capacity[225]. To date, clinical studies have revealed a strong relationship between brain temperature elevation and brain injuries[226]. Therefore, brain temperature monitoring has become a routine for TBI treatment in clinics. One of the potential methods for brain temperature measurement is using a thermochromic liquid crystalline (TLC), which exhibits good reversibility, quick response, and high resolution. In this study, TLCs were obtained by mixing cholesteryl nonanoate (CN), cholesteryl oleyl

carbonate (COC), and cholesteryl benzoate (CB) at a weight ratio of 0.35: 0.55: 0.10 (**Figure 3-21**) following the study conducted by Moreddu et al.[207]. When melted together, the three esters retain their chemical properties whilst experiencing weak inter and intra- molecular interactions. Chiral molecules are rigid and rod-shaped that can form a layered structure with distinct molecular orientations along the helix axis under temperature changes (**Figure 3-21**). The different twisting arrangements can lead to variations in the reflected light of the TLC. The temperature detection range can be varied by mixing them at different ratios. I, therefore, fabricated the temperature sensor using the above method.

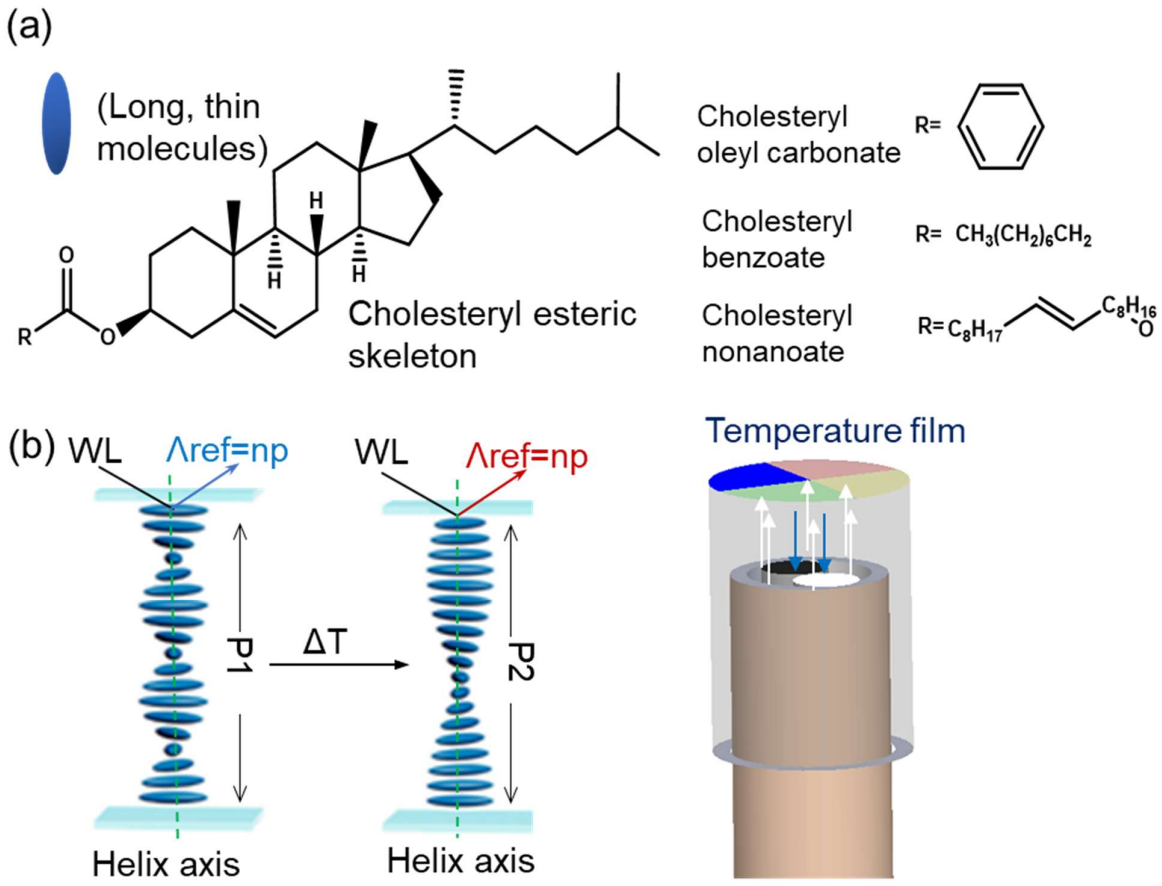


Figure 3-21. Schematic demonstration of the optical fibre temperature sensor, including the sensing principle (i) and structure (ii).

The temperature sensor was tested in 0.1 mmol L^{-1} PBS solutions (pH 7.4), ranging from 34 to 42 °C using the same reflection sensing setup as the pH sensor. The obtained reflection spectra and their color changes in correlation to various buffer temperatures were analysed (**Figure 3-22 (a)**). When the

temperature is raised from 34 to 42 °C, the reflectance peak shifts from 525 to 470 nm linearly with a sensitivity of 6.77 nm/°C (R^2=0.99) (**Figure 3-22 (b)**). The optical temperature sensors were imaged by a smartphone camera with white balance controlled as the same for all photos, and an evident color change from green to violet was recorded as the temperature increased (**Figure 3-22 (b)** inset).

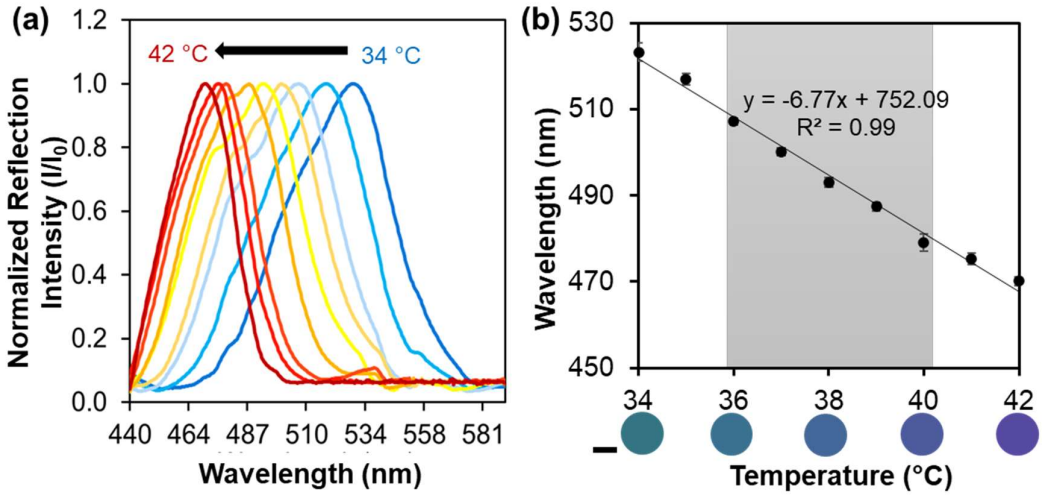


Figure 3-22. Calibration of the optical fibre temperature sensor in PBS solutions (10 mmol L-1, pH 7.4, 25 °C). (a) Reflection spectra of the temperature sensor for sensing in PBS solutions at 34 -42 °C. (b) Calibration curve of the temperature sensor for sensing PBS in 34 -42 °C. Shadows represent the physiological range of human CSF temperature.

A 1931 CIE chromaticity diagram was analysed based on the RGB value of the temperature sensor and demonstrated distinct color changes as temperature shifts from 34-42 °C (**Figure 3-23**).

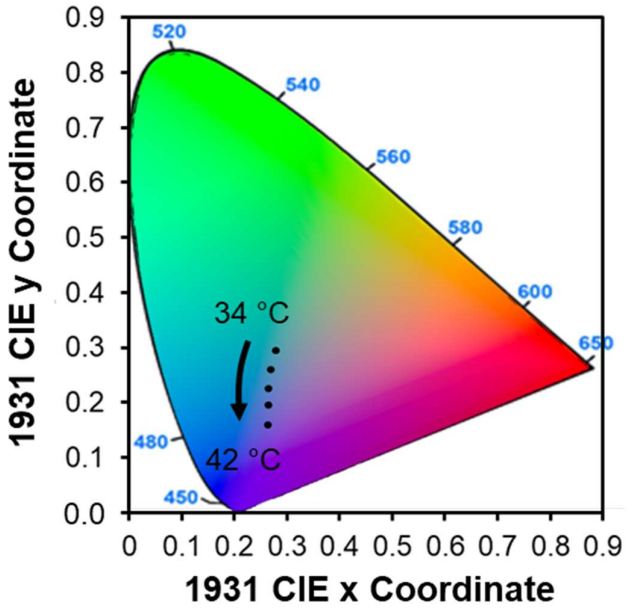


Figure 3-23. 1931 CIE chromaticity diagram. Color changes from 34 -42 °C were denoted.

Repeatability of 3.7% of standard error and an average response time of less than 2 s after 20 cycles were observed when temperature changes between 36°C and 40°C (**Figure 3-24**) as 36 and 40°C are the two edge values for regular human brain temperatures[39], indicating the potential of the optical fibre temperature sensor for real-time and continuous brain temperature monitoring.

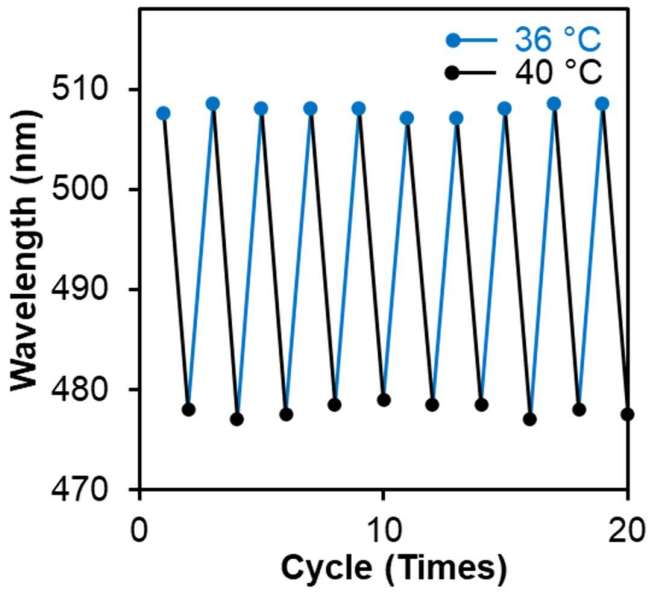


Figure 3-24. Repeatability of the temperature sensor for temperature measurement in PBS solutions between 36.0 °C and 40.0 °C.

No obvious variations in the reflectance of the temperature sensor (pH 7.4, 37 °C) were measured after exposure to the broadband light (20 mW) for 24 hours, showing high stability of the temperature sensor for long-term use (**Figure 3-25 (a)**). Since the liquid crystal is also sensitive to pressure, the reflection spectra of the temperature sensor were measured under physiological pressure ranges at different temperatures (**Figure 3-25 (b)**). The pressure was varied by dipping the optical fibre temperature sensor into the PBS solutions at different depths. The pressure can be calculated as the product of the gravity constant, the solution density, and the depth of the sensor in the solution. The results indicate that no obvious pressure influences the sensor output, suggesting the ability of the sensor for *in vivo* and deep brain CSF temperature monitoring. The leaching test of the temperature indicator from the sensing film in pH 7.4 PBS solutions was also conducted. No leaching was observed in the PBS solution after three days. Therefore, the fabricated optical fibre temperature sensor is safe for implantable measurement for at least 3 days.

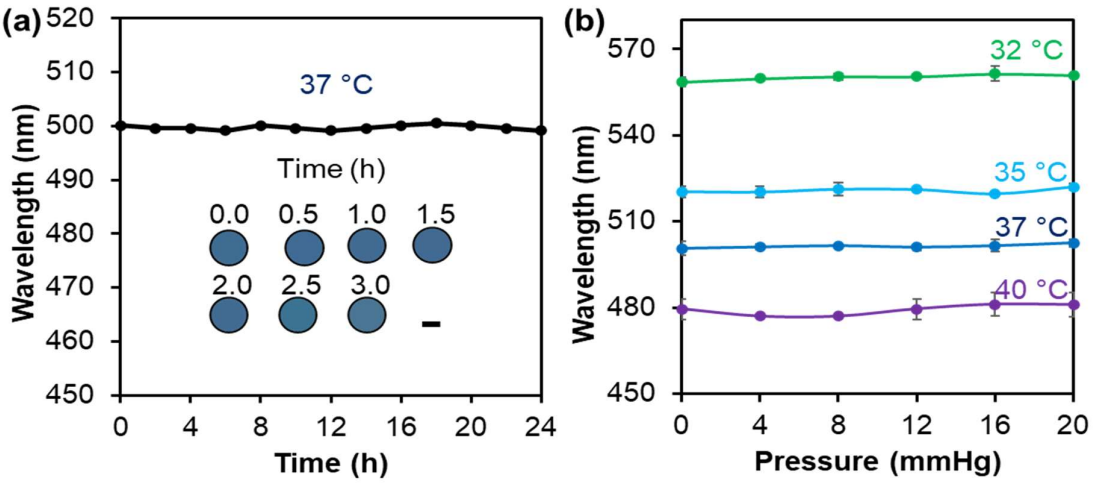


Figure 3-25. Stability and pressure dependence of the pH sensor. (a) Stability of the pH sensor in sensing PBS solution at 37°C for 24 hours. Insets show the corresponding color changes of the sensing film in the first 3 hours. (b) Performance of the pH sensor under different pressure ranges. Error bars (n=3) in the figures represent the standard deviation of the mean of three samples. The scale bars of all subfigures equal to 1 mm.

3.7 Performances of the optical fibre DO sensor

Here, I proposed and fabricated an optical fibre DO sensor to monitor the brain oxygenation by encapsulating fluorophore tris(4,7-diphenyl-1,10-phenanthroline)ruthenium(II) dichloride complex

(Ru(dpp)) as the DO indicator within a sol-gel film, which was integrated at the fibre tip (**Figure 3-26**). Based on the fluorescence quenching effect of oxygen, the emission intensity of Ru(dpp) is negatively correlated to the level of DO in brain CSF. When being excited with a 450 nm LED light, an emission light at 600 nm was detected. The DO calibration buffer solutions were prepared by mixing 100% DO buffer with 0% DO at a certain ratio to achieve buffers with different DO concentrations. A DO benchtop meter was used as a golden standard for the preparation of the buffers and the calibration of the sensing films. This buffer preparation method was tested three times to obtain gradient DO buffers, and a good repeatability was achieved **(Figure 3-4 (b)**).

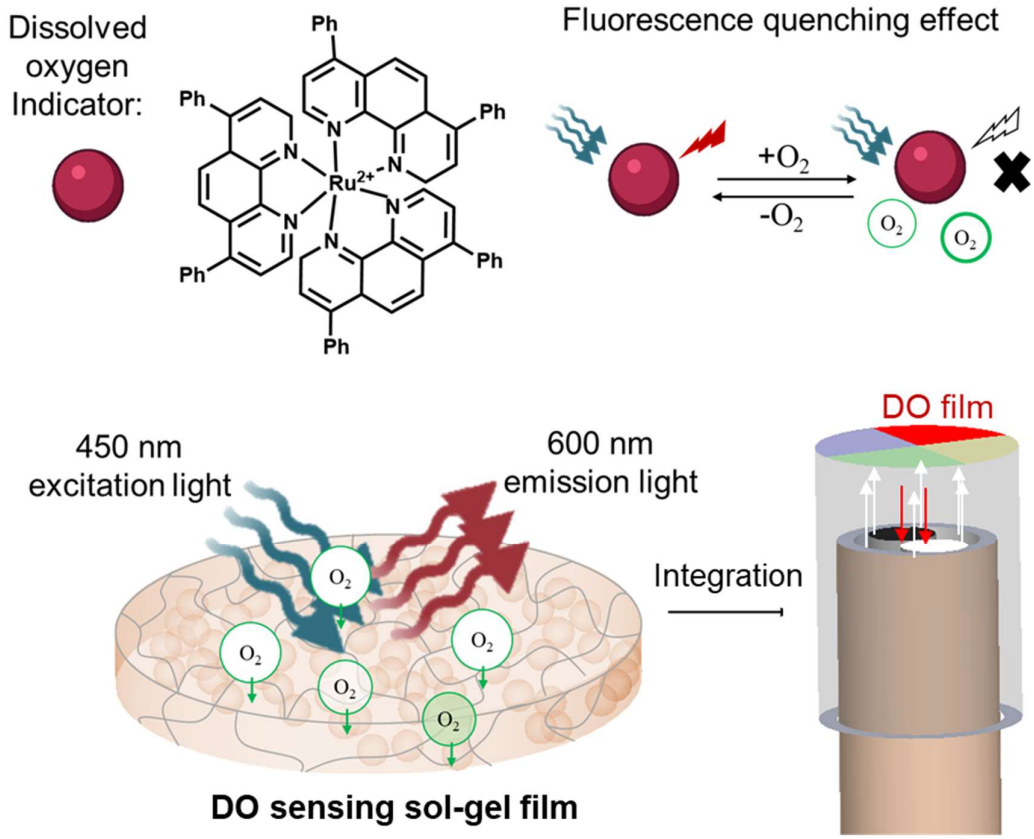


Figure 3-26. Schematic demonstration of the optical fibre DO sensor, including the sensing principle and structure.

As depicted in **Figure 3-27 (a)**, when the DO level increased from 1 to 7 mg·L^{-1}, the emission intensity of the DO sensor decreased to 76% of the original intensity. The maximum emission

intensity of sensing film at different DO levels was calibrated according to the Stern-Volmer equation (eq.1, **Figure 3-27 (b)**). The Stern-Volmer coefficient (K_{sv}) was determined as 0.08.

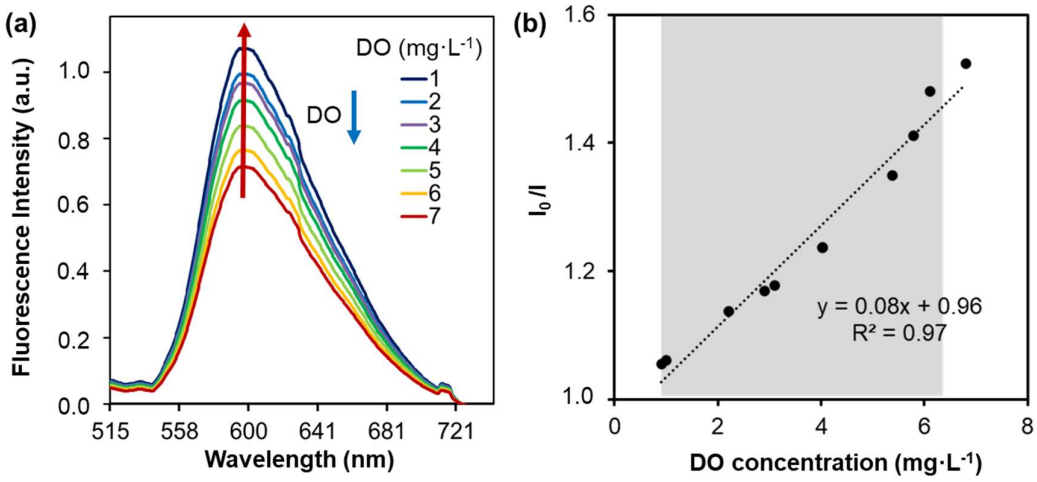


Figure 3-27. Characterisations of the optical fibre DO sensor in PBS solutions (10 mmol L-1, pH 7.4, 25 °C). (a) Fluorescence spectra of the sensor under different DO levels. (b) Calibration curve of the DO sensor using gradient DO PBS solutions. Shadows represent the physiological range of DO concentration in human CSF.

Same as the "asymmetry" response time observed in pH sensing films, when the DO level increased from 1 to 7.5 mg·L^{-1}, a response time of 200 s was recorded, while a response time of 100 s was observed for the reverse process (**Figure 3-28**).

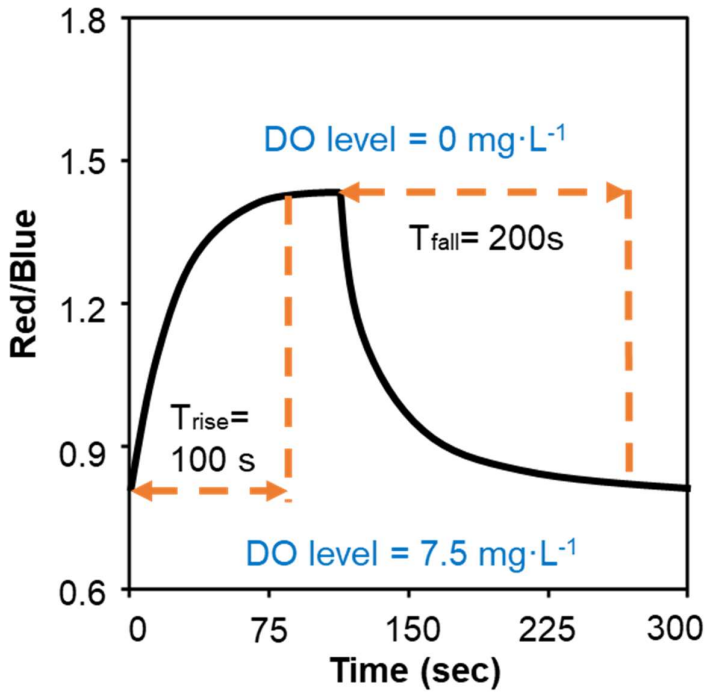


Figure 3-28. Response time of the DO sensor under the alternated 7.5 mg mL-1 and 0 mg L-1 DO buffers.

In continuous and implantable monitoring, good reversibility, stability, and minimum leaching are the prerequisites of the sensor. As is shown in the results, the sensing film can be used reversibly for the measurement of the DO level, although a slightly decreasing trend in the film emission intensity was observed due to the photobleaching effect (**Figure 3-29 (a)**). In the photostability test, the emission intensity was found to decrease during the 24-hour exposure under a stable 7.5 mg·L^{-1} of the DO level (**Figure 3-29 (b)**). The DO sensor became stable after the 6-hour exposure, indicating that the signals measured in the first 6 hours need to be corrected based on the exposure time to obtain an accurate readout. Similar to the pH study, the DO sensing film also has a relatively high leaching percentage of 3.67% in PBS at pH 8.0 after three days, and relatively lower leaching of 1.72% in PBS solution at pH 6.0 (**Figure 3-29 (c)**).

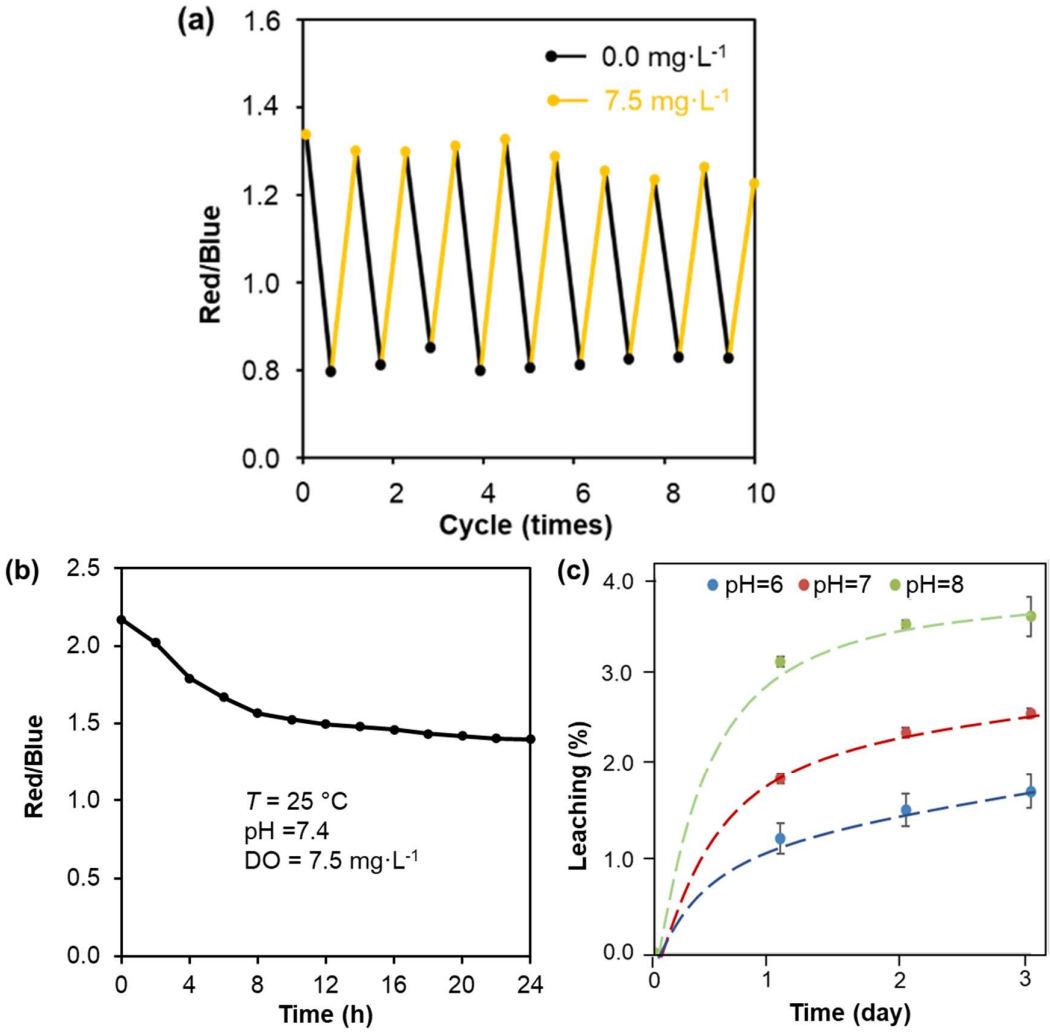


Figure 3-29. Characterisation of the DO sensor for continuous monitoring. (a) Reversibility of the DO sensor. (b) Photostability of the sensing film for 24-h sensing. (c) Leaching results of the sensing film immersed in pH 6, pH 7, and pH 8 PBS for three days.

The performance of the DO sensor under different environmental conditions was also tested. When the temperature increased from 25 to 40°C, an up to 30% decrease was observed in the emission intensity (**Figure 3-30 (a)**), indicating a strong temperature dependence of the sensing film. No evidence has shown the influence of pressure nor pH changes on the emission intensity of the Ru(dpp) sensor (**Figure 3-30 (b,c)**.). To further investigate its potential performance when being implanted in brain CSF, the selectivity of the sensor over the interferences of various neurochemicals was tested (**Figure 3-30 (d)**). The major inferences in aCSF showed negligible influence (<5%) on the emission intensity compared to the intensity measured in pure PBS, suggesting a high selectivity

towards DO. Taken all together, the fabricated optical fibre DO sensor demonstrated a promising result for real-time and continuous monitoring of brain DO in aCSF.

$$\frac{I_0}{I} = 1 + K_{sv} \cdot Concentration\ (O_2) \quad \textbf{(Eq. 3-9)}$$

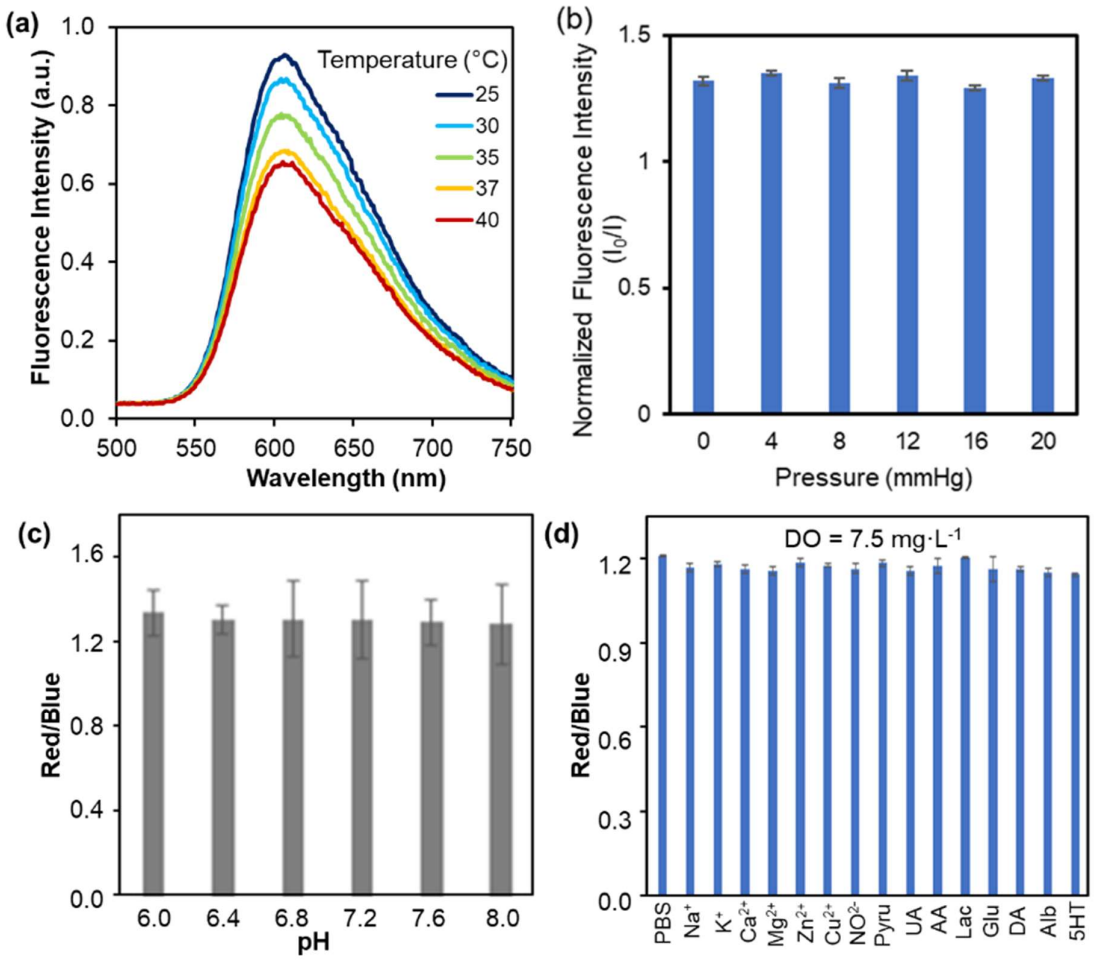


Figure 3-30. Environmental robustness tests of the sensor. (a) Temperature dependence test of the DO sensor. (b) Pressure dependence of the DO sensor. (c) pH dependence test of the DO sensor. (d) Selectivity of the DO sensor over interferences. Error bars (n=3) in the figures represent the standard deviation of the mean of three samples.

3.8 Performances of the optical fibre glucose sensor

The first generation of commercial devices for glucose monitoring was designed based on glucose oxidase catalysed electrochemical sensors[227], where the product of the glucose redox reaction hydrogen peroxide (H_2O_2) is measured for glucose measurement. Glucose oxidase catalysed reaction

has also been used in optical sensors for glucose monitoring based on oxygen transduction[228] and H_2O_2 transduction[229, 230].

I fabricated the glucose sensor by integrating the glucose sensing film to the tip of the flexible optical fibre. The glucose sensing film was fabricated by encapsulating 3,3',5,5'-tetramethylbenzidine (TMB) with glucose enzyme for measuring generated H_2O_2 in the glucose redox reaction. In the first step, glucose is oxidized and H_2O_2 is produced, which is subsequently interacted with TMB to induce a color change in the sensing film (**Figure 3-31**).

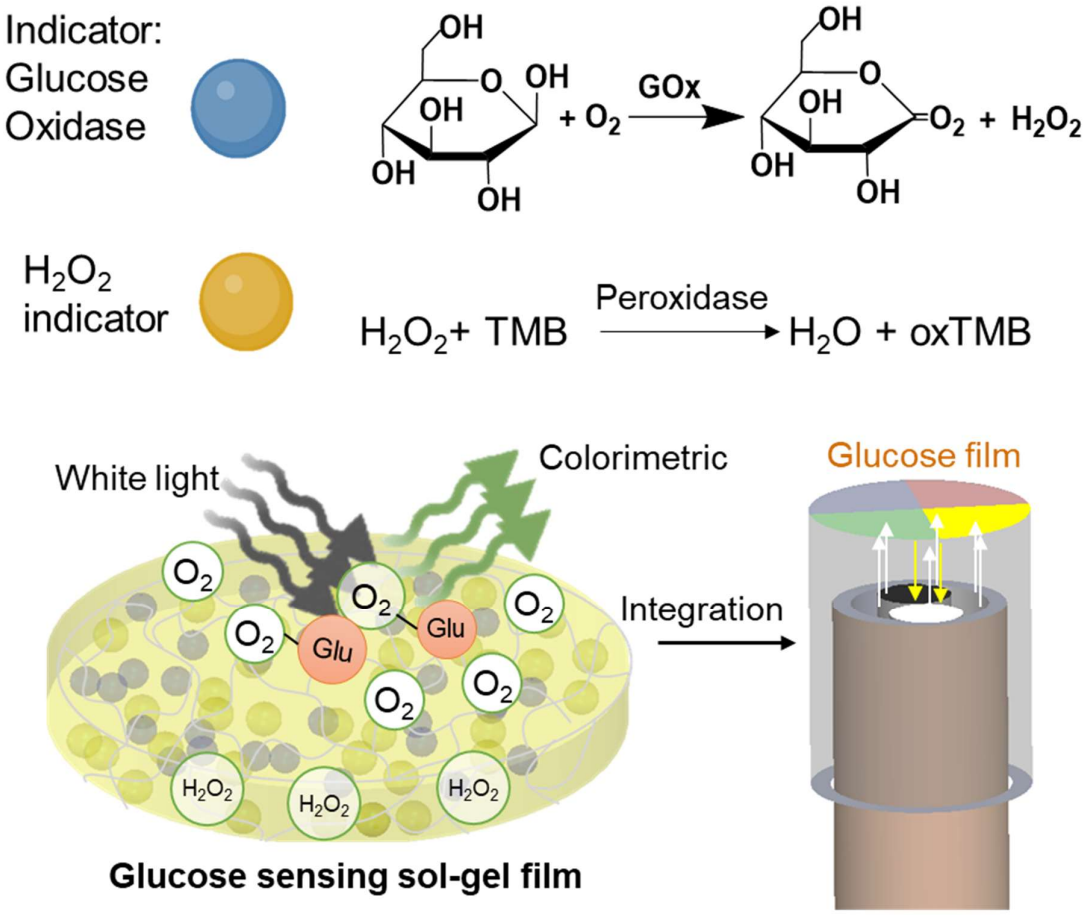


Figure 3-31. Schematic demonstration of the optical fibre glucose sensor, including the sensing principle and structure.

The color change of the sensing film is owing to the changes in the absorbance of TMB at 660 nm. The glucose sensor was calibrated with its reflection spectra in PBS solutions under glucose concentrations ranging from 0.0 to 6.0 mmol·L^{-1} (**Figure 3-32 (a)**). The reflection intensity decreased

2.7/mmol·L^{-1} linearly as the glucose level increased from 0.0 to 6.0 mmol L^{-1} (R^2=0.98) (**Figure 3-32 (b)**). The colors of the glucose sensing films during the measurement were recorded using a smart phone camera with white balance control as the same for all photos, which showed a color transition from yellow to dark blue as the glucose concentrations increased from 0 to 6 mmol L^{-1}.

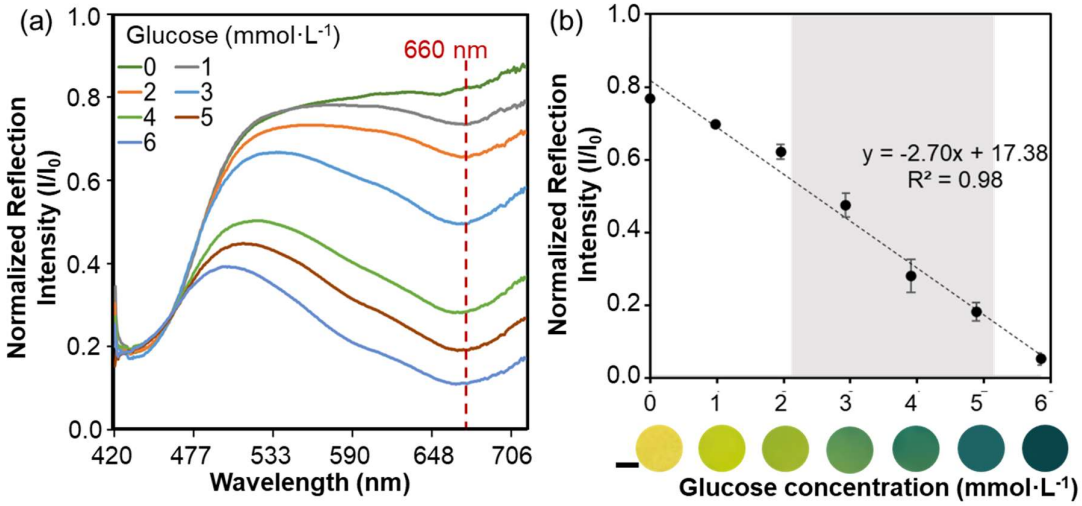


Figure 3-32. Characterisations of the optical fibre glucose sensor PBS solution (10 mmol L-1, pH 7.4, 25 °C). (a) Reflectance spectra of the sensing film under different glucose concentrations. (b) Calibration curve of the sensor for sensing 0 mmol L-1-6 mmol L-1 glucose solutions. Shadows represent the physiological range of glucose concentration in human CSF.

A 1931 CIE chromaticity diagram was analysed with algorithms (**Figure 3-33**) for accurate demonstration of the color shifts of the film, which indicated a good ability in sensing glucose concentrations between 0 to 6 mmol L^{-1}.

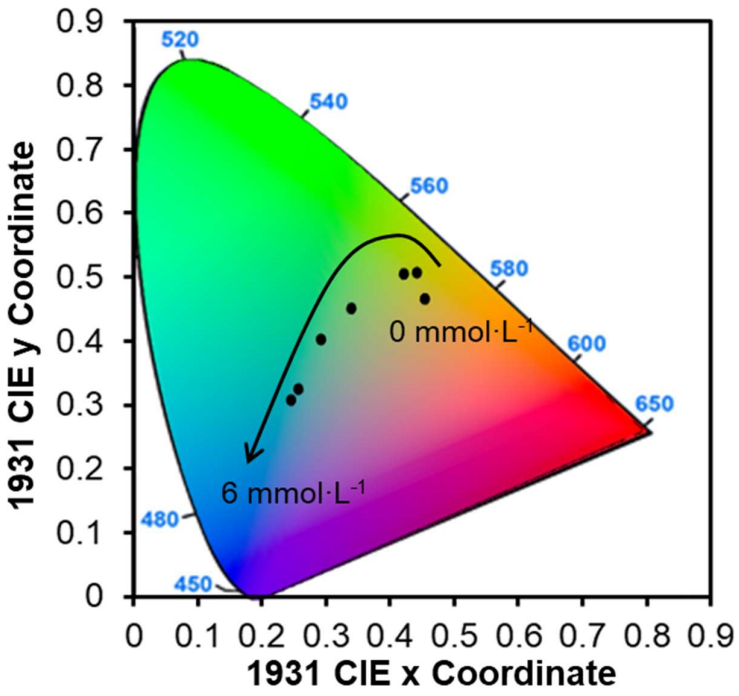


Figure 3-33. CIE image of the sensing film color changing from 0-6 mmol L-1 of glucose. The scale bars of all subfigures equal to 1 mm.

The sensing performance including response time, stability, and leaching rate are evaluated for its ability to perform continuous and real-time measurement. Unlike the other three sensors, glucose sensor is based on the glucose redox reaction, and the reaction is not reversible in human CSF, indicating that the sensing film could only measure the accumulation of glucose level continuously. The sensor needs to be changed on a regular basis to measure both decreasing and increasing trends of the glucose level. A response time within 30 s was obtained, indicating a fast response for real-time monitoring of glucose in aCSF (**Figure 3-34 (a)**). No obvious variation in the reflection intensity of the glucose sensor was observed in glucose of 2 mmol L^{-1} in the PBS solution after exposure to a broadband light (20 mW) for 24 hours, indicating the ability for long-term use (**Figure 3-34 (b)**). Moreover, in the leaching test, less than 4% of indicator leaching was found in the buffer solution after immersing the sensing film in PBS solution for three days (**Figure 3-34 (c)**).

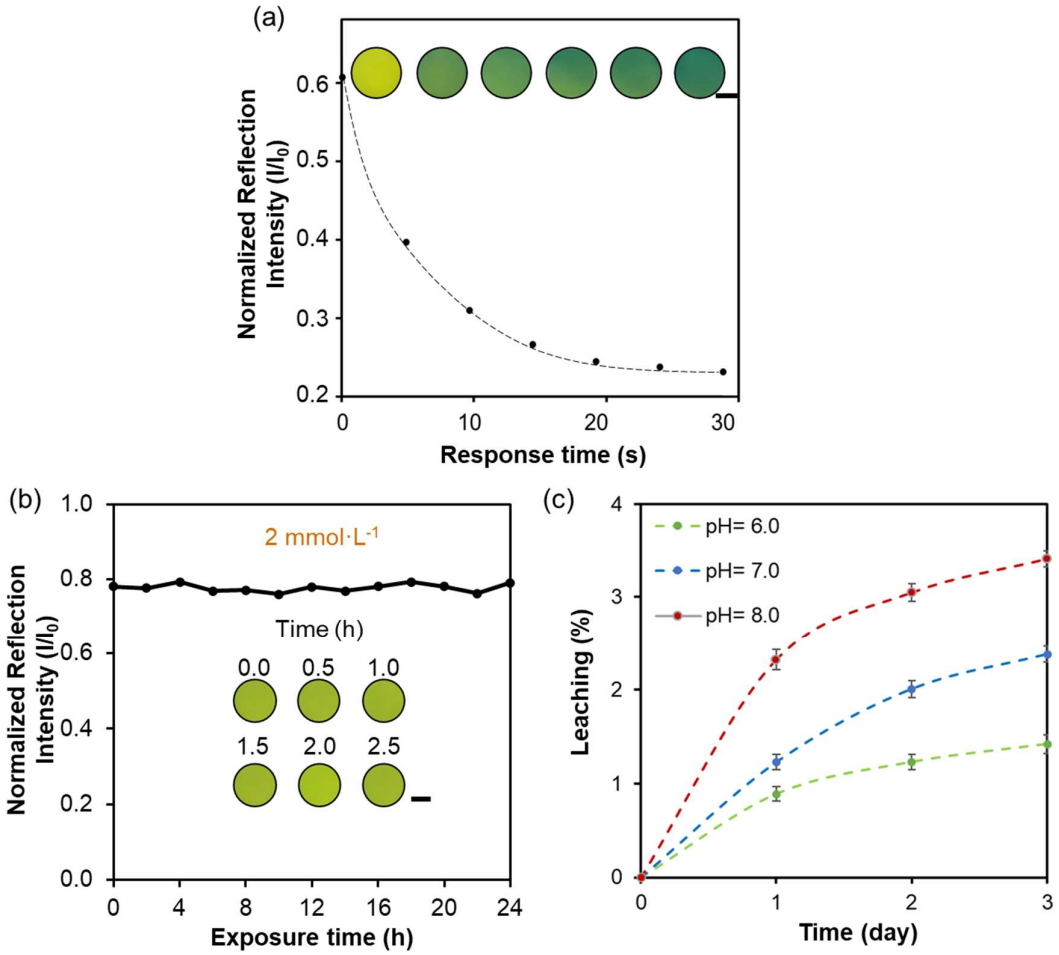


Figure 3-34. Characterisation of the glucose sensor. (a) Response of the sensing film when the glucose concentration increased from 2 to 5 mmol L-1. (b) Stability of the sensing film over 24 hours. Insets show the corresponding color changes of the sensing film in the first 3 hours. (c) Leaching results of the fabricated optical fibre glucose sensor. The scale bars of all subfigures equal to 1 mm.

The temperature dependence of the fabricated optical fibre glucose sensor was tested by using a 96-well microplate from 25 to 40 °C. A slight increase in the absorbance was observed, which might be owing to the increase in the activity of glucose oxidase (**Figure 3-35 (a)**). In the pH dependence test, the glucose sensing film was tested in PBS solutions with different pH values (6.0-8.0). The results showed a negative relationship between the pH value and film absorbance when pH increased from 6.0 to 6.5 and a positive relationship when pH increased from 6.5 to 8.0 (**Figure 3-35 (b)**). This might be owing to a higher glucose oxidase activity in slightly acidic solutions[231]. The sensor can also be used under various pressures, indicating high potential for *in vivo* brain measurement. The performance of the glucose sensor in brain aCSF in the presence of various interferents such as electrolytes, metabolites, and neurotransmitters were also tested (**Figure 3-35 (c,d)**). No obvious

variations in the reflection intensity were observed when the interferences were added to the standard 2 mmol L^{-1} glucose PBS solution (**Figure 3-35 (c)**). In addition, the glucose sensor did not show a major response to the interferents in glucose-free solutions (**Figure 3-35 (d)**), indicating a high selectivity of the optical fibre glucose sensor and a good capability of real-time tracking acid or base neurochemicals.

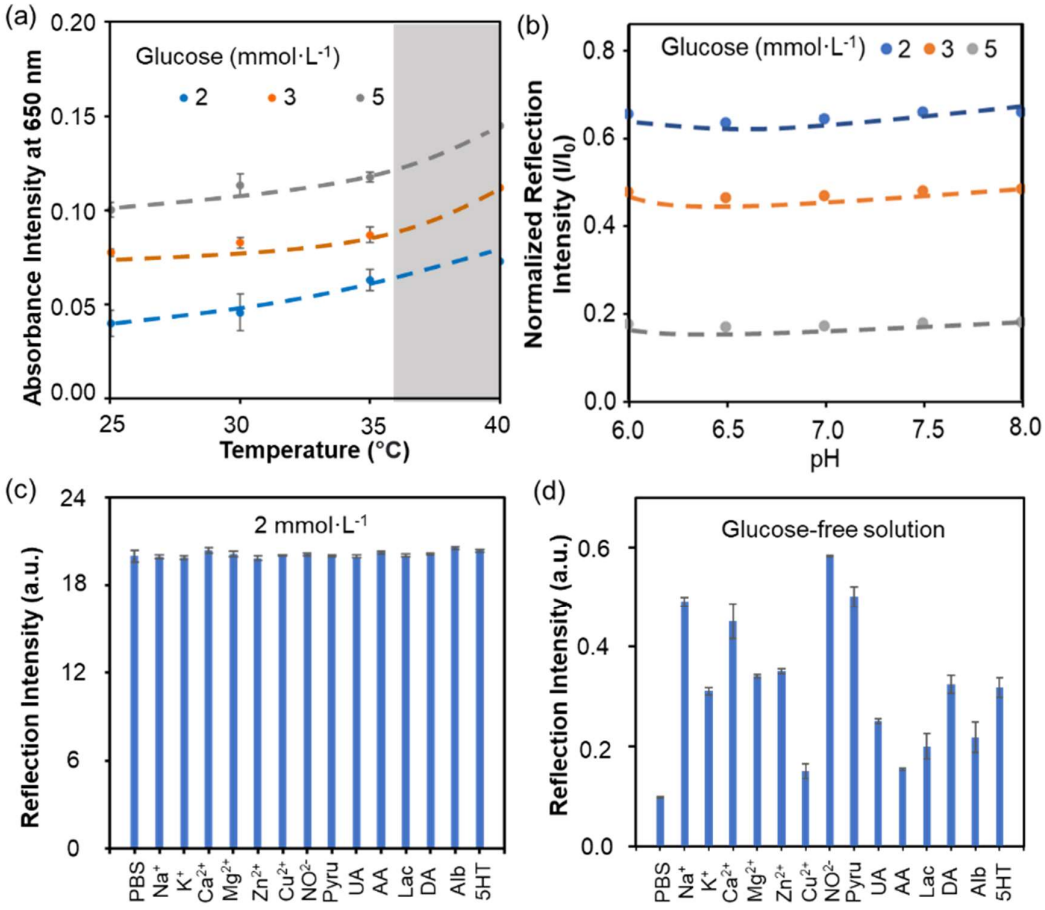


Figure 3-35. Environmental dependence tests of the glucose sensor. (a) Temperature dependence and (b) pH dependence of the glucose sensing film as the glucose concentration at 2, 3, and 5 mmol L-1. Shadows represent the physiological range of human CSF temperature. (c) Selectivity tests of the glucose sensor at the glucose concentration of 2 mmol L-1. (d) Response of the glucose sensing film on the interferences in glucose-free solutions. The error bars (n=3) in the figures represent the standard deviation of the mean of three samples.

These characterisation studies on the designed optical sensors have demonstrated a good sensing performance of the sensors for brain pH, temperature, DO, and glucose sensing. In terms of implantable diagnosis, optical sensors could also provide battery free and remote sensing, and they

can be easily miniaturized. However, the response time of the proposed fibre optical sensors could take several seconds to minutes to respond and might be slower than EC sensors. But it is worth mentioning that the sensing speeds (100-350 s for the pH sensor, 2s for the temperature sensor, 100-200 s for the DO sensor, and 30 s for the glucose sensor) are sufficient for TBI monitoring as the disease usually progress over several minutes to hours[232, 233].

3.9 Multiplexed measurement

After the pH, temperature, DO, and glucose sensors being tested separately, each of them was cut into a quarter with a diameter of 2 mm. The sensing films were placed evenly on a round glass slide and a silicone tube with 2 mm of outer diameter (O.D.) to fabricate a multiplexed sensing film, followed by integrating on the tip of the flexible optical fibre. The sensor was then tested for multiplexed sensing in aCSFs (Section 3.3.7). Aiming to achieve dynamic monitoring of brain CSF biomarkers simultaneously, AI models were trained using the reflection spectra features, which were obtained in the calibration tests, for quantitative readout of the biomarker concentrations. The AI-integrated multiplexed optical fibre sensor was first validated in aCSF, and then in lamb brain for an *ex vivo* dynamic test.

3.9.1 Multiplexed calibration of the optical fibre sensing system

The calibration curves of aCSF measurement using the multiplexed optical fibre sensor are shown in **Figure 3-36**. In the measurement, the mixed reflection spectra of four sensing films were captured using the spectrometer and the reflection intensities at different wavelengths were used for different biomarker detection. In each biomarker's calibration, the other biomarker levels remained constant in the aCSF buffer. The reflection intensity at 623 nm was used for pH calibration. When the pH value changed to 1 pH unit, a 0.11 change in the 623 nm reflection intensity was observed (**Figure 3-36 (a)**). Peak shifts between 470 to 540 nm were used for temperature calibration. For every change of 1 °C in the temperature, a 4.77 nm shift was visualized in the reflection spectra (**Figure 3-36 (b)**). The wavelength of interest for DO measurement was 600 nm under the excitation of a 450 nm LED. A sensitivity of 0.06 (a.u.) per change of 1 mg L^{-1} of DO concentration was obtained (**Figure 3-36 (c)**). In the calibration of the glucose sensor, the relationship between 660 nm of reflection intensity and

glucose concentration was analysed, and a sensitivity of 0.16 (a.u.)/mmol·L^{-1} was achieved (**Figure 3-36 (d)**). Multiplexing the sensors to one channel showed reduced sensitivity of the sensors due to the overlapping in the optical spectra.

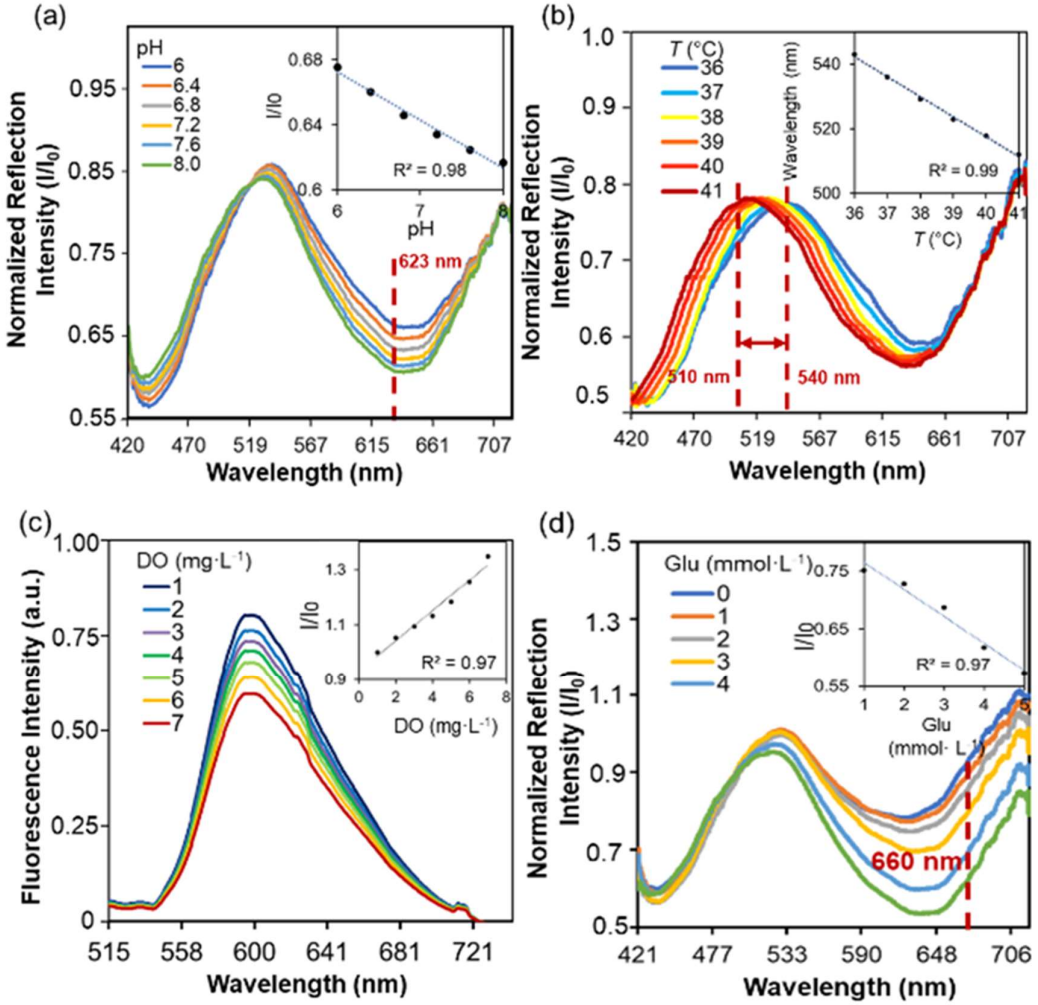


Figure 3-36. Characterisations of the multiplexed optical fibre sensor in aCSF measurement (25 °C). (a) pH calibration curves in aCSF using the multiplexed optical fibre sensor. Inset: Calibration curve of the sensor for 6.0-8.0 pH measurement. (b) Temperature calibration curves in aCSF using the multiplexed optical fibre sensor (pH 7.4). Inset: Calibration curve of the sensor for 36-41 °C temperature measurement. (c) DO calibration curve in aCSF using the multiplexed optical fibre sensor. Inset: Calibration curve of the sensor for 1-7 mg L-1 DO measurement. (d) Glucose calibration curve in aCSF using the multiplexed optical fibre sensor (pH 7.4). Inset: Calibration curve of the sensor for 0-6 mmol L-1 glucose measurement.

pH (**Figure 3-37 (a)**), temperature (**Figure 3-37 (b**), and DO (**Figure 3-37 (c)**) sensors have also demonstrated high reversibility in the aCSF measurement, indicating that the developed multiplexed optical fibre sensors were able to be applied for brain dynamic monitoring. The multiplexed sensor

has also maintained high stability in continuous measurement (**Figure 3-38**). The color changes of the multiplexed sensing film in the aCSF were visualized and imaged using a smartphone camera (**Figure 3-37 (d)**). It can be seen from these images that the color of the sensor was directly related to the biomarker levels of the measured solution. When the biomarker level was changed, the color of the sensor would change accordingly.

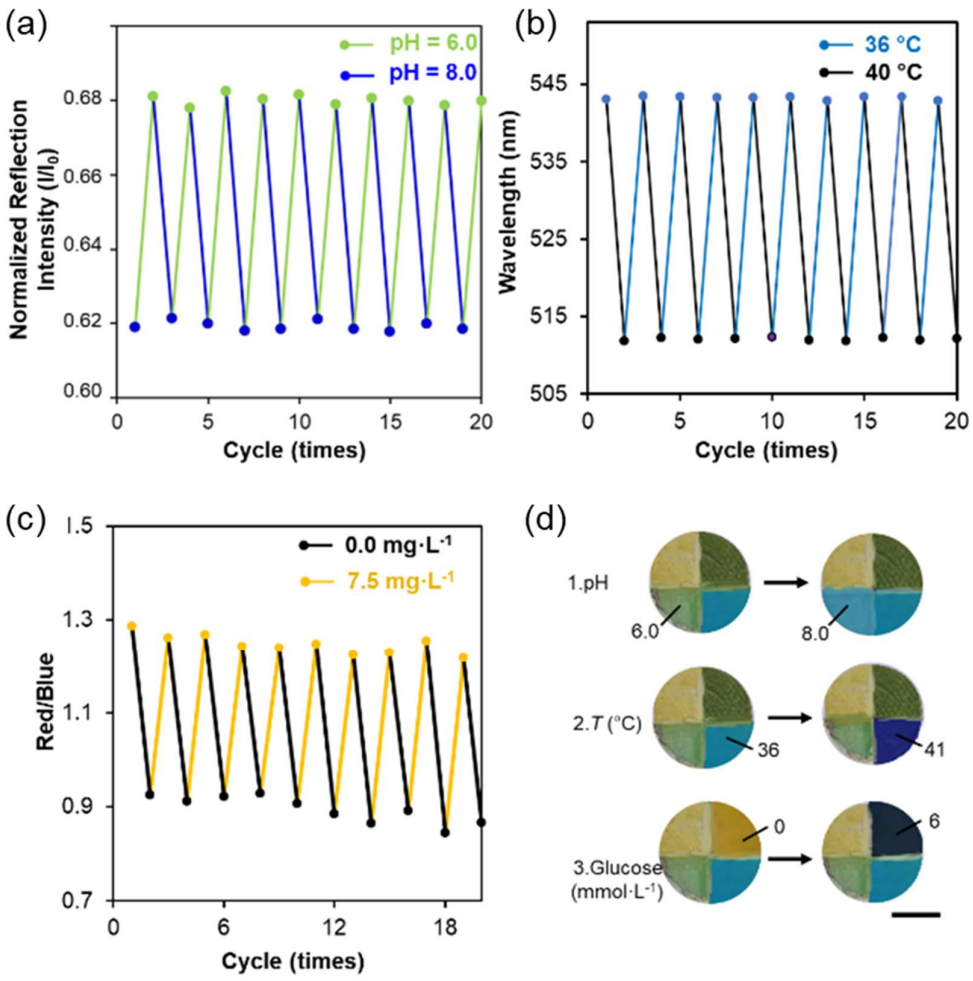


Figure 3-37 Reversibility test of the multiplexed optical fibre sensor in aCSF: (e) pH sensing, (f) temperature sensing (pH 7.4), (g) DO sensing (pH 7.4). (h) Color changes of the multiplexed sensing films in response to different pH values, temperature, and glucose levels. Scale bar = 1 mm. The error bars (n=3) in the figures represent the standard deviation of the mean of three samples. Scale bar = 1 mm.

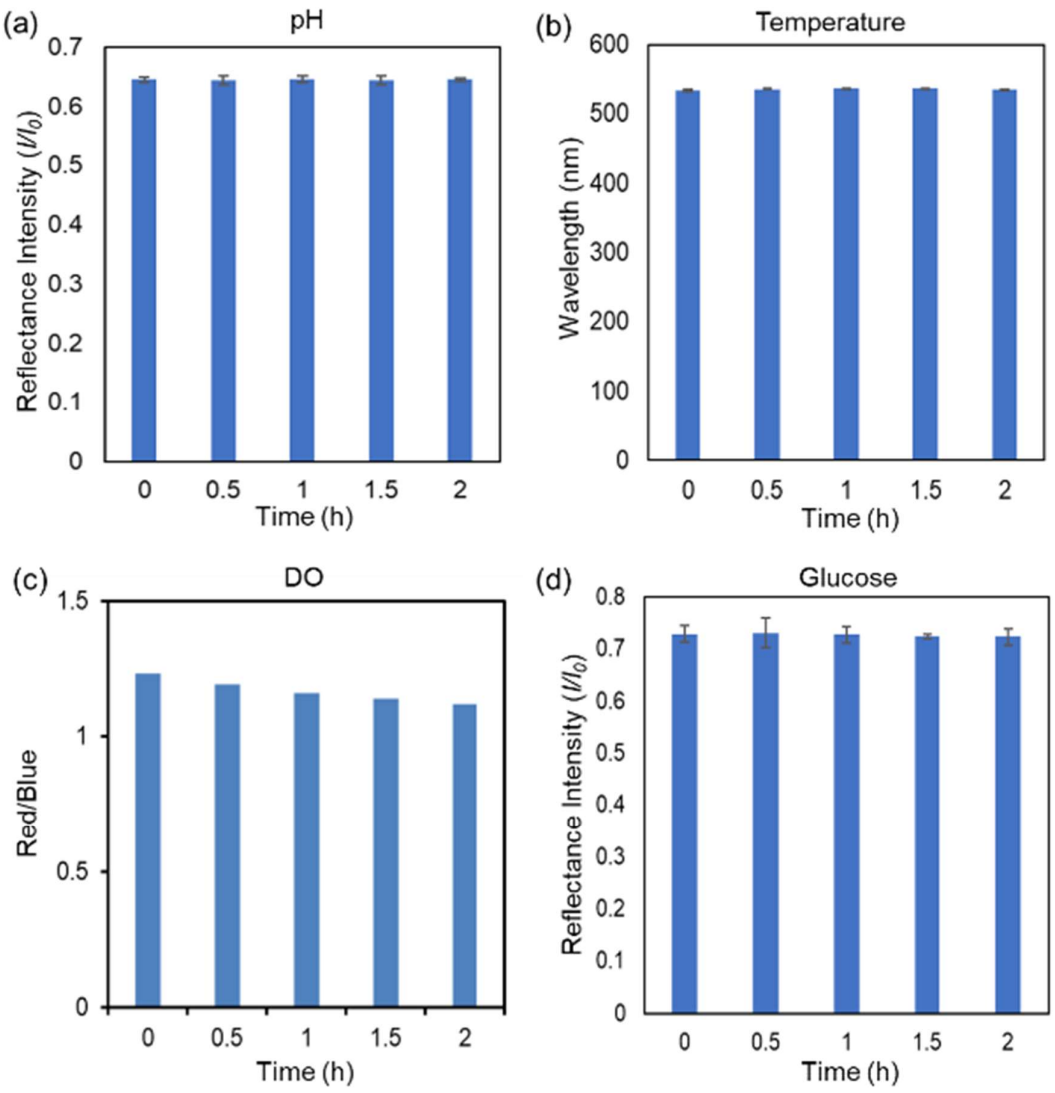


Figure 3-38. Stability measurement in aCSF buffer solutions. (a) pH, (b) temperature, (c) DO, and (d) glucose sensing films. The error bars (n=3) in the figures represent the standard deviation of the mean of three samples.

3.9.2 Regression model-based concentration calculation

It can be noticed from **Figure 3-37** that spectrum overlapping in unavoidable in multiplexed monitoring. To reduce the crosstalk interferences on the multiple biomarker measurement and compensate the environment effects for accurate and robust readout of multiple biomarker concentrations, four machine learning models using different regression methods were trained and compared for the prediction of the concentrations of four biomarkers simultaneously and accurately.

After obtaining the overlapped reflection spectrum, the spectrum was smoothed by calculating the average value of a sliding window. The spectrum was then labelled with four values corresponding to the accurate biomarker concentrations. Features related to each sensor were extracted and fed into different machine learning models for biomarker concentration calculation. Grid search was performed to find the optimal hyperparameters for each model and the selected hyperparameters are listed in **Table 3-6**. The best performed models using the selected hyperparameters were then compared to determine the best prediction model across all models. In these models, decision tree has several hyperparameters need to be defined to construct a tree. A small variance in the selection may lead to a big impact on the model performance. On the contrary, random forest is more robust with hyperparameters as it is a bagging method that involves many weak trees in prediction and can be adapted to diverse scenarios. SVR adjust the kernel, degree of kernel and C. It relies on C values as hyperparameters to set the margin in a prediction, and the optimal combination of hyperparameters was found by applying grid search.

Table 3-6. Hyperparameters selected for each model

Model	Parameters	Hyperparameter
SVR	Kernel type C (penalty parameter): degree	kernel = linear, degree = 1 and C = 0.1
Random Forest	Number of trees: Maximum depth: Minimum samples split:	max_depth=100, criterion=squared error and n_estimatos = 200
Decision Tree	max_depth min_samples_split	max_depth = 10, min_samples_split = 15
Bayesian Regression	alpha_1 alpha_2	alpha_1 = 0.001, alpha_2=1, lambda_1=1, lambda_2=0.001
Linear Regression	n_jobs	n_jobs = 1

The optimized models were then fed with the features from the testing set for comparison. Among four regression models, Bayesian regression showed the best accuracy towards the prediction of biomarker concentrations (**Table 3-7**).

Table 3-7. Biomarker concentration prediction results using different regression models

Biomarker		linear	polynomial	SVR	DT	RF	Bayesian
ph	MAE	0.21	0.64	0.46	0.23	0.26	0.21
	MSE	0.08	0.69	0.41	0.2	0.14	0.08
	R^2	0.84	0.68	0.67	0.77	0.71	0.84
Temperature	MAE	0.32	0.39	0.18	0.37	0.3	0.32
	MSE	0.18	0.29	0.06	0.45	0.19	0.18
	R^2	0.94	0.9	0.94	0.84	0.93	0.93
DO	MAE	0.26	0.41	0.45	0.33	0.48	0.20
	MSE	0.15	0.66	0.09	0.43	0.06	0.10
	R^2	0.80	0.89	0.91	0.87	0.89	0.94
Glucose	MAE	0.10	0.11	0.12	0.12	0.18	0.14
	MSE	0.15	0.19	0.09	0.20	0.05	0.05
	R^2	0.92	0.90	0.93	0.90	0.94	0.94

SVR: Support vector regression; DT: Decision tree; RF: Random forests; DO: Dissolved Oxygen; MAE: Mean absolute error; MSE: Mean square error.

In training the models, ten features were extracted from the obtained reflection spectra and fed into the machine learning models (**Table 3-4, Figure 3-6**). The features included the intensities at 623 nm, 600 nm, and 660 nm and spectra peaks for pH, DO, glucose, and temperature level calculation. Other features including a reference intensity at 450 nm, valley location, and valley height were also extracted from the spectra to eliminate the crosstalks between the four sensing films. The temperature and the excitation time length were also extracted and utilized as two additional features to compensate the temperature influence and photobleaching effect on the DO sensor. A Bayesian model was selected and fed with the features, due to its advantage in taking account the prior knowledge when building the prediction models. The models were trained with 75% of the dataset and tested with 25% of the dataset, and 4-fold validation was applied for the evaluation of the model performance. R^2 equal to 0.84, 0.93, 0.94, and 0.94 were obtained for the pH, temperature, DO, and glucose prediction respectively, indicating a high prediction accuracy of the machine learning model in predicting biomarker concentrations (**Figure 3-39, Table 3-7**). By means of the machine learning algorithms, the temperature influences and photobleaching of the sensors were successfully compensated for the sensing of aCSF DO level. The models also provided quantitative readouts of all biomarkers within a short computational time (<1 ms). The AI-integrated multiplexed optical fibre sensor demonstrates a promising possibility for accurate and multiplexed brain biomarker monitoring.

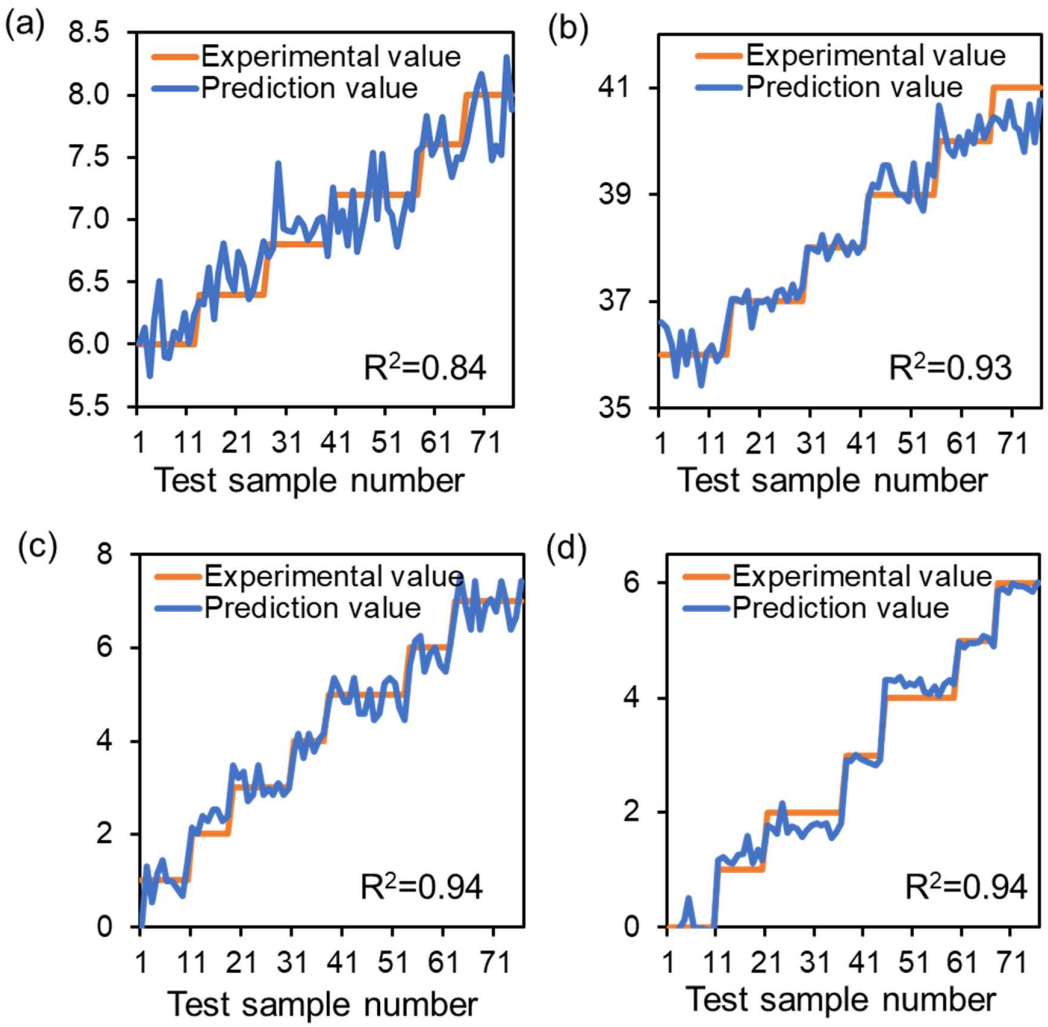


Figure 3-39. Machine learning model results for biomarker concentration prediction. (a) pH value prediction using feature set 1. (d) Temperature prediction using feature set 1. (e) DO prediction using feature set 2. (f) Glucose concentration prediction using feature set 1.

3.9.3 Ex vivo validation for continuous monitoring of brain biomarkers

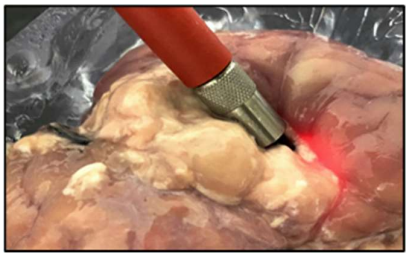


Figure 3-40. Photographs of the ex vivo experimental setup and details about how the sensor interacts with the brain tissue. Scale bar = 1 cm.

Ex vivo measurement was conducted using lamb brains to further validate performances of the developed multiplexed optical fibre sensor (**Figure 3-40**). In clinic, brain catheters were inserted in either brain superior sagittal sinus to withdraw brain CSF or brain tissue for BIF and CSF measurement[234]. In this study, lamb brains were immersed in standard buffer solutions and the fibre sensor was inserted 4 mm into the brain tissue during sensing calibration. The calibration curves of each sensor were measured, and linear relationships were obtained (**Figure 3-41**). Compared with previous experimental results introduced in **Figure 3-36**, a lower intensity and noisy spectra were obtained here due to the background noise form the brain tissue. Besides, the fibre sensing film was also in physical contact with the brain tissue which might reduced the distance between the film and fibre tip as the sheath was soft, leading to a lower intensity and unregular spectra shapes. However, unavoidable crosstalks between the sensing film signals and background noises were observed throughout the *ex vivo* calibration experiment.

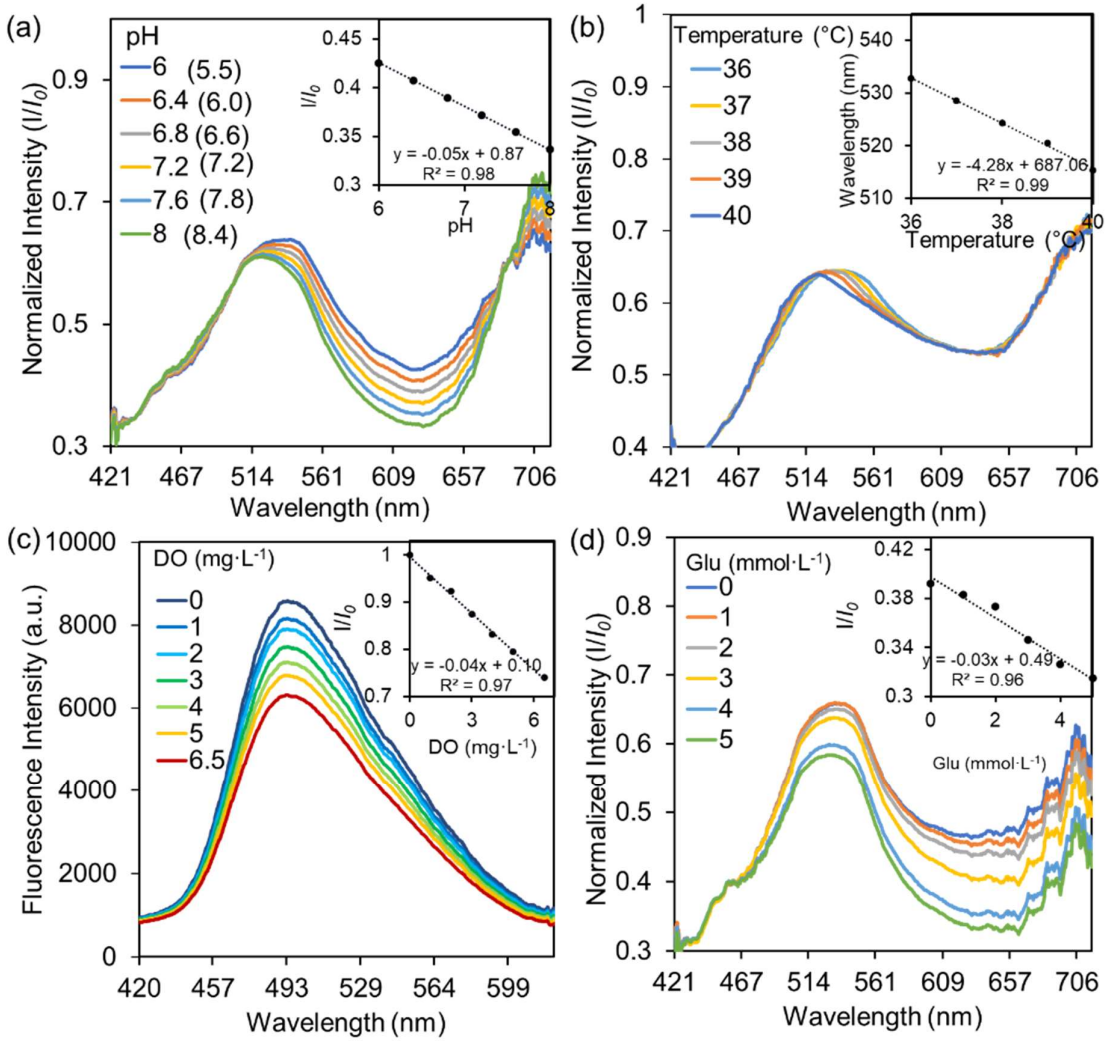


Figure 3-41. Ex vivo measurements using the multiplexed fibre sensor. (a) pH calibration curve in an ex vivo measurement using the multiplexed optical fibre sensor. (b) Temperature calibration curve ex vivo measurement using the multiplexed sensor. (c) DO calibration curve in ex vivo measurement using the multiplexed sensor. (d) Glucose calibration curve in ex vivo measurement using the multiplexed sensor.

To investigate dynamic monitoring for TBI diagnosis and treatment, the developed multiplexed optical fibre sensor was examined using an *ex vivo* model to perform real-time and continuous monitoring of multiple biomarkers in brain aCSF. The pH, temperature, DO, and glucose levels and other biological CSF constituents of the aCSF buffer solution were tuned to mimic the chemical compositions in four stages of TBI patients including pre-TBI (healthy), mild TBI, severe TBI, and back to mild TBI stages (Section 3.3.9). The lamb brain was washed to remove the existing chemicals. Before *ex vivo* measurement, the brain was immersed in the prepared healthy stages aCSF solution to

change the chemical composition of the lamb brain to mimic pre-TBI patient's brain. During the dynamic measurement, the designed optical sensing fibre was inserted into the brain with a depth of 4 mm, and the reflection spectra were obtained every 6 s using a self-designed python program. After the signal stabilized for 4 min, the aCSF of next stage TBI was injected to replace the previous TBI buffer. The acquired reflection spectra were first smoothed to remove noises and the same 10 features were extracted (**Table 3-4**). The machine learning models built with standard calibration spectra were directly used here in python algorithms to predict the biomarker concentrations using the extracted features for continuous and precise readouts. The results of dynamic monitoring are shown in **Figure 3-42**. During the transition from healthy to mild TBI, and mild TBI to severe TBI, a decrease in pH from 7.4-7.0-6.5, an increase in temperature from 37-38-39 °C, a decrease in DO from 8 to 4 $mg \cdot L^{-1}$, and to 3 $mg \cdot L^{-1}$, and an increase in glucose from 2 to 4 $mmol \cdot L^{-1}$, and to 5 $mmol \cdot L^{-1}$ were detected using the multiplexed optical fibre sensor. The biomarker levels were dynamically predicted by the machine learning model with a resolution of 6 s. The non-reversible glucose sensing film can only monitor the one-way increasing trend continuously until the film saturation at a glucose concentration of 50 mmol L^{-1}. When the glucose was decreased into a mild stage, the saturated sensor film was replaced by new glucose sensing film, resulting in the signal drop at 720 s. All the signals stabilized after 120 s, and the biomarkers prediction values exhibited high accuracy. The proposed multiplexed optical fibre sensor demonstrated promising ability in dynamic monitoring of TBI brain biomarkers and has successfully detected the fluctuations in the biomarkers for the indication of disease stages. Medical interventions can be applied to the patients when the disease goes into a worse stage. For example, insulin therapy can be performed when glucose increased to a high level and oxygen supply can be offered to avoid TBI complications, such as brain anoxia. The scenario of a severe TBI patient being proper treated and condition being improved back to mild stage was also mimicked to examine the reversibility of the multiplexed optical fibre sensor in dynamic monitoring. Upon the multiplexed optical fibre sensor, improvements in pH, temperature, DO, and glucose levels were observed in the TBI *ex vivo* model during the transition from severe to mild stages, indicating an promising ability for dynamic monitoring for real-case scenarios.

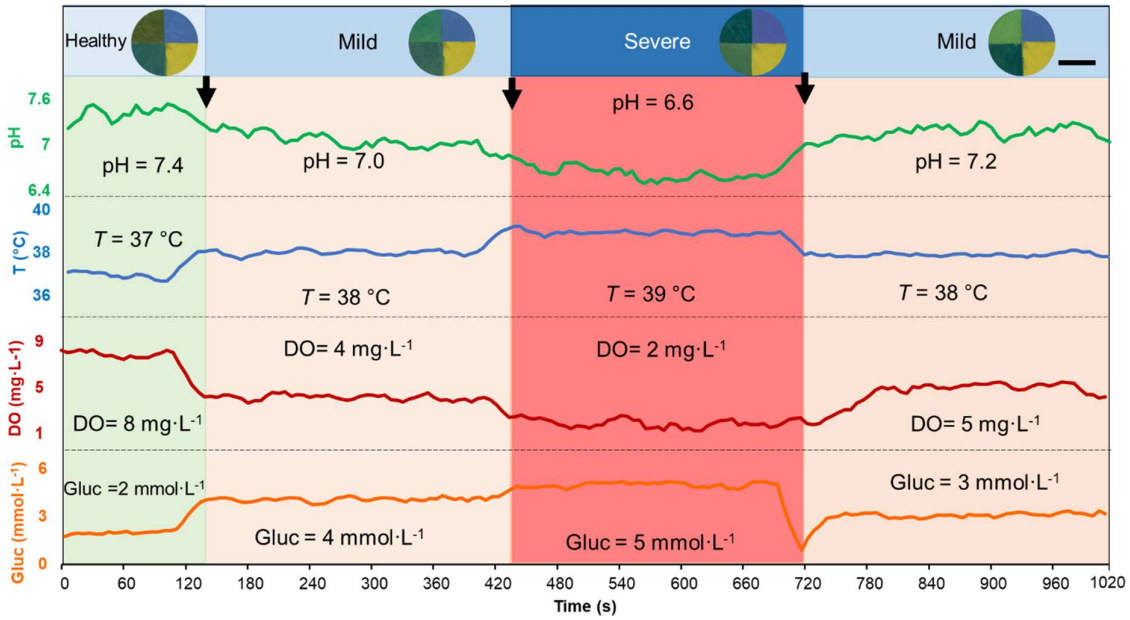


Figure 3-42. Multiplexed and dynamic monitoring for simulated TBI disease using an ex vivo lamb brain. Images of the sensing film in four stages are also presented. Scale bars = 1 mm.

3.10 System biocompatibility and miniaturization

To investigate whether the developed multiplexed optical fibre sensors are safe to be implanted for 7 days, further biocompatibility studies were conducted by evaluating the growth and viability of cells. L929 fibroblasts were cultured in multiwall plates in the presence of sol-gel sensing film (sol-gel film, pH sensing film) (diameter = 9 mm) for 1, 3, 5 and 7 days. The ability of cell proliferation was assessed using a Cell Counting Kit 8 (CCK 8) assay to investigate the effect of the used sensing film on cellular growth and function (**Figure 3-43 (a)**). It was observed that cell proliferation ability increased rapidly during the first 3 days, and it became stable in day 3 to day 7 in all samples. In addition, no significant differences were observed between the growth of cells in the presence of the sensing film, pure sol-gel film, and the control group (pure cells) during the 7-day observation. Cellular viability was also assessed using a Live/Dead staining assay over a 7-day incubation (**Figure 3-43 (b,c)**). It is clearly observed that most of the cells were shown in green (live cells) and only a few cells were in red (dead cells), demonstrating the high cellular viability (>95%) of the develop sensors.

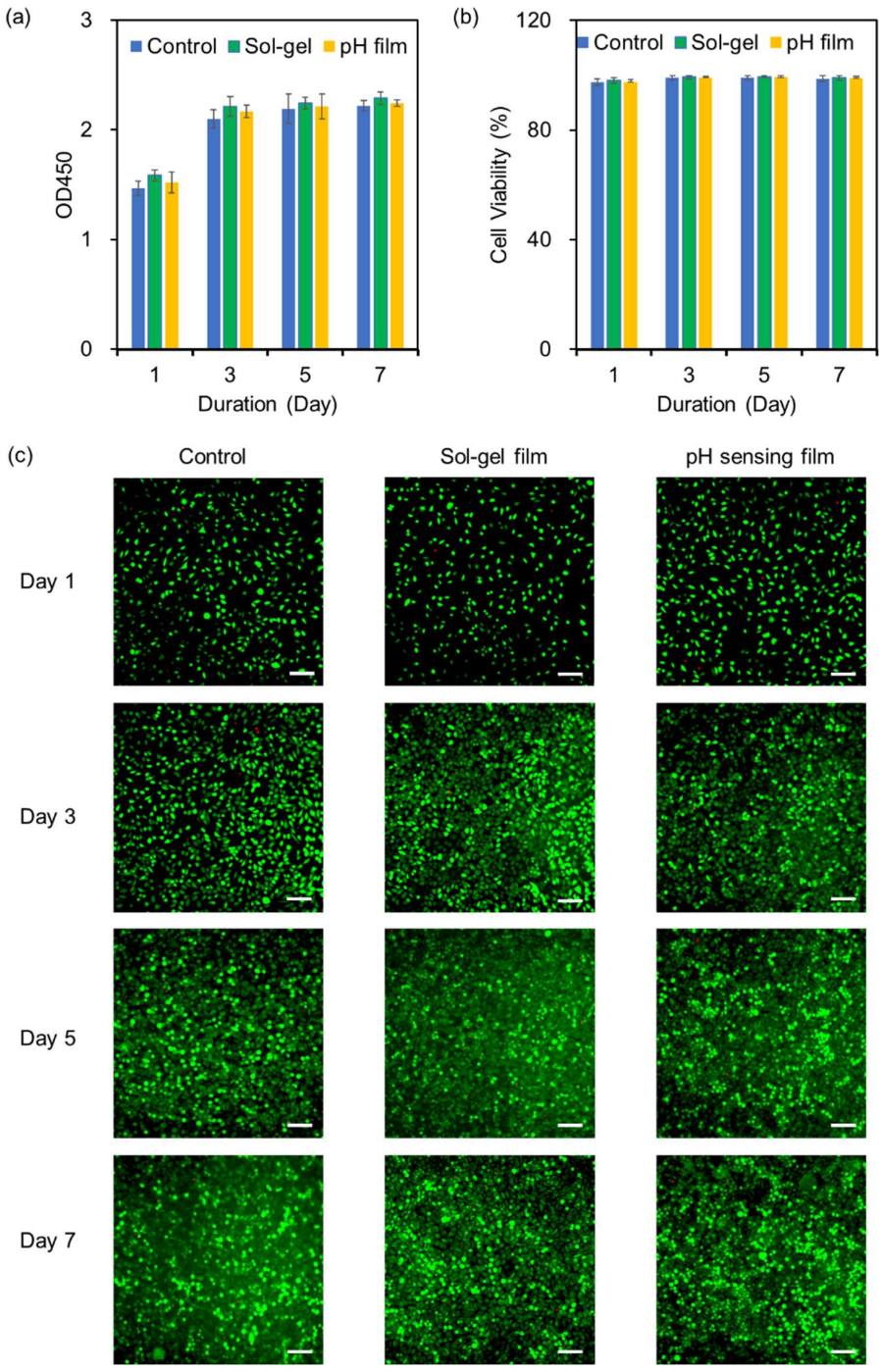


Figure 3-43. Biocompatibility and cytotoxicity study of the sensing film. (a) The ability of cell proliferation. (b) Cellular viability of the sensing film. (c) Live/dead cell imaging. Scale bar = 100 μm.

In the end, fabrication methods for probe miniaturization were explored. The previously used sensing fibre was commercialized, which has a large fibre body due to the protection sleeve covering the

fibres, making the whole fibre body 8mm in diameter. I, therefore, reduced the total fibre body size by simply bundling two bare fibres and successfully reduced the sensing probe from 8 to 1.6 mm without impairing the sensing performance (Section 3.3.11, **Figure 3-44**). However, due to the difficulties in making ¼ sensing films and manually placing them in a round shape and fixing in front of the fibre tips, it was hard to be further minimized, and the smallest I could fabricate was 2 mm.

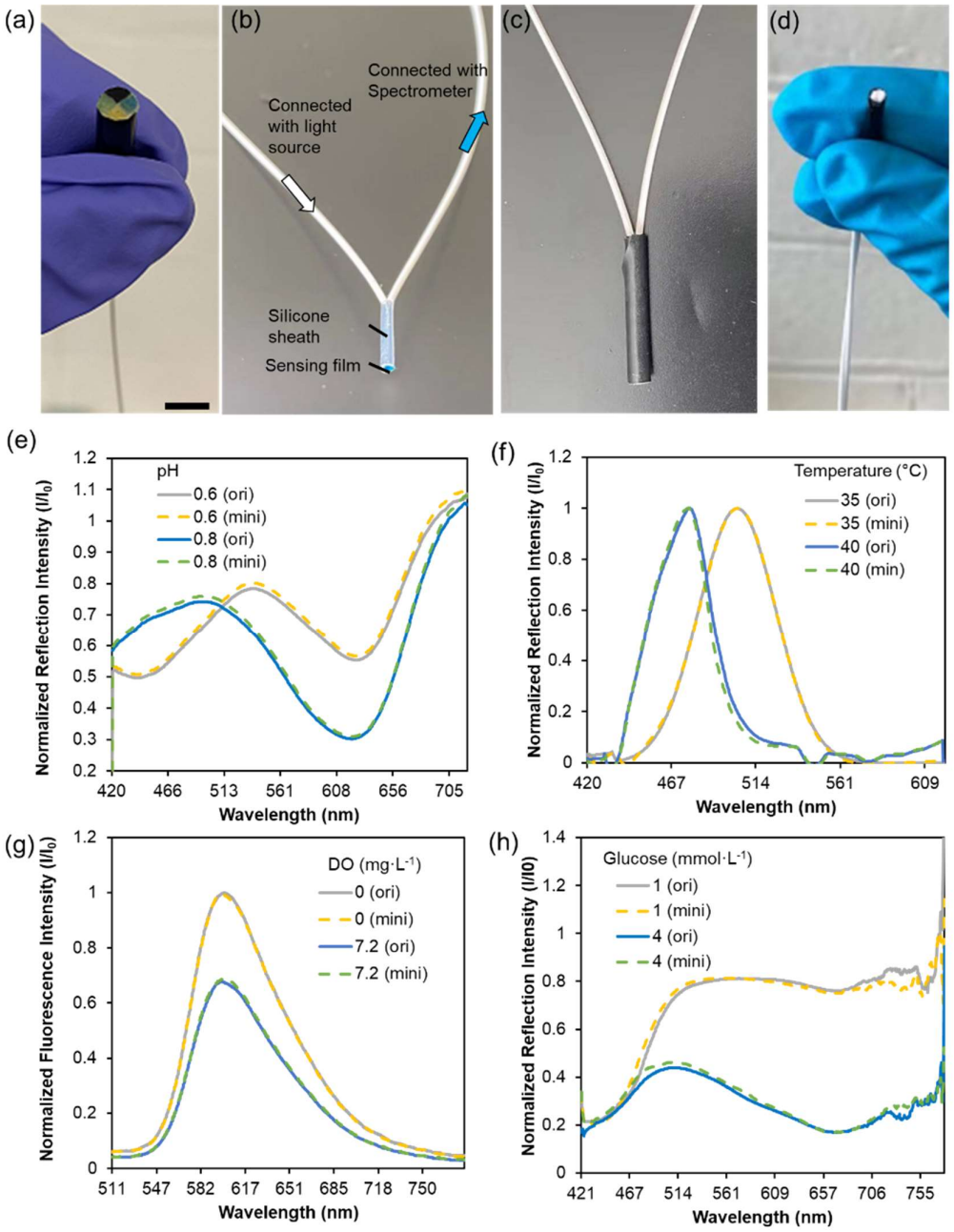


Figure 3-44. Miniaturization of the optical fibre sensor. (a) Sensing probe without the protection jacket. (b) Self-fabricated Y-shape fibre. (c) Black cover was used to block the background noise. (d) Sensing film tip. Isolation film was attached to the tip to enhance reflection and reduce noise. (e) Sensing results for pH 6 and pH 8. (f) Sensing results for temperature 35-40 °C. (g) Sensing results for DO 0-7.2 mg·L-1. (h) Sensing results for glucose 1-4 mmol·L-1. Scale bar = 5 mm.

3.11 Conclusion

A multiplexed optical fibre sensor was developed for dynamic brain pH, temperature, DO, and glucose monitoring simultaneously. The pH, temperature, and DO sensors exhibited high reversibility; however, the developed glucose sensor showed low reversibility. A high reversible detection of glucose could be achieved by using synthetic reversible receptors[235, 236]. The developed optical sensor has also demonstrated high sensitivity, high selectivity, fast response, good stability, and high accuracy for the measurement of the four target biomarkers. In this research, only one fibre channel was utilized to provide multiplexed monitoring, which largely reduced the complexity of the optical system and the costs. However, there are limitations associated with single channel fibre as well. The number of biomarkers to be measured is hard to extent due to the limited sensing area of the single channel fibre and the difficulty in the manually fabrication process. The alternation of light sources (broadband and 450 nm) for excitation of four sensors were manually controlled as two light sources were used in the study, which can be improved by adding wavelength division multiplexers or programmed light source switcher. In the study, AI-based models were first proposed and optimized to provide the brain biomarker concentration readout in real-time. Temperature and photobleaching were successfully compensated using AI models as the model learned the information directly from the training dataset. The training dataset is relatively small here and all datasets were obtained using buffer solution. More data can be included to fully test the model performance including with the presence of human blood. In the validation tests, the AI models were able to provide an accurate and robust prediction of the biomarker concentrations in a short computational time. In the *ex vivo* test using the lamb brain model, the optical fibre sensor successfully identified the changes in the 4 brain biomarkers in a short time. However, due to the sensors were fabricated on a soft silicone shaft, the signal may have large fluctuation when the sensor touches the brain tissue that needs to be optimized in the future. The multiplexed optical sensor has the potential to be extended to detect other biomarkers, including metabolites or neurotransmitters by selecting different indicators. The biocompatibility and cytotoxicity studies of the proposed sensing probe demonstrated a good biocompatibility and high potential for long-term insertion. For better in vivo applications, the silica-

based optical fibre that is used in this study can be further replaced by more bio-compatible and softer materials such as hydrogel fibres for better *in vivo* applications[237]. In addition, *in vivo* tests using living animals are needed to further assess the immunogenicity and foreign body response and test the ability of the fibre sensor for real-case applications.

This study demonstrated a good ability in dynamic monitoring of multiple physiological biomarkers using flexible intracranial optical fibre sensors to assess abrupt metabolic changes, which can continuously reflect the biomarker changes. The developed multiplexed optical fibre sensor can be potentially applied in medical diagnostics to offer new pathways for precise brain diagnosis and treatment.

Chapter 4 Optical Fibre Bundle Sensing System for Multiple Brain Biomarkers Measurement

To overcome the limitations shown in the previous single channel design, here, a multiplexed optical fibre bundle-based sensing system is presented for continuous and simultaneous monitoring of six brain CSF biomarkers through tip-functionalized optical fibres and computational algorithms. Compared with the previous design, the fibre bundled based sensing system is more versatile with the potential for tens or hundreds of biomarkers to be monitored simultaneously and much easier fabrication methods. The sensors are more robust to various environments. The developed minimally invasive fibre optic sensing system presents high reversibility, stability, sensitivity, and selectivity towards target biomarkers. Through monitoring brain metabolic and ionic dynamics, brain biomarker fluctuations following traumatic injury were accurately identified in *ex vivo* brain models. The findings underscore the enormous potential of the multiplexed optical fibre sensing system for brain physiologies monitoring.

4.1 Introduction

In the previous chapter, a multiplexed sensing system was proposed to continuously monitor 4 biomarkers by functionalizing different sensing probes on a single reflection optic fibre tip, however, it suffers from several limitations that may hinder the application in real life scenarios. Firstly, the sensing probe has large fibre dimensions (2 mm head, 8 mm body), which would lead to tissue damage when used on patients. Secondly, the fabrication relies on manually cutting the sensing films and placing them on a silica substrate, leading to low repeatability and difficulties in miniaturization. Therefore, it has limited sensing capacity (up to 4 biomarkers to be measured simultaneously). Furthermore, the previous sensing films are based on colorimetric spectra that have broad absorption peaks, leading to severe spectra cross interferences (**Figure 3-36, Figure 3-41**) and limited flexibility in biomarker selections[238]. Therefore, in this chapter, I will tackle these limitations by leveraging fluorescent sensing techniques, fibre bundle technology, and more advanced mathematical modeling for the accurate detection of 6 brain biomarkers.

Compared with colorimetric sensing techniques, fluorescent sensors have sharper emission peaks that are distinct from the excitation light source, reducing the likelihood of peak overlapping. Because of this, more biomarkers can be measured when a single spectrometer and light source are used. To further improve the fabrication procedure and increase the sensing capability, an optical fibre bundle is utilized as the substrate, where each sensor can be fabricated directly on a single fibre tip. Recently, micron-size optical fibre bundles have shown promise for minimally-invasive and distributed deep brain electrical wave recordings and multisite optogenetics, owing to the high flexibility and small sizes of the optical fibres[239, 240], indicating the potential of optical bundles in multiplexed and miniaturized brain biomarker monitoring. However, with the increasing number of biomarkers to be measured with the same laser light, emission peak overlapping maybe inevitable, thus, overcoming optical signal interferences among different optical fibre sensing signals remains a challenge in providing robust and reliable monitoring.

Therefore, in this chapter, I designed and investigated an optical fibre bundle-based sensing system to address the existing challenges in multiplexed dynamic monitoring of six brain biomarkers. Post-signal processing algorithms were implemented for precise and continuous monitoring of temperature (*T*), dissolved oxygen (DO), pH, sodium ions (Na^+), calcium ions (Ca^{2+}), and glucose, which are highly clinically relevant to brain physiologies and correlate with common TBI complications and stages (Section 2.2)[37, 241-245]. The proposed multiplexed optical fibre sensing system was applied to detect these six brain biomarkers simultaneously and continuously with total diameter less than 1 mm, providing a valuable tool for TBI diagnosis, monitoring and treatment. The optical fibre bundle sensing system was constructed by bundling seven single optical silica fibres, which was then integrated in a CSF drainage catheter. At the tips of the fibre bundle, 6 fluorescent sensing films as reversible optical transducers were functionalized to measure the corresponding 6 biomarkers selectively and continuously.

4.2 Design and construction of optical fibre bundle sensing system

In this chapter, an optical fibre bundle sensing system is proposed for achieving miniaturized sensing of multiple biomarkers simultaneously. A flexible silicone elastomer biofluid extraction catheter

(outer diameter: 2.5 mm, inner diameter: 1.3 mm) is incorporated with the sensing bundle to provide sufficient CSF for real-time and in situ monitoring of 6 biomarkers without causing extra brain damage and surgical procedures apart from the damage caused by the catheter (**Figure 4-1**). The integrated sensing catheter is designed to be inserted into the brain of TBI patients for multiplexed and dynamic brain monitoring (**Figure 4-1 (a,b)**) so as to protect the sensors from direct contact with brain tissue and potential background light noise and ensure a stable readout. The optical fibre sensing bundle system is built by bundling 7 optical fibre sensors, with one side of the fibres fixed, and the other sides inserted into the brain drainage catheter. 6 different fluorescent sensing films, produced by encapsulating fluorescent indicators in polymer films, are individually functionalized on the optical fibre tips (**Figure 4-1 (c)**). Brain CSF is extracted through the catheter holes, and 6 different brain biomarkers in the CSF sample are dynamically monitored via the optical fibre sensors inside the catheter (**Figure 4-1 (d)**). The changes in emission intensity of the fluorescent sensors while interacting with the target biomarkers are used to reflect the biomarker concentrations in CSF in a continuous and real-time manner (**Figure 4-1 (e)**).

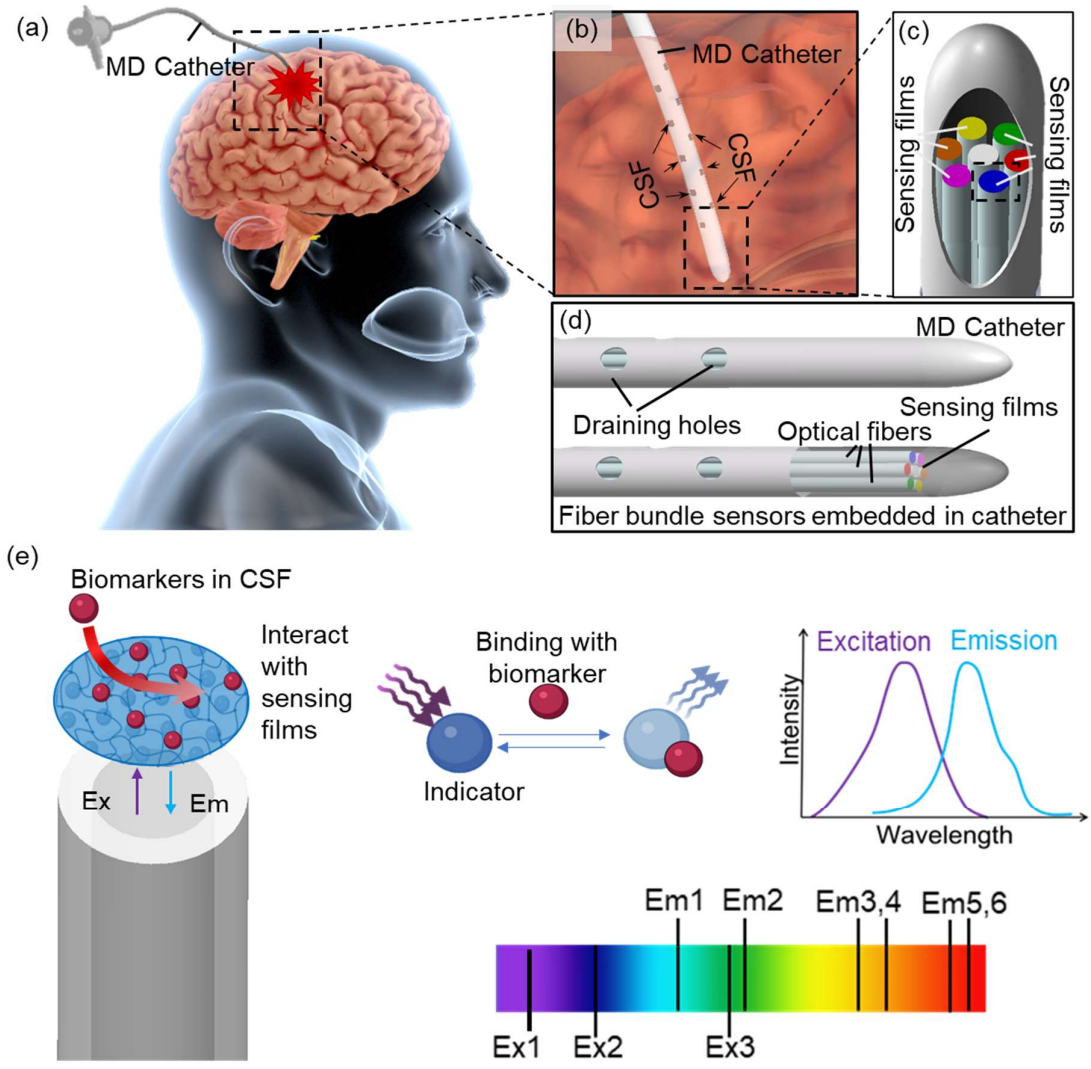


Figure 4-1. Schematic of the optical fibre bundle sensing system for multiplexed biomarker monitoring in brain CSF. (a) Schematic of the designed bundled optical fibre sensor integrated with brain catheter for multiplexed brain biomarker monitoring. (b) The designed bundle and the catheter are inserted into brain tissue for CSF collection and biomarker monitoring. (c) Zoom-in figure of the self-designed optical bundle with 6 fluorescent sensing films on the fibre tips inside the catheter. (d) skeleton view of the catheter and the fibre bundle. (e) Fluorescent probes encapsulated in polymer films on fibre tips for selective measurement of biomarkers. The fluorescent probes have either different excitation or emission wavelength.

Usually, for each optical fibre sensor, one spectrometer and one laser/LED are required for the measurement, and thus, 6 lasers and 6 spectrometers are needed for the monitoring of 6 biomarkers. However, in this design, to optimize the system, 6 optical fibre sensors were designed to have either different excitation or emission wavelengths and bundled together, reducing the requirement to only one spectrometer and one switchable multi-wavelength laser source for monitoring all 6 biomarkers. The connection between the sensor bundle, the laser light source, and the spectrometer was achieved

through an optical coupler (**Figure 4-2**). The multi-wavelength laser contains three different wavelength outputs (405 nm, 450 nm, and 520 nm), which can be manually controlled to excite the 6 fluorescent optical fibre sensors individually, with the corresponding emission spectra collected by the spectrometer under the excitation of different lasers. Signal processing algorithms are then applied to analyze the obtained spectra and output accurate and precise brain biomarker concentrations for clinical references. The developed optical sensing system is shown in **Figure 4-2 (a)**, where the optical sensing bundle is inserted in the medical catheter and the whole sensing system is light-weighted and easy to operate.

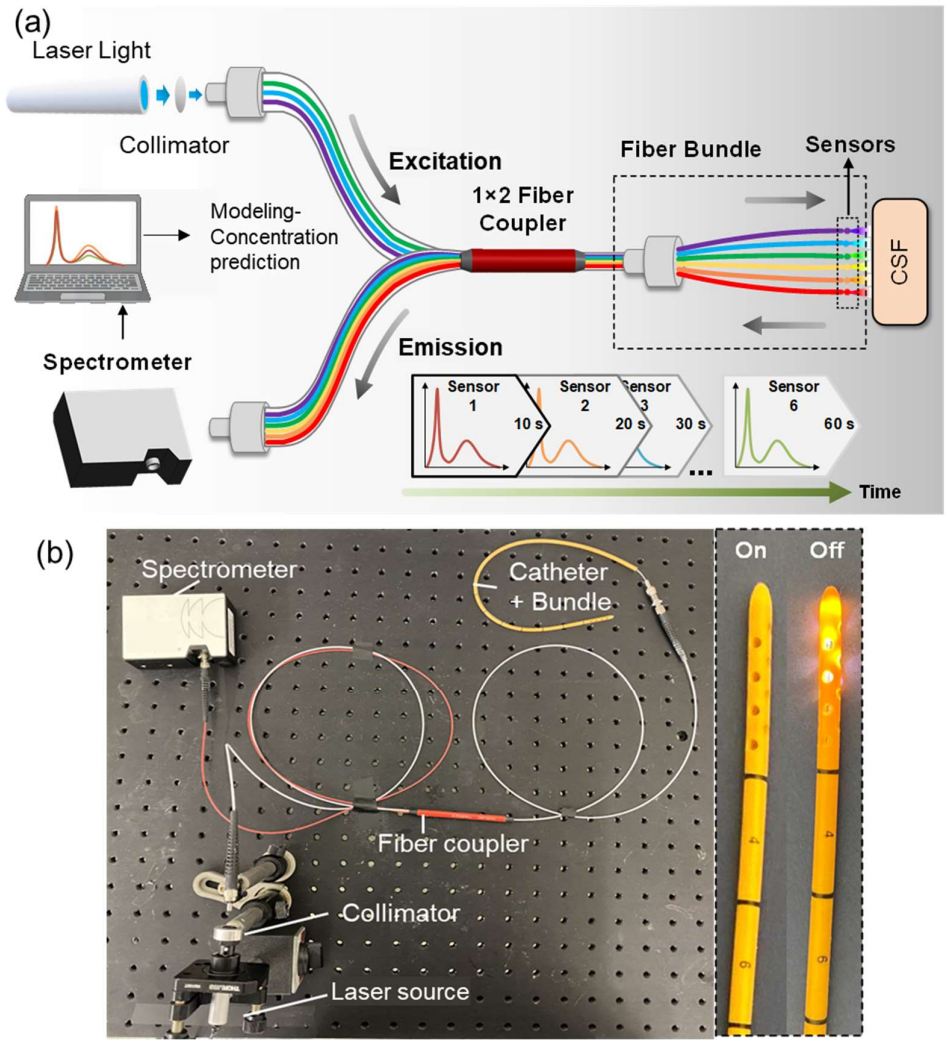


Figure 4-2. Schematic (a) and photograph (b) of the sensing system setup.

In order to maximize the utility of the excitation laser source, enhance transmission efficiency, and minimize the overall dimensions of the sensor bundle, I designed the structure and dimension details for the fabrication of the optical fibre bundle. I have 6 sensors designed using the system, therefore, at least 6 fibres need to be bundled together. However, I bundled one extra fibre in the system for potential signal enhancement and expansion. To ensure a large sensing area for a higher signal to noise ratio, core/cladding diameter of 105/125 μm was selected for the 7 optical fibre (silica, multimode fibre,) and the fibres are bundled together and evenly distributed in a subminiature version A (SMA) connector (380 μm bore size) to ensure equivalent light transmission. The fabrication process of the bundle included 5 steps: fibre tip stripping; fibre fixing into a connector; fibre tip cutting; fibre polishing; and fibre securing (**Figure 4-3 (a)**.

The detailed fabrication process involved the following steps: 1. Optical fibres were stripped to a length of 1 mm and cleaned with ethanol. The fibre connector was soaked in ethanol and placed on a clean, dry surface for cleaning. 2. Epoxy was injected into the connector using a syringe until a small bead appeared on the connector ferrule's outer face. 3. Seven prepared optical fibres were inserted into the connector, and epoxy was applied at the contact area between the connector end and a furcation tubing. The epoxy was left to dry overnight for stability and the fibres were cut using a fibre scribe, ensuring the fibre length above the epoxy was less than 1 mm. 4. The polishing disc and connector were cleaned, and the connector was inserted into the polishing disc. Fibre tips were polished using 1 μm, 3 μm, and 5 μm aluminum oxide polishing film, with gradual pressure increase to maintain light contact between fibres and film. 5. A strain relief boot was placed on the connector for protection, and epoxy was applied to secure the boot. Finally, the polished fibre end faces were inspected using a microscope for preliminary quality assessment. Micrographs of the optical fibre bundles in the SMA connector demonstrate 7 smooth end faces of the optical fibre bundles, facilitating high-quality transmission of the optical signals (**Figure 4-3 (b)**). Minor inconsistency in the detected intensities might be attributed to differences in mode distributions among these 7 multimode optical fibres. Because the bundle is designed as substrate for fluorescent sensors, I tested the bundle and its efficiency in transmitting both excitation light and emission light using fluorescein

solution to provide emission signals for transmission testing. In the experiment, the bundle was inserted to fluorescein solution and excited with 450 nm laser light, the other arm of the coupler was connected to a spectrometer. It is shown that all the bundled optical fibres successfully delivered the laser light to the solution and detected the emission signal by transmitting the emission light to the spectrometer with equivalent intensities (**Figure 4-3 (c)**).

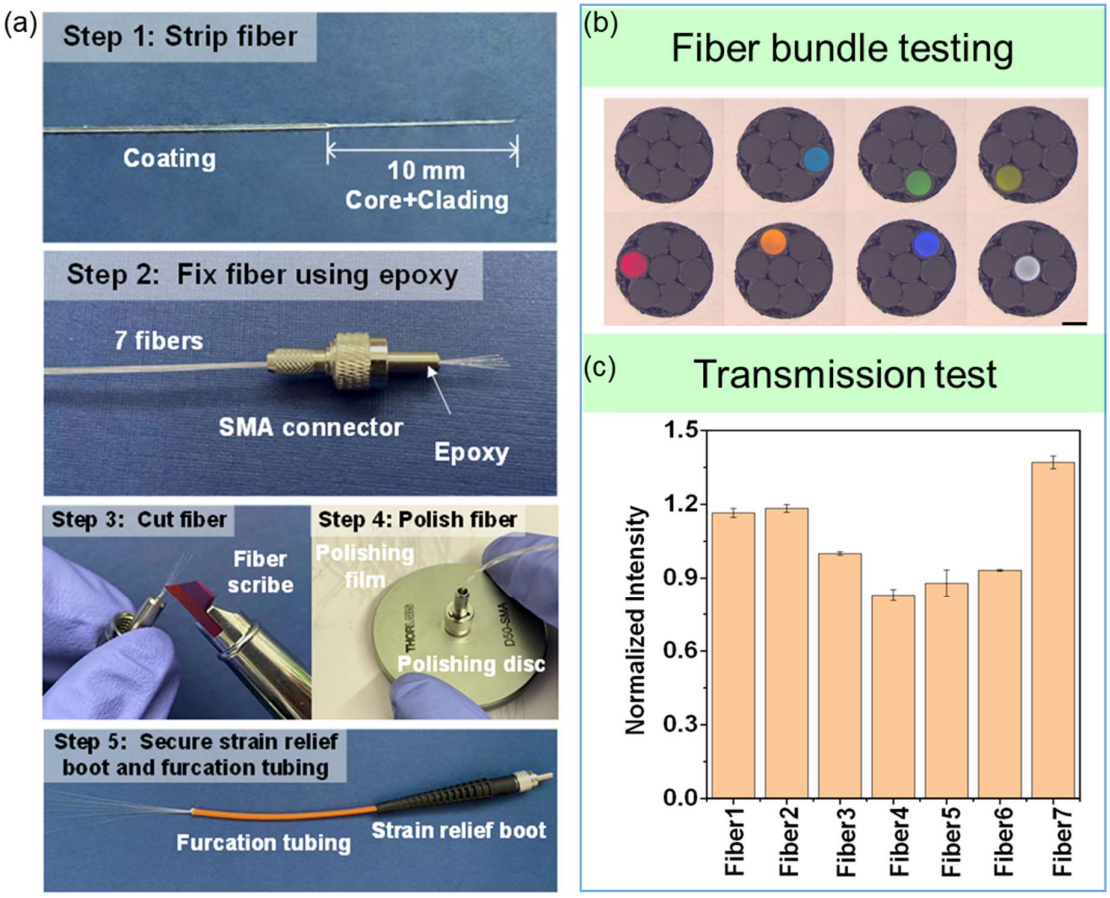


Figure 4-3. Optical fibre bundle manufacturing and testing. (a) The fabrication process of the fibre bundle in 5 steps: fibre stripping, fibre fixing, fibre scribing, fibre polishing, and fibre securing. Scale bar: 1 cm. (b) Micrograph of the end faces of the bundle with 7 optical fibres. Scale bar: 100 μm. (c) Transmission test of the 7 individual fibres in the bundle.

The optical fibre bundle sensors were further treated to functionalize the fibre tips with fluorescent films through dip-coating approach using fluorescein dye. The sensing performances of the system can be optimized by tailoring the dip coating speed and film thickness (coating layer numbers). A faster coating speed or coating multiple layers lead to thicker sensing film layer, and thus, a stronger fluorescent sensing signal is obtained but slower sensing response (**Figure 4-4 (a,b)**) due to the time

needed for the biomarker to diffuse freely into the film and react with the probes. The designed 6 optical sensors were then characterized for their sensing performance individually and when used for multiplexed sensing. The microscope images of the different fluorescent films indicate the bundle successfully delivered excitation light to the fibre tips to excite the fluorescent films (**Figure 4-4 (c)**).

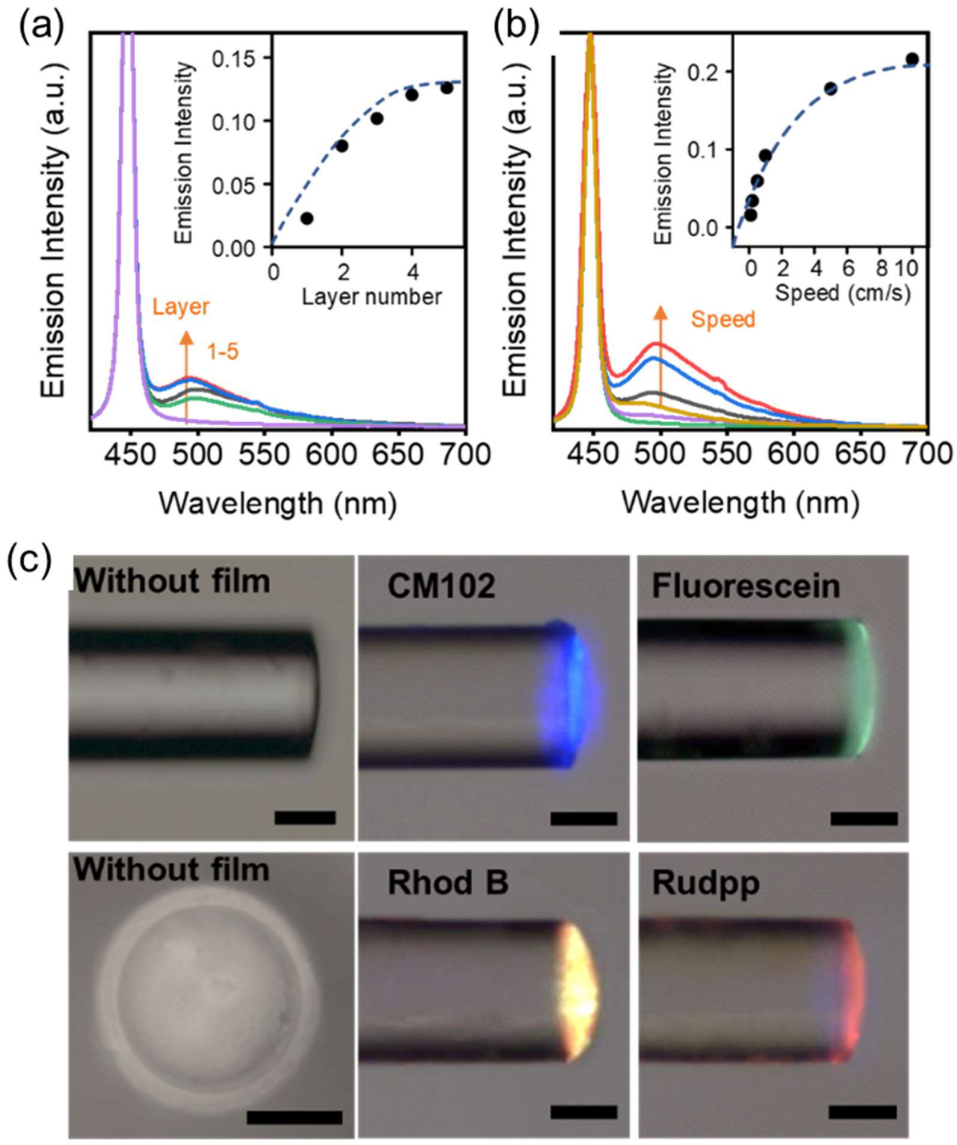


Figure 4-4. Optimization of dip coating speed and layers. (a) Fluorescent emission spectra with different coating layers. Inset: Correlation between dip coating layer numbers and film intensity. (b) Fluorescent emission spectra under different coating speed. Inset: Correlation between dip coating speed and film intensity. (c) Fluorescent film coatings on fibre tips. Scale bar= 50 µm.

4.3 Design of the 6 biomarker sensing films

Another sensing system is proposed for the same purpose that is for multiplexed and continuous brain monitoring. Different from the system introduced in Chapter 3, this system is based on the fluorescent sensing mechanism using fibre bundles. Using this system, the number of biomarkers to be monitored is increased from 4 to 6 with the potential for further extension, the performance is improved, and the total dimension is reduced. Here, six fluorescent based optical fibre sensors are explored for the measurement of brain pH, temperature, DO, Na^+, Ca^{2+}, and glucose levels. In this subsection, the design and selection principles for the six sensors are introduced. The fabrication details, characterisation, multiplexing, and system development are introduced in subsection 4.4.

In order to measure 6 biomarkers simultaneously, the selection of fluorescent sensing probes is of vital importance. There are several criteria for selecting the optimal fluorescent sensing probes for each sensor:

1. Normally fluorescent probes consist of a recognition element that selectively reacts with the target biomarker, including both physical interaction or chemical reaction, and a fluorescent label whose optical property changes with the interaction [246, 247]. In order to achieve long term continuous monitoring, the reaction between the receptor and the biomarker needs to be fully reversible, meaning that both increase and decrease in the biomarker concentration can be detected and thus the reaction needs to be reversible based on the biomarker concentration fluctuations. In this step, many probes were ruled out due to the irreversible reaction.
2. The recognition element of the probe should have a dissociation constant (Kd) that covers the physiological ranges [246, 247]. Many commonly used fluorescent probes may not be suitable for the designed study due to a larger or smaller Kd that causes insufficient sensitivity in measuring the target biomarker. For example, one of the commonly used fluorescent probes is sodium green, which has a Kd of 6 mM, meaning that it is less sensitive to detect Na^+ with concentration at physiological ranges (140 mM). The same applies to other biomarker probes.

3. The fluorescent probe should have high selectivity towards the target biomarker that does not react with other chemicals that coexist in brain CSF. Use the same example of sodium green, it is not only sensitive to Na^+ but also sensitive to K^+ due to similar chemical structures of these two ions, however, considering that K^+ is also a major ion in brain CSF, it is necessary to find a fluorescent probe that could distinguish Na^+ from K^+. Many fluorescent probes may be affected by the environment temperature and pH values, and further test needs to be done to measure the impact on physiological pH and temperature ranges. However, the pH and temperature influence can be corrected using the pH and temperature sensor's readout.
4. Due to the purpose of the project being to measure several biomarkers at the same time based on fluorescent sensing techniques, the fluorescent probes for different sensors should have distinct emission or excitation maximums to ensure that they can be separated from the mixed optical spectrum. Considering that all of the fluorescent emission peaks have some width that span a few nm, it is better to have the sensors' emission peaks distinct from each other as much as possible to avoid overlapping.
5. The fluorescent probe should have a high quantum yield as the sensing area equals the fibre core size and is limited to 100 μm. A high quantum yield ensures a high fluorescent intensity that is measurable with a high signal to noise ratio using a not too expensive and portable spectrometer.

When finding the optimal fluorescent probes for pH, temperature, DO, Na^+, Ca^{2+}, and glucose, Na^+ and Ca^{2+} probes are the hardest to find as there are more options for the other biomarkers. Therefore, I first decided on the probes for Na^+ and Ca^{2+} through market search and literature. I found the following fluorescent probes for the designed system. The fluorescent probes are ensured to be sensitive to the target biomarkers at concentration within physiological ranges. However, due to the limited choices of visible range fluorophore labels, it was hard to find 6 fluorophores that could be excited with the same laser light, have distinct emission spectra, and can bind with biomarker receptors for ideal optical changes.

Table 4-1. Commercially available fluorescent probes for Ca2+ and Na+ detection [246, 247].

Indicator	Ex	Em	Sensitivity	Kd
Calcium ion sensor indicator/probe selection				
Fura-2	340/380 nm	405/485 nm	very limited to concentrations above 1 μM	50 μM
Fluo-5F Fluo-4FF Fluo-5N	488 nm	520 nm	The fluorescence intensity increase on Ca^{2+} binding is typically >100-fold	2.3 μM - 90 μM
Calcium Green™-1	506 nm	531 nm	Like Fluo-4	14 μM
Rhod-2	552 nm	578 nm	Fluorescence intensity increase upon binding Ca^{2+}: >100 fold	570 nM
Rhod-3	550 nm	580 nm	Rhod-3 exhibits a large increase (>2.5 fold) in fluorescence upon binding Ca^{2+}	570 nM
Rhod-5N	551 nm	576 nm	Fluorescence intensity increase upon binding Ca^{2+}: >100 fold 0.02–0.05 mM	320 μM
Sodium ion sensor indicator/probe selection				
SBFI	340,380 nm	500 nm	Little emission maximum change	3.8 mM
Sodium Green™	492 nm	520 nm	15.6 mM	6 mM
CoroNa™ Green	492 nm	516 nm	Better than Sodium Green	80 mM

Therefore, CoroNa™ Green and Rhod-5N were selected for Na^+ and Ca^{2+} sensing, based on the criteria. After determining these two sensors, I selected the rest sensor probes for pH, temperature, DO, and glucose measurements. The measurement of glucose is based on the consumption of oxygen in the redox reaction of glucose; therefore, two oxygen probes are selected.

Table 4-2. Selected fluorescent probes for the 6 target biomarkers.

	Probe	Ex/Em
pH	HCC	380 nm/450 nm
Temperature	Rudpy	470 nm/600 nm
DO	PdOEP	405 nm/660 nm
Glucose	PtOEP	405 nm/640 nm

After deciding the fluorescent probes for the biomarkers, I fabricated the sensors by encapsulating the probes in different matrices according to the probe physical properties. The matrices were designed using polymer techniques, including sol-gel, polymer, and hydrogel techniques with tailored porosity to ensure the optimal environment for the probe. The probe concentration was also optimized for each sensor to ensure a good signal to noise ratio. The detailed fabrication methods are elaborated in the following sections.

4.4 Materials and Methods

Following the design of the optical bundle and the sensing films, the details for the fabrication are introduced here. The results for the following experiments are included in section 4.5-4.7. All tests were repeated 3 times. If the standard deviation was greater than 30% of the value, then another repeat was conducted.

4.4.1 Materials and equipment

Materials: Tris(2,2'-bipyridyl)dichlororuthenium(II) hexahydrate ($Ru(bpy)_3$, 99.95%), 1,4-Bis(2,3-epoxypropoxy)butane, 2,2'-[(1-methylethylidene)bis(4,1-phenyleneoxymethylene)]bisoxirane, 7-Hydroxycoumarin-3-carboxylic acid (HCC, 98%), 2,3,7,8,12,13,17,18-Octaethyl-21H,23H-porphine palladium(II) (PdOEP, 85%), Tetraethyl orthosilicate (TEOS, 98%), (3-Glycidyloxypropyl)trimethoxysilane (GLYMO, 98%), 3-(trimethoxysilyl)propylmethacrylate, Dimethyl sulfoxide (DMSO, 99%), Acetone (99.9%), Poly(ethylene glycol) diacrylate (PEGDA Mn700), Tetrahydrofuran (THF, 99%), Acrylamide, N,N'-Methylenebisacrylamide (MBA), Glucose oxidase, Platinum octaethylporphyrin (PtOEP, 95%), Tris base (99%), Tris hydrochloride (99%),

Phosphate buffered saline, sodium chloride (NaCl) (99.5%), calcium chloride (CaCl2) (93%), potassium chloride (KCl) (99%), magnesium chloride (MgCl2) (98%), zinc chloride (ZnCl2) (98%), sodium phosphate dibasic (Na2HPO4) (99%), sodium phosphate monobasic (NaH2PO4) (99%), copper(II) chloride (CuCl2) (93%), D-(+)-glucose (99.5%), L-ascorbic acid (99%), uric acid (99%), sodium nitrite (NaNO2) (97%), albumin from porcine serum (98%), hydrochloric acid (HCl) (37%), Ammonium persulfate (98%), N,N,N′,N′-Tetramethylethylenediamine (99.5%), nitric acid (HNO3) (70%), sodium hydroxide (NaOH) (97%), 5-hydroxyindole-3-acetic acid (98%), and ethanol (99%) were purchased from Sigma-Aldrich. SYLGARD™ 184 Silicone Elastomer was purchased from Dow. Sodium L-lactate (98%), sodium pyruvate (99%), and dopamine hydrochloride (99%) were purchased from Alfa Aesar. CoroNa Green and Rhod-5n were purchased from Invitrogen™. Human CSF was obtained from St. Marry's Hospital. All chemicals were reagent grade and used as received without further purification.

Equipment: For the fiber bundle fabrication, the following items were purchased from Thorlabs: LF5P-5 µm Grit Silicon Carbide Lapping (Polishing) Sheets, LF3P-3 µm Grit Aluminum Oxide Lapping (Polishing) Sheets, LF1P-1 µm Grit Aluminum Oxide Lapping (Polishing) Sheets, D50-SMA - SMA Connector Polishing Dis, FTS4- Three-Hole Stripping Tool, S90R- Ruby DualScribe Fiber Optic Scribe, FG105UCA-Multimode Fiber, Ø105 µm Core, 10380A-Standard SMA905 Multimode Connector, Ø380 µm Bore, and TT400R5S1B - 1x2 Multimode Fiber Optic Coupler, Low OH, Ø400 µm Core, 0.39 NA, 50:50 Split. FLAME-S-VIS-NIR-ES spectrometer assembly (350–1,000 nm) (Ocean Insight) was used to acquire the fluorescent spectrum. Collimated laser diode modules including 405nm, 4.5mW (CPS405), 450 nm, 4.5 mW (CPS450), and 520 nm (4.5 mW) diodes were purchased from Thorlabs for film excitation. A multiwavelength laser (405nm, 488 nm, 520 nm) was purchased from Integrated Optics for automated system development. Microplate reader (Thermo Scientific Skanlt) was also used for sensing probe characterisation. The micrographs were obtained by an upright microscope for polarization (DM2700 P; Leica). A hotplate stirrer (Fisherbrand Isotemp) was used to homogenize the sol-gel precursor solutions and control the temperature of the buffer solutions during experiments. A pH meter (FiveEasy F20; Mettler Toledo) was used to measure the

pH value. An oxygen benchtop meter (HI-2004 Edge; Hanna Instruments) was used as a golden standard to prepare DO buffer solutions. The obtained spectra obtained during the experiment were analysed offline using Python code. Ocean View 2.0 and Thermo Scientific Skanlt were used as the software to analyze data from the spectrometer and the microplate reader, respectively. iPhone 11 camera was used to capture the photographs and all photos were taken with the same white balance and exposure settings. Brain cerebrospinal fluid drainage catheter was purchased from Codman Bactiseal. A touchscreen was purchased from Waveshare for user interface.

4.4.2 Sensor Fabrication

a. Temperature sensor. Temperature sensor uses the fluorescent probe $Ru(bpy)_3$. The probe is also sensitive to oxygen as it has been used as oxygen sensors. It measures temperature based on the temperature quenching effect which is a physical reaction that does not require direct contact between the probe with the solution. Therefore, to reduce oxygen impact, I used epoxy as the matrix for the encapsulation of the probe as epoxy has low air/oxygen/water permeability (2-10 cc/m^2 per 24 h). The temperature sensor was fabricated by encapsulating $Ru(bpy)_3$ in epoxy polymer. To fabricate it, 0.5 mL of 1 $mmol \cdot L^{-1}$ $Ru(bpy)_3$ was first prepared by dissolving 0.5 mmol $Ru(bpy)_3$ in 0.5 mL pure ethanol and thoroughly mixed with same volume of epoxy resin. Then the mixture was placed on the hotplate at 80 °C for 1 h to remove the ethanol. After that, the epoxy hardener was added to the above mixture in the ratio of 1 (hardener) to 2 (epoxy resin). Dip coating (1cm/s) was then performed to coat the film on the tip of the fibre coupler and the film was cured at room temperature for 72 h. The fibre sensor was washed with pure DI water for several minutes before use.

b. DO sensor. PdOEP was decided for the DO sensor. PdOEP has been widely encapsulated in PDMS as DO sensors due to the great oxygen permeability and low water permeability of PDMS, creating a great environment for the fluorescent probe. Therefore, here I also used PDMS as the encapsulation matrix for the probe following the fabrication steps described in [248]. For the fabrication of PDMS-PdOEP sensing film, 20 mg of pre-polymer (Sylgard 184) was mixed with 2 mg of curing agent with a spatula. The mixture was fully mixed until the formation of a homogeneous and transparent solution. The indicator PdOEP was dissolved in THF with a concentration of 1 mmol L^{-1} for a total

volume of 500 μL. The PDMS mixture was then added to the PdOEP/THF solution and stirred for several minutes until fully mixed. Gas was removed from the mixture using a vacuum. Dip coating was then performed with the prepared solution. The film was left to dry and cure at 80 °C for 3 h.

c. pH sensor. HCC was selected for pH sensing. The maximum excitation wavelength for HCC shifts from 342 nm to 384 nm with pH increasing from 4 to 9 [36]. In this study, 405 nm was used for HCC excitation, therefore, an increase in the emission peak at 450 nm was expected for pH measurement from 6 to 8. Sol gel method was used for HCC encapsulation due to its good permeability for ions, high porosity, and nano-scale pore sizes. The fabrication formula was referenced to the sol-gel matrix in the previous chapter (Section 3.3.3). The probe concentration from 0.001-10 mM diluted using ethanol was first optimized to obtain the maximum intensity. To be specific, 1 mg HCC was dissolved in 1mL ethanol. Then, 40 μL TEOS, 10 μL GLYMO, 100 μL 1mM HCC solution, 20 μL 0.1 mol L^{-1} HCl and 10 μL DI water were mixed and stirred thoroughly for 1 hour to obtain homogenized sol-gel solutions. The mixture was subsequently aged at room temperature for 1 h before coating. Dip coating was performed and left for 3 days for fully gelation.

d. Sodium sensor.

Fabrication: 1 mg CoroNa Green was dissolved in 1.7 mL DMSO to obtain 1 mmol L^{-1} stock solutions.

Probe concentration optimization: Probe concentration varying from 0.04-0.2 mmol·L^{-1} were prepared by diluting the stock solution. 20 μL of the diluted probe DMSO solutions were added to microplate wells and further mixed with 20 μL of 100 mmol·L^{-1} sodium tris buffer (pH=7.4) to yield 0.02-0.1 mmol·L^{-1} sodium probe concentration. Fluorescence spectra under 480 nm excitation were obtained to determine optimal probe concentration, which was then used for sodium sensor fabrication.

The fabricate the PEGDA film followed the method proposed in Reference 182 and 249: 156.5 μL of PEGDA and 10.6 mg of AM were mixed with 2-HMPP (2%, v/v) in DI water with a ratio of 1:2(v/v). Stock solution (1 mmol·L^{-1} CoroNa Green in DMSO) was also added with the amount to result in the

optimized probe concentration. The solution was then dip-coated on the fibre tip and placed under UV light for 3 min.

e. Calcium sensor.

Rhod-5N was used as the Calcium sensor probe. The measurement was based on the crown ether BAPTA in the sensing probe that selectively binds with calcium ion and upon binding, the emission intensity increases proportionally. PolyAcrylamide (polyAM) was selected as the calcium encapsulation matrix. The reason why I chose polyAM over polyPEGDA used for sodium ion sensor is because that poly-PEG has been used as Ca^{2+} receptor and may stop Ca^{2+} from entering the matrix and bind with the fluorescent probes [250]. Due to the calcium sensor is water soluble, the formulation of the PolyAM film was further optimized to reduce the leaching of the calcium probe while ensuring a fast response.

Fabrication: 0.5 mg calcium fluorescence probe Rhod-5N was dissolved in 0.556 mL DI water to obtain 1 mmol L^{-1} stock solutions.

Probe concentration optimization: I designed the calcium sensor's matrix fabrication formulation according to reference 251. Probe concentration varying from 0.04-0.2 mmol·L^{-1} with increments of 0.02 mmol·L^{-1} were prepared by diluting the stock solution. 20 µL of the diluted probe solution were added to microplate wells and further mixed with 20 µL of 1 mmol·L^{-1} calcium tris buffer (pH=7.4) to results 0.02-0.1 mmol·L^{-1} calcium probe concentration. The fluorescence intensity at 580 nm excited with 520 nm light were obtained to find the optimal probe concentration.

Polyacrylamide (PolyAM) hydrogel optimization: PolyAM films with different monomer concentration (w/v%: 25-40%) and crosslinker concentration (w/v% 0-10%) were fabricated and the leaching of the film after 3 days was used to tailor the monomer and crosslinker concentrations.

The optimized polymerization solution consisted of 350 mg acrylamide (35.0% w/v), 20 µL DMSO dissolved (20% w/v) N,N-methylenebis(acrylamide), and 980 µL DI water. Fluorescent probe Rhod-5N stock solution was then added to the polymerization solution to obtain the optimized indicator

concentration. The polymerization was initiated with 24 μL of a 10% ammonium persulfate solution and 12 μL of N,N,N‘,N‘-tetramethylethylenediamine (TEMED), and the solution was stirred at room temperature until well mixed. Dip coating was performed and was left for polymerization in fume hood for 1 hour.

f. Glucose sensor. The glucose sensor structure contains two layers. The top layer is a polyacrylamide-based glucose oxidase layer for glucose oxidation following the same formulation of the Na^+ sensor. The bottom layer is a sol-gel based oxygen sensing layer and was coated on the fibre tip. The sol-gel based oxygen sensing layer was fabricated by mixing 0.46 mL TEOS, 0.04 mL GLYMO, 0.6 mL ethanol, 0.2 mL DI, 8 mg PtOEP and 0.2 mL of HCl (0.1 mol L^{-1}) together and stirring thoroughly for 1 hour to obtain homogenized sol-gel coating solutions according to Section 3.3.4. The sol gel solution was then dip coated to the fibre tip and aged under room temperature to form a clear and homogenous sol-gel oxygen sensing film. The top layer coating solution was prepared by mixing 50 μL 4 mmol L^{-1} glucose oxidase PBS solution with hydrogel precursor solution, prepared by 37.7% (w/v) acrylamide, 15 μL DMSO dissolved (20% w/v) N,N-methylenebis(acrylamide) and 2 μL 2-HMPP in DI water. After coating the top layer on the first layer, the film was polymerized under UV light for 3 min.

4.4.3 Sensing film coating methods

Fibre tip silanization:

In order to ensure the sensing films coated on the fibre tips stably, the fibre tips were salinized before sensing film coating to active the -OH group due to that most sensing matrices are hydrophilic except PDMS-PdOEP. The fibre tips were salinized in a solution of 3-(trimethoxysilyl)propylmethacrylate in acetone at a ratio of 1:50 (v/v) overnight. Once salinization was completed, the fibres were wiped clean and stored in dark.

Film coating method optimization:

Before fabricating sensing films on the fibre tips, coating methods were optimized to obtain the optimal fluorescent signals. The experiment was conducted using sol-gel fluorescent pre-gel solutions and dip coating method were used and optimized for film coating.

Sol-gel solution preparation:

Sol-gel precursor solutions were prepared by mixing 0.46 mL TEOS, 0.04 mL GLYMO, 0.6 mL ethanol, 0.2 mL DI, 8 mg dye or probe, and 0.2 mL of HCl (0.1 mol L^{-1}) and were stirred thoroughly for 1 hour to obtain homogenized sol-gel coating solutions. The mixture was subsequently aged at room temperature for 1 h before coating. Coating optimization was conducted using one 60 μm core pigtail fibre after the fibre tips were stripped, cleaved, and salinized before coating. The thickness of the films was tailored from 5-40 μm by using different coating speed or layer numbers.

Optimization 1: Dip coating speed

To achieve precisely controlled speed, a pump was used to facilitate the dip coating process. One side of the fibre was tied to the pump and the speed was controlled using the pump. 0.1 cm/s, 0.5 cm/s, 1 cm/s, 5 cm/s, 10 cm/s coating speeds were used for dip coating. After coating, the film was air dried for 1 hour before signal measurement. Transmission of the film (optical density) was analysed using a spectrometer to determine the best coating speed.

Optimization 2: Layer numbers

Layer numbers are directly related to coating thickness. The smallest coating speed was used for the dip coating of each layer. The layers were dried in air for 1 h before coating the next layer. 1-5 layers were coated and studied to find the correlation between the film intensity and layer numbers. Transmission of the film (optical density) was analysed using a spectrometer to determine the coating layers.

4.4.4 Sensor characterisation

Basic sensor characteristics were measured here to evaluate the performance of the sensors, including sensitivity, selectivity, reversibility, stability and environmental dependences. Physical properties

including thickness morphology were examined as well for all six sensors. The sensors were characterized within the physiological ranges especially for patients with TBI. To be specific, the details for the evaluation are as follows, a summary of the characterisation methods is in **Table 4-3.**

Temperature sensor

Calibration: The temperature sensor was characterized using 50 mL of pH 7.4 PBS solutions, which was heated incrementally from 33 to 42 ℃. The sensor was placed in the solution and excited with a 450 nm laser light source through a fibre coupler. The spectrum at each temperature was recorded, and the correlation between the solution temperature and 600 nm intensity was analysed.

Reversibility: The temperature sensor was used repeatedly to measure a 36 ℃ PBS solution and a 40 ℃ PBS solution with the same pH for 10 repetitions, recording the intensity at 600 nm each time.

Photostability: The sensor was excited continuously for 3 hours in a 36 ℃ PBS solution, and the excitation intensity at 600 nm was continuously recorded for stability test.

pH dependence: The pH dependence test was performed by immersing the sensor in pH-varied (6.0, 6.4, 6.8, 7.2, 7.6, 8.0) 36 ℃ PBS solutions, and the emission intensity at 600 nm wavelength was analysed for its responses to same temperature solutions with different pH values.

Pressure dependence: The optical fibre sensor was submerged to 36 ℃ PBSbuffer solution at different depths (0–30 cm) to simulate human physiological pressure ranges according to the equation:

$$Pressure = \rho * g * h \quad \textbf{(Eq. 4-1)}$$

, where ρ refers to the buffer solution's density (approximately 1 g/cm^3), g is gravity, and h represents depth. Correlation between dipping depths and 600 nm emission intensity was analysed.

Selectivity: Sensor selectivity was tested for cross-sensitivity to major brain CSF biomarkers. PBS solutions containing major interferent biomarkers were prepared at specific concentrations (**Table 3-2**). The sensor was then dipped into these solutions and the intensity at 600 nm was recorded for further analysis.

Leaching test: In the leaching test, the sensor was immersed in PBS solution for 3 days and the intensity at 600 nm in 25 ℃ PBS solution was measured every 24 hours.

DO sensor

DO sensor calibration: The DO sensor was characterized by mixing different proportions of 0% DO buffer solution (0 mgL^{-1}) and 100% saturated DO buffer solution to create solutions with varying degrees of oxygenation as introduced in 3.3.5, **Figure 3-4**. In this study, a benchtop oxygen meter was used as the reference to measure DO values. The 100% DO buffer solution was prepared by continuously pumping concentrated air into pH 7.4 PBS solution until stabilization, while the 0% DO buffer solution involved pumping nitrogen gas until the DO reaches to 0. A three-neck flak was used for sensor characterisation, where one neck for benchtop oxygen meter probe, one neck for the proposed oxygen sensing fibre, and the third neck for altering DO concentrations using 0% or 100% DO solutions. The same optical measurement system was employed with 405 nm laser excitation and 660 nm emission intensity analysis.

During experiment, DO buffer solution from 0 mg/L to 8 mg/L was prepared by adding 100% DO solution to 0 mg/L DO solution gradually. The spectrum under each DO level after stabilized was captured and used for sensitivity analysis.

Reversibility: Similar to the temperature sensor, the DO sensor's reversibility test involved dipping the sensing fibre between 0 and 8 mg/L DO buffer solutions, and emission intensity at 660 nm was recorded.

Photostability: Photostability test was carried out by exposing the DO fibre sensor to continuous 405 nm laser light for 3 hours in 100% DO (8mg/L) PBS solution. The intensity at 660 nm was measured continuously through this test.

Pressure dependence: Pressure dependence test was carried out in the same way as the pressure dependence test for the temperature sensor, using 100% DO saturated solution.

pH dependence: The same protocol for pH dependence test was conducted for the DO sensor as for the temperature sensor, with 100% DO saturated solution.

Temperature dependence: The temperature dependence was conducted by placing the sensing probe in 100% DO saturated solution with increasing temperature from 25-45 °C. The intensity of 660 nm at each temperature was recorded.

Leaching: The sensor was immersed in a PBS solution for four days, and the intensity at 660 nm was measured every 24 hours to calculate the leaching percentage.

Selectivity: PBS solutions with various interferents were used for the test, and the interferent concentrations are listed in **Table 3-2**. After dissolving the interferents into PBS buffer solutions, N_2 gas was bubbled to make 0% DO solutions. 100% DO solution was used to test the sensor for DO measurement.

pH sensor

pH sensor was characterized using the same way as for the other sensors. 405 nm laser was used for the sensor excitation and the intensity at 450 nm was analysed.

Sensitivity: pH 6.0, 6.4, 6.8, 7.2, 7.6, 8.0 gradient buffer solutions were prepared using NaOH and HCl adjusted PBS solutions for the evaluation of the pH sensor sensitivity.

Reversibility: pH 6 and pH 8 PBS solutions were used for the analysis of the sensor's reversibility. The procedure was the same as for the other sensors.

Photostability: The sensor was exposed continuously to 405 nm laser source (4.5 mw) in pH 7.4 PBS solution for 3 hours and the intensity at 450 nm was measured every 30 min.

Temperature dependence: The temperature dependence was tested using pH 6.8, pH 7.2 and pH 7.6 PBS solution. The temperature of the solution was heated to 35°C-41°C with an increment of 1 °C. The intensity at 450 nm was measured and correlated to the temperature.

Pressure dependence: The pressure dependence was performed using pH 7.4 PBS solution and measured using the same methods as for the other sensors.

Selectivity: In the selectivity test, each interferent was added to a glass of 300 mL pH 7.4 PBS solution and the solution was adjusted to pH 7.4 before testing. The pH sensor was dipped into the solutions and the intensity at 450 nm was recorded (**Table 3-2**).

Sodium ion sensor

Sodium sensor characterisation: The sodium sensor was characterized using 150 mmol L^{-1} pH 7.4 tris buffer. A 450 nm laser light was applied to the sensing film, and emission intensity at 540 nm was used for characterisation.

Sensitivity: Tris buffer solutions with sodium concentration ranging from 0-200 mmol L^{-1} at 40 mmol L^{-1} increments were prepared and used. The solution was continuously stirred during measurement. Intensity at 540 nm was measured when the sensor was in each buffer and the correlation between intensity and sodium concentration was calculated.

Reversibility: The reversibility test for the sodium sensor was performed using 40 mmol L^{-1} and 140 mmol L^{-1} sodium tris buffer. The procedure was the same as for the other sensors.

Photostability: The sodium sensor was exposed to a 450 nm laser for 2 continuous hours in 140 mmol L^{-1} [Na^+] tris buffer solution. The intensity at 540 nm was measured every 20 minutes. The sensor stabilized after 2 hours.

Pressure dependence: The pressure dependence was performed using 140 mmol L^{-1} [Na^+] buffer solution following the method used for other sensors.

Temperature dependence: The sensor was used to measure sodium free and 100 mmol L^{-1} sodium tris buffer with temperature heated from 36 – 40 °C using a hotplate.

pH dependence: Sodium free and 100 mmol L^{-1} [Na^{+}] tris buffer solution with pH ranging from 6-8 were prepare for the pH dependence test. The sensor was placed in these varied sodium buffer solutions and the emission intensity at 540 nm was recorded for each buffer.

Selectivity: Interferent buffer solutions were prepared with 200 mmol L^{-1} tris buffer. To maintain the same ionic strength in tests for other ions, the same ion concentrations (200 mmol L^{-1}) were added to the tris buffer solution. For metabolites, concentrations were as in **Table 3-2**. Sensor emission intensity when measuring these buffer solutions was recorded and normalized to the blank solution (pure tris buffer).

Calcium ion sensor

Same as sodium sensor, calcium sensor was also characterized using 150 mmol L^{-1} tris buffer. A 520 nm laser was used for the excitation of the sensing film.

Sensitivity: Calcium tris buffer solutions were prepared by dissolving $CaCl_2$ into 150 mmol L^{-1} tris buffer solution. 0, 0.25, 0.5, 1.0, 1.5, and 2.0 mmol L^{-1} Ca^{2+} gradient buffer solutions were used for the sensitivity measurement. The sensor was submerged into the solutions for the measurement and the emission spectrum of each solution was recorded. The emission intensity with the corresponding calcium ion concentration was analysed.

Reversibility: The reversibility was evaluated using 0.25 mmol L^{-1} and 1 mmol L^{-1} calcium tris buffer solutions. The same procedure was followed as for the other sensors.

Photostability: The sensor was excited under the exposure of 520 nm laser light for a continuous of 2 hours. The 540 nm emission intensity was recorded every 20 min. 2-hour test was decided due to the low quantum yield of the sensor, which made the sensor signal very weak. After 2-hour exposure, the signal could hardly be distinguished from the background. Therefore, in the following test, two fibres were coated with calcium sensor to enhance the signal.

Pressure, pH, and temperature dependence: The pressure, pH and temperature dependence tests were measured using the same way as the sodium sensor. Instead, here calcium free and 1 mmol L^{-1} calcium buffer solution was used.

Selectivity: The same interferent solution as in the sodium sensor selectivity test was used here (**Table 3-2**). However, for calcium sensor, 1 mmol L^{-1} concentration was used for the ion selectivity test. The procedures were the same as the other sensors.

Glucose Sensor

The same optical setup was used for glucose sensor characterisation. A 520 nm laser (4.5 mW) was used for sensor excitation and emission intensity at 640 nm was recorded for following analysis. The buffer solutions were prepared using pH 7.4 PBS solution and the experiments were conducted under room temperature.

Sensitivity: The glucose sensor's sensitivity was characterized using 0-6 mmol L^{-1} glucose PBS solution (pH = 7.4) with 1 mmol L^{-1} of increment. The sensor's spectrum of each buffer solution was recorded and the emission intensity at 640 nm was correlated to the glucose concentration to obtain the calibration curve of the sensor.

Reversibility: The reversibility test was performed using 1 mmol L^{-1} and 5 mmol L^{-1} glucose buffer solutions. The sensor was dipped reversely in between the two buffer solutions and the intensity at 640 nm was used to indicate sensor reversibility.

Pressure dependence: The pressure dependence was the same as for the other sensors but instead 4 mmol L^{-1} glucose pH=7.4 PBS solution was used here.

Photostability: The glucose sensor was continuously excited using 520 nm laser for 3 hours with the sensor immerged in 4 mmol L^{-1} glucose PBS solution. The intensity at 640 nm was recorded every 30 min.

pH dependence: The enzyme activity is pH dependent. A lower activity may lead to a low emission intensity due to decreased ratio of oxygen consumption speed to oxygen supply speed. In the pH

dependence test, 4 mmol L^{-1} glucose PBS solution was adjusted to a series of pH 6-8 4 mmol L^{-1} glucose buffer. The emission intensity of each solution was measured for analysis of pH dependence.

Temperature dependence: Glucose-free and 1 mmol L^{-1} glucose PBS solution was used for temperature dependence test. The temperature of the solution was controlled to 34-41 ℃ using a hotplate.

Selectivity: Major interferents were dissolved in PBS solutions separately at specific concentration (**Table 3-2**). The pH of the interferent solutions was adjusted to 7.4 before testing. During the test, the glucose sensor was dipped into the interferent solutions sequentially and the emission intensity at 640 nm was recorded and normalized to blank solution.

Table 4-3. Characterisation of the 6 optical fibre sensors.

	pH	DO	Temperature	Na+	Ca2+	Glucose
Sensitivity	pH 6-8 PBS	DO 0 - 8 mg L^{-1} pH 7.4 PBS	33 - 42 ℃ pH 7.4 PBS	0-200 mmol L^{-1} $[Na^+]$ pH 7.4 tris buffer	0-2.0 mmol L^{-1} Ca^{2+} pH 7.4 tris buffer	0-6 mmol L^{-1} glucose pH 7.4 PBS
Reversibility	pH 6 and 8 PBS	DO 0 and 8 mg/L pH 7.4 PBS	36 ℃ and 40 ℃ pH 7.4 PBS	$[Na^+]$ 40 and 140 $mmolL^{-1}$ pH 7.4 tris buffer	Ca^{2+} 0.25 and 1 $mmolL^{-1}$ pH 7.4 tris buffer	glucose 1 and 5 $mmolL^{-1}$ pH 7.4 PBS
Stability	3 hours pH 7.4 PBS	3 hours 8 mg/L DO buffer	3 hours 36 ℃ pH 7.4 PBS	2 hours 140 $mmolL^{-1}$ $[Na^+]$, pH 7.4 tris buffer	2 hours 2 $mmolL^{-1}$ $[Ca^{2+}]$, pH 7.4 tris buffer	3 hours, 4 $mmolL^{-1}$ glucose, pH 7.4 PBS
pH dependence	NA	pH 6-8 100% DO saturated solution,	pH 6-8 36 ℃ PBS solutions	pH 6-8 0 and 100 $mmolL^{-1}$ $[Na^+]$ tris buffer	pH 6-8 1 mmol L^{-1} $[Ca^{2+}]$ tris buffer	pH 6-8 4 mmol L^{-1} glucose PBS
Pressure dependence	0-30 cm	0-30 cm 100% DO	0-30 cm 36 ℃ PBS	0-30 cm 140 mmol L^{-1} $[Na^+]$	0-30 cm 1 mmol L^{-1} $[Ca^{2+}]$	0-30 cm 4 mmol L^{-1} glucose PBS

Temperature dependence	35°C-41°C pH 6.8, pH 7.2 and pH 7.6 PBS solution	25-45 °C 100% DO saturated	NA	36 – 40 °C 100 mmol L^{-1} $[Na^+]$	36 – 40 °C 1 mmol L^{-1} $[Ca^{2+}]$	34-41 °C Glucose-free and 1 mmol L^{-1} glucose PBS solution
Selectivity	Table 3-2	Table 3-2	Table 3-2	Table 3-2	Table 3-2	Table 3-2

4.4.5 Multiplexed sensing characterisation

After the 6 sensors were characterized individually, the optical fibre sensors were bundled together and characterized for multiplexed sensing using prepared aCSF buffer solutions. aCSF was prepared by dissolving KCl, KH_2PO_4, $NaHCO_3$, and $MgCl_2$, in DI water and the concentration of them were 1.0 mmol L^{-1}, 1.2 mmol L^{-1}, and 26 mmol L^{-1} respectively. The temperature, DO, pH, Na^+, Ca^{2+}, and glucose concentrations of the aCSF solutions were prepared as described in **Table 4-4**. The temperature of the solution was controlled using a hot plate. The DO was controlled by pumping nitrogen into the solution. The pH was altered by dipping HCl or NaOH to the solution. The $[Na^+]$, $[Ca^{2+}]$, and glucose level were controlled by dissolving different amount of NaCl, $CaCl_2$, and Glucose. The experimental levels of these biomarkers are listed in **Table 4-4**.

Table 4-4. Buffer solution preparation for multiplexed sensor characterisation

	T (°C)	DO (mg L^{-1})	pH	Na^+(mmol L^{-1})	Ca^{2+}(mmol L^{-1})	Gluc(mmol L^{-1})
T buffer	36-40	8	7.4	140	0.5	2
DO buffer	37	0-8	7.4	140	0.5	2
pH buffer	37	8	6-8	140	0.5	2
Na^+ buffer	37	8	7.4	100-180	0.5	2
Ca^{2+} buffer	37	8	7.4	140	0, 0.25, 0.5, 1, 2	2
Glu buffer	37	8	7.4	140	0.5	0, 1, 2, 4, 6

During the test, the designed fibre bundle was dipped into the solution and excited with corresponding laser light. The spectra after the signal stabilized were recorded and used for calibration. The experiment was repeated three times.

4.4.6 Signal deconvolutional algorithms

This section introduces the computational methods for the processing the obtained multiplexed optical spectra for accurate calculation of biomarker concentrations, including baseline correction, multivariate regression for spectra separation, and environmental compensation methods.

Baseline correction algorithms

Background light noise is usually a big concern in optical related measurements. It plays a major role in the obtained optical spectrum and the fluorescent emission peaks are added on top of the background spectrum that needs to be corrected for intensity-based biomarker concentration calculation. Here, I used a fidelity based adaptive regression model for the spectrum baseline correction.

First, the measured spectrum vector can be defined as $\mathbf{X}=[\boldsymbol{x_1}, \boldsymbol{x_2}, \dots, \boldsymbol{x_m}]^{\mathrm{T}}$, and the corrected spectrum vector is defined as $\boldsymbol{Z}=[\boldsymbol{z_1}, \boldsymbol{z_2}, \dots, \boldsymbol{z_m}]^{\mathrm{T}}$, where m is the spectrum length and the values are the intensities.

Fidelity of **Z** to **X** is defined as follows, meaning the differences between the measured spectrum and the corrected spectrum. A lower F is desired, with F=0 meaning there is no background noise in the spectrum

$$F = \sum_{i=1}^{m} \boldsymbol{w_i}(\boldsymbol{x_i} - \boldsymbol{z_i})^2 \quad \textbf{(Eq. 4-2)}$$

, where w_i is the weight of fidelity to each spectrum value at different wavelengths.

The roughness (R) of Z is defined as Eq. 2-8. The roughness is measured by the differences between the neighbouring intensities, and a lower R means a smooth and flat spectrum.

$$R = \sum_{i=1}^{m-1}(\boldsymbol{z_{i+1}} - \boldsymbol{z_i})^2 = \sum_{i=1}^{m-1}(\boldsymbol{\Delta z_i})^2 \quad \textbf{(Eq. 4-3)}$$

To balance the fidelity and roughness of the fitted spectrum, a combined equation is defined as Q:

$$Q = F + \lambda R = \boldsymbol{W}\|\boldsymbol{X} - \boldsymbol{Z}\|^2 + \lambda\|\boldsymbol{\Delta Z}\|^2 \text{ (Eq. 4-4)}$$

, where $\mathbf{DZ} = \boldsymbol{\Delta Z}$, and λ can be adjusted manually. The larger the λ, the smoother the corrected spectrum.

The ideal corrected spectra **Z** should convey the peak information of the measured spectrum but should also smooth correct the small peaks on the baseline due to background noise. Therefore, the aim of the baseline correction is to minimize Q, which can be achieved by calculating the partial derivatives of Q and make it equal to 0 ($\frac{\partial Q}{\partial z} = 0$).

Therefore,

$$\boldsymbol{Z} = (\boldsymbol{W} + \lambda \boldsymbol{D}'\boldsymbol{D})^{-1}\boldsymbol{W}\boldsymbol{X} \text{ (Eq. 4-5)}$$

The weights were iteratively adjusted based on the location of each data at the spectrum. For example, at the peak of the data, the weight should be set as zero so that it wouldn't be smoothed by the algorithm. Therefore, in the iteration, the weights were updated as following:

$$w_i^t = \begin{cases} 0, & if\ \boldsymbol{x_i} \geq z_i^{t-1}\ (peak) \\ e^{\frac{t(\boldsymbol{x_i} - z_i^{t-1})}{|\boldsymbol{d^t}|}}, & if\ \boldsymbol{x_i} < z_i^{t-1}\ (non-peak) \end{cases} \quad \textbf{(Eq. 4-6)}$$

, where t is the number of iterations, and $\mathbf{d}^t$ denotes the differences between **X** and $\mathbf{Z}^{t-1}$ in the current (t) iteration. The iteration stops when the iteration number is reached or when $|\mathbf{d}^t| < 0.001 \times |\mathbf{X}|$.

A Python program is implemented to iteratively adapt the fidelity rate and calculate the corrected spectrum Z.

Multivariate curve regression (MCR) for peak separation and concentration readout

The proposed MCR method is not a learning-based method and does not require training. However, the sensor needs to be calibrated before measurement. The spectra obtained during calibration were used for the measurement of the concentration.

The measured overlapped spectra are the sum of the spectrum of the 6 sensors. Thus

$$X = X_{temp} + X_{DO} + X_{pH} + X_{Na+} + X_{Ca2+} + X_{Glu} + Error \quad \textbf{(Eq. 4-7)}$$

The spectra of the sensors are only detectable when the sensor is excited by the laser light. For the spectrum of each sensor, it can be further decomposed to the combination of two spectra at different concentration. For sensors that are assumed that the concentration and the spectrum intensity follow a linear correlation within physiological range and, can thus, be decomposed to weighted sum of two standard spectra. Take temperature sensor as an example. All measured temperature spectra can be decomposed into the weighted sum of the spectrum of 34 °C and the spectrum of 41 °C, and the corresponding temperature of the measured spectrum can be calculated as **Eq 4-8**.

$$\boldsymbol{X_{temp}} = \sum c1 \cdot \boldsymbol{X_{temp36}} + c2 \cdot \boldsymbol{X_{temp41}} \quad \textbf{(Eq. 4-8)}$$

$$Temperature = \ c1 \cdot 36 + c2 \cdot 41 \quad \textbf{(Eq. 4-9)}$$

The same correlation also applies to the other sensors that have linear calibration curve. For the ones with non-linear calibration curve, the measured value needs to be in line with its calibration fitting equation.

Thus for the mixed spectrum, it can be defined as:

$$\boldsymbol{X} = c_0 + c_1\boldsymbol{S}_1 + c_2\boldsymbol{S}_2 + \cdots + c_{12}\boldsymbol{S}_{12} = \sum c_i\boldsymbol{S}_i + E = \boldsymbol{C} \cdot \boldsymbol{S} \quad \textbf{(Eq. 4-10)}$$

$$\boldsymbol{C} = \boldsymbol{X}\boldsymbol{S}^{-1} \quad \textbf{(Eq. 4-11)}$$

, where S demotes the standard spectrum for each sensor that is excited under the current laser light. Two standard spectra are needed for each sensor.

Therefore, multivariate curve fitting methods based on least square fitting was used for peak separation and concentration prediction by calculating the ***C*** vector.

Environmental Compensation

Temperature compensation

In the characterisation of the 6 sensors, temperature dependence was observed in all six sensors due to the quenching effect of temperature on fluorescence and thus, the influence of temperature needs to be compensated for a correct estimation of the biomarker concentrations. According to the Stern-Volmer equation, the temperature effect on the fluorescence emission can be seen as:

$$I = \frac{I_c}{1+K_t(T-T_c)} \quad \textbf{(Eq. 4-12)}$$

, where *I* is the measured emission intensity during the experiment. *Ic* is the emission intensity of the indicator when the calibration was performed, *K*t is the temperature dependent quenching constant and *Tc* is the temperature of the solution used for the calibration. *Kt* can be treated as a constant variable when the probes are used under similar environment.

I used the data obtained during sensor characterisation for the estimation of Kt and use it for the temperature compensation during multiplexed sensing. When the multiplexed sensing was performed, the temperature was compensated using **Eq.4-12** to estimate the emission intensity under calibration temperature, which was then used for concentration prediction.

$$I_c = I * (1 + K_t(T - T_c)) \quad \textbf{(Eq. 4-13)}$$

The estimated *K*t for DO, pH, sodium, calcium, and glucose sensors are 0.0047 (R^2=0.95), 0.28 (R^2=0.97), 0.04 (R^2=0.95), 0.015 (R^2=0.97), and 0.058 (R^2=0.96) respectively based on the data reported in Section 4.5.

To correct the temperature influence on the sensors, the factor $(1 + K_t(T - T_c))$ needs to be applied to the coefficient *c* for the calculation of the biomarker values.

$$Ctemp = (1 + K_t(T - T_c)) \cdot C \quad \textbf{(Eq. 4-14)}$$

Photobleaching compensation

Same as temperature compensation, the photobleaching can be modelled using an exponential equation **Eq. 4-15** using the data obtained in the stability test for sensor characterisation.

$$I_f = I_{f0} \times e^{-\frac{t}{\tau}} \quad \textbf{(Eq. 4-16)}$$

, where I_f denotes the emission intensity at the moment of measurement, I_{f0} is the initial emission intensity at t = 0, t is the exposure time, and τ is the photobleaching time constant index.

Therefore, the intensity when the calibration (t=0) is performed can be calculated as:

$$I_{f0} = \frac{I_f}{e^{-\frac{t}{\tau}}} \quad \textbf{(Eq. 4-17)}$$

Using the photostability data obtained for each sensor, the photobleaching constant τ can be calculated for each sensor using least square fitting methods and they were used for the photobleaching compensation.

$$Cphoto, temp = \frac{(1+K_t(T-T_c)) \cdot C}{e^{-\frac{t}{\tau}}} \quad \textbf{(Eq. 4-18)}$$

The constant τ for temperature, DO, pH, Na^+, Ca^{2+}, and glucose are 51.13 (R^2=1), 48.8 (R^2=0.97), 37.0 (R^2=1), 22.0 (R^2=0.99), 38.0 (R^2=0.99), 133.7 (R^2=0.96) respectively based on the data reported in Section 4.5.

Calculation of glucose concentrations at varying oxygen partial pressure

The glucose sensor measures the glucose level based on the consumption of oxygen and it is only accurate when the oxygen level remains constant during the measurement. However, the oxygen level may also change during real-life application. Therefore, the determination of glucose concentration is also influenced by the fluctuation of DO in human tissues. Thus, the reading of the oxygen sensor (SenDO) was used to compensate for the glucose sensor (SenGlu) calculation. The glucose concentration can be derived from the following equations.

In the glucose oxidation reaction induced by glucose oxidase in SenGlu, the consumed oxygen (ΔO_2) is linear with the glucose concentration Con(Glu) (Section 2.2.1 **Eq. 2-1**) and also linear related to the dissolved oxygen level Con(O_2). Therefore,

$\Delta O_2 = k \cdot Con(Glu)$ **(Eq. 4-19)**

$\Delta O_2 = m \cdot Con(O_2)$ **(Eq. 4-20)**

Consequently, the total signal change is

$\Delta O_2 = m \cdot k \cdot Con(Glu) \cdot Con(O_2)$ **(Eq. 4-21)**

The oxygen quenching effect of SenDO follows the linear Stern-Volmer response equation.

$\frac{I_{o0}}{Io} - 1 = K_{sv1} \cdot Con(O_2) = \alpha$ **(Eq. 4-22)**

Where I_{o0} and Io are the fluorescence intensities measured in the absence and presence of oxygen, respectively. Ksv denotes the Stern-Volmer constants.

Both sensors are based on the oxygen quenching effect, but two different indicators were used for separated peaks. SenGlu responds to both oxygen and glucose due to a part of oxygen is consumed in the first layer of the sensor. Therefore, the equation for SenGlu follows:

$\frac{I_{g0}}{I_g} - 1 = K_{sv2} \cdot [Con(O_2) - \Delta O_2] = \beta$ **(Eq. 4-23)**

, where I_{g0} and Ig are the fluorescence intensities measured in the absence and presence of glucose and oxygen, respectively.

Therefore, the concentration of glucose can be calculated by:

$\frac{\alpha}{K_{sv1}} = \frac{\beta}{K_{sv2}} + \Delta O_2$ **(Eq. 4-24)**

$\frac{\alpha}{K_{sv1}} = \frac{\beta}{K_{sv2}} + m \cdot k \cdot Con(Glu) \cdot \frac{\alpha}{K_{sv1}}$ **(Eq. 4-25)**

$Con(Glu) = \frac{K_{sv} \cdot \alpha - K_{sv1} \cdot \beta}{K_{sv2} \cdot m \cdot k \cdot \alpha} = \frac{K_{sv2} \cdot I_g (I_{o0} - 2I_o) - K_{sv1} \cdot I_o (I_{g0} - I_g)}{I_g (I_{o0} - I_o) \cdot m \cdot K_{sv2} \cdot k}$ **(Eq. 4-26)**

4.4.7 System validation using ex vivo brain models

With this study, the performance while performing in situ measurement was evaluated to quantify the sensor performance while implanted in the brain tissue. The proposed system's capability to identify

secondary brain injuries in TBI patients was also tested using the lamb brain models to simulate three TBI complications: hypoxia, energy failure, and excitotoxicity. Hypoxia involves high temperature and oxygen deficiency, energy failure includes low glucose levels along with hypoxia symptoms, and excitotoxicity leads to increased acidity, sodium, and calcium ion levels in the brain.

To mimic these scenarios, corresponding buffer solutions were prepared and introduced into clean lamb brains. The developed fibre bundle sensors, integrated with a medical-grade catheter, were inserted into the brain tissues during the process. Transitions between scenarios were achieved by changing buffer solutions, and spectra were captured every 3 seconds using a python program. Lasers were manually switched between 405 nm, 450 nm, and 520 nm for different sensor excitations and biomarker measurements. Simulated transitions from complications to a healthy state were also conducted to replicate disease recovery situations. Signal processing employed the proposed algorithms for peak separation, environmental compensation, and biomarker concentration calculation.

Table 4-5. aCSF buffer solution preparation for different brain scenarios

	T (℃)	DO (mg L^{-1})	pH	Na^{+}(mmol L^{-1})	Ca^{2+}(mmol L^{-1})	Gluc(mmol L^{-1})
Hypoxia	38	3	7.5	140	1.5	2.5
Energy failure	39	3	7.2	130	1.2	1
Excitotoxicity	37	7	6.4	180	2	3
Healthy1	36	7	7.5	140	1.5	2.5
Healthy2	37	6	7.2	130	1.2	3
Healthy3	37.5	7	7.2	140	1.5	3

4.5 Characterisation of individual fluorescent sensors

4.5.1 Temperature sensor characterisation

Tris(2,2'-bipyridyl)dichlororuthenium(II) hexahydrate ($Ru(bpy)_3$) contains a ruthenium group known for its high sensitivity to temperature changes[252]. The electronic transition from a triplet metal-to-ligand charge transfer (^{3}MLCT) state to ground state leads to the fluorescence emission of $Ru(bpy)_3$. At high temperatures, the ^{3}MLCT state can be thermally populated to metal-localized triplet state (^{3}dd), which subsequently decays to ground state via a non-radiative route[253, 254], resulting in a decreased emission intensity (**Figure 4-5**). However, $Ru(bpy)_3$ is also sensitive to oxygen levels, and thus, an epoxy film with a relative low air permeability (2-10 cc/m² per 24 h) was used to encapsulate the fluorescent indicator, creating a temperature sensing film that minimizes oxygen interference[255].

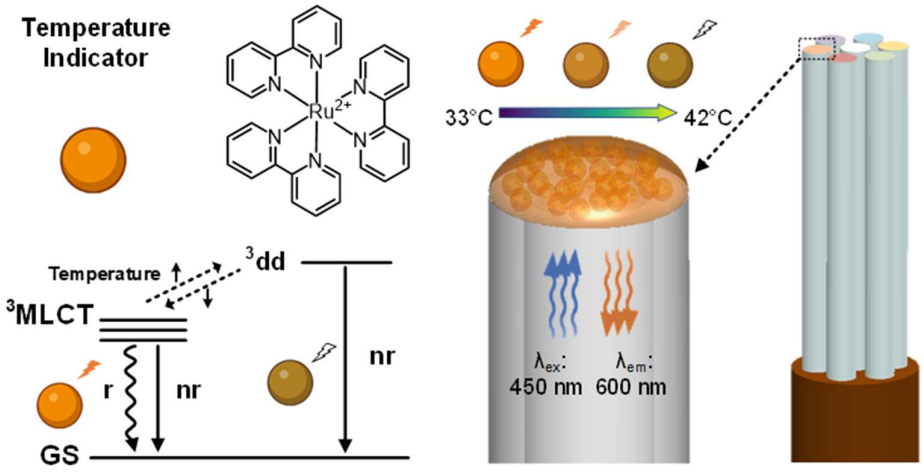


Figure 4-5. Schematic demonstration of the temperature sensing principle

The temperature sensing film was fabricated on the tip of a single optical fibre by dip coating in an epoxy-Ethenol-Ru(dpy)3 pre-gel solution with optimized probe concentration (**Figure 4-6**). The coated fibre was left at room temperature until thorough gelation. The single optical fibre sensor was then connected to a 450 nm laser light and a spectrometer via a fibre coupler.

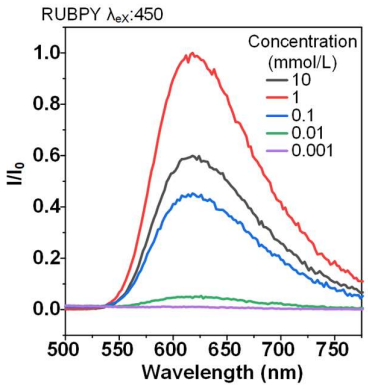


Figure 4-6. Temperature probe Ru(dpy)3 concentration optimization.

Phosphate buffered saline (PBS) solutions with physiological temperatures ranging from 33℃ to 42℃ were used to calibrate the temperature sensor. An evident decreasing trend in the emission intensity of the $Ru(bpy)_3$-containing epoxy-based temperature sensing film was observed as the temperature increased (**Figure 4-7 (a)**). A good linear relationship was established between the emission intensity ratio (I_0/I) and temperature with a sensitivity of 0.04/℃ (R^2 = 0.99) (**Figure 4-7 (b)**). In clinical settings, a reversible sensing ability is crucial for long-term and continuous monitoring. The reversibility of the temperature sensor was tested through repeated measurements between 36℃ and 40℃ in PBS solutions. A high reversibility with little variations among each repeat was demonstrated (**Figure 4-7 (c)**). However, after a 3-h exposure to the excitation laser (450 nm, 4.5 mW), the emission intensity of the sensor reduced by 60% due to photobleaching (**Figure 4-7 (d)**). This photobleaching can significantly impact fluorescent sensing, and it can be reduced by decreasing the laser power using a pulsed laser or introducing compensation by post-signal processing[256].

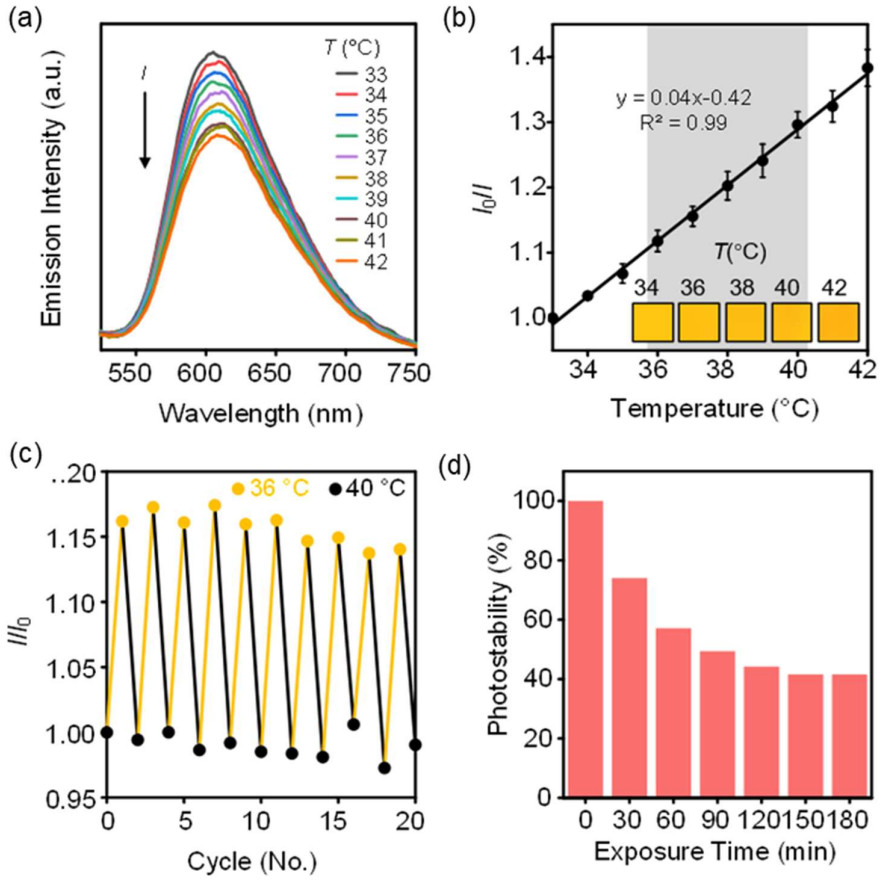


Figure 4-7. Characterisation of the optical fibre sensor for temperature monitoring in PBS solutions (10 mmol L-1, pH 7.4). (a) Emission spectra of the optical fibre sensor for monitoring PBS solution with temperature of 33-42℃. (b) The calibration curve of the temperature sensor for the sensing of temperature from 33-42℃. Shadows represent the physiological range of temperature in human CSF. (c) Reversibility of the sensor for repeated measurements in PBS solutions at 36 and 40℃. (d) Photostability of the sensor with exposure under 4.5 mW 450 nm excitation laser for 3 h in 37°C PBS solutions.

In TBI, increased intracranial pressure is a common consequence due to brain tissue swelling or bleeding[257]. Investigations on pressure dependence revealed little influence of pressure on the sensing performance, indicating its potential for deep tissue measurement under various brain pressures (**Figure 4-8 (a)**). Moreover, the temperature optical fibre sensor showed high stability in different pH and DO microenvironments (**Figure 4-8 (b,c)**) and displayed high selectivity towards other co-existed biomolecules due to the low water permeability of the encapsulation film, making it a promising candidate for clinical brain temperature monitoring (**Figure 4-8(d)**).

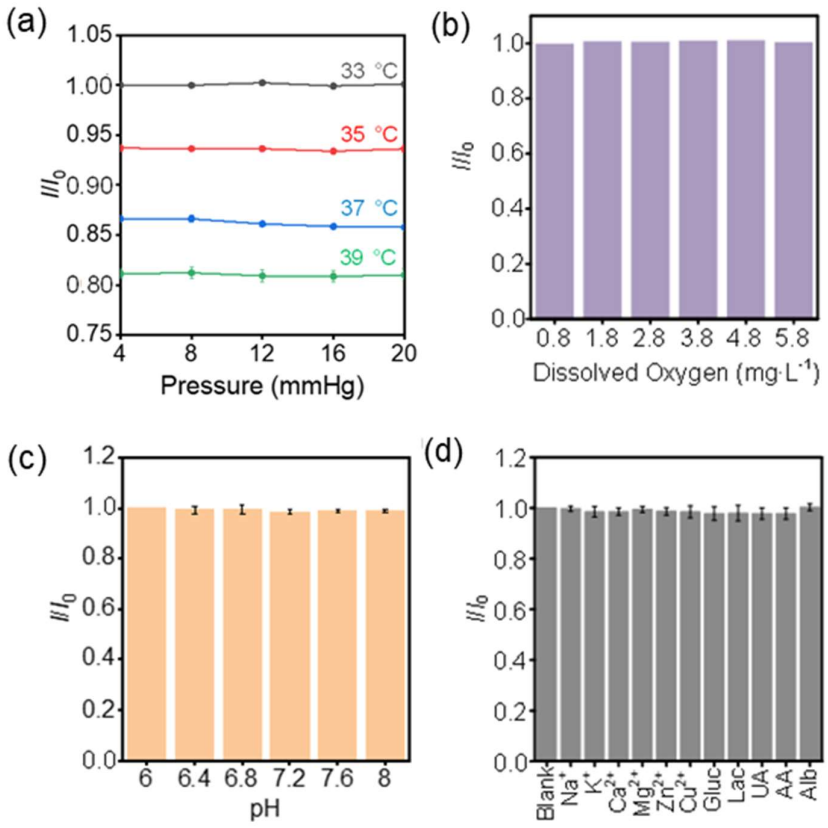


Figure 4-8. Environmental dependence and selectivity of the temperature fibre sensor. (a) Pressure dependence of the sensor in 37°C PBS with 4-20 mmHg pressure. (b) Oxygen dependence test of the temperature sensor in 37°C PBS solution with varying DO (0-6 mg L-1) values. (c) pH dependence test of the sensor in 37°C PBS solution with 6.0-8.0 pH levels. (d) Selectivity test of the temperature sensor in 37°C PBS against major interferences. Gluc: glucose; Lac: lactate; UA: uric acid; AA: ascorbic acid; Alb: albumin. Error bars represent the standard deviation of the mean of three measurements.

4.5.2 Dissolved oxygen (DO) sensor characterisation

For brain DO monitoring, the DO optical fibre sensor was developed by functionalizing Palladium(II) octaethylporphine (PdOEP)-based sensing film on the optical fibre tip. The oxygen sensing principal is based on the fluorescence quenching effect in the presence of oxygen (**Figure 4-9**)[258].

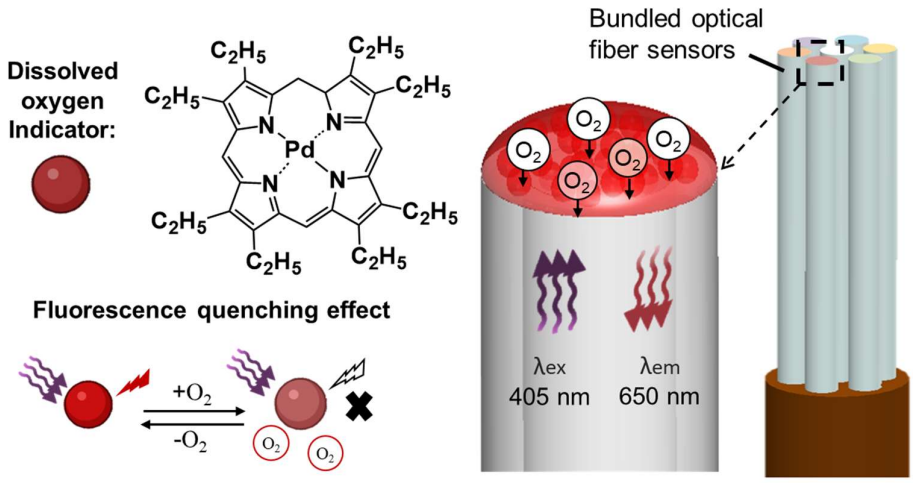


Figure 4-9. Schematic demonstration of the design and principle of the DO sensor.

The oxygen sensing film was fabricated by encapsulating PdOEP at its optimized concentration (**Figure 4-10**) within a PDMS matrix, providing high oxygen permeability and low water permeability to ensure a dry film environment that enhances oxygen sensitivity[179, 259]. In the film characterisation test, the oxygen sensing film demonstrated a high sensitivity towards oxygen with 0.38 increases in I_0/I per oxygen unit. As the DO concentration increased from 0.68 to 7.98 mg·L^{-1}, the emission intensity of the DO sensor reduced by 85.6% (**Figure 4-11(a, b)**). A good reversibility of the DO sensing film was shown in repeated tests between 0% DO PBS to 100% DO PBS solutions, suggesting its potential for long-term and reversible sensing (**Figure 4-11(c)**). Furthermore, the DO sensor exhibited a good photostability with 87% of the emission intensity retained after continuous exposure to excitation light (4.5 mW, 405 nm laser) for 3 hours (**Figure 4-11(d)**).

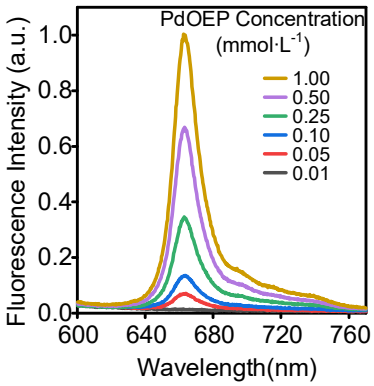


Figure 4-10. DO probe PdOEP concentration optimization.

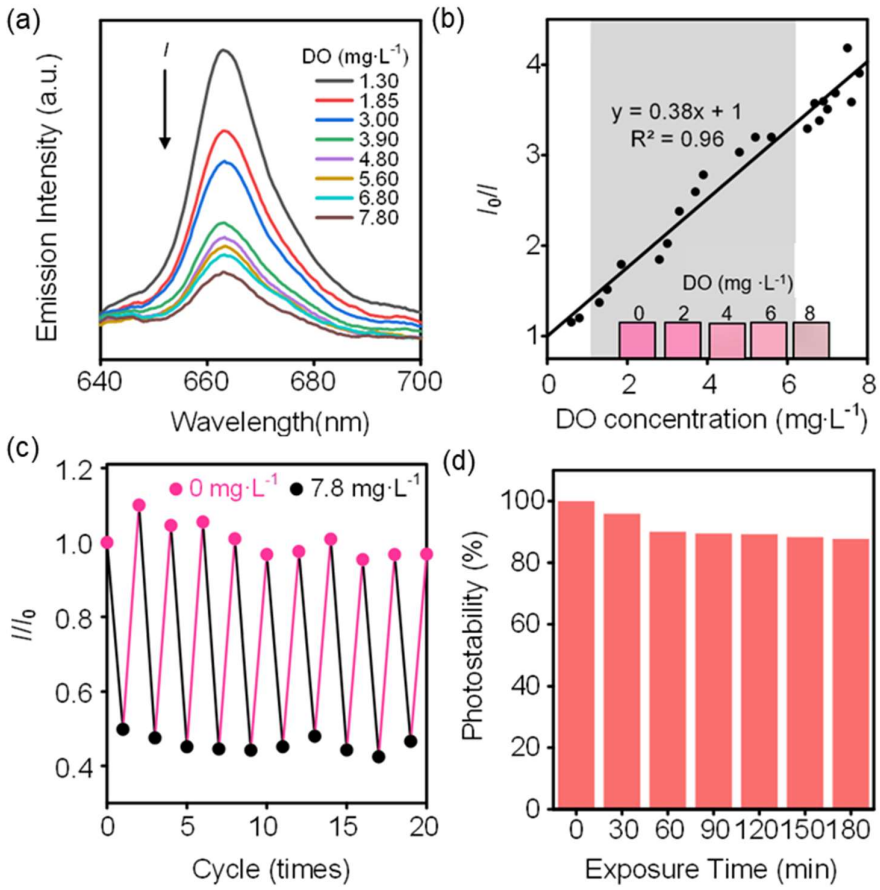


Figure 4-11. Design and characterisation of the PdOEP-containing PDMS DO sensor in PBS solutions (10 mmol L-1, pH 7.4, 25 °C). (a) Fluorescence spectra of the sensor in PBS solutions with different DO concentrations (1-8 mg L-1). (b) The calibration curve of the DO sensor for the measurement of 1-8 mg L-1 DO. Shadows represent the physiological range of DO concentration in human CSF. (c) Reversibility test of the DO sensor in the repeated measurement of 0 and 7.8 mg L-1 DO PBS solution. (d) Photostability of the sensor under exposure to a 4.5 mW 405 nm laser light for 3 hours.

As investigated in **Figure 4-12(a)**, a rising temperature from 25°C to 45°C reduced the emission intensity by 11.4%, while temperature variations in a physiological range showed a limited influence on the emission intensity (reduced 4.6% from 35 to 40°C). Neglectable effects of pressure and pH on the DO sensing were obtained (**Figure 4-12(b, c)**). The DO optical fibre sensor also displayed promising resistance towards other molecules or cations that coexist in CSF, owing to the hydrophobicity of the PDMS sensing film, which indicates a high selectivity for brain CSF DO sensing (**Figure 4-12(d)**).

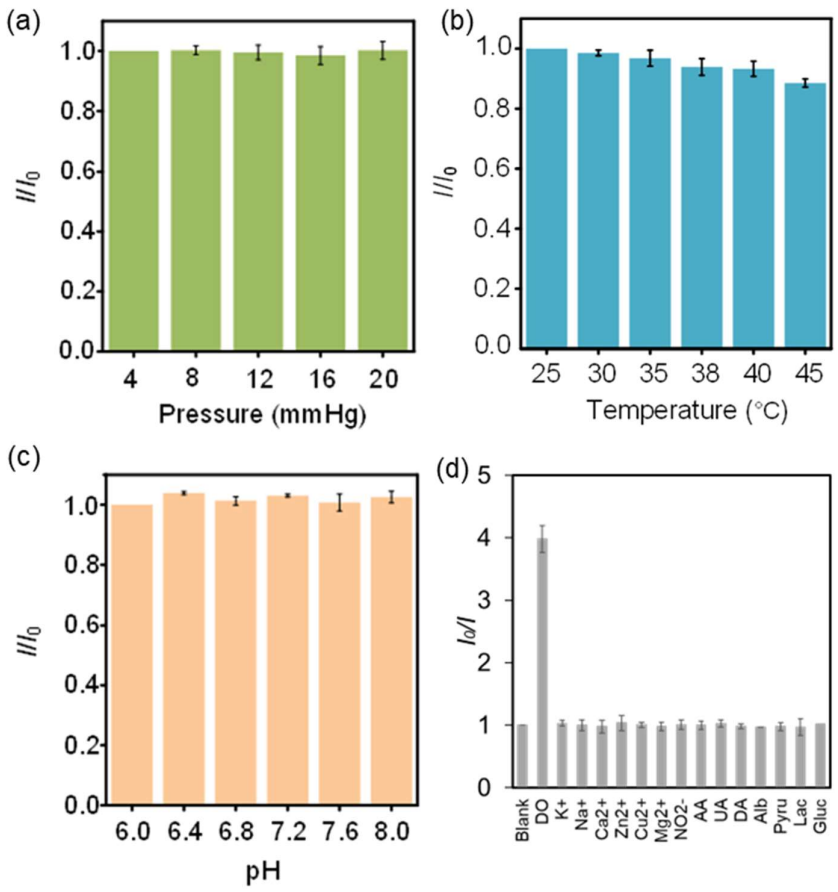


Figure 4-12. Environmental dependence and selectivity of the optical DO sensor. (a) Temperature dependence test of the sensor using 25-45 °C 7.8 mg L-1 DO PBS solution. (b) Pressure dependence of the DO sensor in 7.8 mg L-1 DO PBS solution with pressure from 4-20 mmHg. (c) pH dependence tests of the DO sensor in 7.8 mg L-1 DO PBS solution with pH from 6.0-8.0. (d) Selectivity test of the sensor of measuring 7.8 mg L-1 DO PBS solution against major interferences. UA: uric acid; AA: ascorbic acid; DA: dopamine; Alb: albumin. Pyru: pyruvate; Lac: lactate; Gluc: glucose. Error bars represent the standard deviation of the mean of three measurements.

4.5.3 pH sensor characterisation

Here, fluorophore 7-Hydroxycoumarin-3-carboxylic acid (HCC) was used as the pH indicator and encapsulated in proton-permeable sol-gel films with optimized concentrations (**Figure 4-13**). The pH sensing process of HCC in PBS solution of pH 6 to 8 involves two deprotonation steps: first, the deprotonation of imino group (pKa =2.7), and then the deprotonation of phenol group (pKa =7.8), causing the maximum excitation wavelength of HCC to shift from 352 to 385 nm, and a total pKa of 7.0 for HCC is obtained[36, 260]. Therefore, if the excitation wavelength is set to be larger than 385 nm, the emission intensity would continually increase as pH increases (**Figure 4-14 (a)**). In this study, a

405 nm laser light was used to excite the pH optical fibre sensor, and the emission intensity at 450 nm was correlated with the pH value. The results indicated a sensitivity of 2.624 I/I_0 per pH unit, and the emission intensity increases 5 times as the pH value increased from 6.0 to 8.0, with the calibration curve fitting a sigmoidal model (**Figure 4-14 (b, c)**). The pH sensor demonstrated high reversibility in repeated tests with consistent emission intensities obtained after measuring pH 6 of the pH sensor for measuring pH 6.0 and 8.0 PBS solution .0 and 8.0 PBS solutions for 20 cycles (**Figure 4-14(d)**). The stability of the pH sensing film on the fibre tip was investigated through the leaching rate of the sensing film. Only 3.6% of the signal decreased after soaking the film in the PBS solution for three days, indicating minimal influence on the surrounding tissue and the signal intensities (**Figure 4-14 (e)**). For photostability, the emission intensity reduced by 48% in 3 h, suggesting further efforts may be needed to reduce photobleaching ratios in continuous applications (**Figure 4-14 (f)**). Temperature and pressure effects on the pH sensor were also studied (**Figure 4-14 (g, h)**). Less than 10% of the emission intensity decreased as the temperature increased from 35 °C to 41°C, and neglectable changes were observed with increasing solution pressure (**Figure 4-14 (g, h)**). Moreover, the pH sensor also exhibited good selectivity towards the major protons and biomarkers commonly present in brain CSF (**Figure 4-14 (i)**).

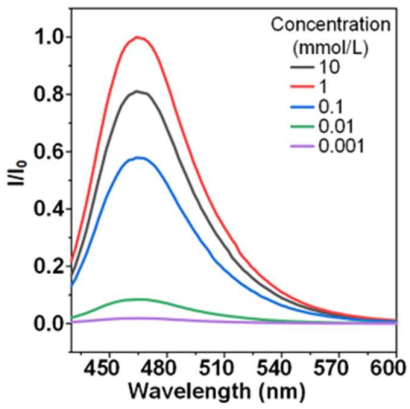


Figure 4-13. pH probe HCC concentration optimization.

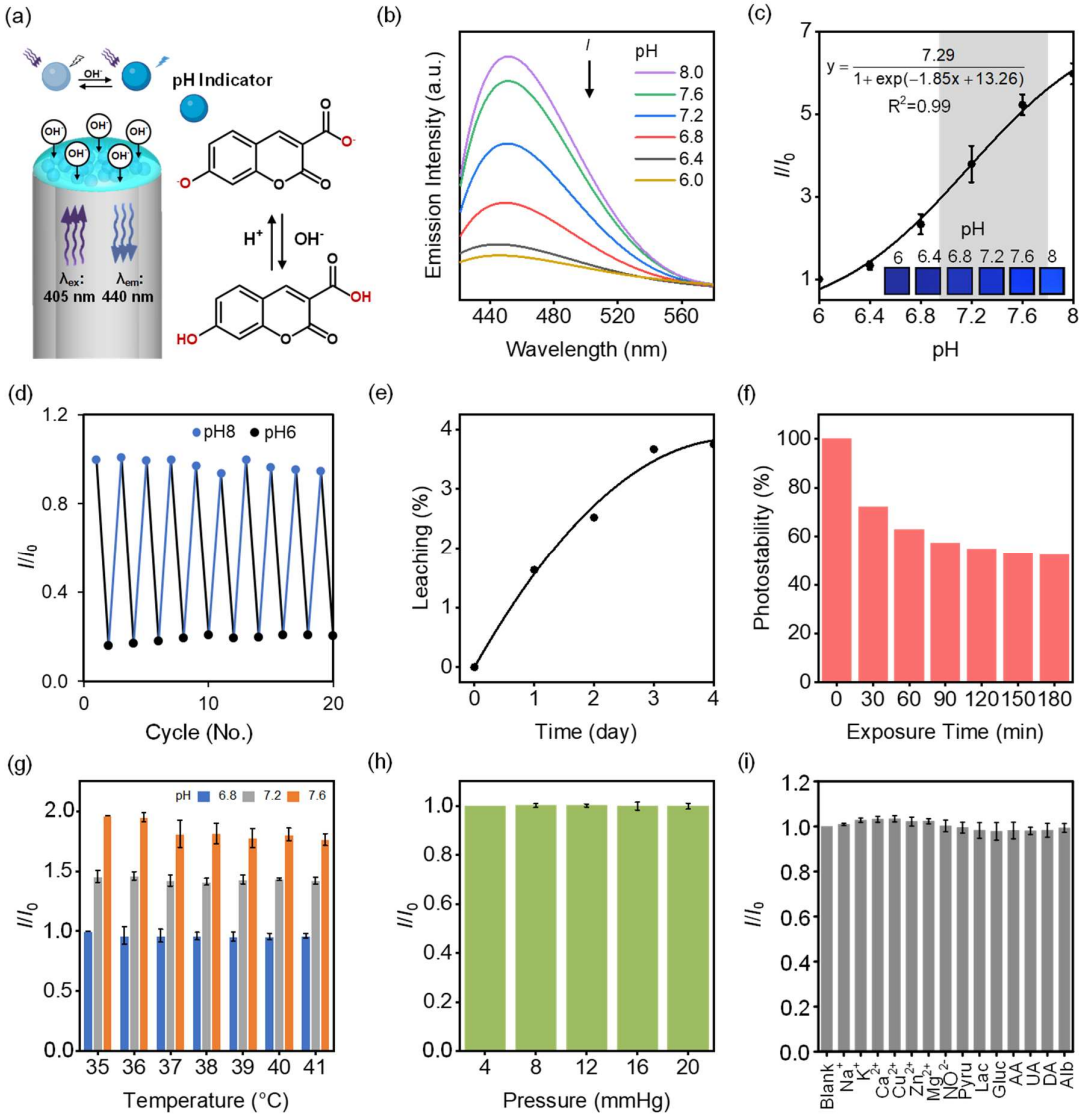


Figure 4-14. Design and characterisation of the HCC-containing sol-gel pH sensor in PBS solutions (10 mmol L-1, 25 °C). (a) Schematic of the optical fibre pH sensor design and sensing principle. (b) Fluorescence spectra of the sensor dipped in pH 6.0-8.0 PBS solutions. (c) The calibration curve of the pH sensor for the measurement of pH 6.0-8.0 PBS solution. Shadows represent the physiological range of pH values in human CSF. (d) Reversibility test of the sensor in sensing pH 6.0 and 8.0 PBS solutions. (e) Leaching test of the pH sensing film for three days. (f) Photostability of the sensor under a continuous exposure of 405 nm laser light (4.5 mW) for 3 hours. (g) A temperature dependence test using pH 7.4 PBS solution with temperature increasing from 35°C to 41°C. (h) Pressure dependence test using pH 7.4 PBS solution with pressure increasing from 4 to 20 mmHg. (i) Selectivity tests of the pH sensor using pH 7.4 PBS solution with different interferents. (Pyru: pyruvate; Lac: lactate; Gluc: glucose AA: ascorbic acid; UA: uric acid; DA: dopamine; Alb: albumin. Error bars represent the standard deviation of the mean of three measurements.

4.5.4 Na^+ sensor characterisation

In patients with TBI, sodium influx is commonly observed due to increased glutamate concentration, leading to sodium-dependent neuronal swelling and excitotoxicity[244]. Therefore, continuous and real-

time measurement of the temporal changes in Na^+ ion concentrations is of great significance in reflecting brain physiology. For this study, CoroNa™ Green probe, which selectively binds with Na^+ ion in the human physiological range (K_d of ~80 mmol·L^{-1}) was utilized to fabricate the optical fibre sodium sensor by encapsulation in a poly(ethylene glycol) diacrylate–acrylamide (PEGDA-AM) hydrogel (**Figure 4-15(a)**) [261]. The probe comprises a fluorescein molecule and a crown ether, which has a cavity size selective for Na^+ ions, exhibiting increased fluorescence emission intensity upon binding with Na^+ ion. The probe concentration was optimized for the fabrication of sensing film (**Figure 4-16**), and PEGDA-AM hydrogel was chosen due to its high biocompatibility and cation permeability. In the sensitivity test, the sodium sensing film exhibited a high sensitivity of 0.064 I/I_0 per change of 10 mmol·L^{-1} in the sodium ion concentration ([Na^+]) across the whole range from 0-200 mmol·L^{-1} of [Na^+] with good linearity (R^2 = 0.98) (**Figure 4-15(b, c)**). The sensor demonstrated its good ability to measure elevated [Na^+] by having a larger I/I_0 and also measuring the recovery of Na^+ ions to the original state in lower [Na^+] samples during the repeating test (**Figure 4-15(d)**). Photostability is crucial for long-term monitoring, and a 32% decrease in emission intensity was observed in the Na^+ sensor after a 2-h exposure under a 4.5 mW 450 nm laser (**Figure 4-15(e)**). The sensing film exhibited little influence on the pressure and pH, but the intensity showed a decreasing trend as the temperature increased due to the quenching effect (**Figure 4-15(f-h)**). Further compensation for photobleaching and temperature effects on the sensor output is needed to accurately reflect the influence from Na^+ ions only. The emission response of the Na^+ sensor showed high selectivity, as a 2.4-fold increase in the emission intensity was observed with the presence of Na^+ ion (200 mmol L^{-1}), whereas only neglectable changes were noticed with the addition of other ions at equivalent concentrations or metabolites (**Figure 4-15(i)**). The high selectivity towards Na^+ ion might be attributed to the cavity size of the indicator, which only fits to bind with Na^+ ions.

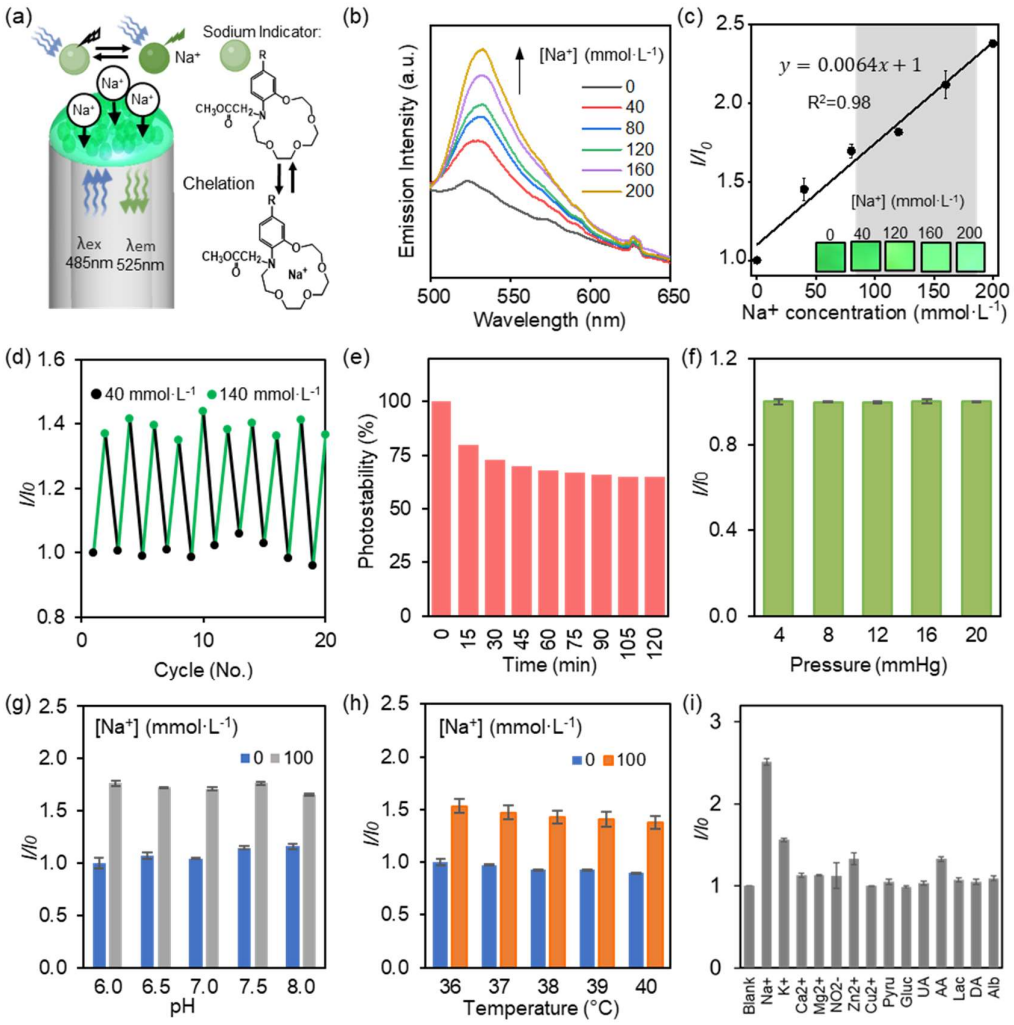


Figure 4-15. Design and characterisation of the optical fibre Na+ ion sensor in Tris buffer solutions (150 mmol L-1, pH 7.4, 25 °C). (a) Schematic drawing of the Na+ sensor and sensing principle. R: fluorescein. (b) Fluorescence spectra of the Na+ sensor in 0-200 mmol L-1 [Na+] Tris buffer solution. (c) The calibration curve of the Na+ sensor for the measurement of 0-200 mmol L-1 [Na+] Tris buffer solution. Shadows represent the physiological range of Na+ in human CSF. (d) Reversibility of the Na+ sensor for repeated measurement of 40 and 140 mmol L-1 [Na+] Tris buffer solution. (e) Photostability of the Na+ sensor with continuous exposure to a 405 nm laser (4.5 mW) for 2 h. (f) Pressure dependence test using 140 mmol L-1 [Na+] Tris buffer solution with pressure from 4-20 mmHg. (g) pH dependence tests using Na+-free and 100 mmol L-1 [Na+] Tris buffer solution with pH from 6.0 to 8.0. (h) Temperature dependence test using Na+-free and 100 mmol L-1 [Na+] Tris buffer solution with temperature from 36 to 40 °C. (i) Selectivity test of the Na+ sensor using 200 mmol L-1 [Na+] Tris buffer solution with different interferents. Pyru: pyruvate; Gluc: glucose; UA: uric acid; AA: ascorbic acid; Lac: lactate; DA: dopamine; Alb: albumin. Error bars represent the standard deviation of the mean of three measurements.

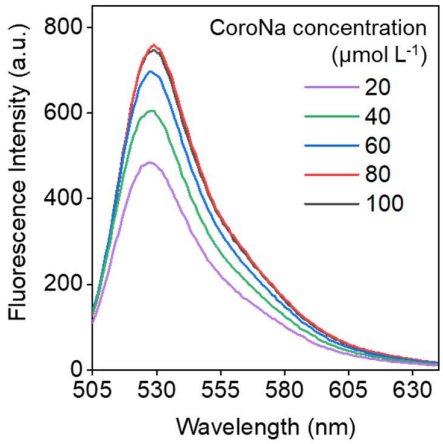


Figure 4-16. Sodium sensing probe CoroNa Green concentration optimization.

4.5.5 Ca^{2+} sensor characterisation

Ca^{2+} ions play an important role in cell development, neurotransmissions, and learning[243], and the maintenance of Ca^{2+} ions and their homeostasis are essential for the function of the nervous system. After TBI, elevated Ca^{2+} ion concentration ($[Ca^{2+}]$) is commonly observed in brain CSF, caused by brain ischemia due to reduced cerebral blood flow and elevated glutamate levels, leading to secondary brain injury[243]. Here, $[Ca^{2+}]$ was detected by encapsulating Rhod-5N, which consists of a 1,2 bis(o-aminophenoxy) ethane-N,N,-N',N'-tetraacetic acid (BAPTA) moiety for Ca^{2+} ion recognition and fluorophore rhodamine, in a polyacrylamide-MBA hydrogel (**Figure 4-17 (a)**). The BAPTA moiety selectively binds with Ca^{2+} ions with a high K_d of 0.5 mmol L^{-1}, ensuring a reversible response and a large detection range.[262] The emission intensity increased proportional with $[Ca^{2+}]$ (**Figure 4-17(a)**). The probe is encapsulated in Poly Acrylamide hydrogel and coated on the top of an optical fibre (**Figure 4-17(b)**).

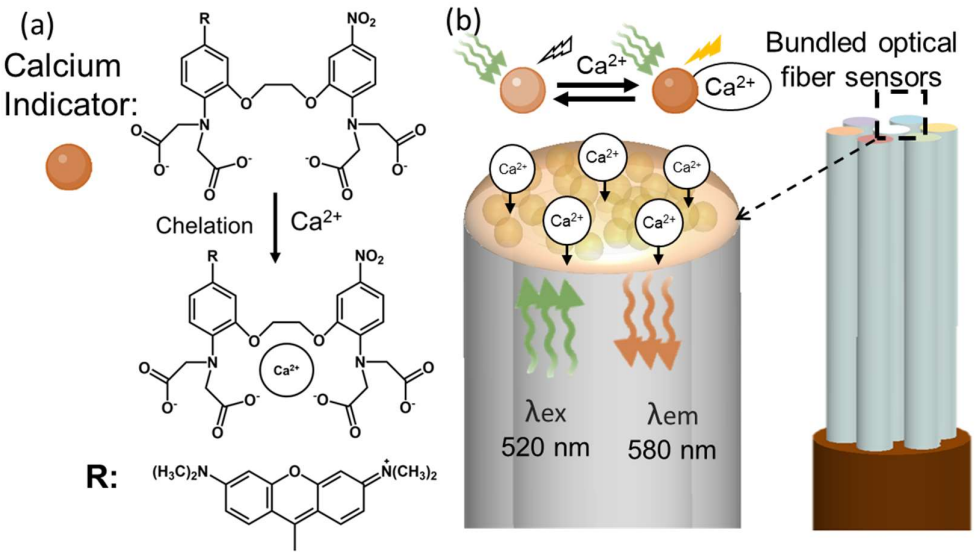


Figure 4-17. Schematic drawing of the Ca2+ ion sensor and sensing principle. (a) Indicator recognition mechanism. (b) Schematic of the Ca2+ ion optical fibre sensor when excited by 520 nm laser light.

The encapsulation concentration of the calcium indicator and the hydrogel fabrication method were optimized to achieve an optimal signal-to-noise ratio (**Figure 4-18**). Same as the other sensors, the intensity increases as the probe concentration becomes higher with the maximum concentration at 0.1 mmol L^{-1}, after which the intensity reduces as the concentration increases due to the aggregation effects of fluorophores. Therefore, 0.1 mmol L^{-1} was used for film fabrication (**Figure 4-18 (a)**). The matrix formulation was also optimized. According to **Figure 4-18 (b),** the encapsulation matrix becomes denser with reduced pore sizes when a higher AM or crosslinker concentration was used for the film fabrication, leading to reduced leaching ratio. However, due to the smaller pore size, the response time was also increased from 3 minutes to 20 minutes. Therefore, there is a tradeoff between the leaching ratio and the response time.

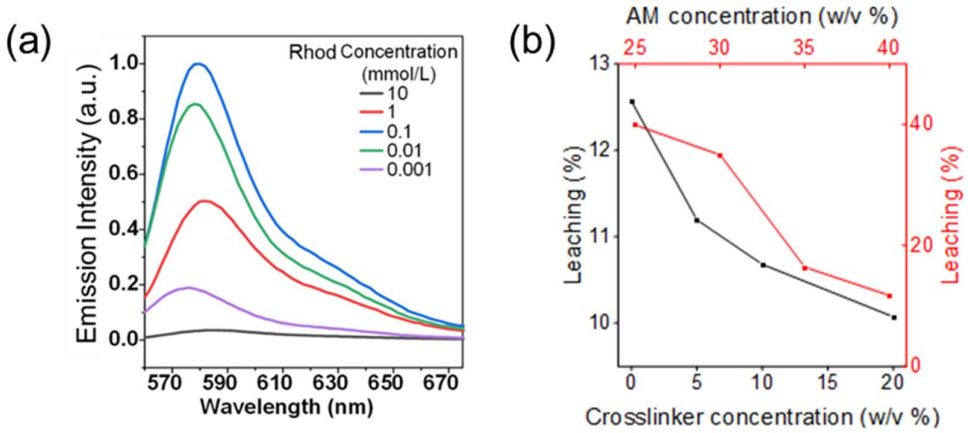


Figure 4-18. Calcium ion sensor optimization. (a) Indicator Rhod-5N concentration optimization. (b) Correlation between crosslinker, AM, and leaching ratios for encapsulation method optimization.

The calcium sensor's characterisation was conducted by dipping in tris-calcium buffer solutions and exposure to a 520 nm laser as the excitation source. The results showed that the fabricated calcium sensor had a sensitivity of 0.41 increase in I/I_0 per Ca^{2+} unit in physiological range (**Figure 4-19(a)**) and demonstrated a sigmoid correlation with R^2=0.98 (**Figure 4-19(b)**). The sensor also exhibited good reversibility, detecting both increases and decreases in [Ca^{2+}] (**Figure 4-19(c)**). In the photostability test, a 30% decrease of intensity was observed after continuous excitation of the sensing film for 2 hours (**Figure 4-19(d)**).

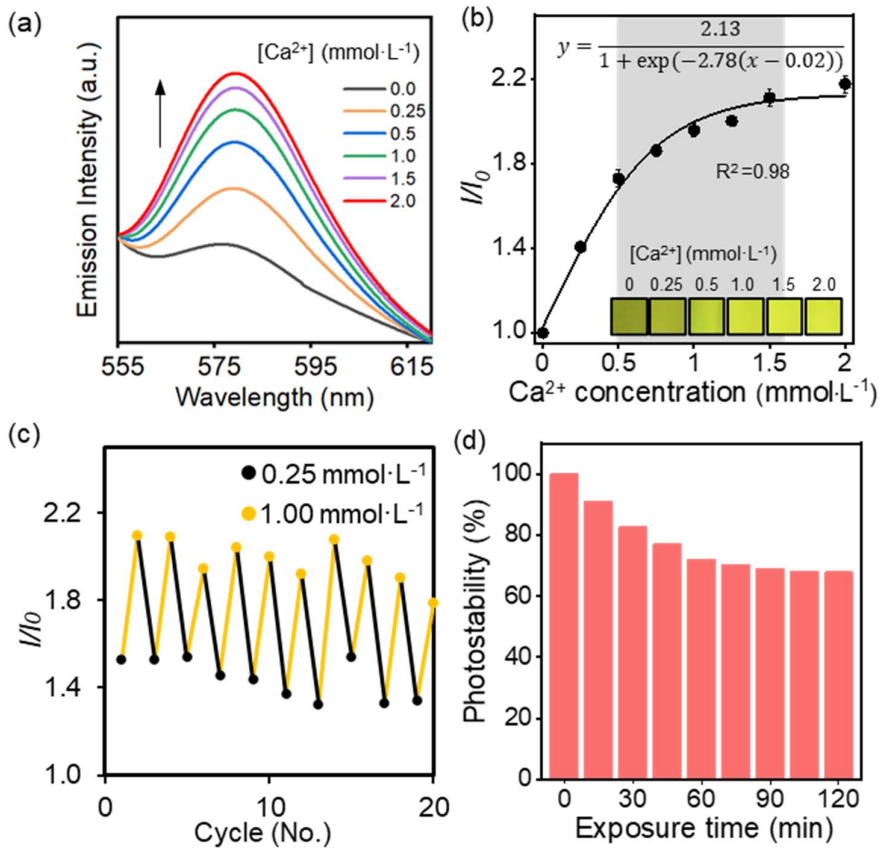


Figure 4-19. Design and characterisation of the optical fibre Ca2+ sensor in Tris buffer solutions (150 mmol L-1, pH 7.4, 25 °C). (a) Fluorescence spectra of the Ca2+ ion sensor for the measurement of 0-2 mmol L-1 [Ca2+] Tris buffer solution. (b) The calibration curve of the Ca2+ ion sensor for the measurement of 0-200 mmol L-1 [Ca2+] Tris buffer solution. Shadows represent the physiological range of Ca2+ in human CSF. (c) Reversibility of the Ca2+ sensor for repeated measurement of 0.25 and 1 mmol L-1 [Ca2+] Tris buffer solution. (d) Photostability of the Ca2+ ion sensor under continuous exposure to 520 nm laser light (4.5 mW) for 2 hours.

The sensor's robustness towards environmental changes was then tested. It is shown that the environmental pressure and pH had little effect on the sensor output (**Figure 4-20(a ,b)**), whereas the sensor's emission intensity decreased with an increase in temperature due to the quenching effect of the temperature on fluorophores (**Figure 4-20(d)**). In the selectivity test, the sensor showed neglectable responses towards most ions except Zn^{2+} and Mg^{2+} ions, though the increment was much smaller than the increase caused by Ca^{2+}. The increases in UA and AA are due to the indicator being protonated in the acidic solutions (**Figure 4-20(d)**). However, the pH in CSF is maintained in the range of 7-8, and thus the indicator would not be affected by the pH levels.

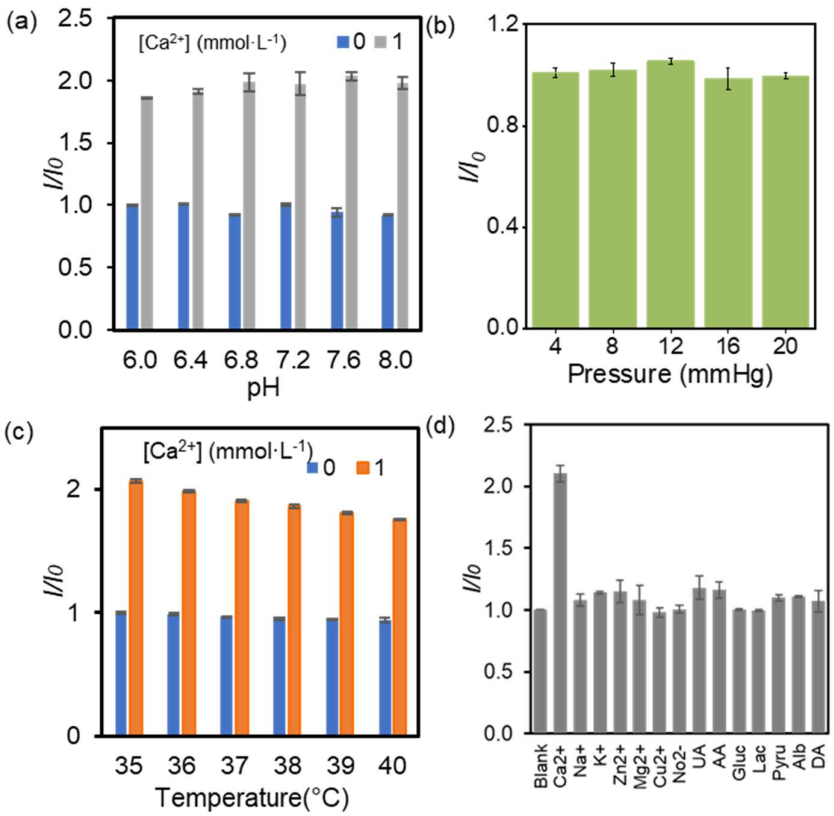


Figure 4-20. Environmental dependence and selectivity of the Ca2+ sensor. (a) Pressure dependence test using 1.0 mmol L-1 [Ca2+] Tris buffer solution with pressure from 4-20 mmHg. (b) pH dependence test using Ca2+-free and 1 mmol L-1 [Ca2+] Tris buffer solution with pH from 6.0 to 8.0. (c) Temperature dependence test using Ca2+ free and 1 mmol L-1 [Ca2+] Tris buffer solution with temperature from 36 to 40 °C. (d) Selectivity test of the Ca2+ sensor using 1 mmol L-1 [Ca2+] Tris-buffer solution with different interferents. Pyru: pyruvate; Gluc: glucose; UA: uric acid; AA: ascorbic acid; Lac: lactate; DA: dopamine; Alb: albumin. Error bars represent the standard deviation of the mean of three measurements.

4.5.6 Glucose sensor characterisation

To achieve dynamic and real-time glucose monitoring, a sensor with two sensing layers was constructed: an outer layer of glucose oxidase-immobilized polyacrylamide hydrogel for glucose redox reaction catalyzation with oxygen; and an inner layer of oxygen-sensitive probe platinum octaethylporphyrin (PtOEP) encapsulated in sol-gel film at its optimum concentration for oxygen measurement (**Figure 4-21**)[263].

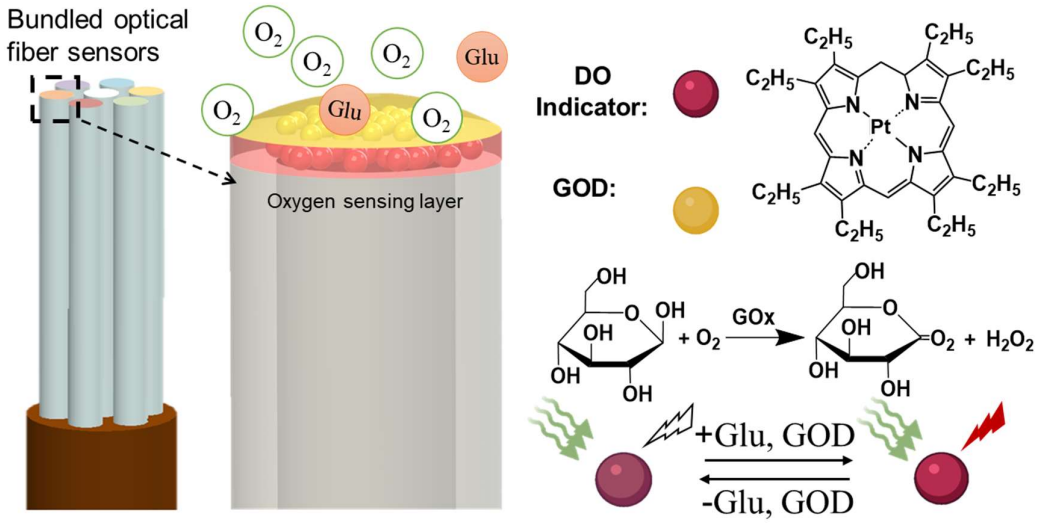


Figure 4-21. Schematic demonstration of the design and principle of the glucose sensor.

The sensor was characterized using PBS solutions with different glucose concentrations ranging from 0 to 6 mmol·L^{-1} (**Figure 4-22(a)**). During the experiment the solution was stirred at a constant speed to ensure an air/oxygen-saturated solution throughout the measurement to minimize oxygen influences. There is an equilibrium between the speed of oxygen consumption and the oxygen supply, and it can be tailored by the concentration of glucose oxidase and the stirring speed. Therefore, using this method, all detection ranges for glucose can be designed by optimizing the glucose oxidase concentration during sensor fabrication. The emission intensity of glucose sensor increased as glucose concentration rose, with a correlation between glucose concentration and emission intensity fitting a sigmoid curve (R^2=0.99), resulting in a 4-fold signal increase from 1 to 5 mmol·L^{-1} of glucose (**Figure 4-22(b)**). Good reversibility of the sensor in repeated sensing cycles were demonstrated, allowing dynamic measurement of both increased and decreased glucose levels (**Figure 4-22 (c)**). However, the sensor also suffered from photobleaching in long term exposure to the excitation light with 80% intensity remaining after 3 hours (**Figure 4-22(d)**).

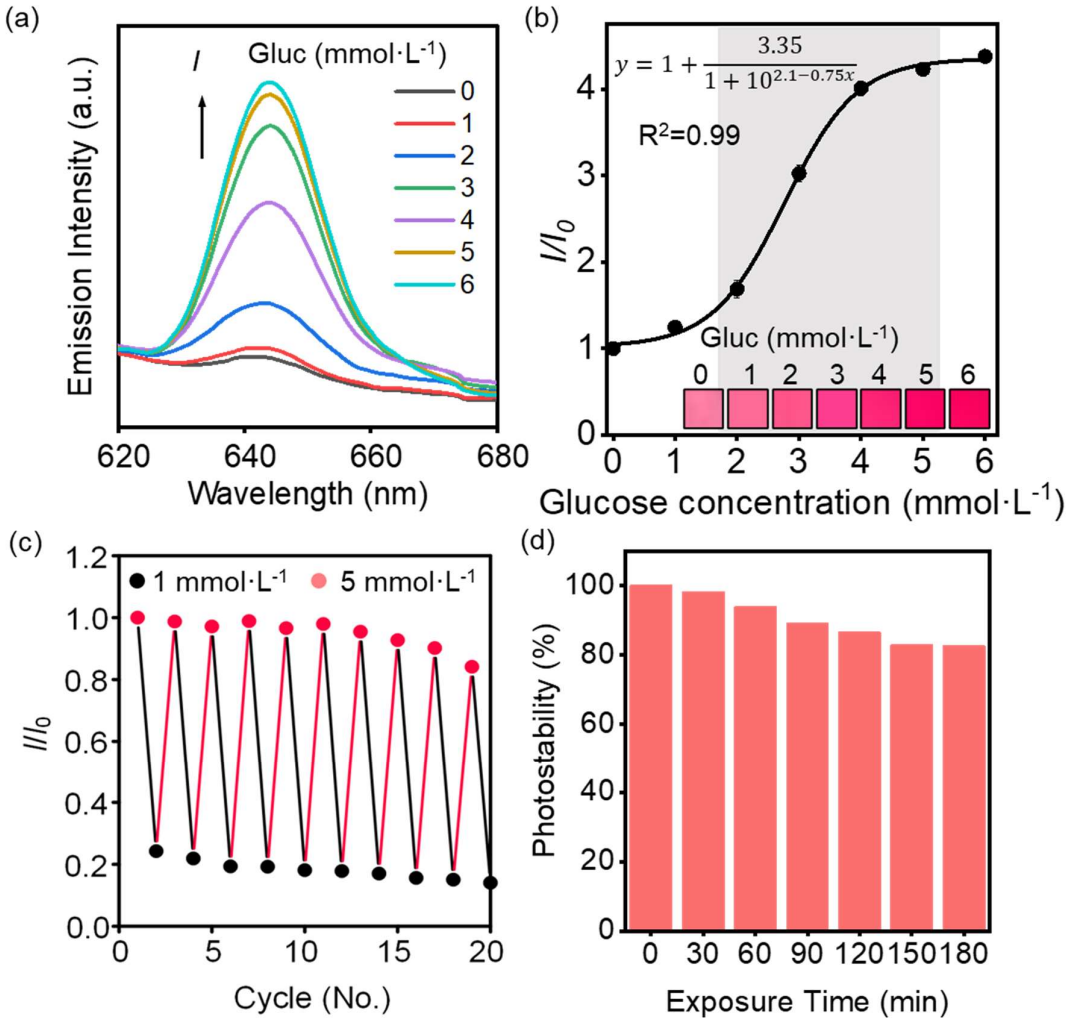


Figure 4-22. Design and characterisation of the optical fibre glucose sensor in PBS solutions (100% DO, 10 mmol L-1, pH 7.4, 25 °C). (a) Fluorescence spectra of the glucose sensor in PBS solutions with different glucose concentrations (0-6 mmol L-1). (b) The calibration curve of the glucose sensor for the measurement of 0-6 mmol L-1 glucose. Shadows represent the physiological range of glucose concentration in human CSF. (c) Reversibility test of the glucose sensor in repeated measurement of 1 and 5 mmol L-1 glucose PBS solution. (d) Photostability of the sensor under exposure to 520 nm laser light (4.5 mW) for 3 hours.

It exhibited a good robustness towards pressure (**Figure 4-23(a)**) but a 27% decrease in intensity was observed in high pH solutions, which might be due to higher glucose oxidase activity in alkaline solutions (**Figure 4-23(b)**). Higher temperature also had a quenching effect on the indicator's fluorescence, similar to the previously discussed 5 sensors (**Figure 4-23(c)**). In the selectivity test, little variation was observed when interferences were added to the solution, indicating a potential for precise glucose measurement in real clinical cases (**Figure 4-23(d)**).

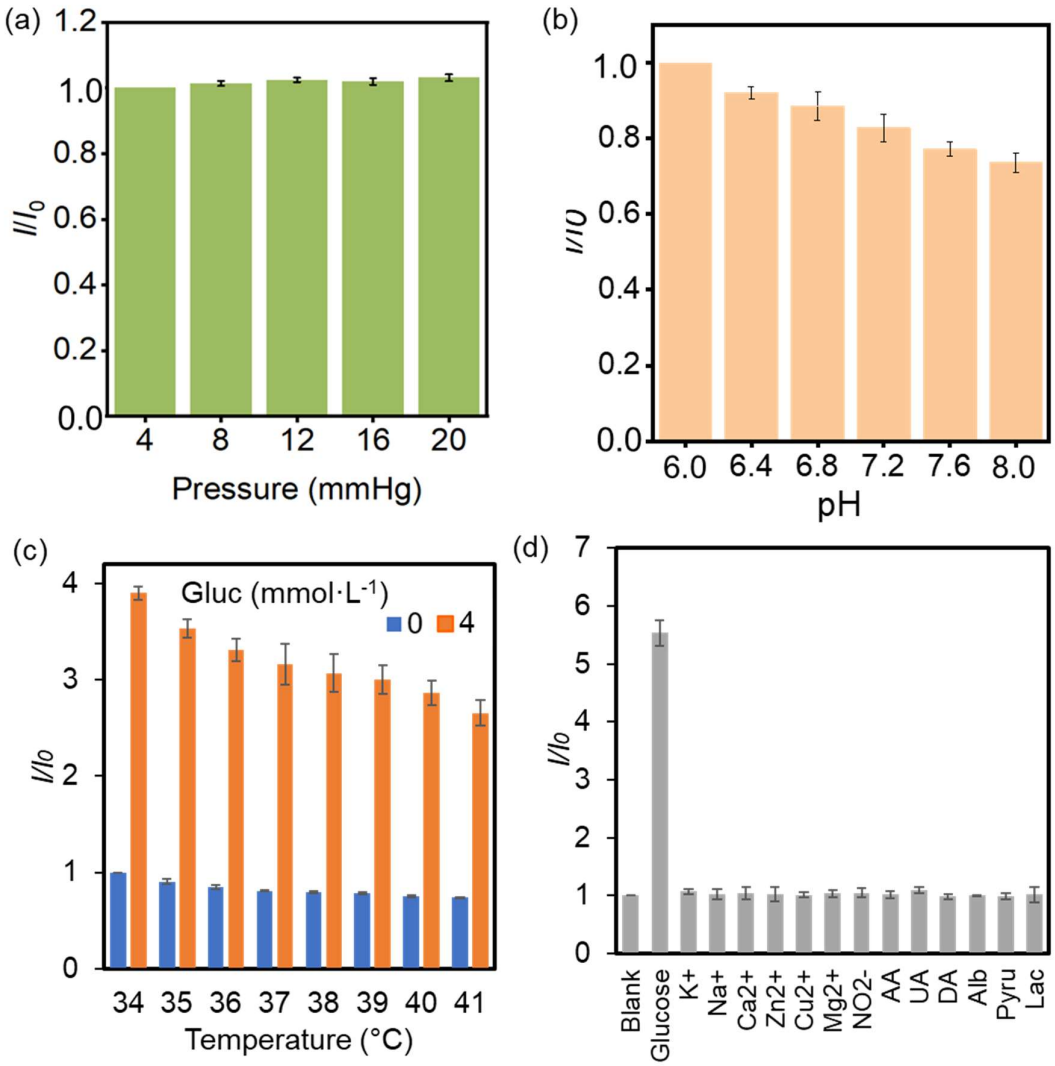


Figure 4-23. Environmental dependence and selectivity of the glucose sensor. (a) Pressure dependence test using 2 mmol L-1 glucose solution with pressure increasing from 4 to 20 mmHg. (b) pH dependence test using 2 mmol L-1 glucose solution with pH from 6 to 8. (c) Temperature dependence test using 0 and 4 mmol L-1 glucose PBS solution with temperature increasing from 34 to 41°C. (d) Selectivity tests of the pH sensor using 7.4 pH PBS solution with different interferents. AA: ascorbic acid; UA: uric acid; DA: dopamine; Alb: albumin; Pyru: pyruvate; Lac: lactate. Error bars represent the standard deviation of the mean of three measurements.

4.6 Multiplexed sensing and concentration calculation

4.6.1 Multiplexed sensing calibration

After fabricating and characterizing the 6 fluorescent sensors individually, they were integrated onto the tips of the optical fibre bundle for multiplexed sensing (**Figure 4-1**). A 405 nm laser was used for pH, DO, and glucose measurements; a 450 nm laser for Na^+ and temperature measurements; and a 520 nm laser for Ca^{2+} measurement. Calibration tests of the 6 sensors in multiplexed sensing mode

were conducted using artificial CSF (aCSF) buffer solutions (**Figure 4-24**). During multiplexed measurement, the Ca^{2+} sensor showed weaker intensity compared to other sensors, so the spare optical fibre in the bundle was coated with the calcium sensing film to enhance the signal. Overlapping emission peaks between multiple sensors were unavoidable due to shared excitation lasers, thus computational methods were used to separate the overlapped peaks and obtain accurate biomarker concentration readouts.

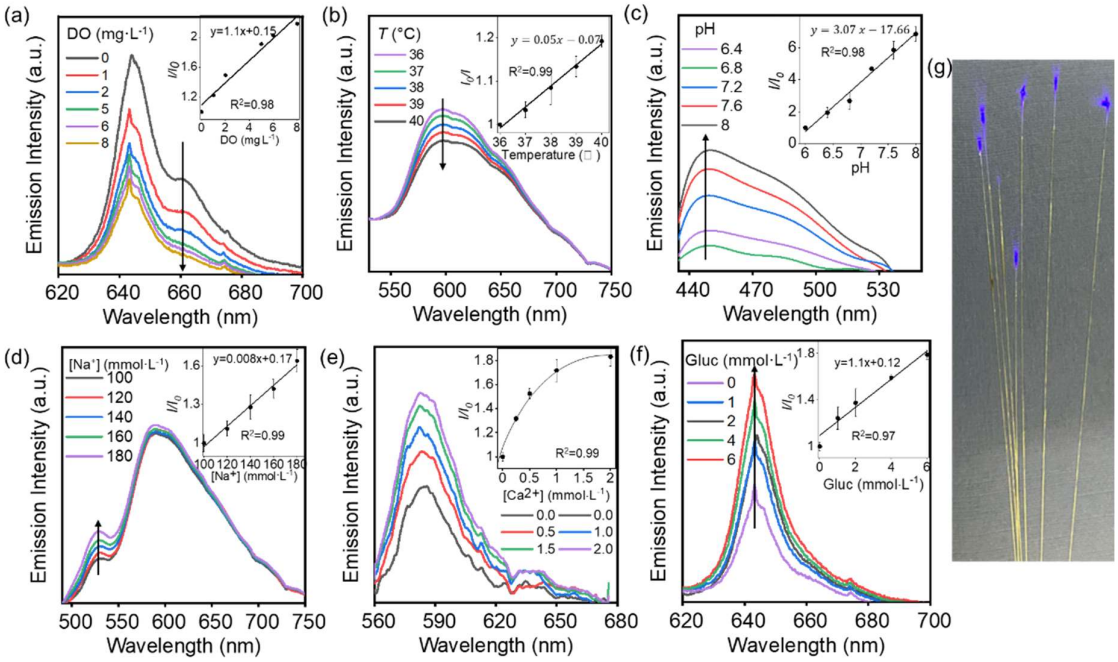


Figure 4-24. Multiplexed sensing of DO (a), temperature (b), pH (c), Na+(d), Ca2+ (e), and glucose (f) using the designed optical fibre bundle in aCSF buffer solutions. Insets are calibration curves for these 6 sensors. Insets: Corresponding calibration curves of the fabricated sensors. (g) Photo of the bundle under the excitation of 450 nm laser light.

4.6.2 Multivariate regression-based concentration calculation

There are two major overlaps in emission spectra: (1) overlapped DO and glucose sensors' spectra when excited by the 405 nm laser and (2) overlapped Na^{+} and temperature sensors' spectra when excited by the 450 nm laser. Therefore, simply calculating the biomarker concentration based on calibration curves cannot provide a reliable readout when more than one biomarker's concentrations are changing. Post-processing algorithms were designed and used after spectra acquisition to obtain reliable biomarker concentration readouts (**Figure 4-25**).

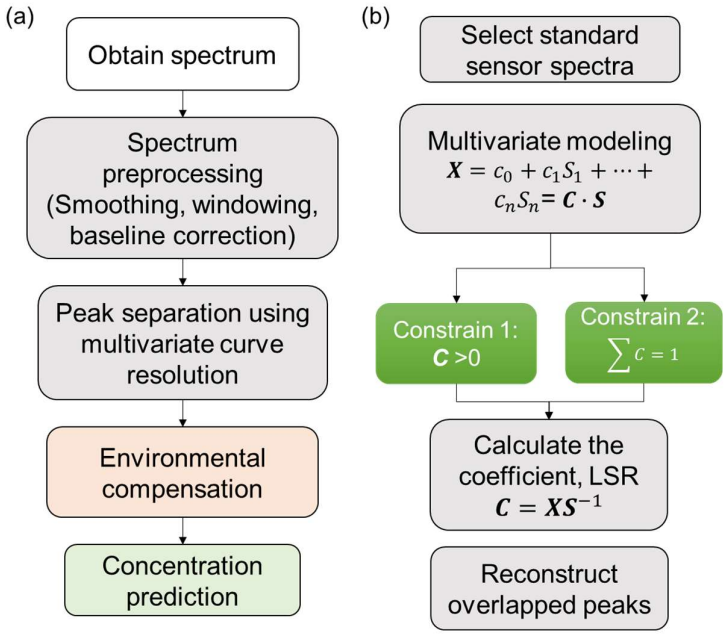


Figure 4-25. Flowchart of the post-processing method for (a) overall biomarker concentration prediction method based on the obtained spectrum. (b) Multivariate regression modelling methods for overlapped spectra processing and biomarker concentration prediction. X: acquired overlapped spectrum, C: coefficient vector, S: standard spectra, LSR: least square regression.

The spectrum was first denoised and baseline-corrected using penalized least square baseline correction algorithm (**Figure 4-26 (a)**)[264]. Multivariate curve regression (MCR) modeling was the used to learn the correlation between each sensor's standard calibration curves and the overlapped spectra for peak separations. In the separation of glucose and DO sensors' spectra, four baseline-corrected standard spectra were selected to form a standard spectra matrix for MCR modeling (**Figure 4-26 (b)**). The coefficient vector **C** obtained in the MCR models was used to separate the overlapped spectra into DO and glucose spectra (**Figure 4-26 (c)**).

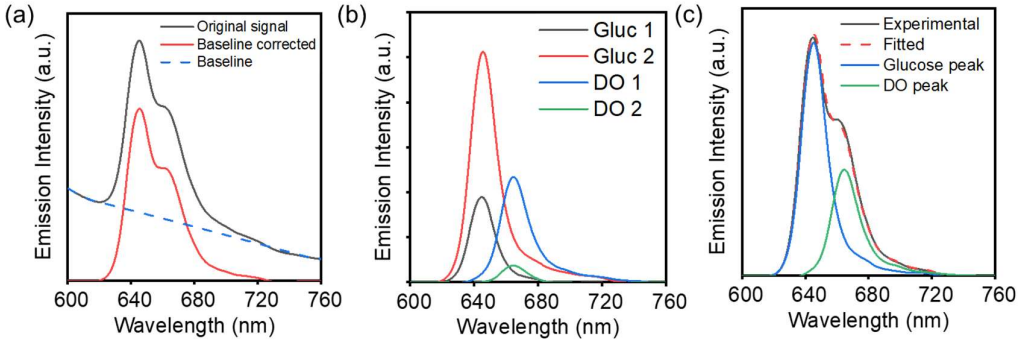


Figure 4-26. Spectrum post processing. (a) Baseline correction. (b) Standard spectra for overlapped glucose and DO spectra processing using proposed MCR. (c) Separation of overlapped DO and glucose spectra using MCR.

Under the excitation of 450 nm laser, Na^+ sensor's spectrum is overlapped with temperature sensor's spectrum. Same as the way to separate glucose and DO spectra, the standard spectrum of Na^+ and temperature are used as the standard variables for MCR model (**Figure 4-27 (a, b)**) for spectra separation and reconstruction. Under 450 nm excitation, the Ca^{2+} sensor might also be excited if the excitation laser is strong enough. The proposed MCR method is also tested for the separation of three peaks, and the algorithm showed great ability in separating three spectra to reconstructed temperature spectrum, Na^+ spectrum, and Ca^{2+} spectrum (**Figure 4-27 (c)**).

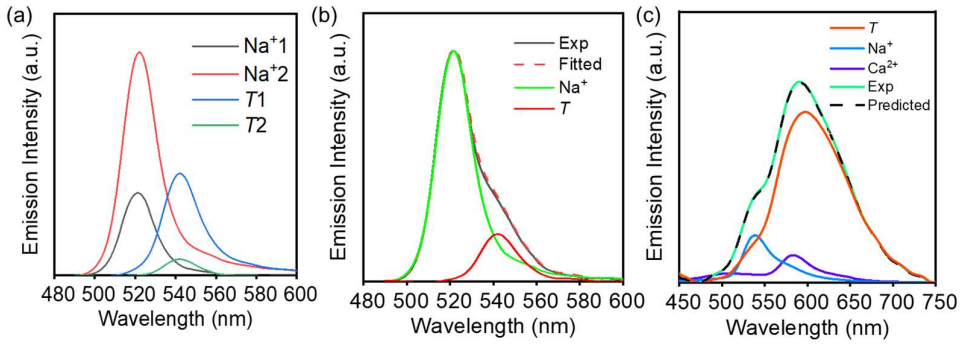


Figure 4-27. Spectra postprocessing method and concentration prediction for sodium and temperature. (a) Overlapped spectrum and separated spectra using a MCR algorithm. (b) Standard spectra selected to perform MCR. (c) Spectra separation results on 3-overlapped spectra.

Furthermore, using the obtained coefficients **C** the concentrations of the biomarkers were calculated (**Figure 4-28**)). The algorithm was applied to 40 different tests and the prediction was high with R^2>0.95. The proposed post-processing algorithms resolved the spectra overlapping problem and compensated for photobleaching and environmental influences, ensuring robust readouts for clinical applications.

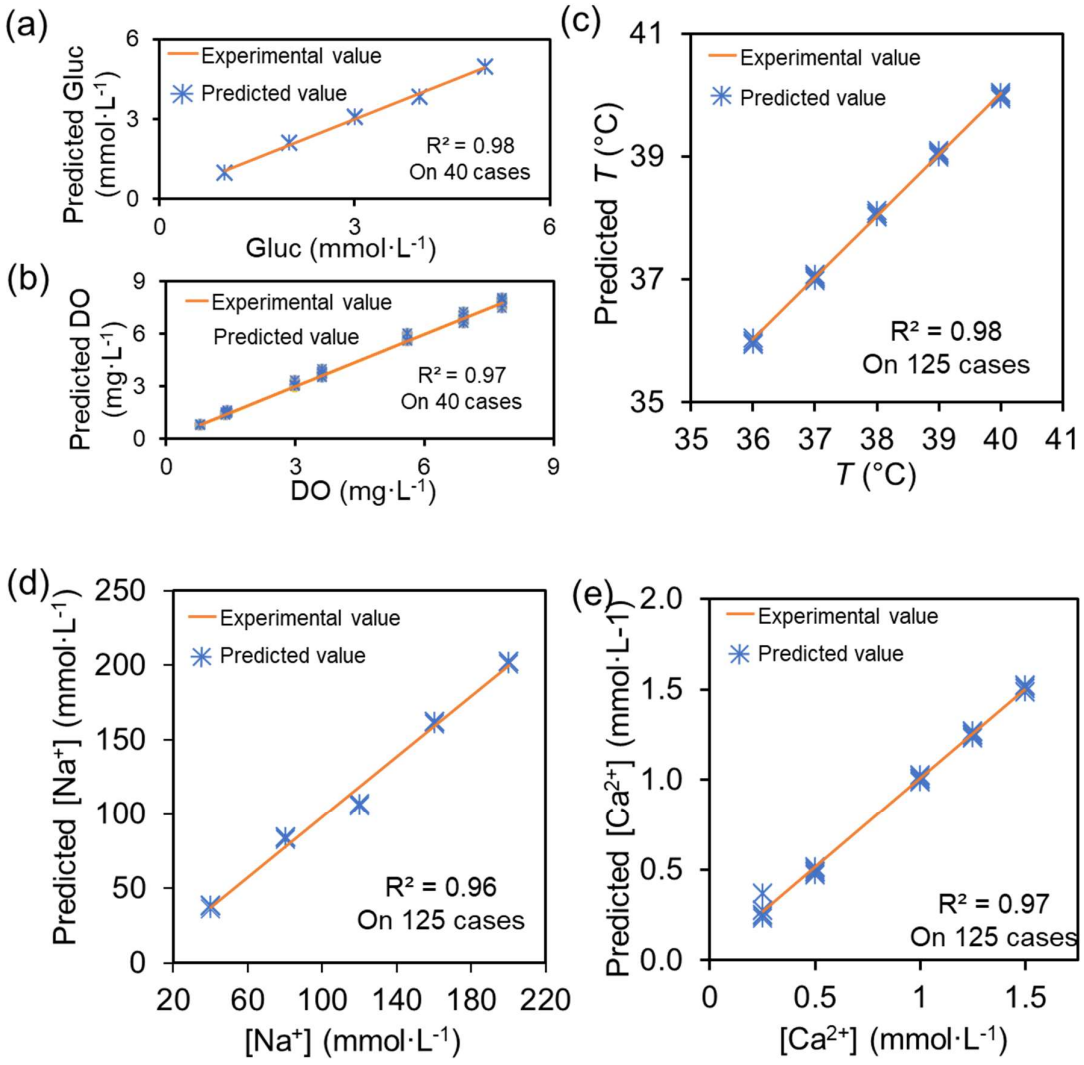


Figure 4-28. Biomarker concentration prediction results using the proposed algorithms for (a) DO (40 tests) and (b) glucose (40 tests) under the excitation of the 405 nm laser, (c) temperature (125 tests) and (d) Na+ ion (125 tests) under the excitation of 450 nm laser, and (e) Ca2+ ion (125 tests) under the excitation of 520 nm laser.

4.4.3 Environmental compensation

To eliminate temperature and photobleaching effects on emission intensities, correlations between emission intensity and environmental temperature and exposure time were modelled and used to estimate the emission intensity values under the same temperature (37 °C) and at the initial exposure (t=0) based on individual sensor characterisation results. After obtaining the correlation between exposure time/temperature and intensity, the obtained intensity is corrected to room temperature and time 0 point for modelling. Glucose concentration was further corrected based on the DO and pH

values (Method). The compensation methods were tested on the individual sensors (**Figure 4-29, 4-30**) and it is shown that the methods could accurately correct the influence of photobleaching and temperature on the sensor emission intensities.

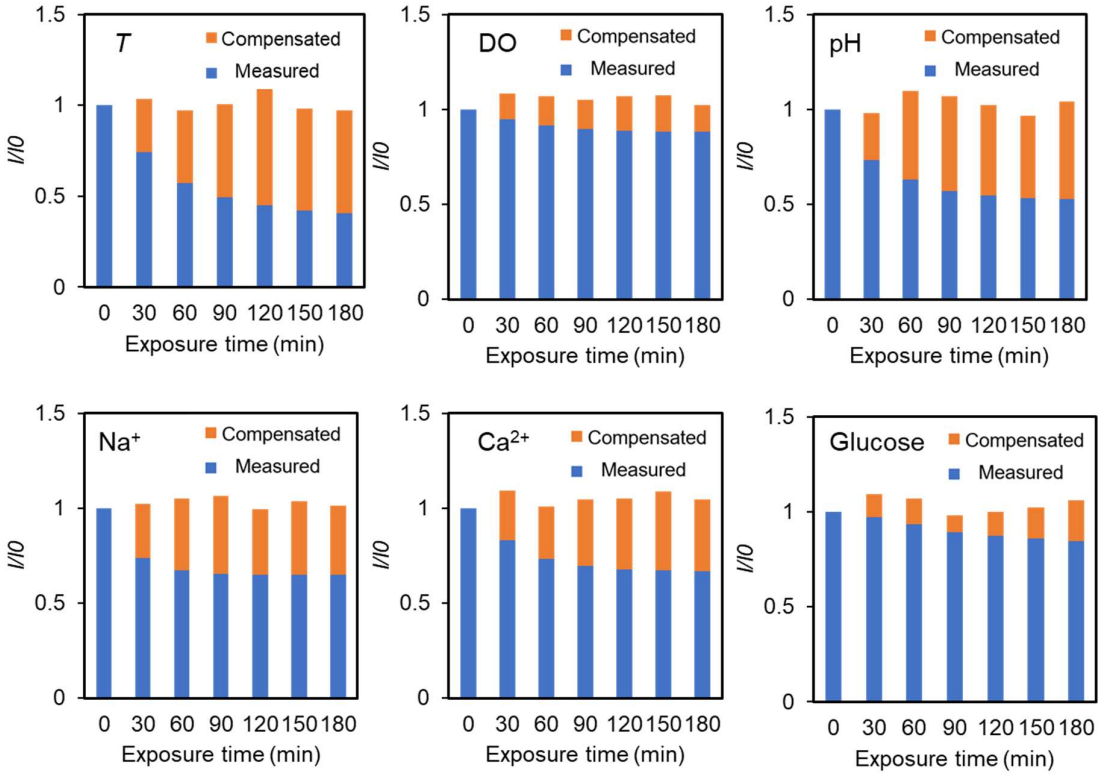


Figure 4-29. Photobleaching compensation algorithm results for the 6 sensors.

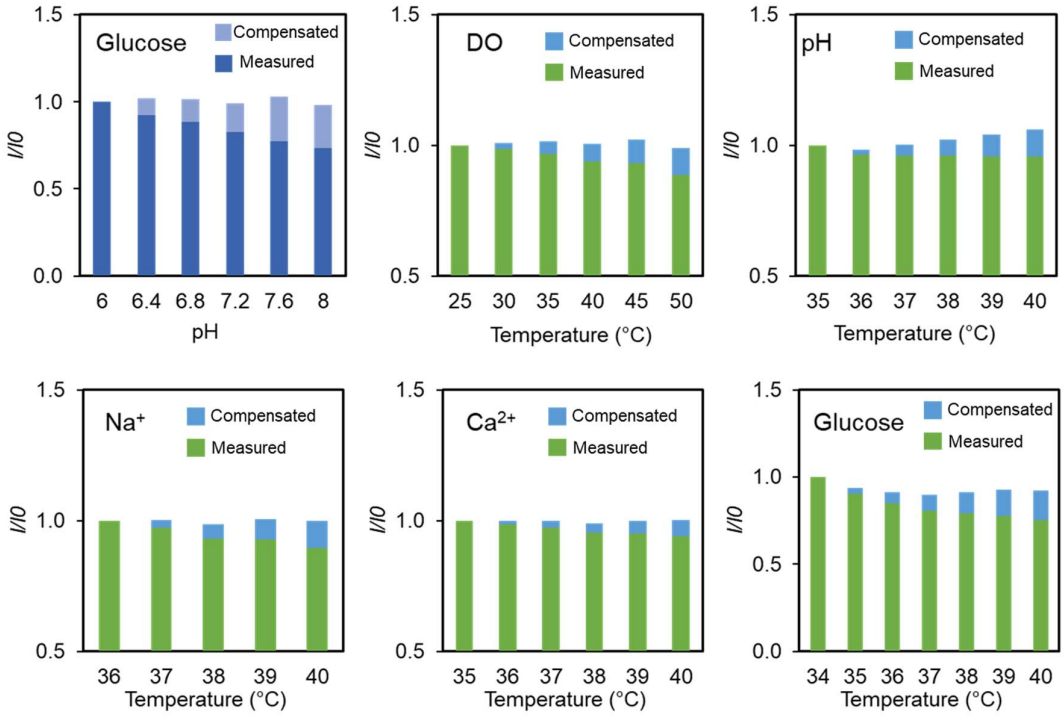


Figure 4-30. Temperature and pH compensation algorithm results for the 6 sensors.

4.7 Multiplexed sensing validation

Secondary injury is a common syndrome in TBI, occurring gradually after the initial brain insult due to brain inflammation, elevated pressure, swelling, etc. It plays a major role in the long-term brain damage and death. Unlike the first insult to the brain, secondary brain injury can be partly prevented through close monitoring of the brain physiologies to identify complications and take immediate interventions. Herein, the proposed system was tested for multiplexed continuous monitoring of these 6 brain biomarkers using lamb brain models and to mimic a simplified TBI secondary injuries[11]. . **Figure 4-31 (a)** demonstrate the designed way of the sensor to be used for brain monitoring. Similar to the ex vivo study using lamb brain conducted in chapter 3, here, I also evaluated the bundle-based sensing system performance in lamb brain models. As observed in the continuous monitoring experiment introduced in Chapter 3, the previous sensing system showed unstable readout while performing continuous monitoring using lamb brain models due to the direct contact between the soft sensing film and the brain tissue. Slight pressure changes while compressing the sensor to the brain tissue would lead to signal intensity changes due to the air gap between the film and the fibre tip.

However, the updated sensing system proposed here could avoid this issue as the sensors are protected in a medical catheter. No direct contact between the brain tissue and the sensor tips was needed for the measurement. The performance in in situ measurement was measured here.

Fluorescent sensors for the 6 biomarkers were coated on the fibre bundle tips (**Figure 4-31 (b)**) and inserted into a CSF drainage catheter, facilitating interactions between the sensing films and brain biomarkers in deep brain tissues. Three laser lights (405 nm, 450 nm, 520 nm) were used in turn to generate real-time fluorescence signals, which were collected by the spectrometer and analysed offline by post-processing algorithms. Artificial CSF buffer solutions were prepared according to references to simulate the brain physiologies after TBI. For the measurement, clean lamb brains were soaked into the prepared solution (Section 4.4.7) with the designed system catheter inserted in, and the brain physiology progression was established by continuous extraction and addition of the prepared aCSF solutions of different phases.

As shown in **Figure 4-31 (c)**, the multiplexed brain monitoring system first indicated the occurrence of hypoxia, shown by a high temperature of 38 °C and low DO of 3.2 mgL^{-1} due to the decrease in cerebral blood flow after the initial insult., By releasing brain pressures, hypoxia can be improved to a normal stage. As the damage keeps progressing, decreased respiratory rates and ATP production in TBI patients lead to glucose and oxygen depletion, causing another brain complication called hypermetabolism. As shown by system readout, elevated temperature (39 °C), decreased DO (3.8 mgL^{-1}), and glucose (1 $mmolL^{-1}$) were observed in this stage. The cascade of mismatched processes of metabolism and cerebral overflow with accumulated sodium and calcium ions creates excitotoxicity as shown by decreased pH (6.5) and increased Na^{+}(180 $mmolL^{-1}$) and Ca^{2+} ions (3 $mmolL^{-1}$) with the proposed sensing system. Prediction accuracy of the system was evaluated using mean square error (MSE) and mean absolute error (MAE) of the predicted value with the prepared buffer concentrations. An MSE of 0.89, 0.07, 0.01, 22.54, 0.04, 0.13, and an MAE of 0.76, 0.21, 0.26, 3.83, 0.50, 0.9 were obtained for temperature, DO, pH, Na^{+} ions, Ca^{2+} ions, and glucose sensors respectively, indicating promising results for continuous and precise biomarker monitoring. The designed system offers long-term monitoring of 6 biomarker simultaneously with high accuracy and the system has a fast response

(< 5 min) for the tracking of disease progress. Both increasing and decreasing biomarker concentrations were correctly identified in three disease complication models, suggesting potential for clinical brain monitoring and timely treatment of secondary brain injuries.

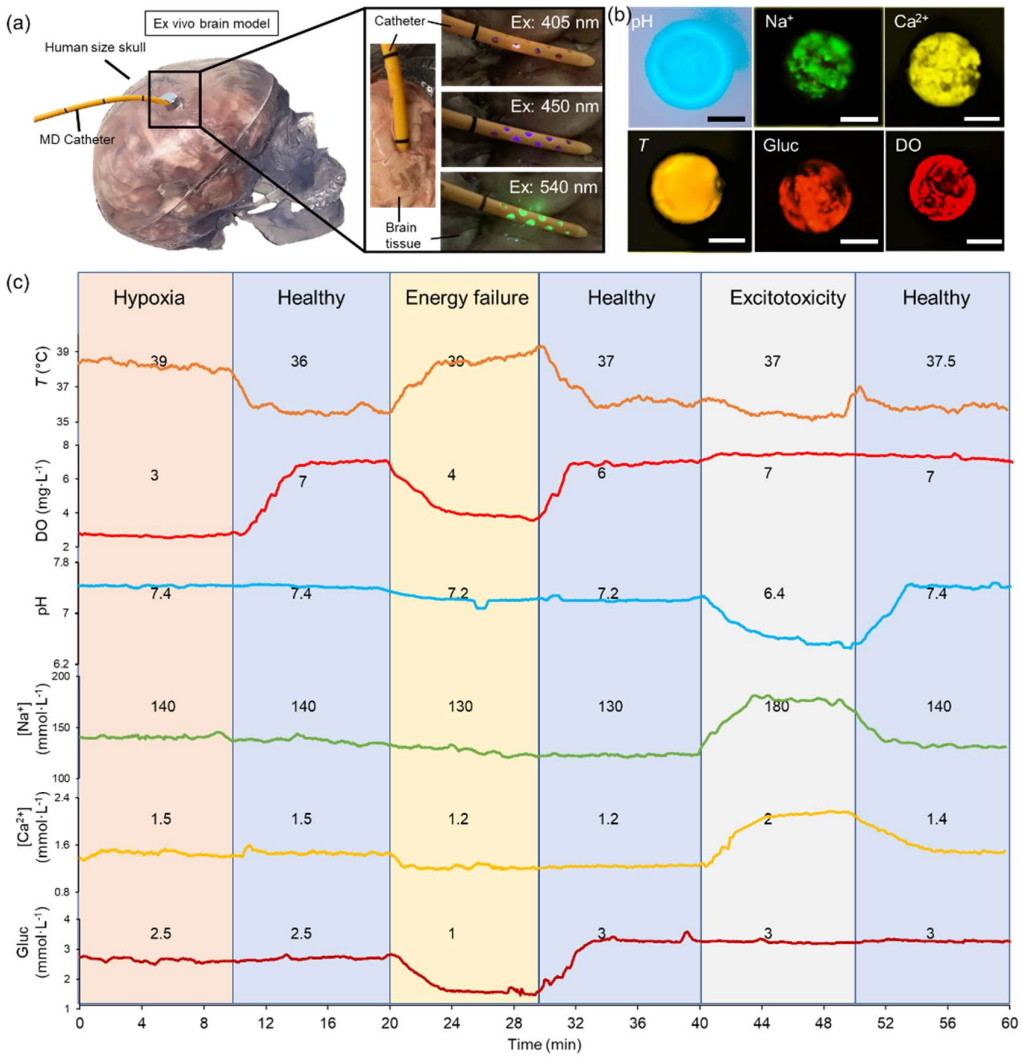


Figure 4-31. Multiplexed sensing using the optical fibre bundle sensors in lamb brain models with three mimicked brain complications in TBI. (a) Photographs of a lamb brain model to demonstrate how the sensor can be used for in situ measurement. Optical fibre sensing system integrated in a microdialysis catheter was inserted into the brain model. Three lasers were switched to excite the sensing films. Scale bar = 50 μm. (b) Fluorescent photos of the 6 sensing films on the tips of the fibre bundle. (c) Continuous monitoring of three complications, hypoxia, energy failure, and excitotoxicity, and the recovery from the complications to healthy stages. The data shows time dependent biomarker changes in different brain physiology stages and stage transitions.

4.8 Conclusion

In this chapter, a miniaturized and multiplexed optical sensing system was developed using self-designed optical fibre bundles and fluorescent sensors for simultaneous measurement of 6 biomarkers

in brain CSF. Different from the previous chapter that uses a single-channel reflection fibre for 4 biomarker measurement, this new design allows multiplexed brain monitoring with more freedom, better performance, and lower sensor dimension. Regression-based computational post-processing algorithms were integrated to provide dynamic and multiplexed biomarker monitoring with high accuracy and robustness in various environmental conditions, showing a promising potential for clinical brain monitoring. In the first part, the optical fibre bundle was designed and fabricated for multiplexed sensing with specific focus on maximizing light transmission and emission collection. However, the small scratches on the fibre surfaces resulted from manual polishing might attenuate the light transmission, which can be improved by adopting better optical fibre bundle fabrication or polishing methods. Six fluorescent sensing films were fabricated and optimized on the bundled optical fibres for temperature, DO, pH, Na^+, Ca^{2+}, and glucose measurement. The fluorescent indicators and the encapsulation polymeric support were optimized according to the properties of the target analytes to provide high sensing sensitivity, selectivity, stability, and reversibility. The number and type of biomarkers to be measured can be further increased and achieved by bundling more optical fibres together and using different recognition probes. The validated biosensing films can be applied in diverse changes in human physiological conditions. In the measurement, a tradeoff exists between fibre sizes and signal intensity as larger fibre cores provide stronger signals but come with increased probe dimensions. In the future, tapered or D-shape fibres with larger sensing areas could be employed to enhance signals without compromising overall sizes[265, 266]. Characterisation of the sensing films revealed great sensing sensitivity and selectivity towards the target biomarkers, however, photostability and environmental influences as two major concerns. Therefore, non-linear regression models were proposed for environmental and exposure compensations and the results have proved the feasibility potential for applications in various environmental conditions. To solve the spectra overlapping challenges in multiplexed sensing, MCR was proposed to separate the overlapped signals from each sensor and predicted the biomarker concentrations with small errors, and advanced peak separation algorithms including deep learning models can be further explored to improve the sensing accuracy[267]. However, the multiplexed monitoring system is still restricted by light sources, since the current lasers need to be switched manually and only have one fixed output power. A multi-

wavelength laser system with adjustable powers would prompt fast and automatic measurement of the biomarkers. In the validation tests, the optical fibre bundle sensing system successfully tracked concentration variations in lamb brain models. The system is minimally invasive, multiplexed, sensitive, selective, robust, fully reversible, and suitable for long-term applications. It holds great promise for precise and continuous monitoring of deep brain physiologies.

Chapter 5 A Fully Automated and AI-assisted Optical Fibre Sensing System for Multiplexed Biomarker Monitoring

Fully-automated and comprehensive monitoring aids in the early identification of any changes or deterioration in the patient's brain function, enabling timely interventions and personalized treatment strategies. In previous chapters, a multiplexed optical fibre sensing system was proposed and optimized for accurate biomarker monitoring. However, the proposed system can hardly achieve fully automated monitoring and requires manually switching the laser lights for the excitation of the films. It also suffers from spectra overlapping. Although a multivariate based regression method was proposed to separate the mixed signals, the accuracy can be further improved. In this chapter, an AI-integrated, fully automated, and miniaturized optical fibre sensing system is prototyped based on the findings of previous chapters to realize continuous accurate brain monitoring. Machine learning based processing and training algorithms for the simultaneous prediction of six brain biomarkers were investigated, including spectrum merging method, baseline correction algorithms, feature extraction and selection, and comparison of four regression models. Furthermore, the application of convolutional neural network (CNN) by learning the correlation between neighbouring fluorescent peaks has greatly improved the prediction results of six biomarker concentrations (average R^2=0.96). The optimized CNN model was then integrated with a user-friendly interface for continuous readout of biomarker concentrations with high precision in real-time. In the end, the proposed sensing system was successfully validated using both aCSF and clinical human CSF samples, indicating its great potential for real life clinical applications.

5.1 Fully-automated and multiplexed sensing system

In this chapter, an optimized and fully automatic sensing system using optical fibre bundle sensors is introduced based on the results from the previous chapters. In order to overcome the limitations of the sensing system presented in the previous chapter- lasers need to be changed manually, non-adjustable power, and lack of proper readout and control system, here a multi-wavelength laser system that contains three programmable lasers is used with a self-developed readout software for user interface

and customized readout. The system is also a prototype for the proposed multiplexed brain monitoring system introduced in the previous chapters to be used directly for on-line continuous biomarker monitoring. As shown in **Figure 5-1(a)**, the fully automatic system includes three major parts, a 3D printed box for holding the optic components and ensuring a stable signal; An optical sensing setup that includes a multi-wavelength laser (405nm, 488nm, 520nm), a spectrometer for fluorescent spectrum measurement, an edge computer for the control of laser light and spectrometer. It is also used for spectrum post-processing and biomarker concentration prediction using computational models. The connection of the laser and spectrometer is realized using a 2*1 optical fibre coupler that one arm of the coupler is connected with the spectrometer and another arm is connected with the lasers. The third arm of the coupler is connected with the functionalized fibre bundle for fluorescent measurement. The bundle-based sensing system is same as introduced in chapter 4. As shown in **Figure 5-1(b,c)**, six different fluorescent sensing films designed for the measurement of pH, DO, temperature, Na^{+}, Ca^{2+}, and glucose are coated on the tips of the fibre bundle. Details of the sensing films can be found in chapter 4. The optical waveguide is as illustrated in subfigure **Figure 5-1(b)**, where the laser light is delivered to the sensing film via the coupler and the fluorescent signal of the sensing films is delivered to the spectrometer and readout by the microcontroller. Communication and control between the components are realized through self-developed software. The software has three functions **(Figure 5-1(d))**, one controls the lasers and spectrometer, one performs calibration of the sensors, and the other one calculates the biomarker concentrations based on the acquired fluorescent spectrum. Two readout methods are provided by the software, single biomarker dynamic readout and multiplexed readout for the users to select.

As introduced in the previous chapter, the calculation of the biomarker concentrations is based on a multivariate regression model which models the correlation of the overlapped spectra with standard biomarker fluorescent spectra, and based on the coefficient value the concentration can be calculated. To further improve the readout precision, machine learning algorithms and deep learning algorithms were also explored in this chapter and compared with the regression models for more accurate and robust readout. For shallow machine learning algorithm, different features were

extracted, and various regression models were built and compared for the best prediction outcomes. For DL models development, CNN architecture with convolutional block for deep feature extraction was used to improve the prediction accuracy.

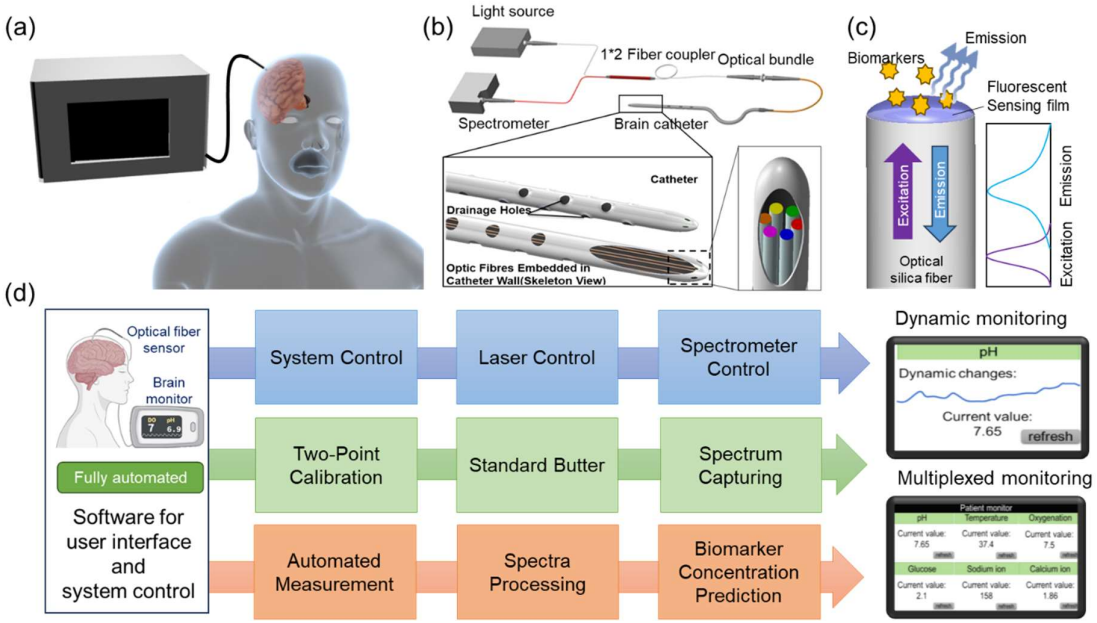


Figure 5-1. A brain monitor based on optical sensors and computational software. (a) A bedside monitor for continuous brain monitoring by inserting a catheter in brain tissues. (b) The optical sensing setup for the monitor, including a multi-wavelength laser source, a spectrometer for spectrum capturing, a catheter-integrated and functionalized optical bundle for multiplexed biomarker measurement. (c) Optical fibre sensor for biomarker measurement based on fluorescent spectroscopy. (d) Software for the development of brain monitor, which includes three parts, hardware control, sensor calibration module, and measurement and readout module.

5.2 Materials and Methods

In this section, the methods for building machine learning and deep learning models for the prediction of 6 biomarker concentrations based on obtained optical spectra are presented. Different from MCR for multiple biomarker concentration calculation, the models proposed here are ML-based models that required a labelled dataset for the training. It involves the processing of the obtained signals, feature extraction methods, and model architectures. The optimized machine learning and deep learning models were further validated using clinical human CSF samples and the experimental procedures are included here.

5.2.1 Machine learning model for multiplexed biomarker concentration prediction

To realize online continuous readout of these 6 brain biomarkers simultaneously, machine learning models were trained and built to realize accurate readout based on the obtained spectra. In this study, three spectra are obtained in each scan, they are fluorescent spectrum including the information of pH, glucose, and DO under the excitation of 405 nm laser light, fluorescent spectrum for the sodium ion and temperature sensors under the excitation of 488 nm laser light, and the fluorescent spectrum for the readout of calcium ion under the excitation of 520 nm laser light. Here, machine learning methods are demonstrated for the calculation of the biomarker concentrations using the obtained spectra, including the dataset generation, feature extraction, and regression modelling (**Figure 5-2**).

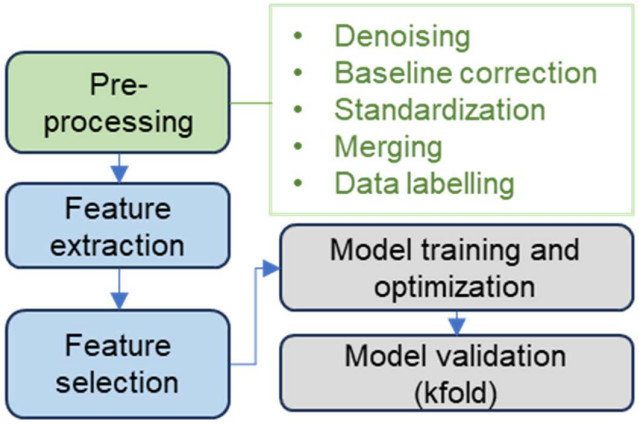


Figure 5-2. Pipeline for machine learning model development.

Dataset

The dataset was obtained by placing the multiplexed fibre bundle in standard PBS buffer solutions with varied biomarker concentrations. Each obtained spectrum was labelled with the biomarker concentrations of the standard buffer solution. A total dataset of 18875 spectra, containing different combinations of the 6 fluorescence sensors under various concentrations were obtained for model training and validation. The total exposure time until the capturing of each spectrum was also recorded for photobleaching correction.

Data preprocessing

Before feeding into the machine models for model training, the spectra were first pre-processed to remove the irrelevant information and noise. The baselines of the spectra were corrected to eliminate the background effects. Then the processed spectra were merged into one spectrum for the model input.

After obtaining the spectrum, Savitzky-Golay filter was used to smooth the spectrum based on local least-squares polynomial approximation, which has been frequently employed for signal processing[268, 269]. Savitzky-Golay filter performs well especially in smoothing noisy data obtained from chemical spectrum analysers as it removes noise while maintaining the shape and height of waveform peaks without causing a shift in the signal. The filter can be seen as a lowpass filter that is capable of both removing high-frequency noises and attenuating low-frequency components of a signal. The algorithm is based on the polynomial fitting of the spectrum and here a polynomial order of 3 was used to correctly smooth the signal while avoiding peak shifts.

Baseline correction

The same baseline correction method was used here as described in 4.4.6. Briefly, the baseline correction algorithm was based on an adaptive regression methods to find the optimal fidelity and roughness balance to find the baseline.

Data merging

Each spectrum obtained contains 741 intensity values, and the independently obtained three spectra of three laser lights are merged into 1 dataset by simply stacking them along the axis to obtain 2,223 intensity values in each set. It is noticed that 842 intensity values are irrelevant to the biomarker concentrations as these values stay the same in every dependent variable, which were then removed from the dataset. Therefore, a total of 1,381 values were utilized in each scan of the 6 sensors (**Figure 5-3**).

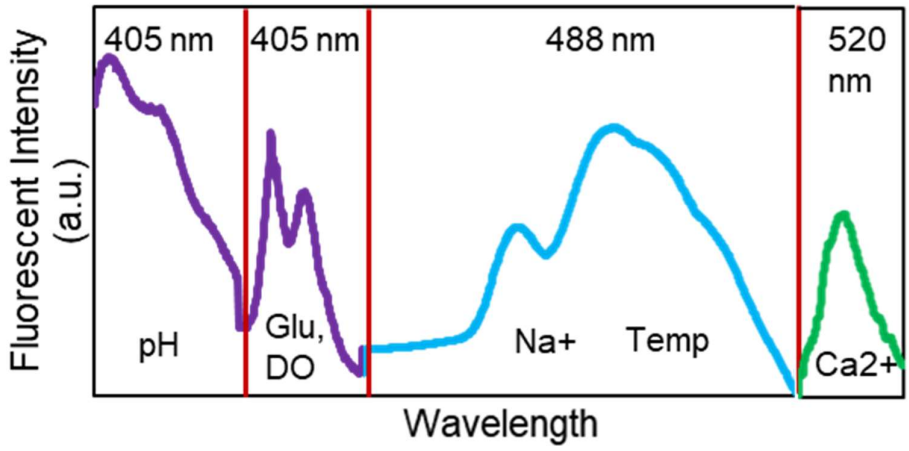


Figure 5-3. Merged signal of three optical spectra obtained with 405nm, 488nm, and 520nm lasers in one scan.

Feature extraction

The following features were extracted for machine learning model trainings for the aim to build a robust intelligent model for accurate biomarker concentration prediction (**Figure 5-4**).

Peak height

The key feature is the peak height because it changes significantly with different values of biomarkers due to the fluorescent sensing principles. There are six major peaks in the spectrum, and they are taken as the intensity value of six fixed wavelengths. The peaks at 450 nm (position 34), 640 nm (position 328), 660 nm (position 341), 540 nm (position 725), 600 nm (position 884), and 580 nm (position 1262) are correlated with the pH, glucose, DO, Na^{+}, temperature, and Ca^{2+} levels of the sample respectively. The peak heights (intensity) at these mentioned points were extracted as the first feature for training.

Peak width

Another feature is peak width, which changes in accordance with the corresponding biomarker concentrations. Although the changes might not be as significant as peak height, it was still extracted from the spectra as an input for model training. Peak width is quantified as the horizontal distance of the peak at half peak height. The width would change when the height shifts at different

concentrations. The feature was extracted using the scipy.signal.find_peaks functions from the SciPy library in python. The returned value from the function included 8 components due to the two additional peaks in the pH region in some datasets. The widths that correspond to the 6 sensor's maximum emission peaks were used for analysis.

Area under curve

The area of each peak was also used as another feature for the model training. It was calculated based on the trapezoidal integration rule. The boundaries of each peak are defined by finding the local minimum values. The areas were divided into 6 areas based on the starting and ending points of each area, defined by the peak properties of the pH, glucose, DO, Na+, temperature, and Ca2+ sensors' emission spectrum.

The trapezoidal portions are divided automatically by function, calculation equation explained in Eq.5-1, 5-2. The areas are separated into six areas by defining the starting and ending points of each area, including pH, glucose concentration, DO, sodium concentration, temperature, and calcium concentration. The calculation of area was realized using the equations below.

$$h = \frac{b-a}{n} \quad \textbf{(Eq. 5-1)}$$

$$Area = \int_a^b y dx \approx \frac{1}{2} h(y_0 + y_n + 2\sum_{n=1}^{n-1} y_n) \quad \textbf{(Eq. 5-2)}$$

a and b are the starting and ending point of an area respectively. n is the number of trapezoidal portions, and y is the height of each trapezoidal portion.

Peak position

It is noticed in the spectra that the peak shifts slightly at different concentrations of biomarkers. Therefore, the peak position is computed as another feature for training the models. The peaks are computed by finding the local maximum in the dataset. Only peaks near the emission maximum wavelength are considered as the accurate emission peaks (450 nm (position 34), 640 nm (position

328), 660 nm (position 341), 540 nm (position 725), 600 nm (position 884), and 580 nm (position 1262)) .

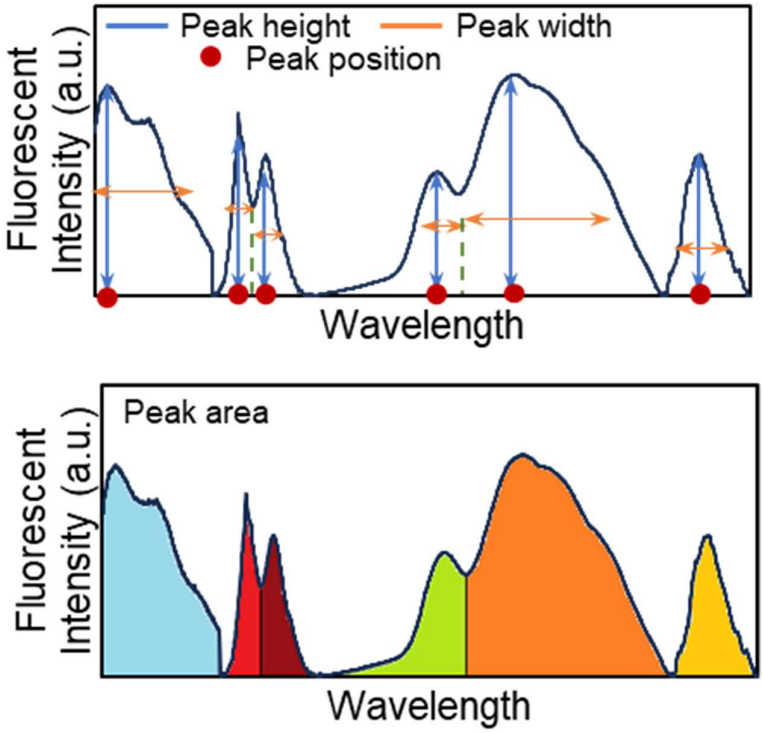


Figure 5-4. Feature extraction.

Feature evaluation selection—Pearson correlation coefficient

For each dataset, a total of 24 features were extracted that indicate the information of the emission peak of the 6 sensors. However, the features were manually extracted based on the assumption that they were related to the biomarker concentrations. To validate the assumption, The Pearson Correlation Coefficient was calculated to study the real correlation between the features and the biomarker concentrations. Only relevant features were used for the calculation of biomarker concentrations and non-relevant features were discarded to reduce the feature dimension and computation complexity. Pearson correlation coefficient (r) is calculated as below:

$$r = \frac{\sum(x_i-\bar{x})\sum(y_i-\bar{y})}{\sqrt{\sum(x_i-\bar{x})^2}\sqrt{\sum(y_i-\bar{y})^2}} \quad \textbf{(Eq. 5-5)}$$

where n is the sample size, x is the feature values, y is the biomarker concentration.

The Pearson correlation was calculated using software Origin. The value of r indicates the correlation between the extracted features and the target biomarker concentrations, where r is always between -1 and 1. A positive r indicates a positive correlation between the feature and the concentration, and a higher r indicates a stronger correlation. A negative r indicates a negative correlation between the features and the concentrations, and a smaller r means a stronger negative correlation. Only strongly correlated features (the absolute coefficient |r|>= 0.3) were included in the model training.

Machine learning regression models

***Linear Regression*:** Linear regression models the relationship between a dependent variable and one or more independent variables by fitting a linear equation to the data. Simple linear regression has one independent variable, while multiple linear regression handles multiple predictors. For linear regression, there is no specific hyperparameters that needs to be tuned.

***Lasso Regression (L1 Regularization)*:** Lasso (Least Absolute Shrinkage and Selection Operator) is a linear regression technique that adds a penalty term based on the absolute values of the coefficients. Lasso can be used for feature selection and helps prevent overfitting by encouraging some coefficients to be exactly zero, effectively eliminating irrelevant features. The hyperparameter to be tuned is *alpha,* which is the inverse value of the L1 regulation degree.

***Ridge Regression (L2 Regularization)*:** Ridge regression is another form of linear regression with a penalty term, but this time based on the squared values of the coefficients. It's used to mitigate multicollinearity (correlations between independent variables) and reduce the impact of large coefficient values. Ridge doesn't force coefficients to zero, but it shrinks them. The hyperparameter to be tuned is *alpha,* which is the inverse value of the L2 regulation degree.

***Bayesian Regression*:** Bayesian regression is a framework that applies Bayesian statistics to linear regression. It estimates the posterior distribution of model parameters, allowing for uncertainty quantification. Bayesian regression is useful when prior knowledge is incorporated, or a better understanding of parameter uncertainty is needed. It provides a distribution of possible parameter values instead of a single point estimate. There are two parameters that need to be tuned alpha1 and

alpha2 which is related to the prior regulation of the model.

Hyperparameter fine tuning and model validation

As described above, four regression models were selected for the task: to estimate the 6 biomarker concentrations using the optical spectra from the 6 sensors. For each regression model, there would be some hyperparameters that need to be tuned for best model performance. Grid search, being one of the most common methods, finds the best hyperparameters by analysing the model performance trained with all possible combinations of hyperparameters. However, due to the comprehensive search methods, grid search might take a long time to find the optimal hyperparameters. Considering that this is a multi-task problem, as the same dataset and model are used for the calculation of 6 biomarker concentrations, the hyperparameters that needed to be tuned for each model are displayed in Table 5-1. The grid search process is the same as introduced in 3.3.8.

Figure 5-5. Tuned hyperparameter list for regression models

Model	Hyperparameter Lists	Value
Linear	-	-
Ridge	alpha	[0.1, 1, 5, 10, 20,100]
Lasso	alpha	[1e-8, 1e-4, 1e-2]
Bayesian	alpha_1, alpha_	[1e-6, 1e-5, 1e-4] [1e-6, 1e-5, 1e-4]

For the training and optimizing process, the complete dataset underwent a 75/25 split for training and testing purposes, with 75% allocated to training and 25% to testing. Parameter tuning and model comparison were conducted on the training dataset using a 10-fold cross-validation approach. This entailed partitioning the training set into 10 subsets, with 9 used for training and 1 for validation, iterated 10 times (**Figure 5-6**). Validation accuracy was assessed using metrics including R^2, MSA, and MSE. Through this iterative validation process, model hyperparameters were optimized, and the most effective model was selected by comparing the outcomes of various regression models. Following the identification of the optimal model, it underwent testing using the reserved testing

dataset, which had not been previously utilized for model training. Performance evaluation was based on metrics including MSE, MAE, and R^2.

The calculation of MSE, MAE, and R^2 were achieved using the metrics function of Scikit-learn library.

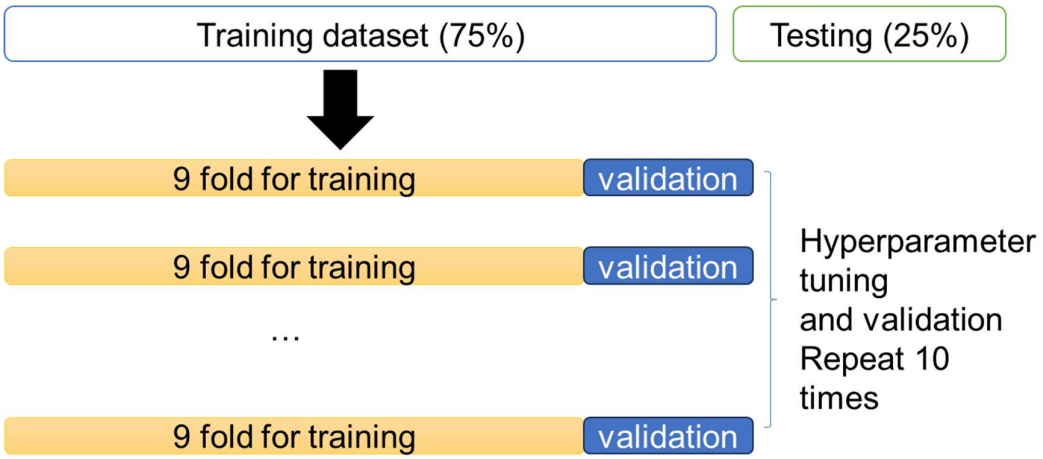


Figure 5-6. Dataset split methods for training, validation, and testing.

Online processing

The final goal of the system is being used in real life scenarios. To achieve this, the developed optimal model would be used for online processing, meaning the model is fed with obtained spectra and the output is the 6 biomarker concentrations. Due to the trained models did not take photobleaching into consideration, in continuous online measurement, before feeding the features into the model, the features were first corrected with exposure time to compensate for the photobleaching following equation $I_{f0} = \frac{I_f}{e^{-\frac{t}{\tau}}}$ (**Eq. 5-7**).

Therefore, for the peak intensity at time 0, it should be I_{f0}. The peak width remains the same. Peak area at t=0 can be estimated as

$$Area0 = \frac{Area}{e^{-\frac{t}{\tau}}} \quad \textbf{(Eq. 5-8)}$$

As described in 4.4.6. The constant τ for temperature, DO, pH, Na^+, Ca^{2+}, and glucose are 51.13 (R^2=1), 48.8 (R^2=0.97), 37.0 (R^2=1), 22.0 (R^2=0.99), 38.0 (R^2=0.99), 133.7 (R^2=0.96) respectively.

5.2.2 Deep Learning model for multiplexed biomarker prediction

The system is designed and proposed for continuous brain monitoring for assistance in brain-related disorder treatment. The accuracy of the model is of vital importance as a single error may lead to severe consequences. The above shallow machine learning models built for biomarker concentration estimation were based on manually extracted simple features and may not be able to convey the whole information or underlying patterns in the dataset. Therefore, I further explored the application of deep learning models for the same task by learning the deep features in the dataset. Therefore, in this section, deep learning methods were explored to provide a simultaneous readout of 6 brain biomarkers as they are capable of extracting deep features in the dataset automatically.

Convolutional neural network (CNN)

CNN is a deep learning algorithm inspired by the visual machinery of animals. CNN represents a quantum leap in the field of various image inferencing, such as image classification, image segmentation, etc [270]. CNNs are made of convolutions with learnable weights and biases for image pattern extraction[271, 272]. The core components in CNN include the convolutional layers, activation functions, pooling and fully-connected layers, which define the model architecture and performance (**Figure 5-7**).

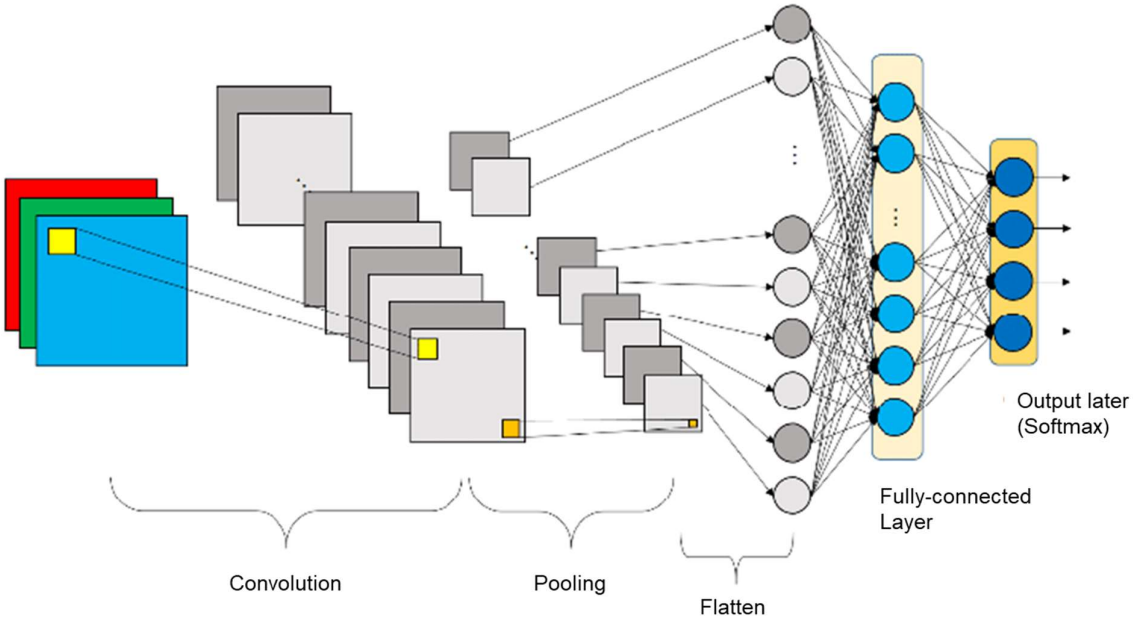


Figure 5-7. The architecture of CNN model.

Convolution layers (Conv layers)

The principal idea of CNN and Conv layers is to mimic the visual cortex of animal brains that reads images and learns image features using neuronal cells [271, 272]. The conv layer is made of several convolutional kernels which consist of learnable weights as neuronal cells for feature extraction. Different convolutional kernels can detect different features, including edges and gradient orientation [271, 272]. The training of the model involves two steps, forward propagation and backward propagation to adjust the weights of each neuron. In forward propagation, the convolutional kernels are convolved across the input matrix or image to extract the features from the image, and if there are n kernels then n feature maps are generated. The output of the conv layer is fed into an activation function layer.

Activation functions or nonlinear functions

In forward propagation, all processes are linear computations, however, data in real world usually follow nonlinear rules. Therefore, activation functions are designed for the nonlinear transformation of the data. There are several different activation functions designed for different purposes and scenarios. The dot products of the kernels and the input are proceeded with the activation function for nonlinear transformation.

Sigmoid

It projects the dot product of the convolutional kernel and the input into ranges between 0 and 1. In sigmoid transformation, large negative and positive inputs are projected close to 0 and unity, respectively.

$$f(x) = \frac{1}{1+e^{-x}} \textbf{ (Eq. 5-9)}$$

Tan hyperbolic

It transforms the input number x to a value between −1 to 1.

$$\tanh(x) = \frac{e^{x}-e^{-x}}{e^{x}+e^{-x}} \textbf{ (Eq. 5-10)}$$

Rectifed linear unit (ReLU)

ReLU is the most commonly used activation function for CNN. This function transforms negative values to 0 and keeps its original value if it is positive. Due to its easiness in computation, it is much faster compared with other functions. Also, it doesn't saturate with larger input values. In this study, we also used ReLU as the activation function.

$$f(x) = \max(x, 0) \textbf{ (Eq. 5-11)}$$

Pooling

Following convolutional layers, pooling layers are used to reduce the size of the convolved features through a nonlinear down sampling function. Pooling reduces spatial size by aggregating data over space, which largely reduces the computation complexity, speeds up the process, and makes the detection more robust.

Max pooling is one of the most popular pooling layers. In max pooling, the input matrix or vector is partitioned into a set of patches, each of which is replaced by the maximum value of the patch to reduce the dimension size and avoid overfitting (**Figure 5-8**).

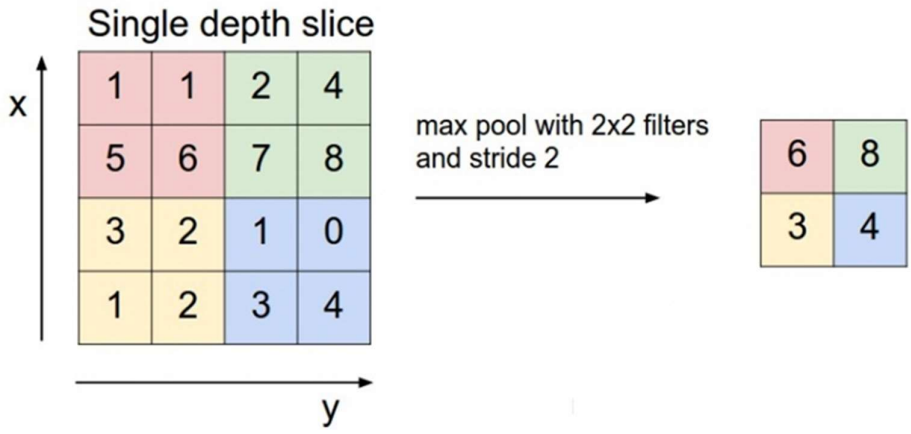


Figure 5-8. Max pooling in CNN for feature dimension reduction.

Fully connected (FC) layer

FC layer is similar to neural network and is made of a certain number of nodes. The output from the CNN block is connected to these nodes with weights associated with each connection. An output is computed by the sum of all the inputs multiplied by the corresponding weights. Then a sigmoid function is performed to the output from FC layer for nonlinear transformation and following classification or regression tasks.

Dataset and input

The obtained spectra were first pre-processed using the previously described smoothing and baseline correction methods. After processing, each spectrum includes three spectrum data with a size of 1*728 obtained under the excitation of three lasers. Each of the three spectra was resized to 26*28, and therefore in each scan, a dataset with a size of 26*28*3 is obtained for biomarker concentration calculation. An example of the 405 scan is shown in **Figure 5-9 (a, b)**. Figure (a) and (b) presented the spectra excited by 405 nm with pH, DO, and glucose at two extreme values: pH 6.0 and 8.0; DO: 0 and 8.0 mgL^{-1}; glucose: 0 and 4 $mmolL^{-1}$.**Figure 5-9(c)** demonstrates the correlation between the heatmap and the original dataset. The overlapping area is also indicated. After resizing the original spectrum to a 2D image, the overlapping peaks are aggregated to neighbouring pixels, which greatly assisted the model in learning the underlying patterns of the neighbouring peaks. In **Figure 5-9 (c)** A total of 18875 datasets were obtained for model training, the same as the dataset used for

machine learning model training. A heatmap was used for better data visualization. Due to the resizing of the dataset, the spectrum was folded, and the adjacent peaks were clustered after resizing, making it easier for the model to learn the correlation between overlapped peaks. The label of each scan contains 6 values corresponding to 6 biomarker concentrations.

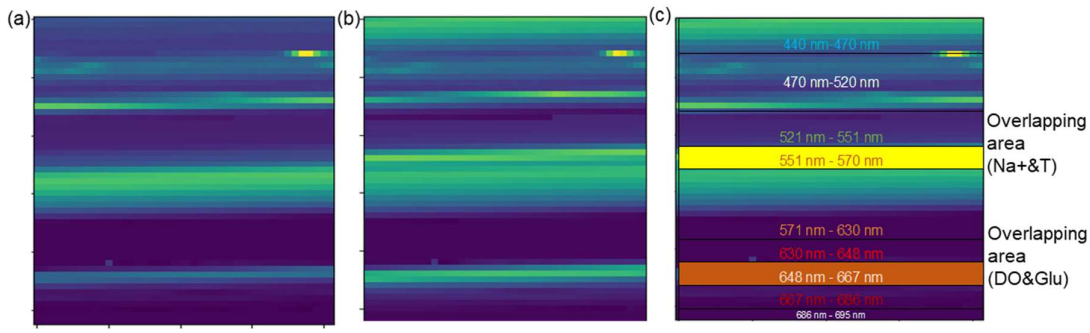


Figure 5-9. Obtained spectrum after resizing before feeding into CNN models.

Multitask learning loss function definition

In a CNN model training, the loss function, also known as the cost or objective function, is a critical component that quantifies the difference between the predicted output of the model and the actual target values in your training data. The primary purpose of the loss function is to measure how well or poorly the model is performing during training. In the training process, the CNN model aims to minimize this loss function by tuning the weight in the layers to make its predictions as accurate as possible. In regression task, Mean Squared Error (MSE) is usually used, which calculates the average of the squared differences between the predicted values and the actual target values.

$$Loss = w_1 MSE\left(pH, pH_{predicted}\right) + w_2 MSE\left(DO, DO_{predicted}\right) + w_3 MSE\left(Temp, Temp_{predicted}\right) + w_4 MSE\left(Na, Na_{predicted}\right) + w_5 MSE\left(Ca, Ca_{predicted}\right) + w_6 MSE\left(Glu,\ Glu_{predicted}\right) \quad \textbf{(Eq. 5-12)}$$

In this project, one model was trained to provide accurate readout of 6 biomarker concentrations simultaneously using the same dataset. Therefore, the definition of the loss function is the weighted sum of the MSE of all 6 correct biomarkers concentrations and their prediction values. However, the weight (w) needs to be tuned to obtain the best results over all datasets. It is worth noting that there is

a tradeoff in the loss function, and changing the weights would lead to better results in some biomarkers while sacrificing the accuracy in the others. Therefore, the weights in the loss function need to be fine-tuned to ensure a balanced prediction accuracy over all biomarkers.

Network structure and optimization

The aim of the project is to explore whether deep learning CNN models could further improve the prediction accuracy. Different from shallow machine learning models, CNN models are much more complex and has much higher computational cost. As this study is designed to be a preliminary exploration, relatively simple structure is used. Two convolutional layers were selected to extract both deep and shallow features as well as maintain a relatively light computational cost. Therefore, the CNN structure consists of an initial input CNN layer, followed by two convolutional layers, one maxpooling layer, and finally fully connected linear layers to provide 6 independent readouts. A block diagram can be found in **Figure 5-10**. Each CNN layer block has one CNN layer with an optimized number of convolutional filters and one relu layer for nonlinear transform. The architecture hyperparameters were selected via grid search.

Same as the machine learning model training and validation, the CNN model training was conducted using 75% of the whole dataset. The rest of the dataset was used for final testing. Within the 75% training dataset, a 10-fold validation method was used to perform grid search and find the optimial hyperparameters, where 90% of the training dataset was used to train the model and the rest 10% of the dataset was used to evaluate the model performance and identify the optimal hyperparameters. In the training, Adam optimizer was used for the optimization of the CNN node weights, and a constant decay learning rate starting from 0.01 with an optimized decay rate was used (results in Section 5.5). The batch size was 5 for the training. The MAEs, R^2, MSEs of the overall output and every individual sensor's output were calculated to indicate the model performance.

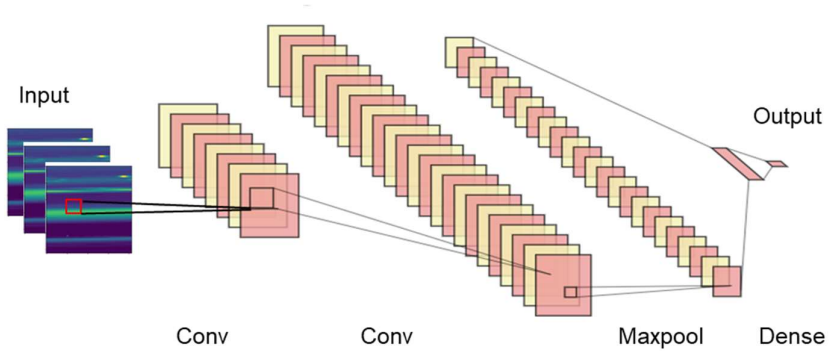


Figure 5-10. Proposed architecture of the CNN model for the processing of captured spectra.

5.2.3 Fully automated brain monitoring system calibration

In order to achieve fully automated measurement of the biomarkers, a multi-wavelength laser that consists of three lasers (405 nm, 488 nm, and 520 nm) was used here instead of using the three collimated individual lasers used in previous chapters that requires manually switch. Therefore, the fibre bundle sensing system consists of a multi-wavelength laser light for fluorescent sensing film excitation, a spectrometer for fluorescent spectra capturing, a self-designed fluorescent sensing film integrated optical fibre bundle for 6 brain biomarker measurements, a fibre coupler for the connection of the optical equipment, a microcontroller (NVDIA Jetson Developer Kit) for laser/spectrometer control, biomarker concentration calculation, and UI readout, and a touch screen for user control and data display.

Before prototyping, the multiplexed sensing system was recalibrated using artificial CSF buffer solutions due to new lasers were used. The following buffer solutions were utilized for the calibration of the sensors one after another. For the procedure, the optical fibre bundled sensors were inserted into the solution together and the corresponding laser (for pH, DO, and glucose; 405 nm, for Na^+, temperature sensor: 488nm, and for Ca^{2+} sensor: 540 nm) was turned on controlled by the edge computer. The sensors' fluorescent intensities and spectra were measured with the spectrometer and saved in the controller for offline analysis. A series of readings of the sensors' intensities under gradient biomarker concentrations (**Table 5-1**) were recorded and the correlations between the

spectrum and the biomarker concentration would be used to validate the sensor's performance. The spectra after the signal stabilized were recorded and used for calibration. The experiment was repeated three times.

Table 5-1. Buffer solution 1preparation for multiplexed sensor characterisation

	T	DO	pH	Na^+	Ca^{2+}	Gluc
T buffer	36-41(1)	8	7.4	140	0.5	2
DO buffer	37	0-8	7.4	140	0.5	2
pH buffer	37	8	6-8 (0.5)	140	0.5	2
Na^+ buffer	37	8	7.4	100-200 (20)	0.5	2
Ca^{2+} buffer	37	8	7.4	140	0-2	2
Glu buffer	37	8	7.4	140	0.5	0-6

5.2.4 Real time monitoring using clinical human CSF sample

In the end, the prototyped brain monitor was tested using human CSF sample. For the system settings, the default setting was used. The biomarker to be monitored was selected to match with the spiking orders of the biomarkers.

The CSF was obtained from a collaborator and the study REC code is 16/lo/0183 'Biomarkers of Delirium after Neck of Femur Fracture (BDA-NOF)' study, gained from London - Stanmore Research Ethics Committee in 2016. The tissues sub bank collection reference is BDA_MF_16_016.

Patient recruitment:

Patients with a fractured neck of femur emergent admitted to St Mary's Hospital, London, UK, were considered for recruitment over an 18-month period [273]. This study received approval from the hospital research governance team at St Mary's Hospital, London, UK (15SM3116), and the London Stanmore Research Ethics Committee (16/LO/0183). All patients gave written, informed consent before taking part in the study, which was taken by the same author (MF). The study conformed to the precepts set out in the Declaration of Helsinki of 1975.

Exclusion criteria were:

Recent use of antiplatelet or anticoagulant medication; Previous lumbar spine surgery; Previous history of post-dural puncture headache; Body mass index > 30 kg/m^2; History of alcohol or drug abuse; Inability to consent to surgery; Pre-existing cognitive impairment or Parkinson's Disease; Psychotropic or corticosteroid medication use.

Specimen collection and storage

All participants who agreed to participate in the study had a spinal catheter inserted in their spine for CSF withdrawal before surgery by an anaesthetist. Before the insertion, a local anaesthetic of 1% lidocaine was given at the insertion site for patient comfort. Once inserted, the initial 2 mL of CSF was discarded, following which 5 mL of CSF was withdrawn from each patient in a polypropylene tube with the name age. Then the catheter was removed. The withdrawn samples were moved to the laboratory and centrifuged at 3000g for 10 min at room temperature after sampling. In total two 500 μL plasma and a further 200 μL aliquots were collected from each patient and stored at − 80 °C until analysis.

Patient monitoring

No formal cognitive testing was performed. Routine blood tests, the anaesthetic used, and the length of hospital stay were recorded. Side effects relating to the insertion of the spinal catheter, withdrawing CSF, bleeding, infection, and other potential side reactions were closely monitored by a clinician.

Experimental protocol:

The developed multiplexed optical bundle sensors were further validated using clinical human CSF samples to examine its ability in reflecting biomarker concentration variations in real CSF samples. Before the spiking test, the sensing system was first calibrated using two standard buffer solutions (**Table 2-9**). The sensors' spectra of the standard buffer solutions were saved for sensing readout correction.

DO testing:

10 mL human CSF sample was used for the DO sensor validation. A three-neck flask was used. The DO was adjusted to 1,3,6,8 mg/L according to the reading of the DO meter. The DO sensor was excited using pulsed 405 nm laser light (5s on, 10s off) and the spectrum was obtained before the light is turned off and labelled according to the DO meter reading.

Temperature testing:

The same 20 mL CSF sample from DO test was used for the temperature sensor validation. The temperature of the sample was adjusted to 34, 36, 38, 40 °C using a hotplate and monitored with a thermometer. The temperature sensor was excited using a pulsed 488 nm laser light.

pH testing:

After temperature sensor testing, the sample was used for the pH sensor validation. During the experiment, both the designed multiplexed bundle sensor and pH meter (reference) were inserted into the sample. For the pH measurement, 405 nm laser light was used. The light and spectrometer worked in pulsed mode and the spectrum of the sensors was taken before the laser is turned off. HCl and NaOH were used to adjust the pH of the sample gradually to 6.5, 7.0, 7.5, and 8.0 in consecutive, and once the pH meter reading stabilized the pH probe was inserted for the measurement. Then the buffer was adjusted to the next level based on the reading of the pH meter.

Sodium ion testing:

10 mL of the diluted human CSF sample was used for the sodium sensor validation. Due to the fact that the existing sodium ion concentration was unknown in the sample, the sensor's performance was measured using NaCl spiked sample. The sodium sensor was excited using 488 nm laser light as described for the other sensors. When the signal stabilized, an additional 20 mmol L^{-1} NaCl was added to the sample with constant stirring. In total 60 mmol L^{-1} of NaCl was added to the sample in three additions.

Calcium ion testing:

30 mL of the diluted human CSF sample was used for the calcium sensor validation. The sensor's performance was measured using $CaCl_2$-spiked sample. The calcium sensor was excited using a 540 nm laser light same as for the other sensors. When the signal stabilized, an additional 0.5 mmol L^{-1} $CaCl_2$ was added to the sample with constant stirring. In total 1.5 mmol L^{-1} of $CaCl_2$ was added to the sample in three additions.

Glucose testing:

10 mL of the diluted human CSF sample was used for the glucose sensor validation. The sensor's performance was evaluated using D-(+)-glucose-spiked sample. The glucose sensor was excited using a 405 nm laser light with settings same as for the other sensors. When the signal stabilized, an additional 2 mmol L^{-1} D-(+)-glucose (4.8 mg) was added to the sample with constant stirring. In total 6 mmol L^{-1} of D-(+)-glucose was added to the sample in three additions.

Each test was repeated three times and the calculated concentrations of each biomarker after environmental compensation were recorded in continuous mode and saved for system evaluation. For pH, DO, and temperature measurement, MSE and MAE were used to evaluate the system's performance. For Na^+, Ca^{2+}, and glucose, recovery rate was used for the evaluation.

5.3 Multiplexed sensing system characterisation using aCSF sample

Since a new laser system is adopted in this chapter, the sensors were characterized again for their ability for multiplexed measurement of 6 biomarkers. The sensors were characterized for multiplexed measurement of 6 biomarkers and the calibration curves were measured. The power of the lasers was tailored to ensure a high signal-to-noise ratio (SNR) especially when measuring extreme biomarker concentrations. The final powers of the three lasers were: 6.5 mW for 405 nm and 488 nm lasers and 7 mW for 520 nm laser. Artificial CSF buffer solutions were prepared for the characterisation of the sensors one after another, and all sensors were inserted into the buffer solutions during the

measurement. The measured spectra and calibration curve for the characterisation of each sensor are shown in **Figure 5-11**. Artificial CSF buffer solutions were prepared for the characterisation of the sensors one after another, but all sensors were inserted into the buffer solutions during the measurement and multiplexed spectra were measured.

The characterisation of the temperature sensor was carried out using aCSF solution with temperature increasing from 36 to 41 ℃. Intensities at 600 nm were used for the calibration as it is the emission maximum. As shown in **Figure 5-11(a)**, the sensor's emission intensity decreased when the temperature increased due to the temperature quenching effect on the fluorophore. A linear correlation was achieved between the emission intensity and the buffer temperature. A sensitivity of 0.064 I/I_0 per ℃ was achieved in measuring temperature calculated as the slope of the calibration curve.

pH sensor was then characterized using the embedded 405 nm laser and a series of aCSF buffer solutions with pH of 6-8. The sensing is based on the fluorescent emission intensity variations when the pH probe HCC is protonated and deprotonated, and the emission at 445 nm is used for the calibration. As shown in **Figure 5-11(b)**, the pH sensor demonstrated a high emission intensity when the pH is high. A good sensitivity of 5.24 I/I_0 per change of pH was obtained using the proposed sensing system and a good linear relationship between the pH and emission intensity was achieved.

Na^+ sensor was then characterized using the prepared standard sodium buffer solution and 488 nm laser. ACSF buffer solutions with $[Na^+]$ from 100 mM to 200 mM were used. Due to the overlapping emission peak of the temperature sensor and sodium sensor, there are two peaks shown in the spectra. The peak at 540 nm is from the sodium indicator and thus was used for the evaluation of the sodium sensor (**Figure 5-11(c)**). The sodium sensor exhibited an increasing emission intensity as the $[Na^+]$ increasing, which is due to the PET effect of the coronaGreen indicator. A good sensitivity of 0.012 /1 $mmolL^{-1}$ Na^+ with a good linearity was obtained in this study.

DO sensor is based on the oxygen quenching effect on the PDMS-PdOEP sensing film, where a reduced fluorescent signal is observed in a DO concentrated buffer solution. The DO sensor has an emission at 660 nm and partially overlapped with the glucose sensor's emission peak at 640 nm. Besides, due to the glucose sensing film is also based the measurement of oxygen, the emission

intensities at both wavelengths were influenced by the DO level and was shown by lower peaks at high DO level. Same as the other sensors, the current system also has a good sensitivity (0.96 I_0/I per increase of 1 mgL^{-1} DO) for the measurement of DO (**Figure 5-11(d)**).

Measurement of Ca^{2+} was realized using a Rhod-5N encapsulated PolyAM-MBA matrix, which can be excited with 520 nm laser and has an emission maximum at 580 nm. Here, as expected, a higher emission intensity was obtained in the solution with higher Ca^{2+} concentration due to the PET effect (**Figure 5-11(e)**). A good sensitivity is obtained here, and the calibration curve fits a sigmoid curve which follows the nature of ion diffusion and binding kinetics.

Characterisation of the glucose sensor was conducted using a series of 0-6 $mmolL^{-1}$ glucose aCSF buffer solution. The glucose sensing film is based on a double layer system, and a higher glucose concentration leads to a higher oxygen consumption rate, which in turn causes a lower oxygen quenching and thus, a higher emission intensity. The emission peak at 640 nm under the excitation of 405 laser was used for the analysis. It is shown that higher emission intensities were obtained in buffer solution with high glucose concentrations with a sensitivity of 0.37/1 mmol L^{-1}glucose (**Figure 5-11(f)**).

The emission intensities of the fluorescent sensing films were measured over time to determine the photostability of the films. For the experiment, the laser was set on for 5 s and off for 10 s and repeated for a continuous 720 cycles (3 hours) controlled using python scripts. The spectrum of the films was also recorded every 15 seconds while the laser is on. For the temperature and sodium senor test, the sensor was immersed in 25 ℃ 150 $mmolL^{-1}$ [Na^+] aCSF throughout the test and pulsed 488 nm laser light was used of the sensor excitations. As shown in **Figure 5-11(h, g)**, good stability results of the two sensors were obtained with decrease less than 10% in the intensities after 3 hours of exposure. For DO, pH, and glucose sensor, the stability was tested using 100% saturated DO, pH 7.4-, and 2-mM glucose aCSF buffer solution. 405 laser light was used for the test of these three sensors, and it was controlled with python scripts for pulsed excitation. After 720 cycles, 89%, 77%, and 76% of the emission intensities were retained for DO, pH, and glucose sensor respectively. For the calcium sensor, the stability was tested using 1$mmolL^{-1}$ standard calcium aCSF buffer solution and pulsed 520

nm laser was used for the film excitation. After 720 cycles, a decrease in the intensity at 580 nm was shown, indicating a good stability for long term applications.

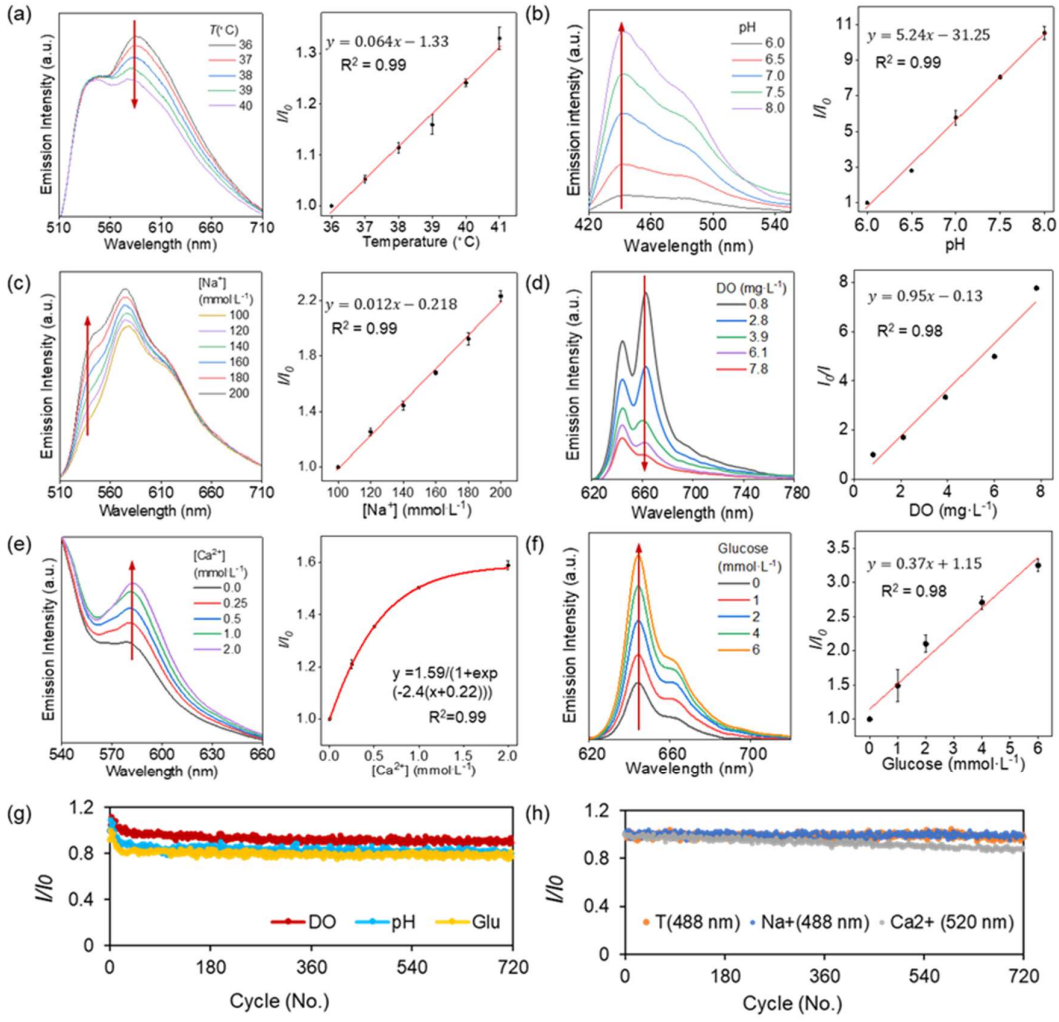


Figure 5-11. Sensor characterisation using the multiplexed optical fibre bundle sensing system. Optical spectra and calibration curve of temperature (a), pH (b), Na+ (c), DO (d), Ca2+ (e), and glucose (f) sensors obtained with series of aCSF buffer solutions under gradient target biomarker concentrations. (g) Photostability of pH, DO, Glucose sensor under the exposure of 405 nm laser. (h) Photostability of Temperature and Na+ sensor under the exposure of 488 nm laser. And stability of the Ca2+ sensor under the exposure of 520 nm laser.

5.4 Machine learning for multi-biomarker concentration calculation

AI has been broadly integrated with various sensors for the enhancement of sensor performance and providing accurate readout. In recent years, the implementation of AI in biosensing area has also made breakthroughs in providing robust calculation of biomarker concentration. Machine learning, being one of the most powerful numeric intelligences, is also implemented to provide accurate readout

of six biomarkers simultaneously based on the multiplexed spectra obtained by the optical bundle system. To achieve this, the process included the following steps (**Figure 5-2**). The first step after obtaining the collected optical spectra using three different laser lights is data preprocessing, which includes spectrum denoising, baseline correction, standardization, spectra merging, and labeling. Signal denoising is achieved using Savitzky-Golay filter, which mitigates the presence of high-frequency noise and also attenuating low-frequency component's including offsets and slopes through differentiation. Baseline correction is a commonly adopted method for optical spectrum analysis as it corrects signal drifts due to background light, which is necessary in continuous measurement as the background light can vary with time. A fidelity based adaptive regression method is applied here to all spectra obtained by the spectrometer during each measurement. In each measurement, three spectra are obtained due to three laser lights being used to excite the films in turn. Therefore, these three spectra were merged together and correctly labeled before feeding into multitask machine learning models (**Figure 5-3**). Each label includes six values corresponding to the concentration of six biomarkers for machine learning model training.

After preprocessing, each data input contains 1381 intensity values as 3 intensities at each wavelength. To reduce the input dimension, several features were extracted from the dataset before training. Based on the sensing principles and observations, the following features were extracted from the spectra dataset: peak height, area under curve, peak width, and peak position (**Figure 5-4**). Detailed descriptions can be found in Section 5.2.1. The features were standardized to be converted into the same unit before following analysis to avoid bias caused by the sensor fabrication, laser light, and environmental variations. Overall, 24 features were obtained from each merged spectrum. The correlation between the extracted features and biomarker concentrations were analysed by calculating the Pearson correlation coefficient. As demonstrated in **Figure 5-12**, strong correlations were observed between the peak height and area under curve with their corresponding biomarker's concentrations. Peak width and peak position have moderate correlation with the corresponding biomarker concentrations, which can be explained that the biomarkers have minimum effect on peak shape and location. Before feeding the features into predefined machine learning models, the features

were corrected based on exposure time to reduce the impact of photobleaching (details in Section 2.4.4).

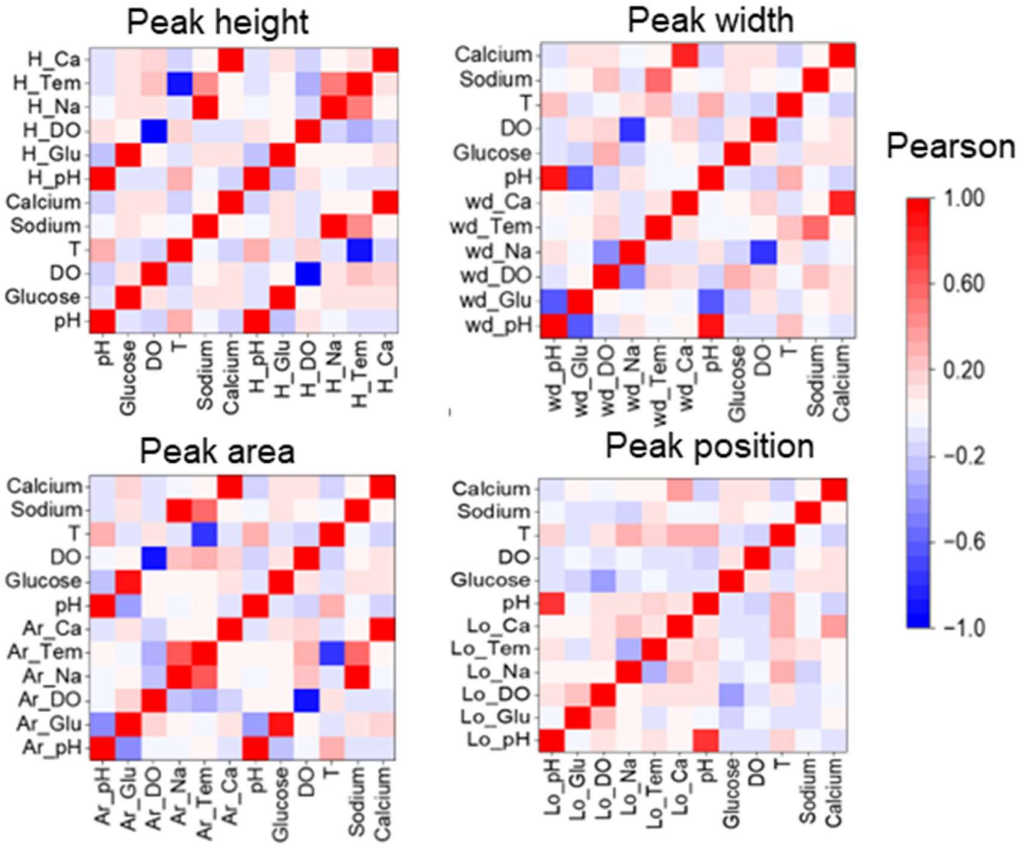


Figure 5-12. Feature evaluation and selection using Pearson correlation coefficient.

The model training was carried out by feeding the extracted features and corresponding labels to predefined regression model. A total dataset of 18875 was obtained for both training and testing. 75% of the whole dataset was used for training and the rest of 25% of the dataset was used for testing. Within the training dataset, it was further divided using 10-fold validation methods for the optimization and validation of the system. In order to achieve the best calculation accuracy, various regression models with different hyperparameters were explored and compared based on the MSE, MAE, and R^2 of the calculation results. The same features were fed into linear regression models, lasso regression models, rigid regression models, and Bayesian regression models and the optimum hyperparameters were used for each model through grid search. The selected hyperparameters are listed in **Table 5-2** after gride search. Tuning parameters can improve the prediction performance in

all models apart from linear regression as it does not have key parameters. Both Lasso and Ridge models added regulation as a penalized term to the linear regression to improve the robustness towards outliers and reduce overfitting. The hyperparameters for these two models are therefore to regulate the penalization in the models, which have a big impact on model performance. The results indicated that when alpha was set to 5 and 0.01 for ridge and lasso respectively, the model obtained the best performance using the validation dataset. Similar to Lasso and Ridge, Bayesian model performs the best when alpha_1=0.001 and alphoa_2=1 (**Table 5-2**)

Table 5-2. The tuned hyperparameters of extracted input obtaining from Grid search CV.

Model	Parameters	Hyperparameter
Linear Regression	n_jobs	n_jobs = 1
Ridge	alpha	alpha = 5
Lasso	alpha	alpha = 0.01
Bayesian Regression	alpha_1 alpha_2	alpha_1 = 0.001, alpha_2=1

After the hyperparameters of each regression model were determined, the testing dataset was fed into each model for model performance comparisons. The results of the models are demonstrated in **Table 5-3**. It is shown that Bayesian model provided the best calculation accuracy tested with 1500 dataset compared to the other models. The final model obtained MSE of 0.05, 0.6, 0.12, 2.05, 0.18, and 0.35, a MAE of 0.04, 0.47, 0.1, 1.5, 0.11, and 0.27, R^2 of 0.98, 0.94, 0.97, 1, 0.95, and 0.95 for the calculation of pH, DO, temperature, Na^+, Ca^{2+}, and glucose calculation respectively. The visualization of the sensor calculation results is shown in **Figure 5-13**, and it indicates that the model has great ability in correctly calculating the biomarker concentrations based on the obtained spectra with good sensitivity and resolution, shown by clear boundaries of close concentration levels.

Table 5-3. Machine learning model results for 6 biomarker concentration calculation.

		Training			Validation			Testing		
Models	Biomarker	R^2	MSE	MAE	R^2	MSE	MAE	R^2	MSE	MAE
Bayesian	pH	0.99	0.1	0.03	0.99	0.07	0.05	0.98	0.05	0.04
	DO	0.94	0.82	0.59	0.92	0.77	0.59	0.94	0.6	0.47
	Temperature	0.97	0.27	0.12	0.98	0.2	0.12	0.97	0.12	0.1
	Sodium	1	1.85	1.31	1	1.87	1.32	1	2.05	1.5
	Calcium	0.95	0.16	0.09	0.95	0.17	0.1	0.95	0.18	0.11
	Glucose	0.96	0.42	0.29	0.94	0.38	0.29	0.95	0.35	0.27
Lasso	pH	-0.02	0.76	0.67	0.24	0.64	0.33	0.32	0.03	0.32
	DO	0.74	1.41	1.24	0.74	1.68	1.53	0.75	0.54	1.42
	Temperature	0.25	1.25	1.1	0.39	1.15	1.12	0.49	0.13	1.12
	Sodium	0.99	4.19	3.15	1	3.83	3.34	1	2.04	3.52
	Calcium	-0.01	0.74	0.66	0.62	0.77	0.6	0.55	0.18	0.61
	Glucose	0.52	1.1	0.9	0.46	1.33	0.77	0.46	0.35	0.89
Linear	pH	0.98	0.1	0.03	0.98	0.1	0.03	1	0.02	0.01
	DO	0.67	1.59	0.52	0.67	1.59	0.52	0.96	0.51	0.42
	Temperature	0.97	0.25	0.12	0.97	0.25	0.12	0.99	0.12	0.09
	Sodium	0.99	2.69	1.51	0.99	2.69	1.51	1	2.07	1.46
	Calcium	0.93	0.2	0.1	0.93	0.2	0.1	0.94	0.19	0.11
	Glucose	0.88	0.56	0.29	0.88	0.56	0.29	0.95	0.39	0.31
Ridge	pH	0.99	0.08	0.04	0.98	0.07	0.05	0.98	0.06	0.04
	DO	0.91	0.82	0.58	0.92	0.76	0.6	0.93	0.64	0.5
	Temperature	0.99	0.17	0.13	0.97	0.19	0.15	0.97	0.16	0.13
	Sodium	0.99	3.78	2.65	0.98	4.38	3.22	0.98	3.3	2.3
	Calcium	0.95	0.16	0.08	0.95	0.17	0.1	0.94	0.18	0.12
	Glucose	0.93	0.42	0.29	0.95	0.34	0.28	0.95	0.37	0.29

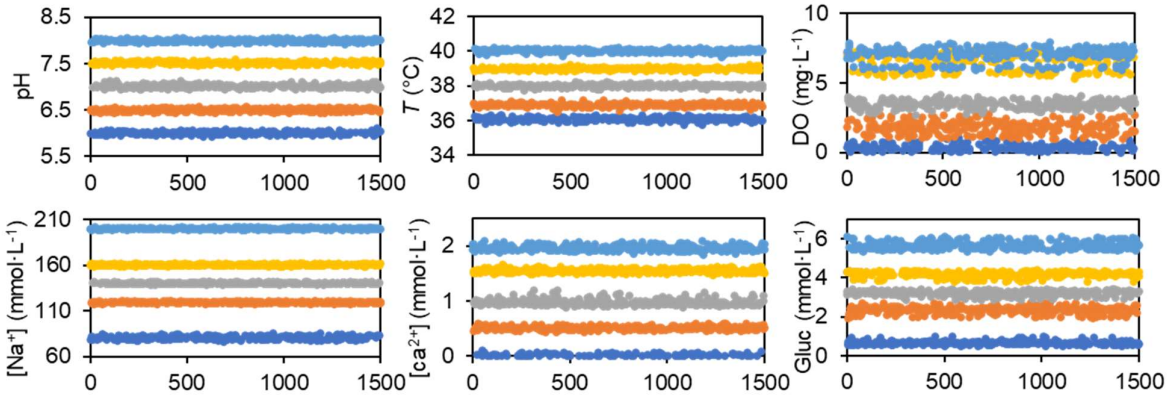


Figure 5-13. Performance of the Bayesian regression model on the calculation of 6 biomarker concentrations.

5.5 CNN-based multitask learning for biomarker calculation

CNN have emerged as a powerful tool for data classification, segmentation, and forecasting. Using machine learning for the prediction of biomarker concentrations requires the extraction of features, which largely determines the model performance. However, in shallow machine learning models, the extracted features can hardly covey all the information held by the original spectra. These shallow features were extracted based on observations and experiences and may introduce bias and limit the model performance. CNN based regression models, on the other hand, are a powerful tool to extract the hidden and deep information contained in the dataset automatically together with their advanced model architecture, which have been widely used due to its great performance in various areas.

Herein, CNN models were utilized for the prediction of biomarker concentrations based on obtained multiplexed spectra. Originally, each of the obtained spectrum is a vector of intensities, and traditional manually extracted features may be confined by the information they could convey. The correlations between overlapped peaks are also difficult to extract. Therefore, in the preprocessing of the obtained spectrum, each obtained 1*726 intensity vector (output from the spectrometer) was reshaped to a 26*28 array and the visualization of the array is shown in **Figure 5-6**, the color at each pixel is the intensity value at the current wavelength. After reshaping, the adjacent peaks are clustered together, and the correlations can be extracted via a convolutional kernel. Due to three lasers being used for the measurement of 6 biomarkers, three spectra are obtained at each scan of all sensors. The obtained three spectra were reshaped to 26*28 array and they are stacked together to form a 26*28*3

array for CNN input. In total 18875 datasets were generated. 75 % of the dataset was used for the training and 25% of the data was used for the model validations. For a multitask learning like this, 6 output values are included in each label, and the definition of the loss function decides the model performance directly. Apart from the optimization of the loss function, fine tuning of the hyperparameters including decay rate, epoch, and node numbers were also conducted to yield the best training and validation results.

The initial loss function was defined as the average of the MSE of 6 sensors (weight = 0.001). However, the results showed a relatively worse prediction results for the temperature sensor compared to other sensors. The relatively low accuracy in temperature prediction might be owing to the low sensitivity and poor signal to noise ratio of the temperature sensor. To improve the temperature sensor prediction accuracy, one solution is modifying the loss function and increase the weight of the temperature MSE. However, increasing the temperature weight might sacrifice the other sensors accuracy (**Figure 5-15**, **Table 5-4**). The results indicate that the sacrificing is negligible. Therefore, a weight of 0.003 was used to enhance the weight of temperature errors in the training (**Table 5-4**).

The learning rate is a crucial hyperparameter in many machine learning algorithms, especially those involving gradient-based optimization methods. It represents the step size that the model takes to update its parameters in the direction of minimizing the loss function. A high learning rate means the model makes large updates to its parameters, potentially converging faster but also at a greater risk of overshooting the minimum and diverging. Conversely, a low learning rate results in smaller, more cautious updates, often leading to a more stable but slower convergence. Tuning the learning rate is essential to achieve optimal performance. An inappropriate learning rate can significantly hamper the model's ability to learn from the data. There are several strategies for tuning the learning rate. One common approach is to use a fixed learning rate schedule, gradually decreasing the learning rate over the course of training. Here, I used a fixed starting learning rate of 0.01 and let it gradually decay to a smaller learning rate as training progressed. The decay rate was tuned and determined to be 1600 to obtain the best convergence and training results (**Figure 5-15**).

Increasing filter numbers increases the feature numbers that are extracted in each layer, and with more features being extracted, more information of the dataset pattern can be learned. However, there are also adverse consequences related to this, including exponentially increased computational time and overfitting in model training. Compared with other image classification or regression tasks such as facial recognition, image segmentation, the given task is relatively simple, which does not require multiple deep features to be extracted from the dataset. Therefore, when selecting the filter numbers, 4-32 number of filters were evaluated and compared. From the result, the model performance quickly converged when increasing the filter number from 4 to 12 and became stable after 12 filters. When the number increased to 24 the best performance achieved with overall MSE equalled to 0.22 and MAE equalled to 0.27 (**Table 5-4**). The learning rate was optimized to an initial value of 1600 and gradually decreased to 100 and a decay of 10 was selected for the training. Therefore, the final model structure adopted is shown in **Figure 5-15**.

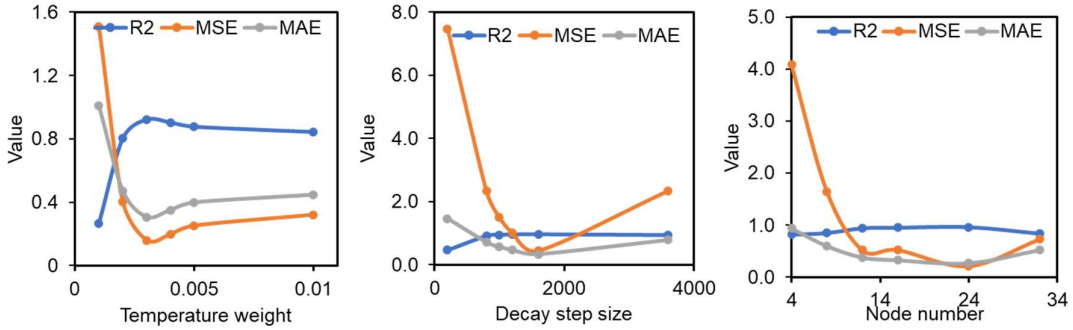


Figure 5-14. Optimization and fine tuning of hyperparameters of the CNN model. (a) decay step size fine tuning. (b) loss function definition fine tuning. (c) network node number fine tuning.

Table 5-4. Model performance with different hyperparameters.

loss function	R^2	MSE	MAE	step size	R^2	MSE	MAE	node	R^2	MSE	MAE
0.001	0.27	1.50	1.01	200	0.47	7.48	1.46	4	0.82	4.08	0.94
0.002	0.80	0.40	0.47	800	0.92	2.33	0.71	8	0.85	1.65	0.60
0.003	0.92	0.16	0.31	1000	0.96	1.51	0.57	12	0.94	0.53	0.38
0.004	0.90	0.20	0.35	1200	0.97	1.02	0.47	16	0.95	0.53	0.33
0.005	0.88	0.25	0.40	1600	0.97	0.46	0.34	24	0.96	0.22	0.27
0.01	0.84	0.32	0.45	3600	0.95	2.35	0.79	32	0.84	0.73	0.52

The optimization results indicated that a structure with 2 hidden layers with 24 nodes, kernel size of 3 perception area, and stride of 1 has the best performance (**Figure 5-15**). After two convolutional layers is a maxpool layer that performs a nonlinear computation and reduces the feature map dimensions. A fully connected dense layer is followed to project the 2D output to a vector and then further reduce the variable number to 6 as the final output. Each of the output value indicates the level of a target biomarker.

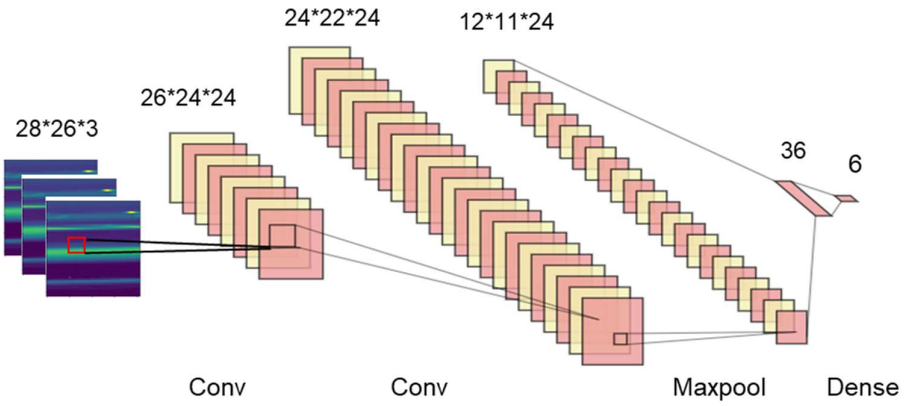


Figure 5-15. Final structure of the optimized CNN model.

The testing results for the calculation of each biomarker are shown in the figure below. MSE of 0.007, 0.06, 0.16, 1.72, 0.002, and 0.007, MAE of 0.07, 0.18, 0.31, 1.03, 0.04, and 0.065, R^2 of 0.99, 0.98, 0.94, 0.99, 0.99, and 0.98 were obtained for the calculation of pH, DO, temperature, Na^+, Ca^{2+}, and glucose respectively. Compared with machine learning based models, CNN model provided slightly better results in biomarker concentration predictions especially for overlapped biomarkers, which might be owing to that deep features between neighbouring peaks were extracted. However, it needs to be mentioned that photobleaching due to long exposure time could not be compensated using the proposed CNN model because spectra at various exposure time were not recorded for the training dataset. The model can be trained with exposure time as an additional feature to be used for CNN model training in the future studies.

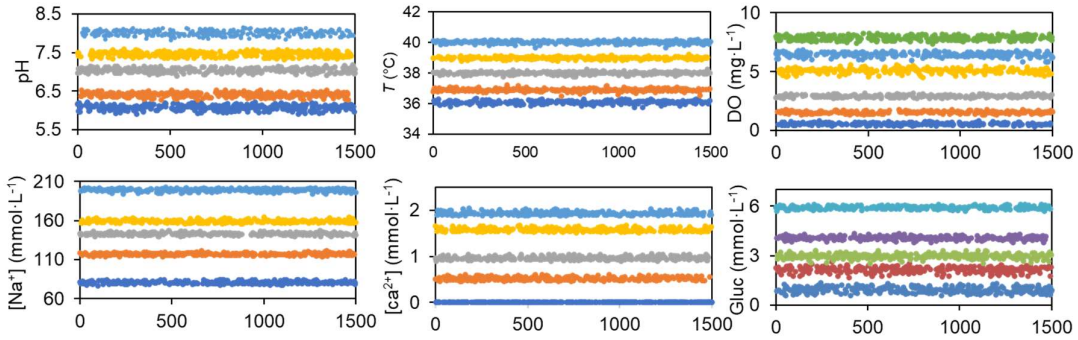


Figure 5-16. Performance of the CNN model for 6 biomarker concentrations monitoring

5.6 System prototyping and validation using clinical CSF samples

5.6.1 System prototyping and assembling

The structure of the readout box was designed using SolidWorks (**Figure 5-17 (a)**), based on which the fabrication of the readout box is completed using 1 cm plastic acetal sheets. To secure the microcontroller, spectrometer, and lasers, different slots were built and screwed on the walls of the readout box. A touchscreen was used for both user interaction and readout display. Black plastic sheets were utilized to block light and minimize background noise on the signals. The designed box has a length of 30 cm, width of 20 cm, and hight of 20 cm. The total weight is 2.5 kg, which is also portable (**Figure 5-17(b)**). Then the system is tested with human CSF samples for validation and mimicking its application in a clinical setting.

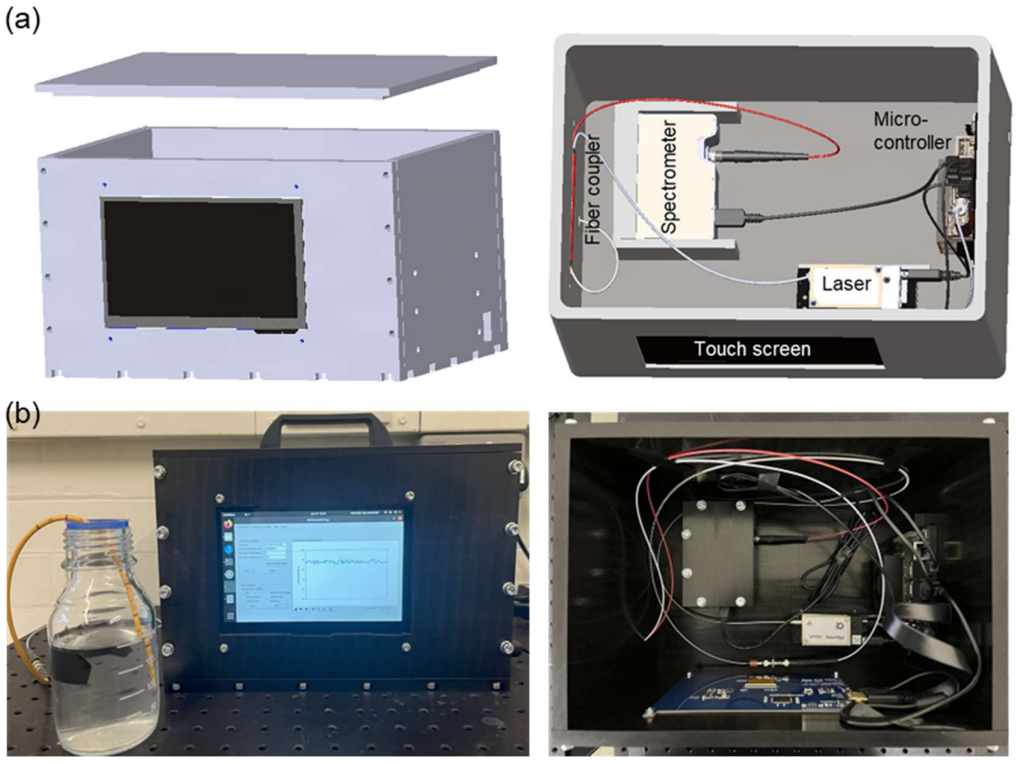


Figure 5-17. Design (a) and photo (b) of the readout using black acetal sheets.

5.6.2 Continuous measurement using clinical human CSF samples

Until now, all the validations of the system were conducted using synthetic PBS buffer solutions that only includes the major biomarkers in CSF, and thus, could not fully reveal the sensors' performance in potential real-life applications. Therefore, clinical human CSF sample was obtained and used for further validation of the proposed system in clinical applications. Human CSF samples were collected from 11 patients admitted to the emergency room of St. Marry Hospital (U.K.). Multiplexed measurement of 6 biomarkers that were spiked in the collected human CSF was performed (Section 5.2.4) in continuous mode to test the system in tracking brain biomarker's accumulation with the presence of various brain molecules. Before measurement, the sensing system was first calibrated using two prepared aCSF buffer solutions that contained the target biomarkers at specific concentrations (Section 5.2.4), and the readout of the measurement was used for accurate measurement of spiked human CSF samples. I measured the spiked signals instead of the biomarker concentrations for Na^{+}, Ca^{2+}, and glucose sensor validation because the CSF sample's base concentration was unknown and thus, the lack of golden standards for the system to compare with. In

the spike measurement, standard and prepared chemicals were spiked to the sample, and the changes in the solution were measured using the system to be compared with the spiked materials. This experiment would reveal the recovery rate of the system and its ability in reflecting the biomarker fluctuations. For pH, temperature, and DO the real values were measured and compared with golden standard values measured with benchtop devices. As shown in **Figure 5-18**, the designed optical fibre bundles sensing system successfully measured series of increasing pH, temperature, and DO values of the CSF sample with an MSE of 0.05, 0.12, and 0.04, and an MAE of 0.29, 0.51, and 0.26, respectively, indicating its ability in accurately measuring brain pH, temperature, and DO values. The system was further tested to evaluate how much percentage of the biomarker's variations can be detected by calculating the system's recovery rate. Despite the existence of numerous non-target molecules in the human CSF sample, the system also demonstrated a good recovery rate of 101±5.3%, 97.7±2.6%, and 106.8±7.6% for the measurement of increased [Na^+], [Ca^{2+}], and glucose, respectively, indicating its capability in revealing elevated ions and metabolites, which are commonly observed in patients experiencing brain excitotoxicity and hypometabolism. As indicated by the continuous readout of the CSF samples, the system exhibited a great stability in long-term measurement after compensation for environmental variations and photobleaching. These findings further imply that the proposed system can selectively and accurately identify the target biomarkers, offering good precision and robustness in real clinical applications.

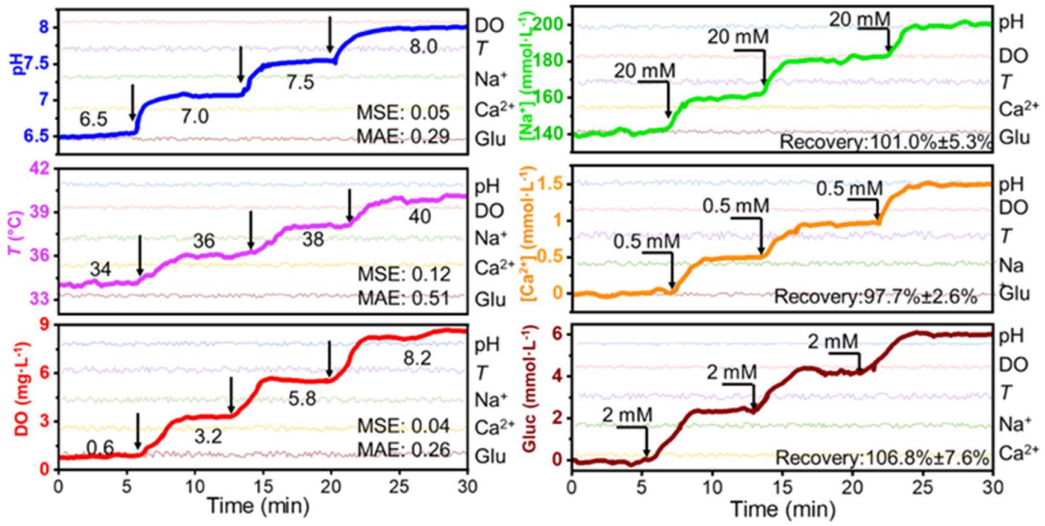


Figure 5-18. Continuous monitoring of clinical human CSF sample using the prototyped system in spiking test. mM: mmol L-1

5.7 Conclusion

In this chapter, a fully automated monitor is prototyped for continuous and multiplexed brain monitoring. To achieve fully automated monitoring, a programmable multi-wavelength laser system is used to replace the manually switched individual lasers. The lasers and spectrometer are controlled and synchronized through the software based on user defined settings. Two modes of monitoring are offered, multiplexed monitoring and single biomarker dynamic monitoring, and based on user's selection, different control methods are conducted. In order to provide highly accurate and robust readout based on multiplexed fluorescent spectra, machine learning algorithms based on feature selection and regression modelling, and deep learning algorithms were explored and optimized. Then the software and the hardware optical sensing system are integrated, and a brain monitor is prototyped and validated for potential clinical applications.

The software controls the laser and spectrometer based on user preferences and offers accurate continuous readout of 6 biomarkers' concentration simultaneously based on the embedded pretrained machine learning model. A pretrained machine is built with the capability to provide highly accurate calculation of biomarker concentrations based on overlapped fluorescent spectra under various environmental conditions and exposure time. A graphical user-friendly UI is also deployed in the microcontroller for direct user interaction. In the validation tests, the optical fibre bundle sensing system successfully tracked concentration variations in three TBI secondary injury brain models. In multiplexed measurement of clinical human CSF samples, the proposed system demonstrated great sensing precision for continuous measurement of multiple biomarkers simultaneously with high selectivity and stability. Therefore, it can be concluded that the sensing system, coupled with intelligent algorithms possess great potential in multiplexed monitoring of deep brain biomarkers for TBI treatment.

Chapter 6 Conclusions and Future Work

This thesis addressed several challenges related to optical sensor application in clinical brain monitoring in three different aspects: optical sensor design and development for brain biomarker monitoring, computational methods for sensing signal post processing, and system prototyping and validation. In this chapter, the findings in each chapter and the correlation between chapters are discussed. The final conclusions and future directions of the thesis are provided.

6.1 Discussions

In the beginning of the thesis, the background of the brain monitoring field is discussed with the urgent requirements of highly sensitive, stable, and robust multiplexed brain monitoring techniques for clinical diagnosis and treatment. The solution for the clinical need is proposed. The first part of the solution is to design and develop novel sensors and sensing system that are capable of measuring target brain biomarkers with high performance including sensitivity, selectivity, reversibility, and stability over long time range. Simultaneous monitoring of multiple biomarkers also needs to be ensured. The second is exploring software solutions that can provide accurate biomarker concentration readout based on the signals detected using the developed sensing hardware and eliminating signal interference and environmental effects. In the first chapter, a thorough literature review is conducted to study and review recent advancements that have been achieved in the biosensing area especially towards commonly measured and clinically relevant brain biomarkers, including metabolites and neurotransmitters. Three widely studied techniques including microdialysis based sensing methods, electrochemical sensing methods, and optical sensing methods were analysed and compared. The sensing principle and application on brain biomarker measurement are discussed. Microdialysis among these different sensing methods is a well-studied technique, as it has been widely used in clinical settings. It offers highly accurate measurement of multiple brain biomarkers by analyzing the extracted brain CSF in an external analyser. However, it requires human intervention and can hardly provide continuous and real-time readout of the brain physiological situations. It is found that electrochemical sensors are the most studied in recent years as it is capable of providing

fast and sensitive measurement of brain biomarkers, and it offers miniaturized and soft sensing probes, having great potential for long term and real-time measurement. However, poor selectivity, the limitation in multiplexed sensing, and signal drifts over long term measurement might hinder the application in brain monitoring. Optical sensing methods turned out to be the most promising methods for our aim as it offers miniaturized sensing of deep brain tissues via optical fibres, and it is immune to magnetic field, which is a great benefit when used along with or next to MR. Furthermore, the technique provides highly sensitive and selective measurement of brain biomarkers utilizing various biomarker receptors. Moreover, optical signals are robust, offering more stable output with lower signal drifts under different conditions if background light can be properly controlled. Therefore, following the review of recent advancements, optical sensing techniques integrated with optical fibre for signal transmission and deep tissue detection were decided as the main approach of the thesis. The review also discussed the computational methods' contribution in biosensor signal processing and biomarker concentration readout. Therefore, proper computational methods were also explored as an important approach in the thesis.

The second chapter presents a comprehensive literature review of the relevant fields, including commonly monitored brain biomarkers and their roles in brain physiology, brain monitoring techniques including both sampling, EC and optical methods. Computational methods for signal post processing are also reviewed and discussed in the chapter. Recent advances and existing gaps are discussed to find the potential solution for the thesis aim and objectives.

The third chapters describe the fabrication and characterization of the proposed methods in brain biomarker development and validation. The sensors are colorimetric and fluorescent based. In order to achieve simultaneous monitoring of 4 biomarkers, 4 sensing films utilizing sol-gel encapsulation methods together with sensitive receptors are developed and placed together on a glass substrate. Computational algorithms were designed to calculate the biomarker concentrations based on the detected mixed reflection signals. Miniaturization methods were applied to further reduce the sensing probe to an outer diameter of 2 mm. The first version of the brain monitoring system was validated using ex vivo brain models with various mimicked brain conditions. As expected, the first method that uses one reflection fibre and four evenly distributed optical sensing film exhibited good but limited

abilities in dynamic and accurate monitoring of multiple brain biomarkers. The sensors together with the designed machine learning regression models were able to provide accurate calculations (R^2> 0.94) of brain biomarker levels. The pH, oxygen, and temperature sensors also exhibited great reversibility in the tests and ensured the potential in long term monitoring. However, as the DO sensor is based on fluorescent whereas the other three sensors are based on colorimetric method, different light sources are required for the excitation of the sensing films. Manually switching of the light source was needed. The glucose sensor which is based on the measurement of H_2O_2 generated from the glucose redox reaction is a non-reversible process, indicating that the film needs to be changed on a regular basis otherwise only accumulation of the glucose level can be detected until saturation, hindering the application in real case scenarios. The four sensing films are evenly placed together by hand, making the miniaturization of the films difficult. Therefore, the second method and sensing system was designed and proposed to overcome the challenges and limitations in the first design.

The fourth chapter introduces the results of the second design: an optical fibre bundle-based multiplexed brain biomarker sensing system. To overcome the challenges in the previous design, an optical fibre bundle-based sensing system was designed. Instead of using a single optical reflection fibre for the delivering and receiving the optical sensing signals of all 4 sensors, optical fibre bundle includes multiple fibres with each sensor has its own fibre as substrate. The methods include the design and fabrication process for the fibre bundle manufacture, the sensing film design and fabrication, and the characterisation and optimization of the optical fibre sensors. Following the fabrication and testing of the individual fluorescent fibre sensors, the sensors were fabricated on the designed bundle and performed multiplexed measurements. Due to the signal overlapping of the bundle sensors, multi-variate regression model was proposed and introduced for the separation of the signals and calculation of biomarker concentrations. Then the system was validated using ex vivo brain model for continuous monitoring and evaluation. In this design, the sensing film was directly coated on the fibre tips using deep coating, avoiding the difficulty of micro scale sensor fabrication. Due to the small size of silica fibres, even 7 fibres were bundled together, the total diameter was still less than 1 mm. Whereas in the previous design, reflection probe was used, where an air gap between the fibre and sensing films was inevitable for reflection signal detection. The air gap led to greater

signal loss and thus a large core diameter (400 um) was needed to capture the reflection signal, leaving a small room for future miniaturization. In the second design, the system was also more versatile in terms of adding or reducing the sensor numbers. Another improvement is the second system adopted fluorescent sensing techniques for all 6 sensors. Different from colorimetric sensors that utilize the absorption abilities of the materials, fluorescent sensors emit a distinct light with the excitation light. Therefore, the emission signal and the excitation signal can be easily separated and distinguished in the spectrum. In addition, broadband light can be replaced by a narrow band laser light to trigger the emission, while in colorimeter, broadband light is used, requiring complex post-processing algorithms to handle the mixed reflection spectrum. In this way, it would be much easier to expand the number of biomarkers can be measured using the second optical fibre bundle sensing system. Another advantage indicated from the characterisation test of the sensors is that all 6 sensors exhibited great reversibility, indicating the sensors' ability in detecting both increasing and decreasing trends in the biomarker levels without the need for sensing film replacement. The fluorescent sensors exhibited great sensitivity and selectivity towards target biomarkers as well as environmental robustness. However, one drawback of the fluorescent sensors compared to the colorimetric sensors is the poor photostability. Photobleaching is inevitable for fluorophores and limits the potential in long-term continuous monitoring. Therefore, computational algorithms and pulsed lasers are introduced in the study to reduce the photobleaching during measurement. Besides, the system still needs to manually switch the three lasers to excite the 6 films in turn for multiplexed measurement. In all, all six sensors exhibited great sensing ability with the assistance of computational algorithms for signal post processing. The overlapping issues in the six sensors' emission spectra are overcome by the proposed multi-variate regression model, providing a highly accurate multiplexed measurement of 6 biomarkers simultaneously. To overcome the temperature, pH, and photobleaching impact on the spectrum readings, compensation algorithms were proposed and utilized based on reversed regression models for signal correction and accurate readout. The validation of the system was carried out using lamb brain and the system showed high proficiency in reflecting the biomarker fluctuations as the disease progresses for the prevention and detection of different secondary injury complications.

In the last research chapter, the bundle based optical fibre sensing system was further improved to achieve fully automated and robust brain biomarker measurement. This chapter mainly focuses on the software design for the sensing system and the prototyping of the multiplexed brain monitor. Due to the limitation of the system in the previous chapters, three lasers needed to be switched manually in turn to excite all fluorescent sensing films for the measurement of 6 brain biomarkers. Therefore, the first task of this chapter was to replace the lasers with a program-controllable multi-wavelength laser. Control program was designed based on Universal Asynchronous Receiver-Transmitter (UART) communication protocols in python for the control of lasers. The spectrometer was also controlled via UART and python scripts to synchronize with the laser for spectra acquisition. Graphical UI was developed for user interface and user settings to control the laser and spectrometer. In the previous chapter, the signal overlapping was solved using multi-variate regression models based on the standards spectra. However, it may not perform very well if large background noise is introduced in the system. Therefore, in this chapter two other methods based on shallow regression models and CNN models were explored to improve the sensing performance and robustness. Machine learning models based on engineered features and CNN models based on extracted shallow and deep features of the acquired fluorescent spectra were evaluated. For environmental compensation, temperature was included as features in training the models. The models demonstrated high calculation accuracy for the target biomarkers, indicating a reliable and great performance for multiplexed brain monitoring. Therefore, the CNN model was deployed in the edge computer for on-line processing of the signal after acquisition in real time. The system was assembled in a portable plastic box with potential for bedside monitoring and has been successfully validated using clinical CSF samples, indicating its potential for real case applications.

6.2 Conclusions

In this thesis, two optical sensing systems are proposed for the accurate monitoring of multiple brain biomarkers with the aim to provide clinical reliable reference and aid in diagnosis and treatment. Various sensor design and fabrication methods are proposed and optimized; optical detection setups are also discussed. Apart from the innovation in the sensing hardware, computational algorithms and

AI modelling methods are also proposed to be used together with the fabricated sensors and provide accurate, fast, reliable, and robust biomarker concentration readout. The hardware design and the software are then integrated together and validated in ex vivo brain models for its potential in performing continuous brain monitoring in patients with TBI.

The first solution, based on a single reflection probe, allows the measurement of 4 brain biomarkers simultaneously. Sensors leverages fluorescent and colorimetric sensing methods are fabricated and placed in front of the reflection fibre. The sensors exhibited high sensitivity, selectivity, and stability when characterized individually, allowing dynamic tracking of these biomarkers in a complex environment. Following individual sensor characterisation, the sensors were multiplexed together for the measurement of 4 biomarkers together. Machine learning models were utilized to solve the spectra overlapping issue. Together with signal post processing algorithm, the developed optical sensors have demonstrated high sensitivity, high selectivity, fast response, good stability, and high accuracy for the measurement of the four target biomarkers. The sensors also exhibited great reversibility for detecting both increase and decrease of the biomarker levels except glucose sensor. It is because that the glucose redox reaction is non-reversible in the measurement environment, which needs to be improved in the future. In this solution, only one fibre channel was utilized to provide multiplexed monitoring, which largely reduced the complexity of the optical system and the costs.

The second system is based the development of the fluorescent optical fibre bundle sensing system, overcoming several limitations in the first design and representing a significant advancement in the field of brain monitoring. Through meticulous design and integration of functionalized fibres, this system enables continuous and simultaneous monitoring of 6 clinically relevant biomarkers in CSF with total diameter of less than 1 mm. The proposed multivariate regression model successfully solved the spectra interferences together with exposure, temperature, and pH compensation methods, offering an accurate prediction of the six-brain biomarker at once with R^2>0.9. The comprehensive validation using ex vivo brain models and clinical CSF samples demonstrates the system's robustness, accuracy, and potential for real-time brain physiology monitoring. The successful identification of TBI complications, including hypoxia, energy failure, and excitotoxicity, underscores the system's ability to track dynamic physiological changes accurately. Additionally, the system's sensitivity and

selectivity in clinical CSF samples exhibit promising prospects for intraoperative and postoperative brain monitoring, offering a gateway for timely interventions and treatments.

In the third part, more advanced computational algorithms based on both machine learning and CNN models are proposed to solve the concentration overlapping issue and calculate brain biomarkers utilizing the same optical fibre bundle sensing system. The advanced algorithms successfully improved the sensing accuracy to 0.95 R2 for all 6 sensors with a short response time and latency. Aided with the algorithms, the system showcases robustness in addressing challenges such as photostability, sensitivity, and environmental influences. The successful deployment of this system onto a microcontroller with a user-friendly interface signifies its potential for practical clinical applications, providing clinicians with dynamic, reliable, and immediate insights into CSF biomarkers.

6.3 Future work

Moving forward, there is still a large room for improvement and further studies, including optimizing sensor performance, computational algorithms, and validation in live animal models and human patients remain pivotal. Collaborative efforts with clinicians and industry partners for clinical validation and commercialization are crucial for translating this innovative sensing system into practical clinical applications. To be specific, technical improvements and future studies can focus on the following directions:

1. Hydrogel fibre-based sensing for improved biocompatibility.

One possible future trajectory is on advancing biocompatibility through the integration of hydrogel fibre-based sensing technology. Hydrogel-based sensor platforms offer superior biocompatibility within the complex biological environment, offering minimized immune responses and improved interaction with cerebrospinal fluid components. In recent years, several studies focusing on hydrogel fibres have been proposed, showcasing its high potential in optical signal transmission and the application in optical biosensing. This direction holds promise for reducing biofouling, fostering a seamless interface between sensing technology and the intricate bioenvironment, paving the way for more reliable and long-term implantable neuro-monitoring applications.

2. Tapered fibre for enhanced sensing performance

The second direction is poised to explore the utilization of tapered fibre to augment sensing capabilities, particularly in enhancing the sensing area and overall performance of the system[266]. Tapered fibre configurations offer a unique opportunity to amplify sensor capabilities by increasing the interaction surface area between the sensor and the surrounding biological environment. Through this approach, sensor sensitivity and resolution are expected to be greatly improved, enabling finer and more precise detection of biomarkers within cerebrospinal fluid. Leveraging the evanescent field effect of the tapered fibre's inherent ability to concentrate light and improve signal-to-noise ratios, sensing sensitivity can be improved, making biomarkers with nano or even pico molar level's detection possible. This direction holds promise for unlocking new horizons in neuro-monitoring, empowering researchers to capture nuanced physiological changes and thus, improved diagnostics and tailored treatment strategies.

3. Optical sensors for larger molecule monitoring

In this study, only small molecules are detected. In the future studies, optical fibre sensors for more complex and larger biomarkers including proteins, DNAs can be explored. There are several protein molecules have been found to be highly related to various brain diseases or disorders, such as Interleukin-6, which reflects brain inflammation status[274], and S100b, which reflects the TBI severity and indicates the disorder progression[275]. The design of the protein fibre sensors can also utilize the fluorescent sensing techniques with proper selection of aptamers/DNA or peptides as receptors. This strategic direction aligns with the increasing recognition of the significance of larger molecular species in neurology, offering a pathway to deciphering intricate biochemical pathways and disease mechanisms.

4. Advanced computational methods for signal processing

Further leveraging cutting-edge algorithms, including deep learning architectures, neural networks, and artificial intelligence-driven models, to extract richer insights from complex spectral data obtained through sensing systems. This endeavor involves refining existing algorithms and exploring novel approaches to enhance signal denoising, baseline correction, and feature extraction for improved accuracy in biomarker concentration calculations. Furthermore, the integration of predictive

analytics and sophisticated data fusion techniques will enable us to discern subtle patterns and correlations within multimodal sensor data, paving the way for more nuanced and precise diagnostics in neurological condition and improved patient care.

6. Animal/clinical verifications

In the end, animal studies and clinical trials are needed to validate the efficacy and translatability of our developed sensing technologies and to assess the real-world performance. The applicability of our sensing systems in capturing biomarker dynamics within biological systems and biocompatibility in long term application will also need to be evaluated. By collaborating with clinicians and researchers, empirical evidence to support the reliability and feasibility of our sensor technologies in real clinical settings will be collected, paving the way for potential regulatory approvals and eventual clinical adoption, thereby contributing to the advancement of neuro-monitoring and personalized healthcare.

To summarize, the proposed optical fibre bundle sensing system holds immense potential as a minimally invasive, multiplexed, and continuous monitoring tool for monitoring brain health, aiding in early diagnosis, and guiding effective treatments for various neurological conditions. This work lays a strong foundation for enhanced diagnostic and monitoring tools in neurology, offering promising avenues for real-time assessment and management of neurological disorders.

References

(1) Le Roux, P. Physiological monitoring of the severe traumatic brain injury patient in the intensive care unit. *Current neurology and neuroscience reports* **2013**, *13*, 1-16.

(2) Toet, M. C.; Lemmers, P. M. Brain monitoring in neonates. *Early human development* **2009**, *85* (2), 77-84.

(3) Wright, W. L. Multimodal monitoring in the ICU: when could it be useful? *Journal of the neurological sciences* **2007**, *261* (1-2), 10-15.

(4) Scheuer, M. L. Continuous EEG monitoring in the intensive care unit. *Epilepsia* **2002**, *43*, 114-127.

(5) Byrom, B.; McCarthy, M.; Schueler, P.; Muehlhausen, W. Brain monitoring devices in neuroscience clinical research: the potential of remote monitoring using sensors, wearables, and mobile devices. *Clinical Pharmacology & Therapeutics* **2018**, *104* (1), 59-71.

(6) Smith, M. Monitoring intracranial pressure in traumatic brain injury. *Anesthesia & Analgesia* **2008**, *106* (1), 240-248.

(7) Bhatia, A.; Gupta, A. K. Neuromonitoring in the intensive care unit. I. Intracranial pressure and cerebral blood flow monitoring. *Intensive care medicine* **2007**, *33*, 1263-1271.

(8) Roozenbeek, B.; Maas, A. I.; Menon, D. K. Changing patterns in the epidemiology of traumatic brain injury. *Nature Reviews Neurology* **2013**, *9* (4), 231-236.

(9) Zink, B. J. Traumatic brain injury outcome: concepts for emergency care. *Annals of emergency medicine* **2001**, *37* (3), 318-332.

(10) Ghajar, J. Traumatic brain injury. *The Lancet* **2000**, *356* (9233), 923-929.

(11) Bayr, H.; Clark, R. S.; Kochanek, P. M. Promising strategies to minimize secondary brain injury after head trauma. *Crit. Care Med.* **2003**, *31* (1), S112-S117.

(12) Zhang, Y.; Jiang, N.; Yetisen, A. K. Brain neurochemical monitoring. *Biosens. Bioelectron.* **2021**, *189*, 113351. DOI: https://doi.org/10.1016/j.bios.2021.113351.

(13) Ou, Y.; Buchanan, A. M.; Witt, C. E.; Hashemi, P. Frontiers in Electrochemical Sensors for Neurotransmitter Detection: Towards Measuring Neurotransmitters as Chemical Diagnostics for Brain Disorders. *Anal. Methods.* **2019**, *11* (21), 2738-2755. DOI: 10.1039/c9ay00055k.

(14) Myers, R. B.; Lazaridis, C.; Jermaine, C. M.; Robertson, C. S.; Rusin, C. G. Predicting Intracranial Pressure and Brain Tissue Oxygen Crises in Patients With Severe Traumatic Brain Injury. *Crit. Care Med.* **2016**, *44* (9), 1754-1761. DOI: 10.1097/CCM.0000000000001838 From NLM Medline.

(15) Wei, Y.; Zhou, J.; Wang, Y.; Liu, Y.; Liu, Q.; Luo, J.; Wang, C.; Ren, F.; Huang, L. A review of algorithm & hardware design for AI-based biomedical applications. *IEEE transactions on biomedical circuits and systems* **2020**, *14* (2), 145-163.

(16) Ardeti, V. A.; Kolluru, V. R.; Varghese, G. T.; Patjoshi, R. K. An overview on state-of-the-art electrocardiogram signal processing methods: Traditional to AI-based approaches. *Expert Systems with Applications* **2023**, *217*, 119561.

(17) Bogdanski, D. F.; Pletscher, A.; Brodie, B. B.; Udenfriend, S. Identification and assay of serotonin in brain. *Journal of Pharmacology Experimental Therapeutics* **1956**, *117* (1), 82-88.

(18) Carlsson, A.; Lindqvist, M.; Magnusson, T.; Waldeck, B. On the presence of 3-hydroxytyramine in brain. *Science* **1958**, *127* (3296), 471-471.

(19) Clark Jr, L. C.; Lyons, C. Electrode systems for continuous monitoring in cardiovascular surgery. *Annals of the New York Academy of sciences* **1962**, *102* (1), 29-45.

(20) Clark Jr, L.; Lyons, C. Studies of a glassy carbon electrode for brain polarography with observations on the effect of carbonic anhydrase inhibition. *J. Med. Sci.* **1965**, *2* (4), 353-359.

(21) Bito, L.; Davson, H.; Levin, E. e.; Murray, M.; Snider, N. The concentrations of free amino acids and other electrolytes in cerebrospinal fluid, in vivo dialysate of brain, and blood plasma of the dog. *Journal of neurochemistry* **1966**, *13* (11), 1057-1067.

(22) Lonnroth, P.; Jansson, P.; Smith, U. A microdialysis method allowing characterization of intercellular water space in humans. *Am. J. Physiol. Endocrinol. Metab.* **1987**, *253* (2), E228-E231.

(23) During, M. J.; Spencer, D. D. Extracellular hippocampal glutamate and spontaneous seizure in the conscious human brain. *The lancet* **1993**, *341* (8861), 1607-1610.

(24) Meyerson, B.; Linderoth, B.; Karlsson, H.; Ungerstedt, U. Microdialysis in the human brain: extracellular measurements in the thalamus of parkinsonian patients. *Life sciences* **1990**, *46* (4), 301-308.

(25) Jobsis, F. F. Noninvasive, infrared monitoring of cerebral and myocardial oxygen sufficiency and circulatory parameters. *Science* **1977**, *198* (4323), 1264-1267.

(26) Mayevsky, A. Brain NADH redox state monitored in vivo by fiber optic surface fluorometry. *Brain Research Reviews* **1984**, *7* (1), 49-68.

(27) Mizuno, A.; Hayashi, T.; Tashibu, K.; Maraishi, S.; Kawauchi, K.; Ozaki, Y. Near-infrared FT-Raman spectra of the rat brain tissues. *Neurosci. Lett.* **1992**, *141* (1), 47-52.

(28) Mizuno, A.; Kitajima, H.; Kawauchi, K.; Muraishi, S.; Ozaki, Y. Near-infrared Fourier transform Raman spectroscopic study of human brain tissues and tumours. *Journal of Raman spectroscopy* **1994**, *25* (1), 25-29.

(29) Jorgenson, R. C.; Yee, S. S. A fiber-optic chemical sensor based on surface plasmon resonance. *Sensors and Actuators B: Chemical* **1993**, *12* (3), 213-220.

(30) Miyawaki, A.; Llopis, J.; Heim, R.; McCaffery, J. M.; Adams, J. A.; Ikura, M.; Tsien, R. Y. Fluorescent indicators for Ca 2+ based on green fluorescent proteins and calmodulin. *Nature* **1997**, *388* (6645), 882-887.

(31) Potyrailo, R. A.; Conrad, R. C.; Ellington, A. D.; Hieftje, G. M. Adapting selected nucleic acid ligands (aptamers) to biosensors. *Analytical Chemistry* **1998**, *70* (16), 3419-3425.

(32) Tsai, T.-C.; Han, H.-Z.; Cheng, C.-C.; Chen, L.-C.; Chang, H.-C.; Chen, J.-J. J. Modification of platinum microelectrode with molecularly imprinted over-oxidized polypyrrole for dopamine measurement in rat striatum. *Sensors Actuators B: Chem.* **2012**, *171*, 93-101.

(33) Elghanian, R.; Storhoff, J. J.; Mucic, R. C.; Letsinger, R. L.; Mirkin, C. A. Selective colorimetric detection of polynucleotides based on the distance-dependent optical properties of gold nanoparticles. *Science* **1997**, *277* (5329), 1078-1081.

(34) Orlowski, P.; Chappell, M.; Park, C. S.; Grau, V.; Payne, S. Modelling of pH dynamics in brain cells after stroke. *Interface Focus* **2011**, *1* (3), 408-416. DOI: 10.1098/rsfs.2010.0025.

(35) Chesler, M. Regulation and modulation of pH in the brain. *Physiological reviews* **2003**, *83* (4), 1183-1221.

(36) Steinegger, A.; Wolfbeis, O. S.; Borisov, S. M. Optical sensing and imaging of pH values: spectroscopies, materials, and applications. *Chem. Rev.* **2020**, *120* (22), 12357-12489.

(37) Gupta, A. K.; Zygun, D. A.; Johnston, A. J.; Steiner, L. A.; Al-Rawi, P. G.; Chatfield, D.; Shepherd, E.; Kirkpatrick, P. J.; Hutchinson, P. J.; Menon, D. K. Extracellular brain pH and outcome following severe traumatic brain injury. *J. Neurotrauma* **2004**, *21* (6), 678-684.

(38) Stewart, C.; Haitsma, I.; Zador, Z.; Hemphill, J. C., 3rd; Morabito, D.; Manley, G., 3rd; Rosenthal, G. The new Licox combined brain tissue oxygen and brain temperature monitor: assessment of in vitro accuracy and clinical experience in severe traumatic brain injury. *Neurosurg.* **2008**, *63* (6), 1159-1164; discussion 1164-1155. DOI: 10.1227/01.NEU.0000333265.19131.7C.

(39) Wang, H.; Wang, B.; Normoyle, K. P.; Jackson, K.; Spitler, K.; Sharrock, M. F.; Miller, C. M.; Best, C.; Llano, D.; Du, R. Brain temperature and its fundamental properties: a review for clinical neuroscientists. *Front Neurosci* **2014**, *8*, 307. DOI: 10.3389/fnins.2014.00307.

(40) Shin, J.; Liu, Z.; Bai, W.; Liu, Y.; Yan, Y.; Xue, Y.; Kandela, I.; Pezhouh, M.; MacEwan, M. R.; Huang, Y. Bioresorbable optical sensor systems for monitoring of intracranial pressure and temperature. *Sci. Adv.* **2019**, *5* (7), eaaw1899.

(41) Rossi, S.; Zanier, E. R.; Mauri, I.; Columbo, A.; Stocchetti, N. Brain temperature, body core temperature, and intracranial pressure in acute cerebral damage. *J Neurol Neurosurg Psychiatry* **2001**, *71* (4), 448-454. DOI: 10.1136/jnnp.71.4.448.

(42) Watts, M. E.; Pocock, R.; Claudianos, C. Brain Energy and Oxygen Metabolism: Emerging Role in Normal Function and Disease. *Front Mol Neurosci* **2018**, *11*, 216. DOI: 10.3389/fnmol.2018.00216.

(43) Wang, C. C.; Kuo, J. R.; Chen, Y. C.; Chio, C. C.; Wang, J. J.; Lin, B. S. Brain tissue oxygen evaluation by wireless near-infrared spectroscopy. *J Surg Res* **2016**, *200* (2), 669-675. DOI: 10.1016/j.jss.2015.10.005.

(44) Ndubuizu, O.; LaManna, J. C. Brain tissue oxygen concentration measurements. *Antioxid Redox Signal* **2007**, *9* (8), 1207-1219. DOI: 10.1089/ars.2007.1634.

(45) Lazaridis, C.; Andrews, C. M. Brain tissue oxygenation, lactate-pyruvate ratio, and cerebrovascular pressure reactivity monitoring in severe traumatic brain injury: systematic review and viewpoint. *Neurocritical care* **2014**, *21* (2), 345-355.

(46) Yu, Y.; Zhang, K.; Zhang, L.; Zong, H.; Meng, L.; Han, R. Cerebral near-infrared spectroscopy (NIRS) for perioperative monitoring of brain oxygenation in children and adults. *Cochrane Database of Systematic Reviews* **2018**, (1).

(47) Dengl, M.; Jaeger, M.; Renner, C.; Meixensberger, J. Comparing brain tissue oxygen measurements and derived autoregulation parameters from different probes (Licox vs. Raumedic). *Acta Neurochir Suppl* **2012**, *114*, 165-168. DOI: 10.1007/978-3-7091-0956-4_31.

(48) Kammerer, T.; Faihs, V.; Hulde, N.; Bayer, A.; Schfer, S. T. Changes of hemodynamic and cerebral oxygenation after exercise in normobaric and hypobaric hypoxia: associations with acute mountain sickness. *Annals of Occupational and Environmental Medicine* **2018**, *30* (1), 66.

(49) Bélanger M; Allaman I; PJ, M. Brain energy metabolism: focus on astrocyte-neuron metabolic cooperation. *Cell Metab* **2011**, *14* (6), 724-738. DOI: doi: 10.1016/j.cmet.2011.08.016.

(50) Mergenthaler, P.; Lindauer, U.; Dienel, G. A.; Meisel, A. Sugar for the brain: the role of glucose in physiological and pathological brain function. *Trends Neurosci* **2013**, *36* (10), 587-597. DOI: 10.1016/j.tins.2013.07.001.

(51) Magistretti, P. P. J. Glutamate uptake into astrocytes stimulates aerobic glycolysis: a mechanism coupling neuronal activity to glucose utilization. *Proceedings of the National Academy of Ences of the United States of America* **1994**, *91* (22), 10625-10629.

(52) Hillered, L.; Hllstro?M, A.; Segersv?Rd, S.; Persson, L.; Ungerstedt, U. Dynamics of extracellular metabolites in the striatum after middle cerebral artery occlusion in the rat monitored by intracerebral microdialysis. *J Cereb Blood Flow Metab* **1989**, *9* (5), 607-616.

(53) Hillered, L.; Persson, L.; Bolander, H. G.; Hallstr??M, S.; Ungerstedt, U. Increased extracellular levels of ascorbate in the striatum after middle cerebral artery occlusion in the rat monitored by intracerebral microdialysis. *Neuroscience Letters* **1988**, *95* (1-3), 286-290.

(54) Hillered, L.; Persson, L.; Ungerstedt, U. Chemical changes in the extracellular fluid of human cerebral cortex during ischemia measured by intracerebral microdialysis. *Neurochem* **1989**, *52*, 55.

(55) Pulsinelli, W. A.; Levy, D. E.; Duffy, T. E. Regional cerebral blood flow and glucose metabolism following transient forebrain ischemia. *Annals of Neurology* **2010**, *11* (5).

(56) Hillered, L.; Persson, L. Microdialysis for neurochemical monitoring of the human brain. *Scand Cardiovasc J* **2003**, *37* (1), 13-17. DOI: 10.1080/14017430310006974.

(57) Mergenthaler, P.; Lindauer, U.; Dienel, G. A.; Meisel, A. J. T. i. n. Sugar for the brain: the role of glucose in physiological and pathological brain function. **2013**, *36* (10), 587-597.

(58) Pascual, J. M.; Wang, D.; Hinton, V.; Engelstad, K.; Saxena, C. M.; Van Heertum, R. L.; Darryl, C. J. A. o. n. Brain glucose supply and the syndrome of infantile neuroglycopenia. **2007**, *64* (4), 507-513.

(59) Dunn, L.; Allen, G. F.; Mamais, A.; Ling, H.; Li, A.; Duberley, K. E.; Hargreaves, I. P.; Pope, S.; Holton, J. L.; Lees, A. J. N. o. a. Dysregulation of glucose metabolism is an early event in sporadic Parkinson's disease. **2014**, *35* (5), 1111-1115.

(60) An, Y.; Varma, V. R.; Varma, S.; Casanova, R.; Dammer, E.; Pletnikova, O.; Chia, C. W.; Egan, J. M.; Ferrucci, L.; Troncoso, J. J. A. s.; et al. Evidence for brain glucose dysregulation in Alzheimer's disease. **2018**, *14* (3), 318-329.

(61) Blanco, M. M. B.; Prashant, G. N.; Vespa, P. M. J. N. C. Cerebral metabolism and the role of glucose control in acute traumatic brain injury. **2016**, *27* (4), 453-463.

(62) Magistretti, P. J.; Allaman, I. Lactate in the brain: from metabolic end-product to signalling molecule. *Nature Reviews Neuroscience* **2018**, *19* (4), 235-249. DOI: 10.1038/nrn.2018.19.

(63) Schurr, A. J. F. i. n. Cerebral glycolysis: a century of persistent misunderstanding and misconception. **2014**, *8*, 360.

(64) Gladden, L. J. T. J. o. p. Lactate metabolism: a new paradigm for the third millennium. **2004**, *558* (1), 5-30.

(65) Hirschhaeuser, F.; Sattler, U. G.; Mueller-Klieser, W. J. C. r. Lactate: a metabolic key player in cancer. **2011**, *71* (22), 6921-6925.

(66) Brown, A. M.; Wender, R.; Ransom, B. R. J. J. o. n. r. Metabolic substrates other than glucose support axon function in central white matter. **2001**, *66* (5), 839-843.

(67) McIlwain, H. J. J. o. n., neurosurgery,; psychiatry. Substances which support respiration and metabolic response to electrical impulses in human cerebral tissues. **1953**, *16* (4), 257.

(68) Suzuki, A.; Stern, S. A.; Bozdagi, O.; Huntley, G. W.; Walker, R. H.; Magistretti, P. J.; Alberini, C. M. J. C. Astrocyte-neuron lactate transport is required for long-term memory formation. **2011**, *144* (5), 810-823.

(69) Alberini, C. M.; Cruz, E.; Descalzi, G.; Bessières, B.; Gao, V. J. G. Astrocyte glycogen and lactate: New insights into learning and memory mechanisms. **2018**, *66* (6), 1244-1262.

(70) Inao, S.; Marmarou, A.; Clarke, G. D.; Andersen, B. J.; Fatouros, P. P.; Young, H. F. J. J. o. n. Production and clearance of lactate from brain tissue, cerebrospinal fluid, and serum following experimental brain injury. **1988**, *69* (5), 736-744.

(71) Rice, A. C.; Zsoldos, R.; Chen, T.; Wilson, M. S.; Alessandri, B.; Hamm, R. J.; Bullock, M. R. J. B. r. Lactate administration attenuates cognitive deficits following traumatic brain injury. **2002**, *928* (1-2), 156-159.

(72) Regenold, W. T.; Phatak, P.; Marano, C. M.; Sassan, A.; Conley, R. R.; Kling, M. A. Elevated Cerebrospinal Fluid Lactate Concentrations in Patients with Bipolar Disorder and Schizophrenia: Implications for the Mitochondrial Dysfunction Hypothesis. *Biological Psychiatry* **2009**, *65* (6), 489-494. DOI: https://doi.org/10.1016/j.biopsych.2008.11.010.

(73) Ryou, M.-G.; Liu, R.; Ren, M.; Sun, J.; Mallet, R. T.; Yang, S.-H. J. S. Pyruvate protects the brain against ischemia–reperfusion injury by activating the erythropoietin signaling pathway. **2012**, *43* (4), 1101-1107.

(74) Clark, J. B.; Land, J. M. J. B. J. Differential effects of 2-oxo acids on pyruvate utilization and fatty acid synthesis in rat brain. **1974**, *140* (1), 25-29.

(75) Grazioli, E.; Dimauro, I.; Mercatelli, N.; Wang, G.; Pitsiladis, Y.; Di Luigi, L.; Caporossi, D. J. B. g. Physical activity in the prevention of human diseases: role of epigenetic modifications. **2017**, *18* (8), 111-123.

(76) Suh, S. W.; Aoyama, K.; Matsumori, Y.; Liu, J.; Swanson, R. A. J. D. Pyruvate administered after severe hypoglycemia reduces neuronal death and cognitive impairment. **2005**, *54* (5), 1452-1458.

(77) Owen, L.; Sunram-Lea, S. I. J. N. Metabolic agents that enhance ATP can improve cognitive functioning: a review of the evidence for glucose, oxygen, pyruvate, creatine, and L-carnitine. **2011**, *3* (8), 735-755.

(78) Yu, Y.-M.; Kim, J.-B.; Lee, K.-W.; Yun Kim, S.; Han, P.-L.; Lee, J.-K. J. S. Inhibition of the cerebral ischemic injury by ethyl pyruvate with a wide therapeutic window. **2005**, *36* (10), 2238-2243.

(79) Du, F.; Zhu, X.-H.; Zhang, Y.; Friedman, M.; Zhang, N.; Uğurbil, K.; Chen, W. J. P. o. t. N. A. o. S. Tightly coupled brain activity and cerebral ATP metabolic rate. **2008**, *105* (17), 6409-6414.

(80) Boyer, P. D. J. N. What makes ATP synthase spin? **1999**, *402* (6759), 247-249.

(81) Eriksen, J. L.; Wszolek, Z.; Petrucelli, L. J. A. o. n. Molecular pathogenesis of Parkinson disease. **2005**, *62* (3), 353-357.

(82) Al-Mosalem, O.; El-Ansary, A.; Attas, O.; Al-Ayadhi, L. J. C. b. Metabolic biomarkers related to energy metabolism in Saudi autistic children. **2009**, *42* (10-11), 949-957.

(83) Bucher, E. S.; Wightman, R. M. Electrochemical Analysis of Neurotransmitters. *Annual Review of Analytical Chemistry* **2015**, *8* (1), 239.

(84) Jamwal, S.; Kumar, P. Insight Into the Emerging Role of Striatal Neurotransmitters in the Pathophysiology of Parkinson's Disease and Huntington's Disease: A Review. *Current Neuropharmacology* **2018**, *16* (2), 165-175.

(85) Day, M.; Wang, Z.; Ding, J.; An, X.; Ingham, C. A.; Shering, A. F.; Wokosin, D.; Ilijic, E.; Sun, Z.; Sampson, A. R. Selective elimination of glutamatergic synapses on striatopallidal neurons in Parkinson disease models. *Nature Neuroscience* **2006**, *9* (2), 251-259.

(86) Fonnum, F. Glutamate: A Neurotransmitter in Mammalian Brain. *Journal of neurochemistry* **1984**, *42* (1), 1-11. DOI: 10.1111/j.1471-4159.1984.tb09689.x.

(87) Wang, H. B.; Wu, Q. J.; Zhao, S. J.; Hou, Y. J.; Li, H. X.; Yang, M. F.; Wang, B. J.; Sun, B. L.; Zhang, Z. Y. Early High Cerebrospinal Fluid Glutamate: A Potential Predictor for Delayed Cerebral Ischemia after Aneurysmal Subarachnoid Hemorrhage. *ACS Omega* **2020**, *5* (25), 15385-15389. DOI: 10.1021/acsomega.0c01472.

(88) Drejer, J.; Benveniste, H.; Diemer, N. H.; Schousboe, A. Cellular Origin of Ischemia-Induced Glutamate Release from Brain Tissue In Vivo and In Vitro. *Journal of Neurochemistry* **2006**, *45* (1), 145-151.

(89) Martin, L. J.; Brambrink, A. M.; Lehmann, C.; Portera-Cailliau, C.; Traystman, R. J. Hypoxia-ischemia causes abnormalities in glutamate transporters and death of astroglia and neurons in newborn striatum. *Annals of Neurology* **2010**, *42* (3), 335-348.

(90) Olney; W., J. Brain Lesions, Obesity, and Other Disturbances in Mice Treated with Monosodium Glutamate. *Science* **1969**, *164* (3880), 719-721.

(91) Zhou Y ; C, D. N. Glutamate as a neurotransmitter in the healthy brain. *Journal of Neural Transmission* **2014**, *121* (8), 799-817.

(92) Wakabayashi, K. T.; Kiyatkin, E. A. Rapid changes in extracellular glutamate induced by natural arousing stimuli and intravenous cocaine in the nucleus accumbens shell and core. *Journal of Neurophysiology* **2012**, *108* (1), 285.

(93) Lenoir, M.; Kiyatkin, E. A. Intravenous nicotine injection induces rapid, experience-dependent sensitization of glutamate release in the ventral tegmental area and nucleus accumbens. *Journal of Neurochemistry* **2013**, *127* (4), 541–551.

(94) Johnston, M. V.; Simon, A.; Cliona, O. D.; Amy, W.; Sakkubai, N.; Kadam, S. D. Twenty-four hour quantitative-EEG and in-vivo glutamate biosensor detects activity and circadian rhythm dependent biomarkers of pathogenesis in Mecp2 null mice. *Frontiers in Systems Neuroscience* **2014**, *8*, 118.

(95) Wise; Roy, A. Dopamine, learning and motivation. *Nature Reviews Neuroscience* **2004**, *5* (6), 483-494.

(96) Hornykiewicz, O.; Kish, S. J. Hornykiewicz O, Kish SJBiochemical pathophysiology of Parkinson's disease. Adv Neurol 45:19-34. *Advances in Neurology* **1987**, *45*, 19-34.

(97) Nestler E J ; C, J. W. A. The Mesolimbic Dopamine Reward Circuit in Depression. *Biological Psychiatry* **2006**, *59* (12), 1151-1159.

(98) Rahim, A.; Barros, S.; Kubota, L. T.; Gushikem, Y. SiO2/C/Cu(II)phthalocyanine as a biomimetic catalyst for dopamine monooxygenase in the development of an amperometric sensor. *Electrochimica Acta* **2011**, *56* (27), 10116-10121.

(99) Xue, C.; Han, Q.; Wang, Y.; Wu, J.; Wen, T.; Wang, R.; Hong, J.; Zhou, X.; Jiang, H. Amperometric detection of dopamine in human serumby electrochemical sensor based on gold nanoparticles doped molecularly imprinted polymers. *Biosensors Bioelectronics* **2013**, *49* (Complete), 199-203.

(100) Xu, G.; Jarjes, Z. A.; Desprez, V.; Kilmartin, P. A.; Travas-Sejdic, J. Sensitive, selective, disposable electrochemical dopamine sensor based on PEDOT-modified laser scribed graphene. *Biosens. Bioelectron.* **2018**, *107*, 184-191. DOI: 10.1016/j.bios.2018.02.031.

(101) Schwerdt, H. N.; Zhang, E.; Kim, M. J.; Yoshida, T.; Stanwicks, L.; Amemori, S.; Dagdeviren, H. E.; Langer, R.; Cima, M. J.; Graybiel, A. M. Cellular-scale probes enable stable chronic subsecond monitoring of dopamine neurochemicals in a rodent model. *Commun Biol* **2018**, *1*, 144. DOI: 10.1038/s42003-018-0147-y.

(102) Demuru, S.; Nela, L.; Marchack, N.; Holmes, S. J.; Farmer, D. B.; Tulevski, G. S.; Lin, Q.; Deligianni, H. Scalable Nanostructured Carbon Electrode Arrays for Enhanced Dopamine Detection. *ACS Sens* **2018**, *3* (4), 799-805. DOI: 10.1021/acssensors.8b00043.

(103) Dutta, P.; Pernites, R. B.; Danda, C.; Advincula, R. C. SPR Detection of Dopamine Using Cathodically Electropolymerized, Molecularly Imprinted Poly-p-aminostyrene Thin Films. *Macromolecular Chemistry Physics* **2011**.

(104) Pathak, A.; Gupta, B. D. Ultra-selective fiber optic SPR platform for the sensing of dopamine in synthetic cerebrospinal fluid incorporating permselective nafion membrane and surface imprinted MWCNTs-PPy matrix. *Biosens. Bioelectron.* **2019**, *133*, 205-214. DOI: 10.1016/j.bios.2019.03.023.

(105) Manciu, F. S.; Manciu, M.; Ciubuc, J. D.; Sundin, E. M.; Ochoa, K.; Eastman, M.; Durrer, W. G.; Guerrero, J.; Lopez, B.; Subedi, M.; et al. Simultaneous Detection of Dopamine and Serotonin-A Comparative Experimental and Theoretical Study of Neurotransmitter Interactions. *Biosensors (Basel)* **2018**, *9* (1). DOI: 10.3390/bios9010003.

(106) Chang, E. H.; Chavan, S. S.; Pavlov, V. A. Cholinergic Control of Inflammation, Metabolic Dysfunction, and Cognitive Impairment in Obesity-Associated Disorders: Mechanisms and Novel Therapeutic Opportunities. *Frontiers in Neuroscience* **2019**, *13*.

(107) Parikh, V.; Pomerleau, F.; Huettl, P.; Gerhardt, G. A.; Sarter, M.; Bruno, J. P. Rapid assessment of in vivo cholinergic transmission by amperometric detection of changes in extracellular choline levels. *European Journal of Neuroscience* **2015**, *20*.

(108) Fenoy, G. E.; Marmisollé, W. A.; Azzaroni, O.; Knoll, W. Acetylcholine biosensor based on the electrochemical functionalization of graphene field-effect transistors. *Biosensors Bioelectronics* **2020**, *148*, 111796.

(109) Kucherenko, D. Y.; Kucherenko, I.; Soldatkin, O.; Topolnikova, Y. V.; Dzyadevych, S.; Soldatkin, A. A highly selective amperometric biosensor array for the simultaneous determination of glutamate, glucose, choline, acetylcholine, lactate and pyruvate. *Bioelectrochemistry* **2019**, *128*, 100-108.

(110) Cohen, E. L.; Wurtman, R. J. Brain acetylcholine: increase after systemic choline administration. *Life Sciences* **1975**, *16* (7), 1095-1102.

(111) Leen, W. G.; Willemsen, M. A.; Wevers, R. A.; Verbeek, M. M. Cerebrospinal fluid glucose and lactate: age-specific reference values and implications for clinical practice. *Plos One* **2012**, *7* (8), e42745. DOI: 10.1371/journal.pone.0042745.

(112) Benoist, J.-F. o.; Alberti, C.; Leclercq, S.; Rigal, O.; Jean-Louis, R.; Ogier de Baulny, H. l.; Porquet, D.; Biou, D. Cerebrospinal Fluid Lactate and Pyruvate Concentrations and Their Ratio in Children: Age-related Reference Intervals. *Clin. Chem.* **2003**, *49* (3), 487-494. DOI: 10.1373/49.3.487 %J Clinical Chemistry (acccessed 12/8/2020).

(113) Erecińska, M.; Silver, I. A. ATP and brain function. *J. Cerebr. Blood F. Met.* **1989**, *9* (1), 2-19.

(114) Klinker, C. C.; Bowser, M. T. 4-Fluoro-7-nitro-2,1,3-benzoxadiazole as a Fluorogenic Labeling Reagent for the in Vivo Analysis of Amino Acid Neurotransmitters Using Online Microdialysis-Capillary Electrophoresis. *Anal. Chem.* **2007**, *79*, 8747-8754.

(115) Goldstein, D. S.; Holmes, C.; Sharabi, Y. Cerebrospinal fluid biomarkers of central catecholamine deficiency in Parkinson's disease and other synucleinopathies. *Brain* **2012**, *135* (Pt 6), 1900-1913. DOI: 10.1093/brain/aws055.

(116) Jia, J. P.; Jia, J. M.; Zhou, W. D.; Xu, M.; Chu, C. B.; Yan, X.; Sun, Y. X. Differential acetylcholine and choline concentrations in the cerebrospinal fluid of patients with Alzheimer's disease and vascular dementia. *Chin. Med. J.* **2004**, *117* (8), 1161-1164, Article. Scopus.

(117) Lamy, E.; Pilyser, L.; Paquet, C.; Bouaziz-Amar, E.; Grassin-Delyle, S. High-sensitivity quantification of acetylcholine and choline in human cerebrospinal fluid with a validated LC-MS/MS method. *Talanta* **2020**, (224), 121881, Article. DOI: 10.1016/j.talanta.2020.121881 Scopus.

(118) Pilotto, A.; Blau, N.; Leks, E.; Schulte, C.; Deuschl, C.; Zipser, C.; Piel, D.; Freisinger, P.; Gramer, G.; Kölker, S. Cerebrospinal fluid biogenic amines depletion and brain atrophy in adult patients with phenylketonuria. *J. Inherit. Metab. Dis.* **2019**, *42* (3), 398-406.

(119) Zhang, Y.; Jiang, N.; Yetisen, A. K. Brain neurochemical monitoring. *Biosens. Bioelectron.* **2021**, *189*, 113351.

(120) Su, C. K.; Sun, Y. C.; Tzeng, S. F.; Yang, C. S.; Wang, C. Y.; Yang, M. H. In vivo monitoring of the transfer kinetics of trace elements in animal brains with hyphenated inductively coupled plasma mass spectrometry techniques. *Mass spectrometry reviews* **2010**, *29* (3), 392-424.

(121) Slaney, T. R.; Nie, J.; Hershey, N. D.; Thwar, P. K.; Linderman, J.; Burns, M. A.; Kennedy, R. T. Push-pull perfusion sampling with segmented flow for high temporal and spatial resolution in vivo chemical monitoring. *Analytical Chemistry* **2011**, *83* (13), 5207-5213.

(122) Ngernsutivorakul, T.; Steyer, D. J.; Valenta, A. C.; Kennedy, R. T. In Vivo Chemical Monitoring at High Spatiotemporal Resolution Using Microfabricated Sampling Probes and Droplet-Based Microfluidics Coupled to Mass Spectrometry. *Anal. Chem.* **2018**, *90* (18), 10943-10950. DOI: 10.1021/acs.analchem.8b02468.

(123) Gowers, S. A. N.; Samper, I. C.; Murray, D. R. K.; Smith, G. K.; Jeyaprakash, S.; Rogers, M. L.; Karlsson, M.; Olsen, M. H.; Moller, K.; Boutelle, M. G. Real-time neurochemical measurement of dynamic metabolic events during cardiac arrest and resuscitation in a porcine model. *Analyst* **2020**, *145* (5), 1894-1902. DOI: 10.1039/c9an01950b.

(124) Samper, I. C.; Gowers, S. A. N.; Rogers, M. L.; Murray, D. R. K.; Jewell, S. L.; Pahl, C.; Strong, A. J.; Boutelle, M. G. 3D printed microfluidic device for online detection of neurochemical changes with high temporal resolution in human brain microdialysate. *Lab Chip* **2019**, *19* (11), 2038-2048. DOI: 10.1039/c9lc00044e.

(125) Gowers, S. A. N.; Rogers, M. L.; Booth, M. A.; Leong, C. L.; Samper, I. C.; Phairatana, T.; Jewell, S. L.; Pahl, C.; Strong, A. J.; Boutelle, M. G. Clinical translation of microfluidic sensor devices: focus on calibration and analytical robustness. *Lab Chip* **2019**, *19* (15), 2537-2548. DOI: 10.1039/c9lc00400a.

(126) Gu, F.; Zhou, X.; Zhu, X.; Zhao, M.; Hao, J.; Yu, P.; Mao, L. In vivo and continuous measurement of bisulfide in the hippocampus of rat's brain by an on-line integrated microdialysis/droplet-based microfluidic system. *Analyst* **2015**, *140* (11), 3814-3819. DOI: 10.1039/c4an01974a.

(127) Ganesana, M.; Trikantzopoulos, E.; Maniar, Y.; Lee, S. T.; Venton, B. J. Development of a novel micro biosensor for in vivo monitoring of glutamate release in the brain. *Biosens. Bioelectron.* **2019**, *130*, 103-109. DOI: 10.1016/j.bios.2019.01.049.

(128) Lourenço, C. F.; Ledo, A.; Laranjinha, J.; Gerhardt, G. A.; Barbosa, R. M. Microelectrode array biosensor for high-resolution measurements of extracellular glucose in the brain. *Sensors and Actuators B: Chemical* **2016**, *237*, 298-307. DOI: 10.1016/j.snb.2016.06.083.

(129) Cordeiro, C. A.; Sias, A.; Koster, T.; Westerink, B. H. C.; Cremers, T. I. F. H. In vivo "real-time" monitoring of glucose in the brain with an amperometric enzyme-based biosensor based on gold coated tungsten (W-Au) microelectrodes. *Sensors Actuators B: Chem.* **2018**, *263*, 605-613. DOI: 10.1016/j.snb.2018.02.116.

(130) Schwerdt, H. N.; Shimazu, H.; Amemori, K. I.; Amemori, S.; Tierney, P. L.; Gibson, D. J.; Hong, S.; Yoshida, T.; Langer, R.; Cima, M. J.; et al. Long-term dopamine neurochemical monitoring in primates. *Proc. Natl. Acad. Sci. USA* **2017**, *114* (50), 13260-13265. DOI: 10.1073/pnas.1713756114.

(131) Demuru, S.; Nela, L.; Marchack, N.; Holmes, S. J.; Farmer, D. B.; Tulevski, G. S.; Lin, Q.; Deligianni, H. Scalable Nanostructured Carbon Electrode Arrays for Enhanced Dopamine Detection. *ACS Sens.* **2018**, *3* (4), 799-805. DOI: 10.1021/acssensors.8b00043.

(132) Raju, D.; Mendoza, A.; Wonnenberg, P.; Mohanaraj, S.; Sarbanes, M.; Truong, C.; Zestos, A. G. Polymer modified carbon fiber-microelectrodes and waveform modifications enhance neurotransmitter metabolite detection. *Analytical Methods* **2019**, *11* (12), 1620-1630. DOI: 10.1039/c8ay02737d.

(133) Kim, J. Comparison Study of Partial Least Squares Regression Analysis and Principal Component Analysis in Fast-Scan Cyclic Voltammetry. *International Journal of Electrochemical Science* **2019**, 5924-5937. DOI: 10.20964/2019.07.03.

(134) Zhu, M.; Zeng, C.; Ye, J.; Sun, Y. Simultaneous in vivo voltammetric determination of dopamine and 5-Hydroxytryptamine in the mouse brain. *Applied Surface Science* **2018**, *455*, 646-652.

(135) Dong, H.; Zhang, L.; Liu, W.; Tian, Y. Label-Free Electrochemical Biosensor for Monitoring of Chloride Ion in an Animal Model of Alzhemier's Disease. *ACS Chem. Neurosci.* **2017**, *8* (2), 339-346. DOI: 10.1021/acschemneuro.6b00296.

(136) Teng, Y.; Liu, F.; Kan, X. Voltammetric dopamine sensor based on three-dimensional electrosynthesized molecularly imprinted polymers and polypyrrole nanowires. *Microchimica. Acta* **2017**, *184* (8), 2515-2522.

(137) Guan, J.-F.; Zou, J.; Liu, Y.-P.; Jiang, X.-Y.; Yu, J.-G. Hybrid carbon nanotubes modified glassy carbon electrode for selective, sensitive and simultaneous detection of dopamine and uric acid. *Ecotoxicol. Environ. Saf.* **2020**, *201*, 110872.

(138) Nimbalkar, S.; Castagnola, E.; Balasubramani, A.; Scarpellini, A.; Samejima, S.; Khorasani, A.; Boissenin, A.; Thongpang, S.; Moritz, C.; Kassegne, S. Ultra-Capacitive Carbon Neural Probe Allows Simultaneous Long-Term Electrical Stimulations and High-Resolution Neurotransmitter Detection. *Sci. Rep.* **2018**, *8* (1), 6958. DOI: 10.1038/s41598-018-25198-x.

(139) Schwerdt, H. N.; Kim, M. J.; Amemori, S.; Homma, D.; Yoshida, T.; Shimazu, H.; Yerramreddy, H.; Karasan, E.; Langer, R.; Graybiel, A. M.; et al. Subcellular probes for neurochemical recording from multiple brain sites. *Lab Chip* **2017**, *17* (6), 1104-1115. DOI: 10.1039/c6lc01398h.

(140) Smith, S. K.; Gosrani, S. P.; Lee, C. A.; McCarty, G. S.; Sombers, L. A. Carbon-Fiber Microbiosensor for Monitoring Rapid Lactate Fluctuations in Brain Tissue Using Fast-Scan Cyclic Voltammetry. *Anal. Chem.* **2018**, *90* (21), 12994-12999. DOI: 10.1021/acs.analchem.8b03694.

(141) Venton, B. J.; Cao, Q. Fundamentals of fast-scan cyclic voltammetry for dopamine detection. *Analyst* **2020**, *145* (4), 1158-1168. DOI: 10.1039/c9an01586h.

(142) Oh, Y.; Heien, M. L.; Park, C.; Kang, Y. M.; Kim, J.; Boschen, S. L.; Shin, H.; Cho, H. U.; Blaha, C. D.; Bennet, K. E.; et al. Tracking tonic dopamine levels in vivo using multiple cyclic square wave voltammetry. *Biosensors and Bioelectronics* **2018**, *121*, 174-182. DOI: https://doi.org/10.1016/j.bios.2018.08.034.

(143) Oh Y; Park C; Kim DH; Shin H; Kang YM; DeWaele M; Lee J; Min HK; Blaha CD; Bennet KE; et al. Monitoring In Vivo Changes in Tonic Extracellular Dopamine Level by Charge-Balancing Multiple Waveform Fast-Scan Cyclic Voltammetry. *Analytical Chemistry* **2016**, *88* (22), 10962-10970.

(144) Kucherenko, D. Y.; Kucherenko, I. S.; Soldatkin, O. O.; Topolnikova, Y. V.; Dzyadevych, S. V.; Soldatkin, A. P. A highly selective amperometric biosensor array for the simultaneous determination of glutamate, glucose, choline, acetylcholine, lactate and pyruvate. *Bioelectrochemistry* **2019**, *128*, 100-108. DOI: 10.1016/j.bioelechem.2019.03.010.

(145) Wang, B.; Wen, X.; Cao, Y.; Huang, S.; Lam, H. A.; Liu, T. L.; Chung, P. S.; Monbouquette, H. G.; Chiou, P. Y.; Maidment, N. T. An implantable multifunctional neural microprobe for simultaneous multi-analyte sensing and chemical delivery. *Lab Chip* **2020**, *20* (8), 1390-1397. DOI: 10.1039/d0lc00021c.

(146) Cordeiro, C. A.; de Vries, M. G.; Ngabi, W.; Oomen, P. E.; Cremers, T. I.; Westerink, B. H. In vivo continuous and simultaneous monitoring of brain energy substrates with a multiplex amperometric enzyme-based biosensor device. *Biosens. Bioelectron.* **2015**, *67*, 677-686. DOI: 10.1016/j.bios.2014.09.101.

(147) Yu, Z.; Jiang, N.; Kazarian, S. G.; Tasoglu, S.; Yetisen, A. K. Optical sensors for continuous glucose monitoring. *Prog. Biomed. Eng.* **2021**, *3* (2). DOI: 10.1088/2516-1091/abe6f8.

(148) Yu, J.; Ling, W.; Li, Y.; Ma, N.; Wu, Z.; Liang, R.; Pan, H.; Liu, W.; Fu, B.; Wang, K.; et al. A Multichannel Flexible Optoelectronic Fiber Device for Distributed Implantable Neurological Stimulation and Monitoring. *Small* **2021**, *17* (4), e2005925. DOI: 10.1002/smll.202005925.

(149) **!!! INVALID CITATION !!! 68**.

(150) Ling, W.; Yu, J.; Ma, N.; Li, Y.; Wu, Z.; Liang, R.; Hao, Y.; Pan, H.; Liu, W.; Fu, B.; et al. Flexible Electronics and Materials for Synchronized Stimulation and Monitoring in Multi-Encephalic Regions. *Adv. Funct. Mater.* **2020**, *30* (32). DOI: 10.1002/adfm.202002644.

(151) Baluta, S.; Malecha, K.; Zając, D.; Sołoducho, J.; Cabaj, J. Dopamine sensing with fluorescence strategy based on low temperature co-fired ceramic technology modified with conducting polymers. *Sensors and Actuators B: Chemical* **2017**, *252*, 803-812.

(152) Amiri, M.; Dadfarnia, S.; Shabani, A. M. H.; Sadjadi, S. Non-enzymatic sensing of dopamine by localized surface plasmon resonance using carbon dots-functionalized gold nanoparticles. *J. Pharm. Biomed. Anal.* **2019**, *172*, 223-229.

(153) Lu, L.; Gutruf, P.; Xia, L.; Bhatti, D. L.; Wang, X.; Vazquez-Guardado, A.; Ning, X.; Shen, X.; Sang, T.; Ma, R.; et al. Wireless optoelectronic photometers for monitoring neuronal dynamics in the deep brain. *Proc. Natl. Acad. Sci. USA* **2018**, *115* (7), E1374-E1383. DOI: 10.1073/pnas.1718721115.

(154) Rithesh Raj, D.; Prasanth, S.; Vineeshkumar, T. V.; Sudarsanakumar, C. Surface plasmon resonance based fiber optic dopamine sensor using green synthesized silver nanoparticles. *Sensors and Actuators B: Chemical* **2016**, *224*, 600-606. DOI: 10.1016/j.snb.2015.10.106.

(155) Kruss S; Salem DP; Vuković L; Lima B; Vander Ende E; Boyden ES; MS., S. High-resolution imaging of cellular dopamine efflux using a fluorescent nanosensor array. *Proc. Natl. Acad. Sci. USA* **2017**, *114* (8), 1789-1794.

(156) Moreau, F. O.; Yang, R.; Nambiar, V.; Demchuk, A. M.; Dunn, J. F. Near-infrared measurements of brain oxygenation in stroke. *Neurophotonics* **2016**, *3* (3), 031403.

(157) Moody, A. S.; Payne, T. D.; Barth, B. A.; Sharma, B. Surface-enhanced spatially-offset Raman spectroscopy (SESORS) for detection of neurochemicals through the skull at physiologically relevant concentrations. *Analyst* **2020**, *145* (5), 1885-1893. DOI: 10.1039/c9an01708a.

(158) Rickard, J. J. S.; Di-Pietro, V.; Smith, D. J.; Davies, D. J.; Belli, A.; Oppenheimer, P. G. Rapid optofluidic detection of biomarkers for traumatic brain injury via surface-enhanced Raman spectroscopy. *Nat. Biomed. Eng.* **2020**, *4* (6), 610-623. DOI: 10.1038/s41551-019-0510-4.

(159) Lu, J.; Xu, C.; Nan, H.; Zhu, Q.; Qin, F.; Manohari, A. G.; Wei, M.; Zhu, Z.; Shi, Z.; Ni, Z. SERS-active ZnO/Ag hybrid WGM microcavity for ultrasensitive dopamine detection. *Applied Physics Letters* **2016**, *109* (7), 714-846.

(160) Pathak, A.; Gupta, B. D. Ultra-selective fiber optic SPR platform for the sensing of dopamine in synthetic cerebrospinal fluid incorporating permselective nafion membrane and surface imprinted MWCNTs-PPy matrix. *Biosens. Bioelectron.* **2019**, *133*, 205-214. DOI: 10.1016/j.bios.2019.03.023.

(161) Sharma, S.; Gupta, B. D. Surface Plasmon Resonance Based Highly Selective Fiber Optic Dopamine Sensor Fabricated Using Molecular Imprinted GNP/SnO2 Nanocomposite. *Journal of Lightwave Technology* **2018**, *36* (24), 5956-5962. DOI: 10.1109/jlt.2018.2882608.

(162) Amiri, M.; Dadfarnia, S.; Haji Shabani, A. M.; Sadjadi, S. Non-enzymatic sensing of dopamine by localized surface plasmon resonance using carbon dots-functionalized gold nanoparticles. *Pharm. Biomed. Anal.* **2019**, *172*, 223-229. DOI: 10.1016/j.jpba.2019.04.037.

(163) Li, N.; Lu, Y.; Li, S.; Zhang, Q.; Wu, J.; Jiang, J.; Liu, G. L.; Liu, Q. Monitoring the electrochemical responses of neurotransmitters through localized surface plasmon resonance using nanohole array. *Biosens. Bioelectron.* **2017**, *93*, 241-249. DOI: 10.1016/j.bios.2016.08.105.

(164) Govindaraju, S.; Ankireddy, S. R.; Viswanath, B.; Kim, J.; Yun, K. Fluorescent Gold Nanoclusters for Selective Detection of Dopamine in Cerebrospinal fluid. *Sci Rep* **2017**, *7*, 40298. DOI: 10.1038/srep40298.

(165) Beyene, A. G.; Delevich, K.; Del Bonis-O'Donnell, J. T.; Piekarski, D. J.; Lin, W. C.; Thomas, A. W.; Yang, S. J.; Kosillo, P.; Yang, D.; Prounis, G. Imaging striatal dopamine release using a nongenetically encoded near infrared fluorescent catecholamine nanosensor. *Science advances* **2019**, *5* (7), eaaw3108.

(166) Liu, X.; Hu, X.; Xie, Z.; Chen, P.; Sun, X.; Yan, J.; Zhou, S. In Situ Bifunctionalized Carbon Dots with Boronic Acid and Amino Groups for Ultrasensitive Dopamine Detection. *Anal. Methods* **2016**, *8*, 3236–3241.

(167) Patriarchi, T.; Cho, J. R.; Merten, K.; Howe, M. W.; Marley, A.; Xiong, W. H.; Folk, R. W.; Broussard, G. J.; Liang, R.; Jang, M. J.; et al. Ultrafast neuronal imaging of dopamine dynamics with designed genetically encoded sensors. *Science* **2018**, *360* (6396). DOI: 10.1126/science.aat4422.

(168) Sun, F.; Zhou, J.; Dai, B.; Qian, T.; Zeng, J.; Li, X.; Zhuo, Y.; Zhang, Y.; Wang, Y.; Qian, C.; et al. Next-generation GRAB sensors for monitoring dopaminergic activity in vivo. *Nat. Methods* **2020**, *17* (11), 1156-1166. DOI: 10.1038/s41592-020-00981-9.

(169) Patriarchi, T.; Mohebi, A.; Sun, J.; Marley, A.; Liang, R.; Dong, C.; Puhger, K.; Mizuno, G. O.; Davis, C. M.; Wiltgen, B.; et al. An expanded palette of dopamine sensors for multiplex imaging in vivo. *Nat Methods* **2020**, *17* (11), 1147-1155. DOI: 10.1038/s41592-020-0936-3.

(170) Farooq, H.; Genis, H.; Alarcon, J.; Vuong, B.; Jivraj, J.; Yang, V. X.; Cohenadad, J.; Fehlings, M. G.; Cadotte, D. W. High-resolution imaging of the central nervous system: how novel imaging methods combined with navigation strategies will advance patient care. *Progress in Brain Research* **2015**, *218*, 55-78.

(171) Zhou, Y.; Liu, C.-H.; Wu, B.; Yu, X.; Cheng, G.; Zhu, K.; Wang, K.; Zhang, C.; Zhao, M.; Zong, R. Optical biopsy identification and grading of gliomas using label-free visible resonance Raman spectroscopy. *Journal of biomedical optics* **2019**, *24* (9), 095001.

(172) Matousek, P.; Clark, I. P.; Draper, E. R.; Morris, M.; Goodship, A.; Everall, N.; Towrie, M.; Finney, W.; Parker, A. Subsurface probing in diffusely scattering media using spatially offset Raman spectroscopy. *Applied spectroscopy* **2005**, *59* (4), 393-400.

(173) Hu, Y.; Cheng, H.; Zhao, X.; Wu, J.; Muhammad, F.; Lin, S.; He, J.; Zhou, L.; Zhang, C.; Deng, Y.; et al. Surface-Enhanced Raman Scattering Active Gold Nanoparticles with Enzyme-Mimicking Activities for Measuring Glucose and Lactate in Living Tissues. *ACS Nano* **2017**, *11* (6), 5558-5566. DOI: 10.1021/acsnano.7b00905.

(174) Zama, T.; Takahashi, Y.; Shimada, S. Simultaneous EEG-NIRS Measurement of the Inferior Parietal Lobule During a Reaching Task With Delayed Visual Feedback. *Front. Hum. Neurosci.* **2019**, *13*, 301. DOI: 10.3389/fnhum.2019.00301.

(175) Anja; Demel; Katharina; Feilke; Martin; Wolf; Christian; F.; Poets; Axel. Correlation between skin, bone, and cerebrospinal fluid layer thickness and optical coefficients measured by multidistance frequency-domain near-infrared spectroscopy in term and preterm infants. *Journal of Biomedical Optics* **2014**, *19* (1), 017004.

(176) Scheeren, T. W. L.; Kuizenga, M. H.; Maurer, H.; Struys, M.; Heringlake, M. Electroencephalography and Brain Oxygenation Monitoring in the Perioperative Period. *Anesth. Analg.* **2019**, *128* (2), 265-277. DOI: 10.1213/ANE.0000000000002812.

(177) Schasfoort, R. B. *Handbook of surface plasmon resonance*; Royal Society of Chemistry, 2017.

(178) Hu, W.; Huang, Y.; Chen, C.; Liu, Y.; Guo, T.; Guan, B.-O. Highly sensitive detection of dopamine using a graphene functionalized plasmonic fiber-optic sensor with aptamer conformational amplification. *Sensors Actuators B: Chem.* **2018**, *264*, 440-447. DOI: 10.1016/j.snb.2018.03.005.

(179) Witthauer, L.; Cascales, J. P.; Roussakis, E.; Li, X.; Goss, A.; Chen, Y.; Evans, C. L. Portable oxygen-sensing device for the improved assessment of compartment syndrome and other hypoxia-related conditions. *ACS Sens.* **2020**, *6* (1), 43-53.

(180) Thompson, I. A.; Saunders, J.; Zheng, L.; Hariri, A. A.; Maganzini, N.; Cartwright, A. P.; Pan, J.; Yee, S.; Dory, C.; Eisenstein, M. An antibody-based molecular switch for continuous small-molecule biosensing. *Science Advances* **2023**, *9* (38), eadh4978.

(181) Desroches, J.; Jermyn, M.; Pinto, M.; Picot, F.; Tremblay, M.-A.; Obaid, S.; Marple, E.; Urmey, K.; Trudel, D.; Soulez, G. A new method using Raman spectroscopy for in vivo targeted brain cancer tissue biopsy. *Scientific reports* **2018**, *8* (1), 1792.

(182) Yetisen, A. K.; Jiang, N.; Fallahi, A.; Montelongo, Y.; Ruiz-Esparza, G. U.; Tamayol, A.; Zhang, Y. S.; Mahmood, I.; Yang, S. A.; Kim, K. S. Glucose-sensitive hydrogel optical fibers functionalized with phenylboronic acid. *Advanced materials* **2017**, *29* (15), 1606380.

(183) Gonalves, T. Peer Review #1 of "The coefficient of determination R-squared is more informative than SMAPE, MAE, MAPE, MSE and RMSE in regression analysis evaluation (v0.2)". *PeerJ* **2021**.

(184) Ho, C.-S.; Jean, N.; Hogan, C. A.; Blackmon, L.; Jeffrey, S. S.; Holodniy, M.; Banaei, N.; Saleh, A. A.; Ermon, S.; Dionne, J. Rapid identification of pathogenic bacteria using Raman spectroscopy and deep learning. *Nature communications* **2019**, *10* (1), 4927.

(185) Fuentes, A. M.; Narayan, A.; Milligan, K.; Lum, J. J.; Brolo, A. G.; Andrews, J. L.; Jirasek, A. Raman spectroscopy and convolutional neural networks for monitoring biochemical radiation response in breast tumour xenografts. *Sci. Rep.* **2023**, *13* (1), 1530.

(186) Huang, L.; Sun, H.; Sun, L.; Shi, K.; Chen, Y.; Ren, X.; Ge, Y.; Jiang, D.; Liu, X.; Knoll, W. Rapid, label-free histopathological diagnosis of liver cancer based on Raman spectroscopy and deep learning. *Nature Communications* **2023**, *14* (1), 48.

(187) Yoshida, K.; Shimizu, Y.; Yoshimoto, J.; Takamura, M.; Okada, G.; Okamoto, Y.; Yamawaki, S.; Doya, K. J. P. o. Prediction of clinical depression scores and detection of changes in whole-brain using resting-state functional MRI data with partial least squares regression. **2017**, *12* (7), e0179638.

(188) Fonville, J. M.; Richards, S. E.; Barton, R. H.; Boulange, C. L.; Ebbels, T. M.; Nicholson, J. K.; Holmes, E.; Dumas, M. E. J. J. o. C. The evolution of partial least squares models and related chemometric approaches in metabonomics and metabolic phenotyping. **2010**, *24* (11-12), 636-649.

(189) Rodríguez-Entrena, M.; Salazar-Ordóñez, M.; Sayadi, S. J. F. P. Applying partial least squares to model genetically modified food purchase intentions in southern Spain consumers. **2013**, *40*, 44-53.

(190) Rukundo, I. R.; Danao, M.-G. C.; Weller, C. L.; Wehling, R. L.; Eskridge, K. M. J. J. o. N. I. S. Use of a handheld near infrared spectrometer and partial least squares regression to quantify metanil yellow adulteration in turmeric powder. **2020**, *28* (2), 81-92.

(191) Meunier, C. J.; Mitchell, E. C.; Roberts, J. G.; Toups, J. V.; McCarty, G. S.; Sombers, L. A. J. A. c. Electrochemical selectivity achieved using a double voltammetric waveform and partial least squares regression: differentiating endogenous hydrogen peroxide fluctuations from shifts in pH. **2018**, *90* (3), 1767-1776.

(192) Cheng, J.-H.; Sun, D.-W. J. F. e. r. Partial least squares regression (PLSR) applied to NIR and HSI spectral data modeling to predict chemical properties of fish muscle. **2017**, *9* (1), 36-49.

(193) Abdi, H. J. W. i. r. c. s. Partial least squares regression and projection on latent structure regression (PLS Regression). **2010**, *2* (1), 97-106.

(194) Johnson, J. A.; Wightman, R. M. J. E. S. I. Cyclic Voltammetric Measurements of Neurotransmitters. **2017**, *26* (3), 53.

(195) Costas A. Anastassiou; Parker, K. H.; O'Hare, D. Determination of Kinetic and Thermodynamic Parameters of Surface Confined Species through ac Voltammetry and a Nonstationary Signal Processing Technique: The Hilbert Transform. *Anal. Chem.* **2005**, *77*, 3357-3364.

(196) Papadimitriou, K. I.; Wang, C.; Rogers, M. L.; Gowers, S. A.; Leong, C. L.; Boutelle, M. G.; Drakakis, E. M. High-Performance Bioinstrumentation for Real-Time Neuroelectrochemical Traumatic Brain Injury Monitoring. *Front Hum Neurosci* **2016**, *10*, 212. DOI: 10.3389/fnhum.2016.00212.

(197) Limnuson, K.; Narayan, R. K.; Chiluwal, A.; Golanov, E. V.; Bouton, C. E.; Li, C. A User-Configurable Headstage for Multimodality Neuromonitoring in Freely Moving Rats. *Front Neurosci* **2016**, *10*, 382. DOI: 10.3389/fnins.2016.00382.

(198) Tian, Z.; TaeHyun Hwang; Kuang., R. A hypergraph-based learning algorithm for classifying gene expression and arrayCGH data with prior knowledge. *Bioinformatics* **2009**, *25* (21), 2831.

(199) Lee, J.; Kim, S. J.; Chen, R.; Herskovits, E. H. Brain tumor image segmentation using kernel dictionary learning. In *2015 37th Annual International Conference of the IEEE Engineering in Medicine and Biology Society (EMBC)*, 2015.

(200) Irimia, A.; Wei, S.; Lu, N.; Moore, C. M.; Kennedy, D. N. Mobile Monitoring of Traumatic Brain Injury in Older Adults: Challenges and Opportunities. *Neuroinformatics* **2017**.

(201) Lee, S. T.; Gin, J.; Nampoori, V.; Vallabhan, C.; Unnikrishnan, N.; Radhakrishnan, P. A sensitive fibre optic pH sensor using multiple sol-gel coatings. *Journal of Optics A: Pure Applied Optics* **2001**, *3* (5), 355.

(202) Pierre, A. The sol-gel encapsulation of enzymes. *J Biocatalysis Biotransformation* **2004**, *22* (3), 145-170.

(203) Parale, V. G.; Lee, K.-Y.; Park, H.-H. Flexible and transparent silica aerogels: an overview. *J. Korean Ceram. Soc.* **2017**, *54* (3), 184-199.

(204) Jurmanović, S.; Kordić, Š.; Steinberg, M. D.; Steinberg, I. M. Organically modified silicate thin films doped with colourimetric pH indicators methyl red and bromocresol green as pH responsive sol–gel hybrid materials. *Thin Solid Films* **2010**, *518* (8), 2234-2240. DOI: 10.1016/j.tsf.2009.07.158.

(205) Makote, R.; Collinson, M. M. Organically modified silicate films for stable pH sensors. *Anal. Chim. Acta* **1999**, *394* (2-3), 195-200. DOI: 10.1016/S0003-2670(99)00305-0.

(206) Frontera, J.; Ziai, W.; O'Phelan, K.; Leroux, P. D.; Kirkpatrick, P. J.; Diringer, M. N.; Suarez, J. I.; Investigators, S. N. C. R. C. Regional brain monitoring in the neurocritical care unit. *Neurocritical Care* **2015**, *22* (3), 348-359.

(207) Moreddu, R.; Elsherif, M.; Butt, H.; Vigolo, D.; Yetisen, A. K. Contact Lenses for Continuous Corneal Temperature Monitoring. *RSC Advances* **2019**, *9* (9), 11433-11442.

(208) Wang, X. D.; Wolfbeis, O. S. Optical methods for sensing and imaging oxygen: materials, spectroscopies and applications. *Chemical Society Reviews* **2014**, *43*.

(209) Yetisen, A. K.; Moreddu, R.; Seifi, S.; Jiang, N.; Vega, K.; Dong, X.; Dong, J.; Butt, H.; Jakobi, M.; Elsner, M. Dermal tattoo biosensors for colorimetric metabolite detection. *Angewandte Chemie* **2019**, *131* (31), 10616-10623.

(210) Shiogai, T.; Nara, I.; Saruta, K.; Hara, M.; Saito, I. Continuous monitoring of cerebrospinal fluid acid-base balance and oxygen metabolism in patients with severe head injury: pathophysiology and treatments for cerebral acidosis and ischemia. In *Neuromonitoring in Brain Injury*, Springer, 1999; pp 49-55.

(211) Martini, R. P.; Deem, S.; Treggiari, M. M. Targeting brain tissue oxygenation in traumatic brain injury. *Respir Care* **2013**, *58* (1), 162-172. DOI: 10.4187/respcare.01942.

(212) Thelin, E. P.; Nelson, D. W.; Ghatan, P. H.; Bellander, B. M. Microdialysis Monitoring of CSF Parameters in Severe Traumatic Brain Injury Patients: A Novel Approach. *Front Neurol* **2014**, *5*, 159. DOI: 10.3389/fneur.2014.00159.

(213) Probes, M. *LIVE/DEAD ® Viability/Cytotoxicity Kit for mammalian cells*. https://www.thermofisher.cn/document-connect/document-connect.html?url=https://assets.thermofisher.cn/TFS-Assets%2FLSG%2Fmanuals%2Fmp03224.pdf (accessed.

(214) Khan, M. I.; Mukherjee, K.; Shoukat, R.; Dong, H. A review on pH sensitive materials for sensors and detection methods. *Microsystem Technologies* **2017**, *23* (10), 4391-4404.

(215) Wanke, E.; Carbone, E.; Testa, P. L. The sodium channel and intracellular H+ blockage in squid axons. *Nature* **1980**, *287* (5777), 62-63. DOI: 10.1038/287062a0.

(216) Zauner, A.; Doppenberg, E. M.; Woodward, J. J.; Choi, S. C.; Young, H. F.; Bullock, R. Continuous monitoring of cerebral substrate delivery and clearance: initial experience in 24 patients with severe acute brain injuries. *Neurosurg.* **1997**, *41* (5), 1082-1093. DOI: 10.1097/00006123-199711000-00011.

(217) Lanin, A. A.; Chebotarev, A. S.; Pochechuev, M. S.; Kelmanson, I. V.; Kotova, D. A.; Bilan, D. S.; Ermakova, Y. G.; Fedotov, A. B.; Ivanov, A. A.; Belousov, V. V.; et al. Two- and three-photon absorption cross-section characterization for high-brightness, cell-specific multiphoton fluorescence brain imaging. *J Biophotonics* **2020**, *13* (3), e201900243. DOI: 10.1002/jbio.201900243.

(218) Tang, X.; Zhu, Z.; Wang, Y.; Han, J.; Ni, L.; Wang, L.; Zhang, H.; Li, J.; Qiu, Y. A dual site controlled probe for fluorescent monitoring of intracellular pH and colorimetric monitoring of Cu2+. *Sens. Actuators B Chem.* **2018**, *270*, 35-44. DOI: 10.1016/j.snb.2018.04.173.

(219) Dong, H.; Zhao, L.; Zhou, Y.; Wei, X.; Xu, C.; Zhang, Y.; Xu, M. Novel Self-Calibrating Amperometric and Ratiometric Electrochemical Nanotip Microsensor for pH Measurement in Rat Brain. *Anal Chem* **2021**, *93* (41), 13815-13822. DOI: 10.1021/acs.analchem.1c02436.

(220) Promphet, N.; Rattanawaleedirojn, P.; Siralertmukul, K.; Soatthiyanon, N.; Potiyaraj, P.; Thanawattano, C.; Hinestroza, J. P.; Rodthongkum, N. Non-invasive textile based colorimetric sensor for the simultaneous detection of sweat pH and lactate. *Talanta* **2019**, *192*, 424-430. DOI: 10.1016/j.talanta.2018.09.086.

(221) Andrews, R. J.; Bringas, J. R.; Alonzo, G. Cerebrospinal fluid pH and PCO2 rapidly follow arterial blood pH and PCO2 with changes in ventilation. *Neurosurgery* **1994**, *34* (3), 466-470; discussion 470. DOI: 10.1227/00006123-199403000-00012.

(222) Kassal, P.; Šurina, R.; Vrsaljko, D.; Steinberg, I. M. Hybrid sol–gel thin films doped with a pH indicator: effect of organic modification on optical pH response and film surface hydrophilicity. *J Solgel Sci. Technol.* **2014**, *69* (3), 586-595. DOI: 10.1007/s10971-013-3261-9.

(223) Wu, S.; Cheng, W.; Qiu, Y.; Li, Z.; Shuang, S.; Dong, C. Fiber optic pH sensor based on mode-filtered light detection. *Sens. Actuators B Chem.* **2010**, *144* (1), 255-259. DOI: 10.1016/j.snb.2009.10.058.

(224) Fohlmeister, J. F.; Cohen, E. D.; Newman, E. A. Mechanisms and distribution of ion channels in retinal ganglion cells: using temperature as an independent variable. *J. Neurophysiol.* **2010**, *103* (3), 1357-1374. DOI: 10.1152/jn.00123.2009.

(225) Yu, Y.; Hill, A. P.; McCormick, D. A. Warm body temperature facilitates energy efficient cortical action potentials. *PLoS Comput Biol* **2012**, *8* (4), e1002456. DOI: 10.1371/journal.pcbi.1002456.

(226) Dietrich, W. D.; Atkins, C. M.; Bramlett, H. M. Protection in animal models of brain and spinal cord injury with mild to moderate hypothermia. *J Neurotrauma* **2009**, *26* (3), 301-312. DOI: 10.1089/neu.2008.0806.

(227) Steiner, M. S.; Duerkop, A.; Wolfbeis, O. S. Optical methods for sensing glucose. *Chem. Soc. Rev.* **2011**, *40* (9), 4805-4839. DOI: 10.1039/c1cs15063d.

(228) Ramon-Marquez, T.; Sesay, A. M.; Panjan, P.; Medina-Castillo, A. L.; Fernandez-Gutierrez, A.; Fernandez-Sanchez, J. F. A microfluidic device with integrated coaxial nanofibre membranes for optical determination of glucose. *Sens. Actuators B Chem.* **2017**, *250*, 156-161. DOI: 10.1016/j.snb.2017.04.140.

(229) Zhou, Z.; Qiao, L.; Zhang, P.; Xiao, D.; Choi, M. M. F. An optical glucose biosensor based on glucose oxidase immobilized on a swim bladder membrane. *Anal. Bioanal. Chem.* **2005**, *383* (4), 673-679. DOI: 10.1007/s00216-005-0023-8.

(230) Lenarczuk, T.; Wencel, D.; Głąb, S.; Koncki, R. Prussian blue-based optical glucose biosensor in flow-injection analysis. *Analytica. Chimica. Acta* **2001**, *447* (1-2), 23-32. DOI: 10.1016/S0003-2670(01)01289-2.

(231) Briones, A. V.; Sato, T. Encapsulation of glucose oxidase (GOD) in polyelectrolyte complexes of chitosan–carrageenan. *React. Funct. Polym.* **2010**, *70* (1), 19-27. DOI: 10.1016/j.reactfunctpolym.2009.09.009.

(232) Pavlovic, D.; Pekic, S.; Stojanovic, M.; Popovic, V. Traumatic brain injury: neuropathological, neurocognitive and neurobehavioral sequelae. *Pituitary* **2019**, *22* (3), 270-282.

(233) Adrian, H.; Mårten, K.; Salla, N.; Lasse, V. Biomarkers of traumatic brain injury: temporal changes in body fluids. *Eneuro* **2016**, *3* (6). DOI: 10.1523/ENEURO.0294-16.2016.

(234) Sakka, L.; Coll, G.; Chazal, J. Anatomy and physiology of cerebrospinal fluid. *Eur. Ann. Otorhinolaryngol. Head Neck Dis.* **2011**, *128* (6), 309-316. DOI: 10.1016/j.anorl.2011.03.002.

(235) Jiang, N.; Davies, S.; Jiao, Y.; Blyth, J.; Butt, H.; Montelongo, Y.; Yetisen, A. K. Doubly Photopolymerized Holographic Sensors. *ACS Sensors* **2021**, *6* (3), 915-924. DOI: 10.1021/acssensors.0c02109.

(236) Sun, F.; Zhou, J.; Dai, B.; Qian, T.; Zeng, J.; Li, X.; Zhuo, Y.; Zhang, Y.; Wang, Y.; Qian, C.; et al. Next-generation GRAB sensors for monitoring dopaminergic activity in vivo. *Nat. Methods* **2020**, *17* (11), 1156-1166. DOI: 10.1038/s41592-020-00981-9.

(237) Guo, J.; Liu, X.; Jiang, N.; Yetisen, A. K.; Yuk, H.; Yang, C.; Khademhosseini, A.; Zhao, X.; Yun, S. H. Highly stretchable, strain sensing hydrogel optical fibers. *Advanced Materials* **2016**, *28* (46), 10244-10249. DOI: 10.1002/adma.201603160.

(238) Zhang, Y.; Hu, Y.; Liu, Q.; Lou, K.; Wang, S.; Zhang, N.; Jiang, N.; Yetisen, A. K. Multiplexed optical fiber sensors for dynamic brain monitoring. *Matter* **2022**, *5* (11), 3947-3976.

(239) Jiang, S.; Patel, D. C.; Kim, J.; Yang, S.; Mills III, W. A.; Zhang, Y.; Wang, K.; Feng, Z.; Vijayan, S.; Cai, W. Spatially expandable fiber-based probes as a multifunctional deep brain interface. *Nature communications* **2020**, *11* (1), 6115.

(240) Badt, N.; Katz, O. Real-time holographic lensless micro-endoscopy through flexible fibers via fiber bundle distal holography. *Nat. Commun.* **2022**, *13* (1), 6055.

(241) Karaszewski, B.; Wardlaw, J. M.; Marshall, I.; Cvoro, V.; Wartolowska, K.; Haga, K.; Armitage, P. A.; Bastin, M. E.; Dennis, M. S. Early brain temperature elevation and anaerobic metabolism in human acute ischaemic stroke. *Brain* **2009**, *132* (4), 955-964.

(242) Hillered, L.; Persson, L.; Nilsson, P.; Ronne-Engstrom, E.; Enblad, P. Continuous monitoring of cerebral metabolism in traumatic brain injury: a focus on cerebral microdialysis. *Curr. Opin. Crit. Care* **2006**, *12* (2), 112-118.

(243) Arundine, M.; Tymianski, M. Molecular mechanisms of glutamate-dependent neurodegeneration in ischemia and traumatic brain injury. *Cell. Mol. Life Sci.* **2004**, *61*, 657-668.

(244) Gerhalter, T.; Chen, A. M.; Dehkharghani, S.; Peralta, R.; Adlparvar, F.; Babb, J. S.; Bushnik, T.; Silver, J. M.; Im, B. S.; Wall, S. P.; et al. Global decrease in brain sodium concentration after mild

traumatic brain injury. *Brain Commun.* **2021**, *3* (2), fcab051. DOI: 10.1093/braincomms/fcab051 From NLM PubMed-not-MEDLINE.

(245) Koepsell, H. Glucose transporters in brain in health and disease. *Pflugers Arch.* **2020**, *472* (9), 1299-1343.

(246) Sabnis, R. W. Handbook of Fluorescent Dyes and Probes. *Wiley* **2015**.

(247) Wiederschain, G. Y. The Molecular Probes handbook. A guide to fluorescent probes and labeling technologies. *Biochemistry (Moscow)* **2011**, *76* (11), 1276-1276. DOI: 10.1134/S0006297911110101.

(248) Shinar, R.; Zhou, Z.; Choudhury, B.; Shinar, J. Structurally integrated organic light emitting device-based sensors for gas phase and dissolved oxygen. *Analytica Chimica Acta* **2006**, *568* (1-2), 190-199.

(249) Guo, J.; Liu, X.; Jiang, N.; Yetisen, A. K.; Yuk, H.; Yang, C.; Khademhosseini, A.; Zhao, X.; Yun, S. H. Highly Stretchable, Strain Sensing Hydrogel Optical Fibers. *Adv Mater* **2016**, *28* (46), 10244-10249. DOI: 10.1002/adma.201603160 From NLM.

(250) Ponsot, F.; Shen, W.; Ashokkumar, P.; Audinat, E.; Klymchenko, A. S.; Collot, M. PEGylated red-emitting calcium probe with improved sensing properties for neuroscience. *ACS sensors* **2017**, *2* (11), 1706-1712.

(251) Shortreed, M.; Kopelman, R.; Kuhn, M.; Hoyland, B. Fluorescent fiber-optic calcium sensor for physiological measurements. *Analytical chemistry* **1996**, *68* (8), 1414-1418.

(252) Tsvirko, M.; Tkaczyk, S.; Kozak, M.; Kalota, B. Luminescent temperature sensor based on [Ru (bpy) $_3$] $^{2+}$ incorporated into chitosan. *Funct. Mater.* **2013**.

(253) Mills, A.; Tommons, C.; Bailey, R. T.; Tedford, M. C.; Crilly, P. J. Luminescence temperature sensing using poly (vinyl alcohol)-encapsulated Ru (bpy) 3 2+ films. *Analyst* **2006**, *131* (4), 495-500.

(254) Maruszewski, K.; Strommen, D. P.; Kincaid, J. R. Zeolite-entrapped ruthenium (II) complexes with bipyridine and related ligands. Elimination of ligand-field-state deactivation and increase in 3MLCT state lifetimes. *J. Am. Chem. Soc.* **1993**, *115* (18), 8345-8350.

(255) Osman, M. A.; Mittal, V.; Morbidelli, M.; Suter, U. W. Epoxy-layered silicate nanocomposites and their gas permeation properties. *Macromolecules* **2004**, *37* (19), 7250-7257.

(256) Song, L.; Hennink, E.; Young, I. T.; Tanke, H. J. Photobleaching kinetics of fluorescein in quantitative fluorescence microscopy. *Biophys J.* **1995**, *68* (6), 2588-2600.

(257) Haider, M. N.; Leddy, J. J.; Hinds, A. L.; Aronoff, N.; Rein, D.; Poulsen, D.; Willer, B. S. Intracranial pressure changes after mild traumatic brain injury: a systematic review. *Brain Inj.* **2018**, *32* (7), 809-815.

(258) Amao, Y.; Miyashita, T.; Okura, I. Optical oxygen sensing based on the luminescence change of metalloporphyrins immobilized in styrene–pentafluorostyrene copolymer film. *Analyst* **2000**, *125* (5), 871-875.

(259) Jiang, K.; Thomas, P. C.; Forry, S. P.; DeVoe, D. L.; Raghavan, S. R. Microfluidic synthesis of monodisperse PDMS microbeads as discrete oxygen sensors. *Soft Matter* **2012**, *8* (4), 923-926.

(260) Offenbacher, H.; Wolfbeis, O. S.; Fürlinger, E. Fluorescence optical sensors for continuous determination of near-neutral pH values. *Sens. Actuators* **1986**, *9* (1), 73-84.

(261) Meier, S. D.; Kovalchuk, Y.; Rose, C. R. Properties of the new fluorescent Na+ indicator CoroNa Green: comparison with SBFI and confocal Na+ imaging. *J. Neurosci. Methods* **2006**, *155* (2), 251-259.

(262) de la Fuente, S.; Fonteriz, R. I.; Montero, M.; Alvarez, J. Dynamics of mitochondrial [Ca2+] measured with the low-Ca2+-affinity dye rhod-5N. *Cell calcium* **2012**, *51* (1), 65-71.

(263) Steiner, M.-S.; Duerkop, A.; Wolfbeis, O. S. Optical methods for sensing glucose. *Chem. Soc. Rev.* **2011**, *40* (9), 4805-4839.

(264) Zhang, Z.-M.; Chen, S.; Liang, Y.-Z. Baseline correction using adaptive iteratively reweighted penalized least squares. *Analyst* **2010**, *135* (5), 1138-1146.

(265) Yu, H.; Chong, Y.; Zhang, P.; Ma, J.; Li, D. A D-shaped fiber SPR sensor with a composite nanostructure of MoS2-graphene for glucose detection. *Talanta* **2020**, *219*, 121324.

(266) Pisano, F.; Pisanello, M.; Lee, S. J.; Lee, J.; Maglie, E.; Balena, A.; Sileo, L.; Spagnolo, B.; Bianco, M.; Hyun, M. Depth-resolved fiber photometry with a single tapered optical fiber implant. *Nature methods* **2019**, *16* (11), 1185-1192.

(267) Cui, F.; Yue, Y.; Zhang, Y.; Zhang, Z.; Zhou, H. S. Advancing biosensors with machine learning. *ACS sensors* **2020**, *5* (11), 3346-3364.

(268) Huang, J.; Shi, T.; Gong, B.; Li, X.; Liao, G.; Tang, Z. Fitting an Optical Fiber Background with a Weighted Savitzky–Golay Smoothing Filter for Raman Spectroscopy. *Applied Spectroscopy* **2018**.

(269) Çağatay; Candan; Hakan; Inan. A unified framework for derivation and implementation of Savitzky–Golay filters. *Signal Processing* **2014**.

(270) Kayalibay, B.; Jensen, G.; Patrick, V. D. S. CNN-based Segmentation of Medical Imaging Data. **2017**.

(271) Albawi, S.; Mohammed, T. A.; Alzawi, S. Understanding of a Convolutional Neural Network. In *The International Conference on Engineering and Technology 2017*, 2017.

(272) Gu, J.; Wang, Z.; Kuen, J.; Ma, L.; Wang, G. Recent Advances in Convolutional Neural Networks. *Pattern Recognition* **2015**.

(273) Fertleman, M.; Pereira, C.; Dani, M.; Harris, B. H. L.; Di Giovannantonio, M.; Taylor-Robinson, S. D. Cytokine changes in cerebrospinal fluid and plasma after emergency orthopaedic surgery. *Scientific Reports* **2022**, *12* (1), 2221. DOI: 10.1038/s41598-022-06034-9.

(274) Spooren, A.; Kolmus, K.; Laureys, G.; Clinckers, R.; De Keyser, J.; Haegeman, G.; Gerlo, S. Interleukin-6, a mental cytokine. *Brain research reviews* **2011**, *67* (1-2), 157-183.

(275) Rothermundt, M.; Peters, M.; Prehn, J. H.; Arolt, V. S100B in brain damage and neurodegeneration. *Microscopy research and technique* **2003**, *60* (6), 614-632.

Appendices

1. Readout box design and UI design

The readout box was designed using Solidworks. It was fabricated using 1cm thick black acetal plastic sheets. The readout box includes a spectrometer, a multi-wavelength laser system, an edge computer (Nvidia, Jetson Xavier), a touch screen for user-interface, and a fibre coupler. The edge computer is utilized for signal processing, laser and spectrometer control, and result readouts. The fibre coupler is used for light transmission between laser system, designed optical bundle sensor, and the spectrometer. All components were fixed using screws. The readout box is miniaturized, compact, and lightweight.

A user-interface was developed using Tkinter in python for user control of the system and biomarker concentration continuous readout. It includes four parts. The first part is system control, where the users can input the desired readout options, including the temporal resolution, single biomarker continuous temporal readout, or multiplexed 6 biomarker readout. The parameters for the spectrometer reading, including integration time and smooth level can also be determined. The control of the lasers and spectrometer was realized via USB communication protocol by using serial library in python.

The second part is the calibration module. In this module, the fabricated multiplexed bundle is instructed to be placed in standard buffers (**Table S1**). Once immersed in the buffer, the multi-wavelength laser is powered on to shine the lasers one by one at the sample, and the corresponding spectra are recorded in the system. Then the users are instructed to switch to the second calibration buffer, and once the button is clicked, the lasers are lit on one after another with spectra taken and saved in the controller memory for continuous readout correction.

Table S1. Calibration buffer solutions

	T (°C)	DO (mg L^{-1})	pH	Na^{+}(mmol L^{-1})	Ca^{2+}(mmol L^{-1})	Gluc(mmol L^{-1})

Buffer solution 1	25	8	8	140	0	0
Buffer solution 2	40	0	6	200	2	6

The third part is the single biomarker temporal readout. In this module, the users can select the target biomarker they are interested to monitor. Based on their selection, the corresponding laser is turned on with a pulse frequency of 3s. The spectrum is taken and processed using the algorithm proposed in section 4.6. For continuous readout of single biomarker, multivariate curve regression is used to provide fast and reliable calculation of the biomarker concentration. The time series of the biomarker concentration value is plotted on the software UI for user visualization.

The fourth part is multiplexed biomarker readout. In this module, the software allows the user to visualize the concentration of 6 biomarkers simultaneously. In this mode, the laser lights are turned on one by one, and the spectra are recorded and fed into the machine learning or CNN model described in Section 5.2.1 and 5.2.2, depending on their performance tests.

2. Results—UI design

To achieve a fully automated brain monitoring system for the continuous measurement of multiple brain biomarkers, a software is developed for both system control and user interaction to achieved customized readout (**Figure S1**). The software consists of three panels, a control panel for multi-laser switches and synchronized spectrometer readings via UART communication, a calibration panel for the sensor calibration instruction and calibration signal readings before each measurement, and a measurement panel for spectra signal post processing, where the obtained spectra is filtered to remove high frequency noise, baseline corrected to eliminate background optical signal and drift, and processed with prebuilt models for biomarker concentration readout. The software was built using python and the graphical UI was developed using Tkinter.

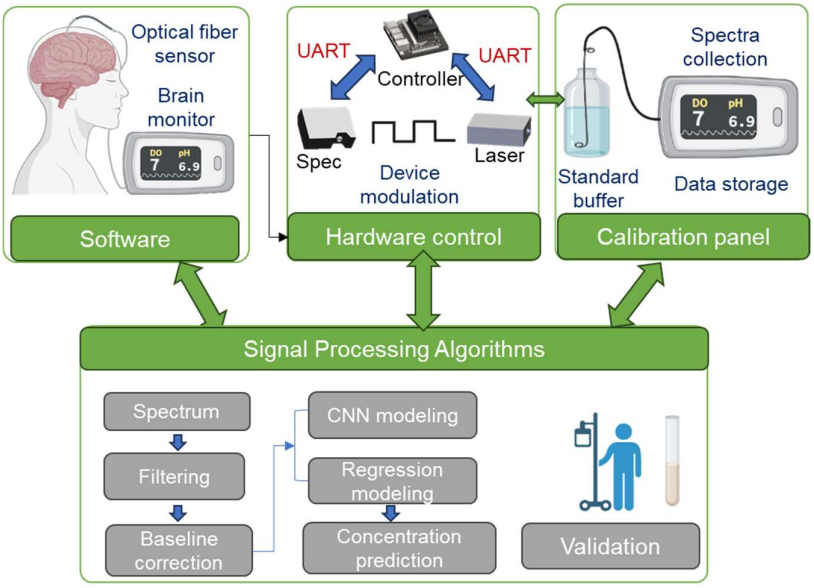


Figure 1. Software design of the whole sensing system. Three panels are included, hardware control, calibration panel, and measurement panel for signal processing and biomarker concentration readout.

2.1 Control panel

As shown in the figure below, the hardware control panel is designed to coordinate the lasers and spectrometer according to user's settings. Communications between the controller and spectrometer and lasers were built using UART protocol via python scripts. In this panel (**Figure S2**), which is also the main frame of the graphical UI software, the users are allowed to select the mode they would like to use, single mode and multiplexed mode. In single mode, only one biomarker concentration is displayed with dynamic concentration fluctuations over a time periods. In the multiplexed mode, 6 biomarkers' concentrations are displayed simultaneously. After selecting the mode, the users can put in preferred settings to control the spectrometer's temporal resolution by changing the integration time, and the signal smooth correction rate based on the background situation. Sample frequency is another independent variable the users can define, which decides how many seconds to have one value readout. In the biomarker selection section, the users can choose which biomarker to measure from the six biomarkers, and the temporal readout is displayed in the right part of the UI.

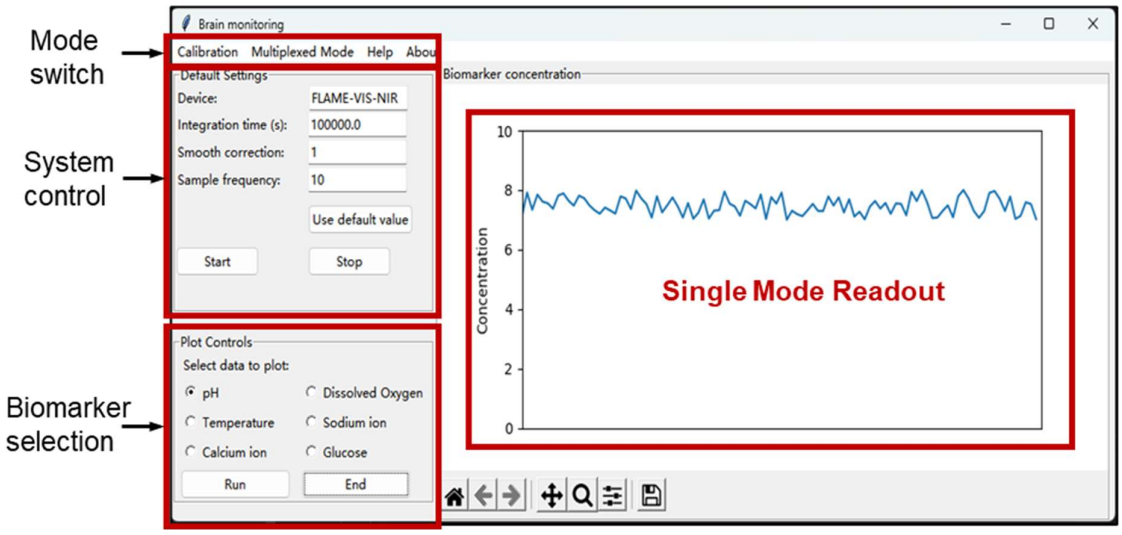


Figure S2. Main frame and control panel of the system, where user can select the measurement mode and sensing parameters.

The communication between the controller and the devices are built through UART, and the protocol for the communication is shown in **Figure S3**. After connecting the devices to the controller via USB, the port number can be used for communication through authentication codes. Based on the selected mode and the selected biomarker, different codes are sent to the laser for correct measurement. If single mode is selected, based on the target biomarker, different laser is switched on. In this mode pulsed laser is used to reduce photobleaching. Thus, the corresponding laser is put on for 1 second and off for another few seconds based on the sample frequency (equals to the input sample frequency minus 1 seconds). Here, if the selection is pH/DO/Glucose, 405 laser is switched on. If the selection is temperature/sodium, 488 laser is switched on. If the selection is calcium, 520 laser is switched on. The process is repeated until the user stops the measurement. The spectrometer is also controlled using UART, and it acquires the spectrum right before the laser is switched off in each cycle.

If multiplexed mode is selected, then all biomarker concentration readout is provided. In this mode, the lasers are switched on one by one controlled by the controller using UART. The codes for laser on/off and switch are sent to the multiwavelength laser. Each laser is switched on for 3s, after which it is switched off and the next laser is switched on for another 3 second. The process is repeated until the user stops the measurement. The spectrometer obtains one spectrum right before each laser is switched off.

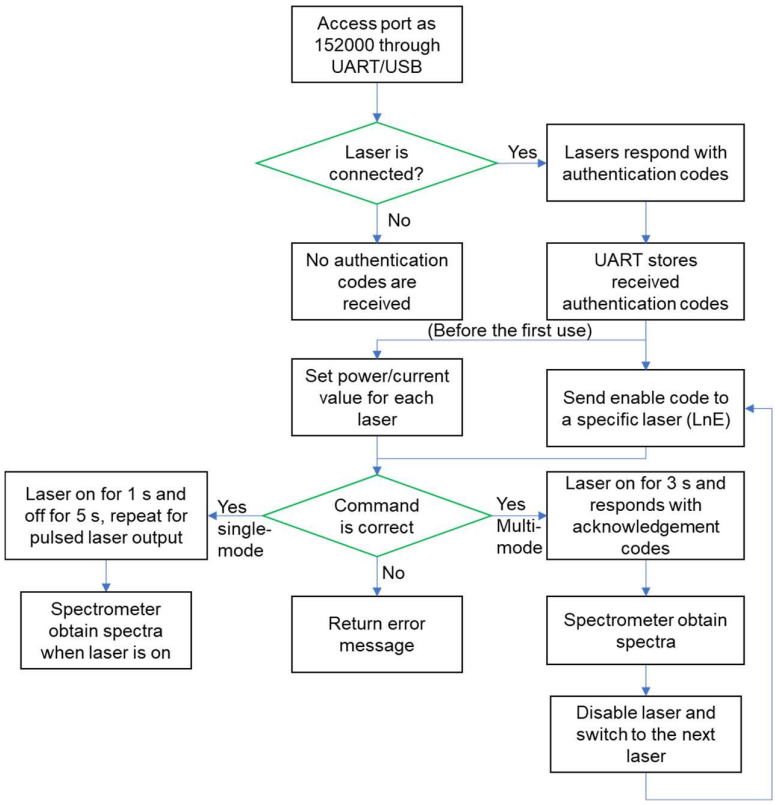


Figure S3. UART protocol for laser control.

2.2 Calibration panel

Before each measurement, the sensors need to be calibrated first for accurate readout due to the variations between each sensing film. The calibration was carried out using two standard aCSF buffer solutions prepared with specific biomarker concentrations (**Figure S4**). A graphical UI frame was designed for the instruction of calibration and the processing of the calibration spectra. The results of the calibration buffer were saved for the correction of the biomarker concentration during the measurements.

For the calibration, two-point calibration is conducted, where two buffers with specific values are prepared for the calibration. For each buffer, the sensing probe is inserted into the buffer and the user selects the buffer solution id, after which the lasers are switched on one after each as discussed in multiplexed mode. The obtained spectra are saved in the microcontroller for future readout correction. In the right-hand side of the UI shows the real-time spectrometer reading for user reference.

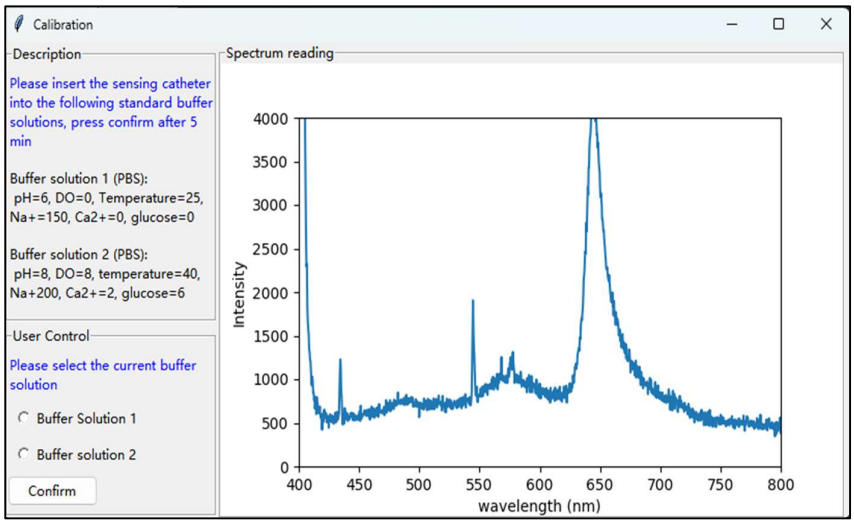


Figure S4. Calibration panel of the software. Instruction for calibration is provided to perform before each measurement.

2.3 Measurement panel

Signal processing algorithms are introduced in the previous chapter, and they were deployed in the microcontroller for spectrum processing following spectrometer readings. In short, the obtained spectrum was first filtered, and the baseline was corrected to remove the background noise and then based on the mode selection, the spectrum was either send to the multivariate regression model (Section 4.4.6) for single dynamic biomarker concentration prediction or a CNN model for multiplexed concentration prediction. The output was then displayed on the user interface. All the models were pretrained, optimized, and validated using aCSF buffer solution.

For dynamic reading, a circular buffer is generated to store the concentration value measured at each cycle (**Figure S5**). The concentration fluctuation is displayed for up to 100 mins with temporal resolution optional from 2s to 1 min decided by users. After the buffer is full, the new reading replaces the first reading in the buffer and the measurement continuous. The measurement and calculation of the concentration is based on the algorithm introduced in chapter 4.4.6 after obtaining each spectrum. Environmental compensation is also applied to correct the signal for more accurate readout.

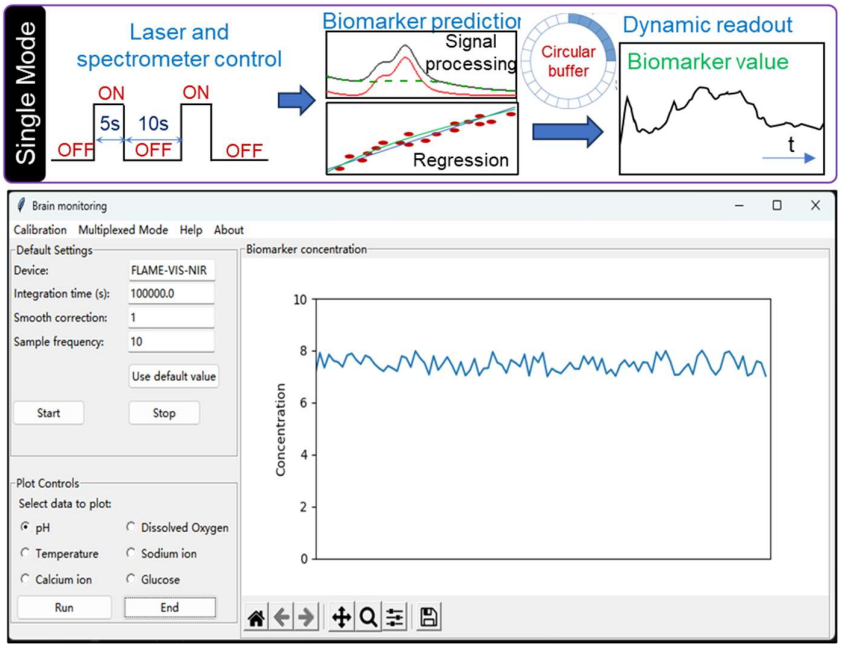


Figure S5. Dynamic monitoring mode of the system and user readout frame.

In multiplexed mode, 6 biomarkers are monitored simultaneously using the proposed CNN method, and the concentrations are displayed together in one frame for reference (**Figure S6**). The spectra collected by the spectrometer is on-line processed by the embedded regression model. Although in the multiplexed sensing mode, the dynamic of each biomarker is not presented due to the limited computational memory of the controller, the average biomarker concentration of the past 5 min is calculated and presented to indicate the trend of each biomarker concentration.

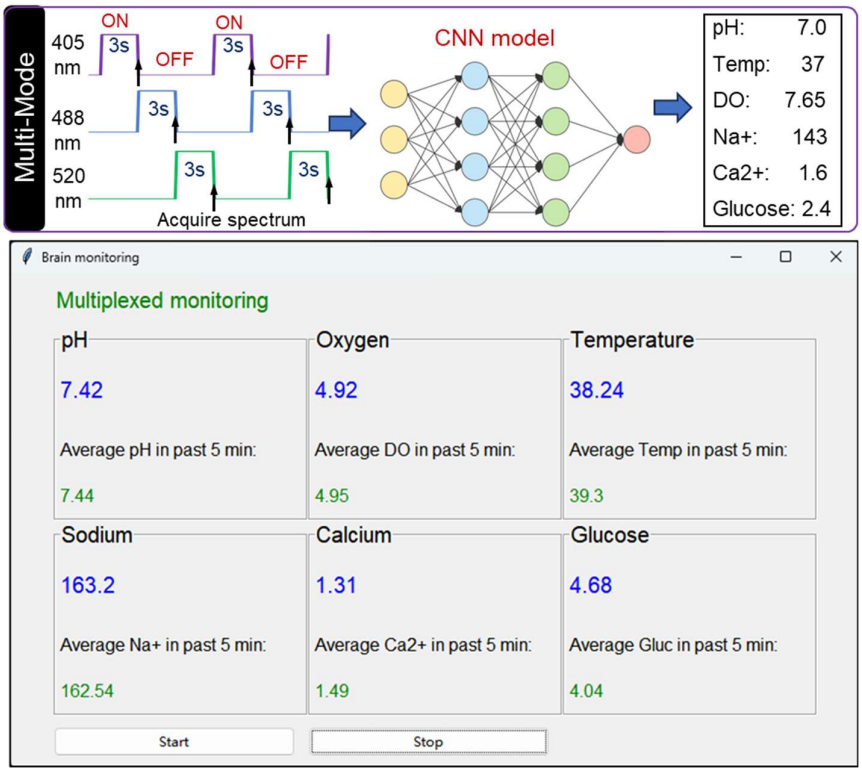


Figure S6. Multiplexed monitoring mode of the system and the software readout frame.

Permissions summary

Page No.	Work No.	Type of work:	Source of work	Copyright holder and contact	permission requested on	I have permission yes /no	Permission note
24	Figure 2-1	figure	Brain neurochemical monitoring	© 2021 Elsevier B.V.	04/03/2023	yes	Out of copyright
25	Figure 2-2	Figure	Brain neurochemical monitoring	© 2021 Elsevier B.V.	04/03/2023	yes	Out of copyright
27	Figure 2-3	Figure	Sugar for the brain: the role of glucose in physiological and pathological brain function	© 2013 Elsevier B.V.	23/11/2020	Yes	Out of copyright
33	Figure 2-4	Figure	Brain neurochemical monitoring	© 2021 Elsevier B.V.	04/03/2023	Yes	Out of copyright
34	Figure 2-5	Figure	Brain neurochemical monitoring	© 2021 Elsevier B.V.	04/03/2023	Yes	Out of copyright
35	Figure 2-6	Figure	Real-time neurochemical measurement of dynamic metabolic events during cardiac arrest and resuscitation in a porcine model	© Royal Society of Chemistry 2020	23/05/2024	Yes	Out of copyright
36	Figure 2-7	Figure	In vivo and continuous measurement of bisulfide in the hippocampus of rat's brain by an on-line integrated microdialysis/droplet-based microfluidic system.	© The Royal Society of Chemistry 2015	23/05/2024	Yes	Out of copyright

37	Figure 2-8	Figure	In Vivo Chemical Monitoring at High Spatiotemporal Resolution Using Microfabricated Sampling Probes and Droplet-Based Microfluidics Coupled to Mass Spectrometry	© 2018 American Chemical Society	23/05/2024	Yes	Out of copyright
38	Figure 2-9	figure	Brain neurochemical monitoring	© 2021 Elsevier B.V.	04/03/2023	Yes	Out of copyright
40	Figure 2-10	Figure	A highly selective amperometric biosensor array for the simultaneous determination of glutamate, glucose, choline, acetylcholine, lactate and pyruvate	© 2019 Elsevier B.V.	23/05/2024	Yes	Out of copyright
41	Figure 2-10	figure	In vivo continuous and simultaneous monitoring of brain energy substrates with a multiplex amperometric enzyme-based biosensor device	© 2014 Elsevier B.V.	23/05/2024	Yes	Out of copyright
41	Figure 2-11	figure	An implantable multifunctional neural microprobe for simultaneous multi-analyte sensing and chemical delivery	© The Royal Society of Chemistry 2020	27.05.15	yes	Out of copyright
42	Figure 2-12	figure	A Multichannel Flexible Optoelectronic Fiber Device for Distributed Implantable	© 2021 Wiley-VCH GmbH	27.05.15	yes	Out of copyright

			Neurological Stimulation and Monitoring				
43	Figure 2-13	figure	Flexible Electronics and Materials for Synchronized Stimulation and Monitoring in Multi-Encephalic Regions	© 2020 WILEY-VCH Verlag GmbH & Co. KGaA, Weinheim	27.05.15	yes	Out of copyright
44	Figure 2-14	figure	Long-term dopamine neurochemical monitoring in primates	Not required. Open access	27.05.15	yes	Out of copyright
44	Figure 2-15	figure	Brain neurochemical monitoring	© 2021 Elsevier B.V.	04/03/2023	Yes	Out of copyright
45	Figure 2-16	figure	Brain neurochemical monitoring	© 2021 Elsevier B.V.	04/03/2023	Yes	Out of copyright
48	Figure 2-17	figure	Wireless optoelectronic photometers for monitoring neuronal dynamics in the deep brain	Not required. Open access	27.05.15	yes	Out of copyright
49	Figure 2-18	figure	Brain neurochemical monitoring	© 2021 Elsevier B.V.	04/03/2023	Yes	Out of copyright
50	Figure 2-19	figure	Surface-Enhanced Raman Scattering Active Gold Nanoparticles with Enzyme-Mimicking Activities for Measuring Glucose and Lactate in Living Tissues	© 2017 American Chemical Society	27.05.15	yes	Out of copyright

52	Figure 2-20	figure	Brain neurochemical monitoring	© 2021 Elsevier B.V.	04/03/2023	Yes	Out of copyright
53	Figure 2-21	figure	Monitoring the electrochemical responses of neurotransmitters through localized surface plasmon resonance using nanohole array	© 2016 Elsevier B.V.	27.05.15	yes	Out of copyright
55	Figure 2-22	figure	Highly sensitive detection of dopamine using a graphene functionalized plasmonic fiber-optic sensor with aptamer conformational amplification	© 2018 Elsevier B.V.	27.05.15	yes	Out of copyright
57	Figure 2-23	figure	Portable oxygen-sensing device for the improved assessment of compartment syndrome and other hypoxia-related conditions	© 2020 American Chemical Society	27.05.15	yes	Out of copyright
58	Figure 2-24	figure	An antibody-based molecular switch for continuous small-molecule biosensing	Not required. Open access	27.05.15	yes	Out of copyright
60	Figure 2-25	figure	A new method using Raman spectroscopy for in vivo targeted brain cancer tissue biopsy	Not required. Open access	27.05.15	yes	Out of copyright
60	Figure 2-25	figure	Glucose-sensitive hydrogel optical fibers	Not required.	27.05.15	yes	Out of copyright

			functionalized with phenylboronic acid	Open access			
65	Figure 2-26	figure	Comparison Study of Partial Least Squares Regression Analysis and Principal Component Analysis in Fast-Scan Cyclic Voltammetry	Not required. Open access	27.05.15	yes	Out of copyright
66	Figure 2-27	figure	A User-Configurable Headstage for Multimodality Neuromonitoring in Freely Moving Rats	Copyright © 2016 Limnuson, Narayan, Chiluwal, Golanov, Bouton and Li.	27.05.15	yes	Out of copyright
73-136	Figure 3-1-Figuure 3-44	Figure	Multiplexed optical fiber sensors for dynamic brain monitoring	Open access and I am the author	27.05.15	yes	Out of copyright